Infrared spectroscopic characterization of functional molecular ions isolated in the gas phase

Fingerprinting redox pairs

M. (Musleh) U. Munshi

Musleh Uddin Munshi
Infrared spectroscopic characterization of functional molecular ions isolated in the gas phase: Fingerprinting redox pairs
PhD Thesis, Radboud University Nijmegen, The Netherlands

ISBN: 978-94-028-1668-6

Cover design by Musleh Uddin Munshi
Printed by Ipskamp Printing
Sint Annastraat 99
6524 EK Nijmegen

Infrared spectroscopic characterization of functional molecular ions isolated in the gas phase

Fingerprinting redox pairs

Proefschrift

ter verkrijging van de graad van doctor
aan de Radboud Universiteit Nijmegen
op gezag van de rector magnificus prof. dr. J.H.J.M. van Krieken,
volgens besluit van het college van decanen
in het openbaar te verdedigen op
dinsdag 15 oktober 2019
om 16:30 uur precies

door

Md Musleh Uddin Munshi

geboren op 31 december 1983
te Comilla (Bangladesh)

Promotor:

Prof. dr. Jos Oomens

Copromotor:

Dr. Giel Berden

Manuscriptcommissie:

Prof. dr. Wybren Jan Buma (voorzitter)

Prof. dr. Jana Roithová

Prof. dr. Nicolas C. Polfer
(University of Florida, Gainesville, Verenigde Staten van Amerika)

Dit werk is mede mogelijk gemaakt door financiering van de Nederlandse Organisatie voor Wetenschappelijk Onderzoek (NWO), Chemische Wetenschappen, middels VICI-project nr. 724.011.002. Berekeningen in dit werk zijn uitgevoerd op de Nederlandse nationale e-infrastructuur met steun van Coöperatie SurfSARA en het NWO-programma Rekentijd. Het experimentele deel van dit werk is uitgevoerd binnen het FELIX Laboratorium.

Infrared spectroscopic characterization of functional molecular ions isolated in the gas phase

Fingerprinting redox pairs

Doctoral Thesis

to obtain the degree of doctor
from Radboud University Nijmegen
on the authority of the Rector Magnificus prof. dr. J.H.J.M. van Krieken,
according to the decision of the Council of Deans
to be defended in public on
Tuesday 15 October 2019
at 16:30 hours

by

Md Musleh Uddin Munshi

born on 31 December 1983
in Comilla (Bangladesh)

Supervisor:

Prof. dr. Jos Oomens

Co-supervisor:

Dr. Giel Berden

Doctoral Thesis committee:

Prof. dr. Wybren Jan Buma (Chair)

Prof. dr. Jana Roithová

Prof. dr. Nicolas C. Polfer
(University of Florida, Gainesville, United States of America)

This work has been supported by funding from the Netherlands Organization for Scientific Research (NWO), Chemical Sciences, through VICI project no. 724.011.002. Calculations in this work were performed on the Dutch national e-infrastructure with the support of SurfSARA and the NWO program "Rekentijd". The experimental part of this work was performed within the FELIX Laboratory of the Radboud University.

List of Publications

The research described in this thesis is based on the following articles:

- Musleh Uddin Munshi, Jonathan Martens, Giel Berden and Jos Oomens, Gas-Phase Infrared Ion Spectroscopy Characterization of Cu(II/I)Cyclam and Cu(II/I)2,2′-Bipyridine Redox Pairs,
  J. Phys. Chem. A **2019**, 123, 19, 4149-4157 (chapter 3).
- Musleh Uddin Munshi, Stephanie M. Craig, Giel Berden, Jonathan Martens, Andrew F. DeBlase, David J. Foreman, Scott A. McLuckey, Jos Oomens and Mark A. Johnson, Preparation of labile Ni^+(cyclam) cations in the gas phase using electron-transfer reduction through ion–ion recombination in an ion trap and structural characterization with vibrational spectroscopy,
  J. Phys. Chem. Lett. **2017**, 8, 5047-5052 (chapter 4).
- Musleh Uddin Munshi, Jonathan Martens, Giel Berden and Jos Oomens, Vibrational spectra of the ruthenium-tris-bipyridine dication and its reduced form in vacuo,
  (Manuscript under preparation) (chapter 5).
- Musleh Uddin Munshi, Giel Berden, Jonathan Martens and Jos Oomens, Gas-phase vibrational spectroscopy of triphenylamine: the effect of charge on structure and spectra,
  Phys. Chem. Chem. Phys. **2017**, 19, 19881-19889 (chapter 6).
- Musleh Uddin Munshi, Jonathan Martens, Giel Berden and Jos Oomens, Proto-isomerization of indigo and isoindigo dyes confirmed by gas phase infrared ion spectroscopy,
  (Accepted for publication *J. Phys. Chem. A* **2019** (chapter 7).

The author has also contributed to the following body of work:

- Y. Zhu, L.A. Hamlow, C.C. He, H.A. Roy, N. A. Cunningham, M. U. Munshi, G. Berden, J. Oomens and M. T. Rodgers, Conformations and N-Glycosidic Bond Stabilities of Sodium Cationized 2′-Deoxycytidine and Cytidine: Solution Conformation of $[\mathrm{Cyd+Na}]^+$ is Preserved upon ESI,
Int. J. Mass Spectrom. **2018**, 429, 18-27
- Y. Zhu, H. A. Roy, N. A. Cunningham, S. F. Strobehn, J. Gao, M. U. Munshi, G. Berden, J. Oomens and M. T. Rodgers, IRMPD Action Spectroscopy, ER-CID Experiments, and Theoretical Studies of Sodium Cationized Thymidine and 5-Methyluridine: Kinetic Trapping During the ESI Desolvation Process Preserves the Solution Structure of $[\mathrm{Thd+Na}]^+$,
J. Am. Soc. Mass Spectrom. **2017**, 28, 2423-2437
- Y. Zhu, H. A. Roy, N. A. Cunningham, S. F. Strobehn, M. U. Munshi, G. Berden, J. Oomens and M. T. Rodgers, Effects of sodium cationization versus protonation on the conformations and N-glycosidic bond stabilities of sodium cationized Urd and dUrd: solution conformation of $[\mathrm{Urd+Na}]^+$ is preserved upon ESI,
Phys. Chem. Chem. Phys. **2017**, 19, 17637-17652.
- Jean-François Boily, Merve Yeşilbaş, Munshi Md. Musleh Uddin, Lu Baiqing, Yulia Trushkina and Germàn Salazar-Alvarez, Thin water films at multifaceted hematite particle surfaces,
Langmuir, **2015**, 31, 48, 13127-13137.

To my respected teachers

List of Abbreviations

IR	**I**nfra**R**ed
IRIS	**I**nfra**R**ed **I**on **S**pectroscopy
IRMPD	**I**nfra**R**ed **M**ultiple **P**hoton **D**issociation
IRPD	**I**nfra**R**ed **P**ree-**D**issociation
MS	**M**ass **S**pectrometry
3D	**3 D**imensional
ESI	**E**lectro**S**pray **I**onization
QIT	**Q**uadruple **I**on **T**rap
FTICR	**F**ourier **T**ransform **I**on **C**yclotron **R**esonance
SWIFT	**S**tored **W**aveform **I**nverse **F**ourier **T**ransform
CID	**C**ollisional **I**nduced **D**issociation
ETD	**E**lectron **T**ransfer **D**issociation
ETR	**E**lectron **T**ransfer **R**eduction
LINAC	**LIN**ear **AC**celerator
FEL	**F**ree **E**lectron **L**aser
FELIX	**F**ree **E**lectron **L**aser for **I**nfrared e**X**periment
OPO	**O**ptical **P**arametric **O**scillator
MALDI	**M**atrix **A**ssisted **L**aser **D**esorption **I**onizatio
DSSC	**D**ye **S**ensitized **S**olar **C**ell
TPA	**T**ri**P**henyl**A**mine
IVR	**I**ntramolecular **V**ibrational **R**edistribution
RF	**R**adio **F**requency
CI	**C**hemical **I**onization
UV	**U**ltra**V**iolate
TDAE	**T**etrakis(**D**imethyl**A**mino)**E**thylene

DoS	**D**ensity of **S**tates
MLCT	**M**etal-to-**L**igand **C**harge **T**ransfer
LIT	**L**inear **I**on **T**rap
APCI	**A**tmospheric **P**ressure **C**hemical **I**onization
BO	**B**orn-**O**ppenheimer
DFT	**D**ensity **F**unctional **T**heory
HF	**H**artree **F**ock
SCF	**S**elf-**C**onsistent **F**ield
KS	**K**ohn-**S**ham
XC	e**X**change-**C**orrelation
LCAO	**L**inear **C**ombination of **A**tomic **O**rbitals
LSDA	**L**ocal **S**pin **D**ensity **A**pproximation
GGA	**G**eneralized **G**radient **A**pproximation
RSH	**R**ange-**S**eparated **H**ybrid
STO	**S**later **T**ype **O**rbitals
GTO	**G**aussian **T**ype **O**rbitals
ADF	**A**msterdam **D**ensity **F**unctional
ECP	**E**ffective **C**ore **P**seudopotential
MP2	2nd order **M**øller-**P**lesset **P**erturbation **T**heory
CCSD	**C**oupled-**C**luster with **S**ingle and **D**ouble excitations
CASPT2	**C**omplete **A**ctive **S**pace with **S**econd **O**rder **P**erturbation **T**heory

Contents

Chapter 1

General Introduction and Experimental Methods

1.1 Introduction

Molecular vibrational frequencies are extremely sensitive to the intramolecular chemical environment, so that IR spectra reveal deep insight into the structure of a molecule. For instance, presence or absence of functional groups, presence and location of charge, symmetry, secondary structure of proteins and hydrogen bonding interactions can all be derived from IR spectral investigations. This thesis is concerned with determining molecular structures for ionized molecules based on gas-phase IR measurements. Conventional absorption spectroscopy of molecular ions is challenging due to the inherently low ion densities ($<10^8$ ion cm^{-3}) of gaseous ions as a consequence of Coulombic repulsion. Such low densities give unobservably small absorption signals and infrared ion spectroscopy (IRIS) is used here to overcome to this problem.

Infrared ion spectroscopy has been exceedingly successful in elucidating ionic molecular geometries in terms of conformations, protonation sites, radical sites, metal ion coordination motifs, including also structures of MS/MS fragments in tandem mass spectrometry. Tunable infrared lasers coupled to mass spectrometry platforms allow one to record infrared action spectra of molecular ions [1–8]. Ion spectroscopy has become a key technology in ion chemistry over the past decades especially to reveal structural information that is not obtainable from MS/MS experiments only [9, 10].

Experimental IR spectra are now routinely compared to the theoretically calculated linear infrared spectra to interpret the spectra and then to extract the corresponding 3D structural information of the system. With the current level of sophistication and efficiency of theoretical modeling based on quantum mechanics, this has become an extremely reliable method to understand and predict the electronic and geometric properties of molecules.

IRIS basically constitutes the coupling of tunable IR lasers with tandem mass spectrometers, which enables one to record IR spectra based on the wavelength-dependent photo-dissociation of the ions in the mass spectrometer. In this thesis a set of functional molecular ions has been investigated using both experiment and theory. We employ the features offered by a newly developed quadrupole ion trap (QIT) mass spectrometry platform in combination with the widely tunable radiation from the FELIX free-electron laser [11].

Our aim is especially to take advantage of the electron transfer dissociation (ETD) option of the QIT MS, which was initially designed for peptide dissociation in order to determine the amino acid sequence of peptides and proteins. Here, this ETD option is employed to induce one-electron charge reduction (without dissociation) of multiple positively charged metal-ligand complex ions, which enables us to investigate the gas-phase structure of these systems both in their oxidized as well as in their reduced form. In this first chapter, after an introduction to the systems of interest, the experimental method is described starting from a brief overview of infrared ion spectroscopy, highlighting in particular infrared free electron laser (IR FEL) based methods. Theoretical methods used in this thesis are described separately in chapter 2.

1.2 The dawn of infrared ion spectroscopy

In the late 1970s, the first demonstration of infrared (IR) laser-induced photodissociation of gaseous trapped ions was performed with relatively high-power CO_2 lasers [12–15]. The narrow wavelength tunability of CO_2 lasers (9 to 11 μm) was a severe limitation in probing useful and structurally diagnostic IR spectra. Within this wavelength range, the wavelength of these lasers is line tunable as dictated by rotational/vibrational emission lines of the excited CO_2 molecules. Nevertheless, despite these limitations, the CO_2 laser has been applied to various cationic and anionic systems in the 10 μm region often for isomeric identification up to the 1990s. In these early studies, experimental spectra were generally not yet compared to quantum-chemically calculated spectra, which further limited the structural detail that could be obtained from the spectra.

Over the past 3 decades, the development and construction of new wavelength tunable IR laser sources, especially free electron (FEL) lasers and optical parametric oscillator/amplifiers (OPO/OPA), has renewed the interest in recording IR spectra of gaseous ions, ranging in size from simple amino acids to entire proteins [1, 6, 16–20]. The main advantage of these two laser sources is their wavelength coverage of the chemically important IR fingerprint region (3 to 20 μm). Characteristics of these laser sources are provided in brief in section 1.8. Continuous and broad wavelength tunability and high pulse energies make these sources ideal for action spectroscopic applications.

Infrared action spectra have been recorded employing various experimental apparatuses especially involving different types of mass spectrometers, such as time-of-flight, FTICR, and quadrupole ion trap (QIT) MS systems. Various comprehensive articles [1, 21] and reviews [5, 6, 17, 22, 23] have been published in the last decade giving good overviews of the type of photodissociation measurements and the variety of systems that have been studied [7].

The use of IR photodissociation spectroscopy has been particularly successful with electrospray ionization (ESI) [24] sources as well as and matrix assisted laser desorption ionization (MALDI) [25] techniques are introduced in Fourier transform ion cyclotron resonance (FTICR) mass spectrometers [26–28], which are able to bring (large) biomolecular ions into the gas phase without fragmentation.

For infrared ion spectroscopy, a commonly used scheme is infrared multiple photon dissociation (IRMPD), which requires relatively high energy laser source in order to dissociate a covalent bond of a molecular ion. In this technique slow absorption of many photons results in a gradual increase of the ion internal energy until unimolecular dissociation occurs [7, 29]. Although not discussed in detail here, we note that there are numerous alternative action spectroscopy techniques available to provide infrared spectra of ionized species [7, 30–36]. All of these methods have in common that the vibrational modes of the molecule are probed with resonant photoexcitation with tunable IR lasers.

One very popular alternative infrared ion spectroscopy technique pioneered by Y.T. Lee and co-workers in the 1980s [37] is infrared pre-dissociation (IRPD) spectroscopy. Here, a weakly bound neutral gas molecule or a rare gas atom (known as the "tag") is non-covalently condensed onto the cationic or anionic system of interest at cryogenic temperatures. The tag evaporates upon resonance excitation of a vibrational modes of the analyte ion by a tunable IR laser, where a single IR photon is sufficient to remove the weakly bound tag. This event is monitored as a function of IR wavelength, generating an IRPD spectrum. It is common practice also to compare IRPD spectra to theoretically calculated linear IR spectra for structural elucidation. A key challenge is the generation of tagged-ions where tag minimally influences the analyte. It has been a very powerful and sensitive technique to obtain IR spectra of gaseous molecular ions at cryogenic temperatures. Many research groups employ IRPD ion spectroscopy using tunable lasers with relatively low pulse energies [38–44].

In this thesis, mostly the IRMPD technique was used, although IRPD was used for one particular system, which also highlights the similarities between the techniques. An example of a bare complex and an analogous N_2-tagged complex shows the contrasts and similarities between IRMPD and IRPD in subsection 1.10.3.

1.3 IRMPD spectroscopy with FELs

A large number of IR ion spectroscopy studies have been carried out employing the various MS platforms at one the international FEL user facilities, the Free Electron Laser for Infrared eXperiment (FELIX) at Radboud University, Nijmegen, the Netherlands and the Centre Laser Infrarouge Orsay (CLIO) in Orsay, France [45, 46]. The FEL in Nijmegen was previously located at the FOM-Institute for Plasma Physics Rijnhuizen in Nieuwegein, the Netherlands [11] and was moved to Nijmegen in 2013. A brief overview of the mass spectrometry instruments used in these experiments is presented here.

The earliest FEL-based ion spectroscopy experiments were carried out with relatively simple tandem mass spectrometers. At the FEL facility in Rijnhuizen, a radio frequency Paul-type QIT was used and this instrument was modified to enable optical access to the stored ion cloud facilitating irradiation of the trapped ions. The main modification involved the introduction of two holes in the ring electrode of the QIT [29]. In this instrument, ions were generated via non-resonant UV laser photo-ionization of (poly-)aromatic molecules which were evaporated from a small oven.

Next, in collaboration with researchers from the NHFML in Tallahassee and the University of Florida in Gainesville, a homebuilt FTICR MS was constructed at the FELIX Laboratory utilizing a 4.7 T superconducting magnet [47, 48]; this instrument is briefly described in subsection 1.7.4. Optical access to the ion cloud in the ICR cell is enabled in such a way that the polished copper excite-electrodes of the ICR cell act as a multi-pass reflection cell for the lasers (FEL, OPO/OPA). In addition, on-axis single pass optical access is also possible for a second laser, for instance, a CO_2 laser, which can either be used as an alternative to collision induced dissociation (CID) or as a post-excitation method to boost the IRMPD effciency [6, 49–51].

At CLIO, early IRMPD experiments were carried out in an FTICR MS having a portable permanent magnet, MICRA [52]. Later, a 7 T Bruker FTICR MS was coupled to the FEL at CLIO [53]. A commercial Paul-type quadrupole ion trap MS (Bruker Esquire 3000) was modified to enable FEL access and installed at CLIO as well [54]. All of these instruments feature a single pass of the FEL beam producing adequate fragmentation of the trapped ions. In addition to the FELIX and CLIO facilities, a smaller number of experiments were reported from the FEL facility at the Science University Tokyo (SUT), where a commercial (Bruker) 4.7 T FTICR MS [55] was utilized and from the Fritz-Haber institute in Berlin, where a relatively new IR FEL has been constructed and used for recording IR ion spectra in various homebuilt MS platforms [56].

In contrast to FEL sources, OPO/OPA lasers have limited pulse energies and are therefore somewhat restricted for use in IRMPD spectroscopy. However, OPO/OPA lasers have been successfully utilized in IRMPD spectroscopy for many systems in the wavelength range around 3 μm [6, 18, 51, 57]. The McLafferty group reported the first coupling of an OPO/OPA laser system to an FTICR MS reporting IR spectra of gaseous protonated proteins [58]. Similarly, the Williams laboratory at UC Berkeley also coupled an OPO/OPA system covering wavelengths from 1.35 to 5 μm to a laboratory-built FTICR MS [57]. Polfer and Eyler at the University at Florida coupled a continuous-wave OPO source to an FTICR-MS instrument [17, 59].

In the ongoing development of the FEL based IR ion spectroscopy, the recent coupling of a commercial Paul-type QIT MS (Bruker amaZon speed ETD) to the FELIX beamline [60] opens the possibility of utilizing the on-board MS^n features, that were especially designed for proteomics studies, in ion chemistry and ion spectroscopy studies. This type of mass spectrometers are also optimized for analytical applications, such as for the analysis of human metabolites, due to its high-sensitivity towards low-abundance analytes (down to nM) and fast mass analyzing power. Integration of IR ion spectroscopy with such analytical MS applications especially in the identification of unknown compounds is also a rapidly growing application in our lab. A more detailed description of this instrument will be provided in the following sections.

1.4 Comprehensive gas-phase chemical analysis using IRIS

In the field of ion spectroscopy, mass spectrometers with ion storage capability are crucial as they enable the irradiation of the ions for longer periods of time, such that the number of laser pulses can be varied depending on the dissociation threshold of the species under study. In addition, storage mass spectrometers with MS^n-capability allow one to spectroscopically study MS/MS reaction products. Although FTICR MS and QIT MS have been employed in this thesis, both having ion storage capability, the QIT MS is used almost exclusively because of its sensitivity, high duty cycle, and its extensive CID and ETD options. An impression of this commercial QIT MS and its coupling to the IR laser beam [60] is shown in Figure 1.1. A brief overview is presented below focusing on the different features and showcasing some previous studies employing this QIT MS.

The QIT is a versatile mass analyzer [62] offering multistage mass spectrometry (MS^n) analyses, allowing multiple CID and isolation of one of the fragment ions [63]. CID is by far the most widely used method for ion dissociation, and is for instance routinely used in protein and peptide sequencing [64]. It is interesting to note that the reaction mechanisms underlying peptide fragmentation have been elucidated using IR-IS [10]. Apart from this, the QIT allows for ion/ion reactions between cationic and anionic species, as is for instance

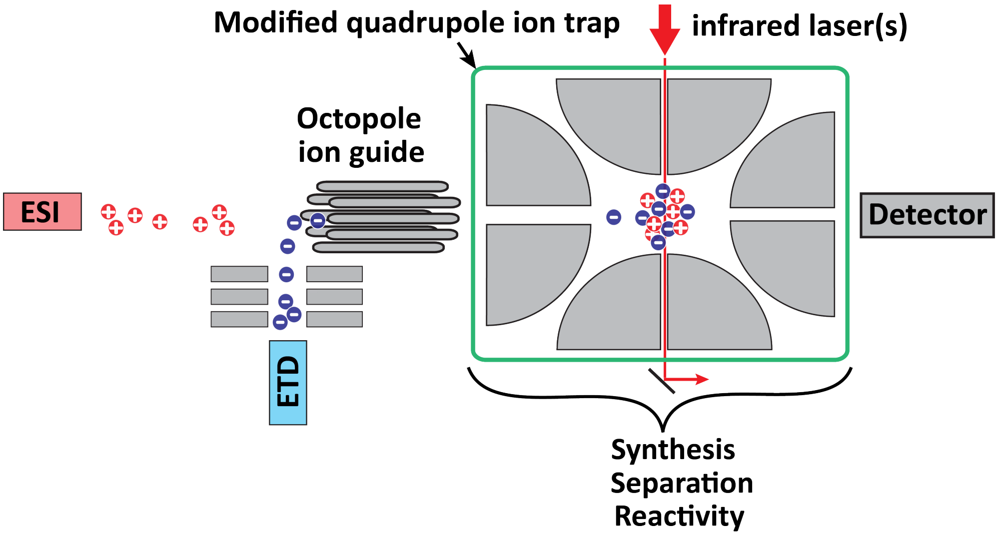

Figure 1.1. Schematic diagram of the modified QIT MS for ion spectroscopic measurements where modification involved making holes (3 mm diameter) through the ring electrode for optical access. Ions generated *via* electrospray (ESI) are transferred and guided through the octopole ion guides to the trap. Ions are recognized and separated based on their *m/z*, then subjected to CID, ETD and ion-molecule reactions [2, 61] prior to IR-IS. Additional negative chemical ionization source (ETD source) from where an electron donor reagent (fluoranthene radical anion [8]) can be extracted out and added with the previously isolated cations for ion/ion reaction. For instance, if the previously isolated ions are dication, charge reduced (monocation) ion can be generated from the ion/ion reaction. After donating an electron, the fluoranthene-radical-anion leaves the trap as a neutral. To record IR spectra of the trapped ions, the QIT is modified so that tunable lasers can pass through the trapped ion cloud—which enables photofragmentation. (see Figure 1.2).

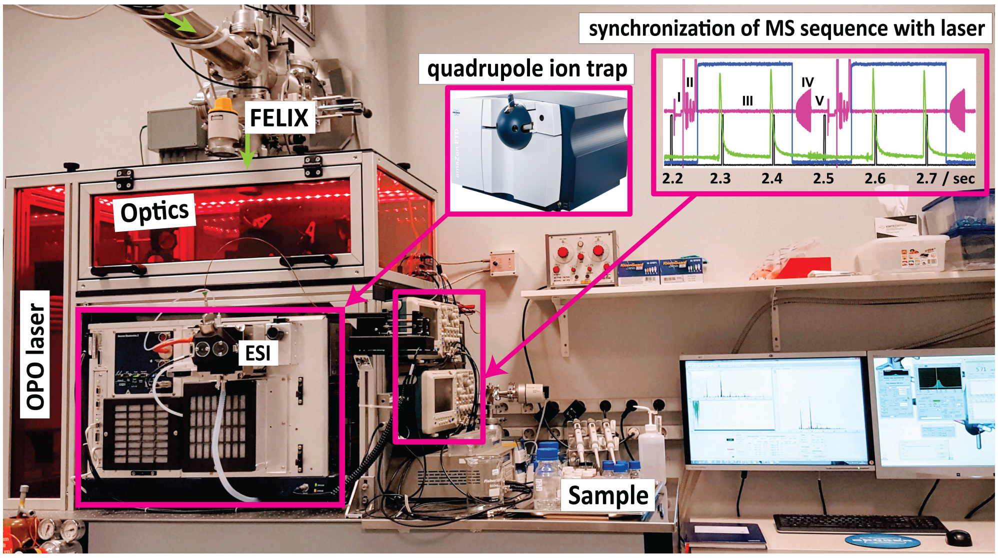

Figure 1.2. IR laser(s) coupled to the modified QIT MS for ion spectroscopy at the FELIX laboratory, Nijmegen. Synchronization of MS sequence with laser is described in Figure 1.20.

used in electron transfer dissociation (ETD), another dissociation method used in peptide sequencing [64]. In ETD, an electron is transfered from a negative to a multiply charged positive ion inducing dissociation of the latter; it is also employed in sequencing and can provide more extensive sequence coverage [65, 66]. Although ETD was believed to be a non-ergodic process, this has been disproved. In ETD, the reduced, odd-electron species undergo dissociation mainly at the peptide backbone N-C_α bond, in contrast to dissociation at the peptide (N-CO) bonds observed mostly upon CID [67]. Structural characterization of ETD induced product ions by IR ion spectroscopy has also been demosntrated recently, yielding valuable information on ETD fragmentation mechanisms [8, 10].

In this thesis, we apply a commercial QIT platform coupled to FELIX (Figure 1.2) to investigate a group of important molecules which have direct applications in various fields, including catalysis, dye sensitized solar cells (DSSC), charge-induced mechanical devices. These systems cover both metal and non-metal species where the change of the charge state plays a crucial role in their various functions.

1.5 Why study functional molecules in the gas phase?

Functional molecular species govern many important chemical reactions, but understanding their reactivity in the condensed phase is often complicated by **(a)** the presence of the solvent environment, **(b)** various isomeric forms that may be present, **(c)** reactions involving radicals (cation/anion), **(d)** charge states with their spin multiplicities and **(e)** reactions involving heterogeneous catalysis. As a result, understanding the structure-function relationship is often inadequate.

Isolating the molecular system in the gas-phase has the advantage that it removes the crowded environment, which brings greater simplicity not only to the experiment, but also to the theoretical modeling. For instance, density functional theory (DFT) based modeling has been used to predict spectroscopic and electronic structure properties, and usually return accurate results thanks to the absence of any solvent environment. In general, despite the enormous successes of DFT, it is often challenging to predict the physical and spectroscopic properties for *open-shell* systems [68, 69]. Moreover, *open-shell* electronic systems with transition metals are notoriously difficult to model because of the presence of near-degeneracy correlation among the partially filled d shells [70, 71]. Experimental data of these systems can aid in the development of theoretical methods, especially when the data are taken in pure isolation, mitigating complications arising from including the effects of an environment in the calculations. Gas-phase experimental data of *open-shell* systems are therefore not only extremely valuable for the theoretical development, but also help understand the existing limitations of theoretical methods. Theory would thus serve to predict the best systems for molecular functionality on the one hand, and it would help to better understand experiment on the other hand. In this regard, mass spectrometry coupled with tunable infrared laser(s) (Figure 1.1) offers an opportunity to scrutinize the intrinsic spectroscopic and structural properties of ionic complexes in the gas phase.

Transition metal complexes as homogeneous catalysts have been investigated in organic synthesis for more than two centuries. Transition metal-ligand complexes form coordination bonds which are interestingly different from covalent and ionic bonds [72]. An important aspect of these studies involves the catalyst geometry: design of the ligand, manipulation of the charge state and determination of the electronic excited states have continued to be productive areas of active research in homogeneous catalysis.

Transition metal ions form variable oxidation states that can be divided into naturally occurring and non-naturally occurring; the former are stable whereas the latter are generally unstable and short lived in condensed media. Transition metal ion complexes change their oxidation states through oxidation-reduction (redox) reactions during catalysis. The resulting oxidation states which are not naturally occurring are extremely difficult to synthesize and isolate, prohibiting their detailed characterization. In addition, spin multiplicity of such complexes can vary depending on the charge state and coordination environment [73] around the metal ion. Spin states can also be temperature dependent as was shown for the ^{54}Fe(phen)$_2$(NCS)$_2$ complex, being low-spin at 100 K while high-spin at 298 K, as determined by IR absorption spectroscopy [74]. The geometry of transition metal-ligand complexes in charge states differing by one would allow us to explore how the number of the d-electrons (on metal ion) affects the global geometry, as the system converts from oxidized to reduced form and vice versa.

The QIT has been used to study ion chemistry of transition metal complexes where the oxidation states of the complexes were limited by what can be produced by the ion source. For instance, an ESI source is only capable to generate coordination complexes with the metal ion in one of its natural oxidation states. In this regard, the ETD option of the QIT offers an interesting solution as the ion/ion reaction can convert a multiply-charged cation into its one-electron reduced oxidation state by the donation of an electron from the ETD reagent. The only challenge here is that this is an exothermic charge recombination process releasing energies up to $\sim$8 eV, which may cause dissociation of the reduced complex; note that the ETD option is used exactly for this purpose in protein/peptide fragmentation, namely as an activation method which results extensive product formation [64, 66]. In this thesis, we aim to use this ETD option to induce charge reduction of metal-ligand complexes without further dissociation, i.e., to form the intact, charge-reduced coordination complex. We refer to this process as electron transfer reduction (ETR) instead of ETD. Experimentally, this gives us access to both members of a redox pair in the gas-phase. As such, we devise a general experimental approach to generate metal-ligand complexes, manipulate their charge and ligand environment selectively, and characterize them using IRIS. Also, this allows to investigate differences between *open-shell* and *closed-shell* systems. In general, experimental information about *open shell* systems is scarce.

Several practical examples are presented involving the study of intrinsic geometrical changes induced by charge. Below, a brief overview of the different studies is presented. In the first one we validate our ideas investigating the charge reduction of a doubly-charged metal-ion ligand complex with different methods (including ETR) to access both members of the redox pair. Following this example, similar redox pairs are considered, including some non-metal systems, where molecular charge plays a crucial role in the physico-chemical transformations of functional molecules that find applications in different fields. Here, the charge state of the neutral functional molecular system, of relevance for instance in catalysis, sensitizers in DSSCs and molecular machines, is manipulated through oxidation and protonation in an ESI source.

1.5.1 Method validation: Cu-ligand redox pairs

Figure 1.3 shows the first example of a redox pair, the [$Cu^{2+/+}$(2,2′-bipyridine)$_2$] complex which is selected to validate our proposed experimental method. The dications form in solution and were brought into the QIT *via* ESI, enabling us to record their IR spectra employing IRIS. Next, the charge-reduced species is generated in the gas phase *via* ETR of the dication and its IR spectrum was recorded as well. The spectra were found to be different and diagnostic (chapter 3). As an alternative, the charge-reduced ion was also generated directly *via* ESI from solution. Its IR spectrum was found to be identical to that recorded for the ion formed by ETR. These observations indicate that the geometries thermalize upon charge reduction and that the monocation survives the energy deposited into the system by the charge recombination reaction.

After validation of our experimental method further investigations were undertaken. We changed the ligand from bidentate bpy to a chelating cyclic ligand (cyclam). This ligand forms a tetradentate complex with the metal ion which was compared with the coordination of two bpy ligands, which showed that the final geometry is dictated not only by the metal ion charge but also by the steric constraints of the ligand (chapter 3). Next, the metal center was changed, for instance investigating Ni(II/I)-cyclam complexes which has interesting applications in catalysis.

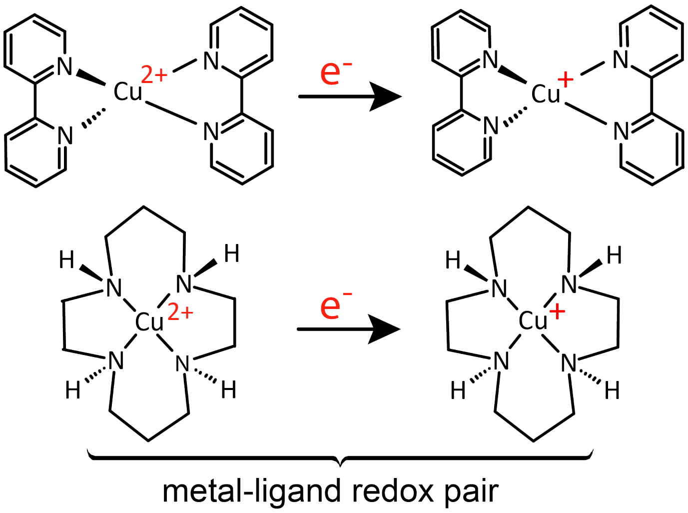

Figure 1.3. (*top*) Generation of [$Cu^{2+/+}$(2,2′-bipyridine)$_2$] and (*bottom*) [$Cu^{2+/+}$(cyclam)] redox pairs *via* an electron transfer reaction.

1.5.2 Catalysis

Transition metal organometallic complexes are known for their catalytic activation of small molecules. CO_2 activation by Ni^+ tetraaza macrocyclic ligand complexes has recently been reported in the gas-phase and in the bulk [75], where the oxidation state of the metal appeared to be key for the electrochemical reduction of CO_2. Structural characterization is essential in order to understand the mode of operation of this type of catalyst. Of central interest is the complex Ni(I)-cyclam (shown in Figure 1.4), which is difficult to generate in the gas phase by ESI from a solution of Ni salts and cyclam. However, the ETR technique allows us to generate the complex in the 1+ oxidation state by first forming the corresponding Ni(II)-cyclam complex by ESI, followed by charge reduction *via* ETR. The structural characterization of both these complexes by IRIS is described in detail in chapter 4.

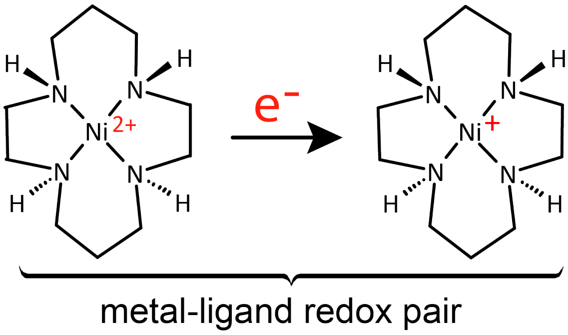

Figure 1.4. Generation of $[Ni^{2+/+}(cyclam)_2]$ redox pair *via* an electron transfer reaction.

1.5.3 Dye sensitized solar cells

Dye sensitized solar cells (DSSCs) were proposed by Brian O'Regan and Michael Grätzel in 1988 and are based on thin-film photovoltaic cells. The tris(2,2′-bipyridyl)Ru(II) complex has been the inspiration as a prototype metal-ligand based sensitizer in DSSC research ever since its introduction in 1991 [76]. A substantial body of work has been performed on this important complex and many of its derivatives, both experimental and theoretical, aiming at improved light-to-energy conversion efficiencies (chapter 5). The efficiency is yet to exceed ∼12% [77–80].

In DSSCs, redox reactions of the dye (i.e., the sensitizer) are essential for its

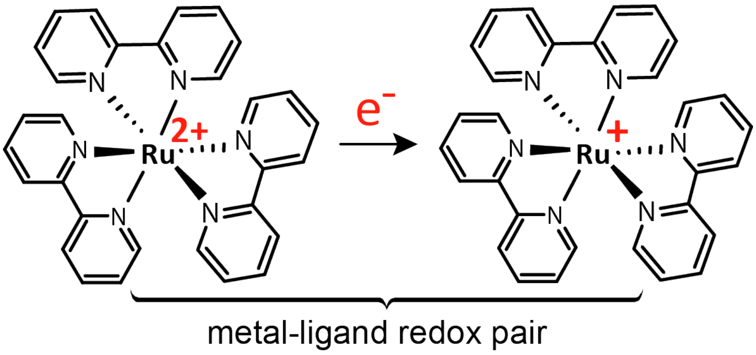

Figure 1.5. Generation of Tris(2,2′-bipyridyl)ruthenium redox pair via an electron transfer reaction.

functioning, involving shuttling between different charge states. Dye degradation over time is a critical issue, relating to the redox stability. In this perspective, we aim to understand the intrinsic structural changes upon a change of charge state, for instance, how the geometry changes as the dye is reduced from 2+ to 1+, or vice versa.

Previously, Nielsen et. al. [81, 82] recorded gas-phase UV-vis photo-dissociation spectra of tris(2,2′-bipyridyl)ruthenium complex for both of these charge states (Figure 1.5) in the gas phase, where the monocation was generated by charge reduction of the mass-selected (*m/z*) dication. Based on the observations and the theoretical interpretations using time-dependent DFT, they concluded that the charge-reduced species was less stable than the dication analogue. The experimental spectra of the charge-reduced species were much broader than the dication due to the overlap of the metal-to-ligand charge transfer (MLCT) transitions with the $\pi - \pi^*$ transition of the bpy ligand. As well, the reducing electron is mostly delocalized over the three bipyridyl ligands, instead of being localized at the ruthenium center, in agreement with earlier predictions [72]. Bear in mind that there are three equivalent bpy ligands. Opposing arguments exist on the location of the added electron, especially on whether it is localized on one of the bpy ligands or delocalized over all three of them, or on the metal center? These interesting questions triggered us to investigate the two members of this redox pair using IRIS.

In our QIT MS coupled to FELIX, we generate the isolated, gaseous tris(2,2′-bipyridyl)Ru(II) complex ion *via* ESI. The Ru(II) complex is then charge-reduced to Ru(I) using ETR, which mimics the charge reduction/oxidation in DSSCs mediated by a redox shuttle (I^-/I_3^-) [77]. Reduction of the dye by the same redox shuttle before oxidation by solar absorption is known as reductive quenching, which influences the solar cell efficiency. Understanding these reduction processes are crucial in the DSSCs. We record the fingerprint IR spectra of the tris(2,2′-bipyridyl)Ru(II) and tris(2,2′-bipyridyl)Ru(I) redox pair which are used to provide 3D geometrical information aided by DFT calculations (chapter 5).

1.5.4 Triphenylamine (TPA): diverse functions

Triphenylamine (Figure 1.6) and its derivatives have widely been incorporated as additional moieties in DSSC devices with the ruthenium dyes as sensitizers [83, 84] to suppress dye aggregation due to the propeller-like structure of TPA. TPA derivatives alone are also used in organic photovoltaics (OPV) as the core sensitizers [85, 86]. As well, TPA influences the charge recombination of the oxidized dye due to solar light absorption which increases the efficiency of the solar cell [87, 88]. The TPA molecule has been extensively studied [89](see chapter 6) as illustrated by the number of papers and citations (Figure 1.6).

Surprisingly the IR spectra of the radical cation of TPA has to our knowledge not been reported, neither in the condensed phase nor in the gas phase. IR spectrum of the neutral TPA in the gas phase is available [90]. Here, we provide the IR spectrum of the gaseous radical cation of TPA, with complete structural characterization and comparison to neutral TPA. Results are interpreted in terms of conjugation of the nitrogen lone pair electron(s) with the three phenyl rings in neutral and radical cation TPA (see chapter 6).

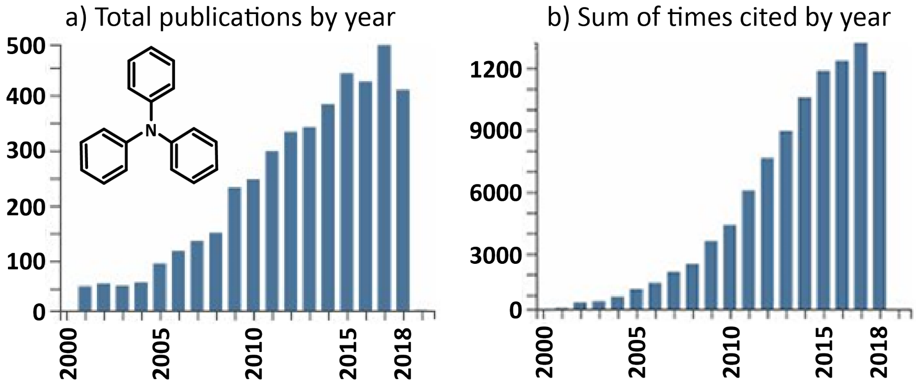

Figure 1.6. Shows the '**Web of Science**' search results for the topic 'triphenylamine' over the last 20 years which indicate number of publications (a), number of times cited (b) by year respectively (data retrieved Dec. 2018).

1.5.5 Charge induced mechanical properties

Ben L. Feringa, James F. Stoddart, Jean P. Sauvage (2016 'Nobel Prize') and co-workers contributed to the idea of switchable molecular systems — molecules which respond mechanically to external stimuli [91] — to employ mechanical properties such that molecular-sized switches and motors can be built. Light-driven *cis-trans* isomerization of double bonds of organic compounds is known for decades [92]. Apart from light, a wide range of catalysts such as addition of transition metal ion, proton or Lewis acids can trigger the interconversion from trans to cis isomer [93].

Indigo and thioindigo have been considered as prototypes of such systems, where thioindigo isomerized while indigo did not, because of the two strong H-bonds in indigo (see Figure 1.7) in its neutral form, which are absent in thioindigo [92, 93]. A recent theoretical study also supported this idea showing that protonated indigo has high transition state barrier which prevents pro-toisomerization [94]. Since this isomerization was well described in the condensed phase, our aim was to understand it in the gas phase instead, which adds intrinsic molecular characteristics devoid of interference from the solvent or surrounding environment.

To investigate the isomerization of indigo induced by proton attachment in the gas phase, we bring protonated indigo into the QIT MS using ESI. The protonated ions are then characterized by IRIS, which showed that indigo and isoindigo (isomer of indigo) did isomerize from trans to cis upon protonation, where *trans* was the only isomer in the neutral form (detail chapter 7).

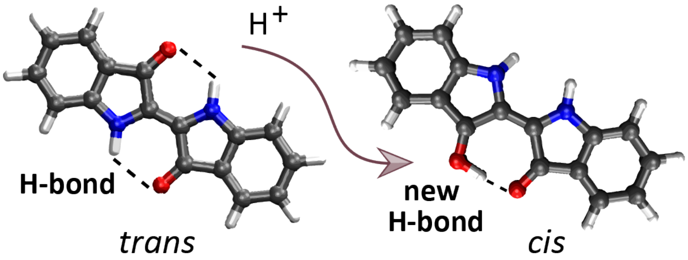

Figure 1.7. Proto-isomerization of indigo from trans to cis is shown.

1.6 Infrared ion spectroscopy

In this thesis, all molecular ionic systems are studied using IR ion spectroscopy (IRIS). This technique probes the IR spectra of gaseous ionized molecules.

Figure 1.8 outlines the concept to obtain IRMPD spectra of mass-isolated (*m/z*) ions. The mass-isolated ion (e.g., radical cation of triphenylamine) is irradiated with a tunable IR laser source. Once the laser frequency is in resonance with a vibrational mode of the molecule, the ion absorbs many IR photons. Due to this absorption the internal energy of the molecular ion increases. This energy then statistically distributes over all the internal degrees of freedom through intramolecular vibrational redistribution (IVR), until the molecule unimolecularly dissociates along the minimum energy pathway producing frequency-dependent fragment ion intensities along with reduced precursor ion intensities, simultaneously in the MS. The decrease of the precursor ions through unimolecular dissociation is directly related to the efficiency of the photon absorption at that particular laser frequency.

At any frequency the photo-fragmentation yield can be calculated by the Equation 1.1 which is related to the fragmentation rate k for a given IR pulse energy and the irradiation time t [95, 96].

$$\text{Yield} = \frac{\sum \text{Intensity}_{\text{Fragments}}}{\sum \text{Intensity}_{\text{Fragments}} + \text{Intensity}_{\text{Precursor}}} = 1 - \text{e}^{-\text{kt}} \tag{1.1}$$

In practice, Yield or -ln(1-Yield) is plotted (Figure 1.8) as a function of the laser frequency in order to construct IRMPD spectra (detail Appendix A, Figure A.1, A.2). -ln(1-Yield) can be considered as the fragment fluence and it turns out that this quantity scales linearly with the laser pulse energy and the irradiation time.

Theoretical modeling using DFT (section 2.1) yields a prediction for the (harmonic) vibrational frequencies of the molecular ion, which can be compared with the experimental spectrum in order to interpret the IRMPD spectra. A decent agreement is found in this example (Figure 1.8), validating the 3D structure of $\text{TPA}^{\cdot+}$.

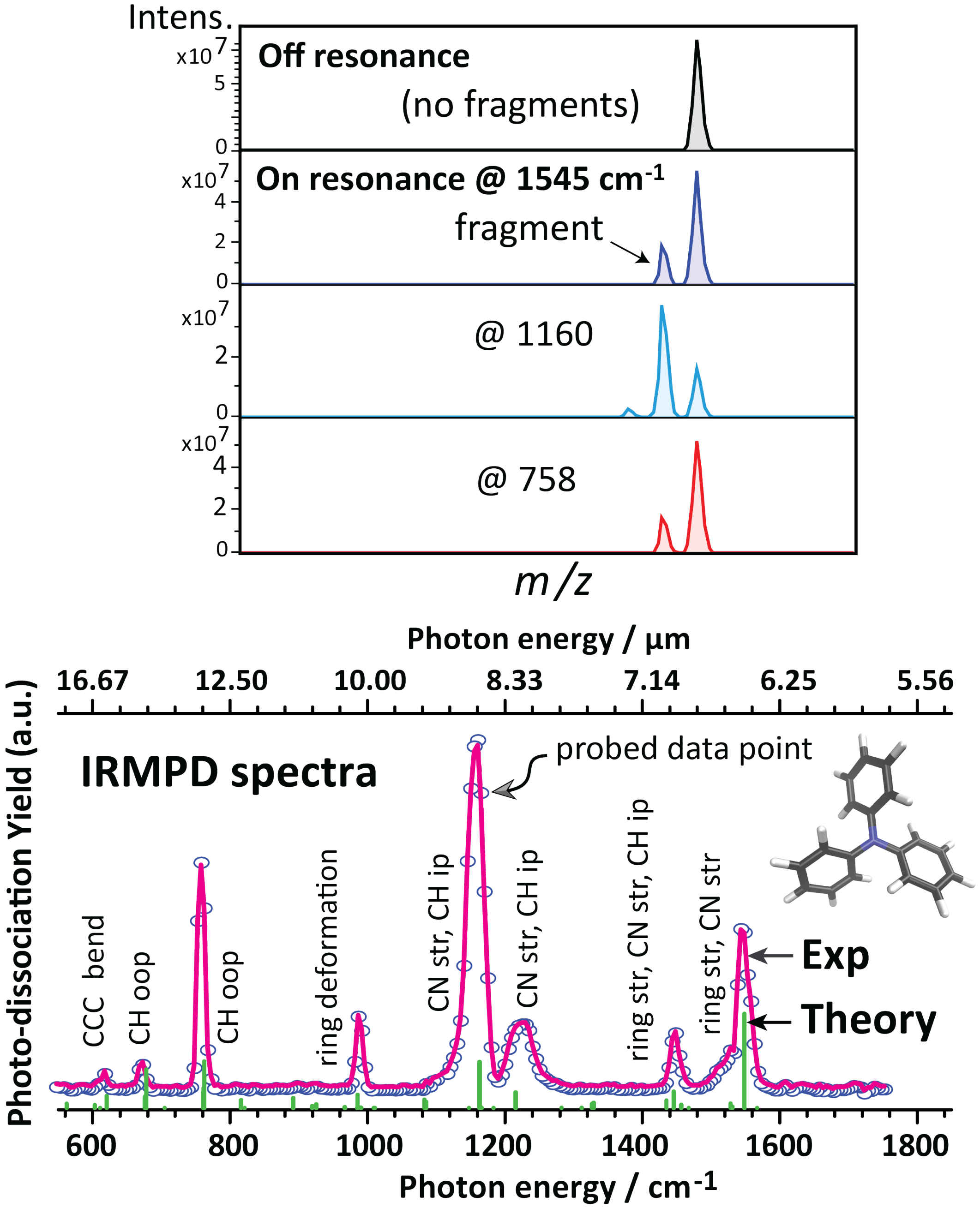

Figure 1.8. *Top panel*: Mass spectra of the triphenylamine radical cation (TPA$^{\cdot+}$) off-resonance and on resonance irradiation using 2 macro pulses from IR free electron laser (FEL) with near constant power. *Bottom panel*: Experimental IRMPD spectrum of mass-to-charge (*m/z* 245) isolated TPA$^{\cdot+}$ (magenta trace) which was generated stepping the laser frequency by 5 cm^{-1}. This spectrum was produced by connecting the measured frequencies (blue circles). Experimental spectrum is compared to the theoretically computed linear absorption spectrum using DFT. For more detail about TPA, see chapter 6.

1.7 Mass spectrometer

Experiments are performed in a commercial QIT MS (Bruker AmaZon Speed ETD, Bremen, Germany) which is modified for IRIS. This section briefly explains the operation of the QIT MS, including the ETD process and the modifications made to the instrument to enable optical access to the ion cloud inside the trap. The lasers are described in section 1.8 and the communication between the QIT and the tunable IR laser sources during spectroscopic measurement is explained in section 1.9. The QIT incorporates a negative chemical ionization source to produce the anionic reagent for electron transfer dissociation (ETD) experiments. In this thesis, this ETD source will be used to charge-reduce transition metal-ligand complex ions in order to spectroscopically investigate the structural differences between the gaseous complex with the metal center in different oxidation states. Characteristics of the ETD source are described in subsection 1.7.3.

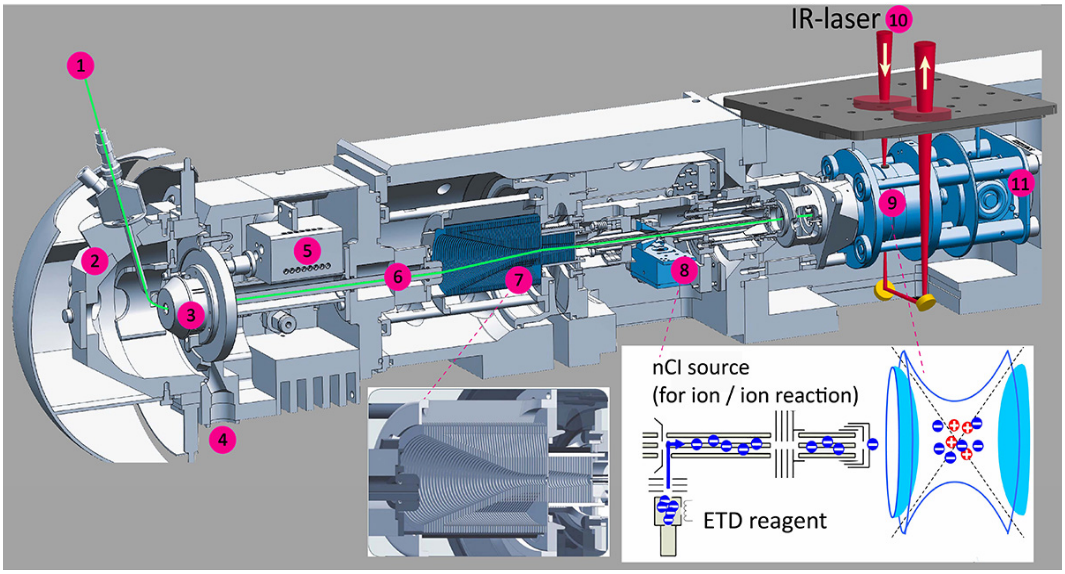

Figure 1.9. Schematic of the modified QIT MS. The ion path from the ESI source to the quadrupole trap is indicated by the green line. The negative chemical ionization source (nCI) produces electron/proton donor reagent ions (as required) which are brought into the trap, co-trapping them with the previously isolated cation to induce an ion/ion reaction (shown inset). Reaction products can be mass-isolated (*m/z*) for spectroscopic investigations. Access of an IR laser to the trapped ions is made possible by 3 mm holes at the top and bottom of the ring electrode. Two mirrors have been installed to guide the laser beam back out of the trap. The labels used in this Figure indicate (1) ESI sprayer, (2) Spray chamber, (3) Spray shield and capillary cap, (4) Waste, (5) Dry gas heater, (6) Inlet capillary, (7) Ion funnel, (8) nCI source, (9) RF-quadrupole trap, (10) IR laser access and (11) Ion detection. Figure modified from [60]

1.7.1 Quadrupole ion trap mass spectrometer

Figure 1.9 shows the schematic of the modified QIT MS. Modifications include optical access to the trap in order to record the IR spectra of the trapped ions [60].

Ions are generated using an electrospray ionization source (ESI). Typical solutions have concentrations of $\sim 10^{-6}$ down to 10^{-9} mol L^{-1} and are introduced at a flow rate of 120-180 μL per hour; nebulization is aided by an N_2 gas flow. In addition, a heated drying N_2 gas (180-220 °C, 4-5 L min^{-1}) flows in a direction opposite to that of the ions in order to remove solvent molecules.

The ESI sprayer is kept at ground potential and the entrance of the capillary is at 2-6 kV (for positive ions). Ions migrate to the capillary entrance and are then transported through the capillary due to the pressure gradient between the spray chamber and the first pumping stage. The exit end of the capillary (metal-coated) has a potential about 80-280 V. Once the ions exit the capillary, they are drawn electrostatically and fluid-dynamically into the ion funnel. Their path is slightly off-axis with respect to the capillary, which avoids excessive contamination by neutral solvent or analyte molecules. In addition, the wide entrance of the first funnel accepts the ions from the exit capillary having a considerable range in kinetic energy, which reduces due to the collisional damping in the funnel. The stacked ring ion guides carry an RF-voltage, which generates an effective potential that confines the ion beam inside the funnel. A DC plate between the funnels pushes the ions further down where in-source CID can occur. After exiting the second ion funnel, ions are transferred using a high-precision multipole guide with a gate lens and focusing lens assembly. In this region, ETD reagent radical anions are extracted out of the nCI source (for details see subsection 1.7.3).

Ions enter the trap typically for 0.05-50 ms (ion accumulation time) through the first end-cap, where they are trapped with in an RF-potential (Ω =781 kHz) fed to the ring electrode, while the end-cap electrodes are held at ground. This RF-field can trap ions of a particular mass range (subsection 1.7.2) depending on the applied RF amplitude. This quadrupolar field can be thought of as a three-dimensional pseudo-potential well. The depth of the well is related to the *m/z* of the ion and the amplitude of the RF-voltage. The auxiliary voltages on both end-caps are used in ion isolation, fragmentation *via* ion excitation, and during the mass analysis phase of the scan sequence.

A damping gas (helium) at 10^{-3} mbar is used in the trap to capture and thermalize the incoming ions. The ion trap works as a storage device, therefore, ions can be accumulated over an extended period (up to 5 s) for weak signals; shorter periods (down to 10^{-5} s, typically several 10^{-3} s) can be used for strong ion signals. Trapped ions are mass-selectively scanned out of the trap and detected using a conversion dynode (Daly) detector, which can detect both negative and positive ions.

To irradiate the trapped ion cloud with the laser light, the ring electrode of the trap is modified by making two 3 mm holes in the top and bottom (shown inset in Figure 1.9). In addition, right above the trap, two IR transparent KRS-5 (Thallium Bromo-Iodide crystal) windows are mounted on the vacuum housing. Furthermore, two gold-coated mirrors are installed below the trap inside the vacuum housing, such that the IR laser travels through the trap, interacts with the ion cloud and is guided back out of the instrument onto a power meter monitoring the pulse energy (illustrated in Figure 1.9). For the window material, KRS-5 is selected because of its wide transmission range (0.6 to 32 μm), although with a considerable reflection loss (28% at 10 μm) [97]. Due to the holes in the ring electrode, buffer gas can escape more easily, requiring an increased flow into the trap for standard operation. A gas controller regulates the flow into the trap via a closed loop controlled proportional valve, which is backed by helium at 5 bar and can be set to any value between 0% (off) and 100% (maximum). The maximum flow gives a pressure of 10^{-3} mbar in the trap. The helium gas pressure was optimized after installation of the modified ring electrode and found to be 78%, giving $\sim 10^{-3}$ mbar pressure.

1.7.2 Stability diagram

The ion trajectory in the quadrupole field can be described mathematically by the solution to the second-order linear differential equation known as Mathieu equation [62]. Figure 1.10 shows the stability diagram based on Mathieu equation. The stability diagram is a two dimensional plot where the DC potential of the end caps is plotted against the RF amplitude of the ring electrode. This plot determines which range of masses can be trapped simultaneously under a particular condition. As well, ions of a particular m/z value are going to be stable or unstable within the field. QIT MS employs the stability of the trajectories in oscillating fields in order to separate the ions based on their m/z. The

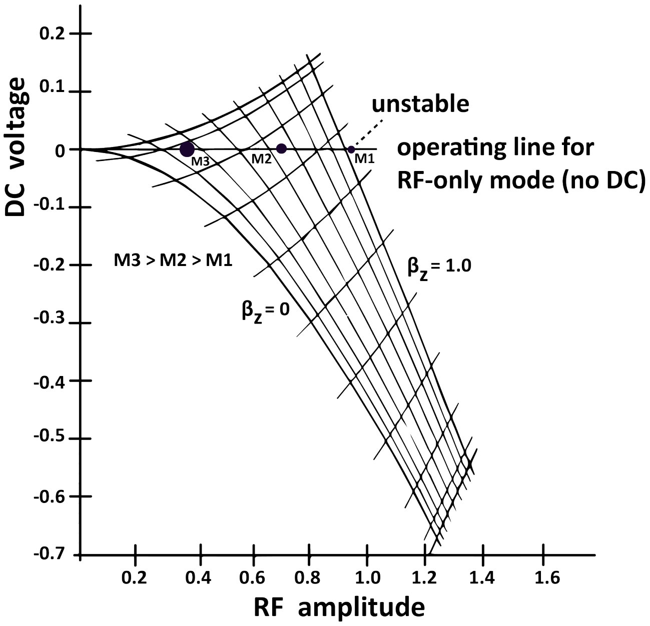

Figure 1.10. Stability diagram for a 3D QIT, derived from the solution of Mathieu equations [62] that describe the ion trajectories in the AC quadrupolar field. Mass M3 and M2 are stable because they are within stability boundary, but M1 is unstable as it is outside of this boundary. Adopted from March [62].

smaller masses are found to the right of higher masses in the stability diagram. With the increased RF voltage, the corresponding point for a given mass on the plot will move to the right. This plot indicates that there is a stable boundary along the $\beta_z = 1$, increases with RF voltage, decreases with increasing mass of the ions. Once an ion reaches the boundary of the stability ($\beta_z = 0$ or $\beta_z = 1$), the ion trajectory becomes unstable and eventually the ion leaves the trap in the axial direction. This implies that for a given RF potential there is always a low mass limit in the field (low mass cut-off), and below this limit all masses are unstable.

The ions inside the QIT undergo harmonic motions along the radial and the axial directions. The net harmonic frequency of the ion oscillation (secular frequency) is determined by their mass (*m/z* ratio) and the RF voltage. A lower *m/z* value yields in a higher secular frequency than a higher *m/z*.

A resonant excitation/ejection scheme is used to mass-selectively manipulate ions in the trap, which includes mainly ion isolation and ion activation, i.e. controlled ion excitation *via* CID. This is accomplished by an additional dipolar field generated by an RF signal fed to the end caps. Upon resonance of the dipolar frequency with the secular frequency of ions of a particular *m/z* value, the oscillatory motion of these ions is enhanced. Through such a resonant ejection scheme, the ion trap is capable of isolating precursor ions (from 50 *m/z* to 3000 *m/z*), or even a specific isotope: by resonantly exciting all ions except the desired one, isolation is effected. As well, this resonance scheme is used to excite ions of a particular *m/z* to induce CID with the background helium gas. To this end, a small frequency band is chosen just around the precise resonance frequency, with lower amplitude ($\sim$1 volt) than for resonant ejection. CID MS/MS is a common technique in structure elucidation because the fragment patterns are reproducible. In addition, the combination of resonant ejection and ramping of the RF voltage are utilized to generate a mass spectrum. The ions are pushed towards their resonance frequency (which is set at one-third of 781 kHz) and ejected out of the trap. Once the ions hit the detector an electrical current is produced, which is plotted as a function of time to generate the mass spectrum. Changing the ramp rate (e.g., 20 μs per mass unit) can be used to manipulate the mass resolution.

The low mass cut-off can cause problems in CID, ETD and IRMPD (Appendix A Figure A.2), because below this limit fragment ions are not stable (do not remain trapped) and are therefore not detected. Of course, the low mass cut-off should be below the mass of the reagent anion (*m/z* 202, fluoranthene radical anion) during ETD. How the low mass cut-off influences the production of charge-reduced ions during an ETD reaction will be shown in the following section.

1.7.3 Electron transfer reduction (ETR)

The QIT MS has the ability to trap ions of opposite polarities simultaneously [98], which enables ion/ion reactions. ETD is such an ion/ion recombination reaction between multiply positively charged precursor ions (e.g., protein or peptide) and a singly charged radical anion, which acts as an electron donor reagent. This reagent anion is produced in the negative chemical ionization (nCI) source. During cation accumulation and precursor ion isolation, a repulsive voltage is applied to block the reagent anions at the gate lens of the nCI source (Figure 1.11). Once the cations are trapped, the reagent anions are orthogonally transferred and added to the trap while cations from the ion source are blocked at the capillary exit.

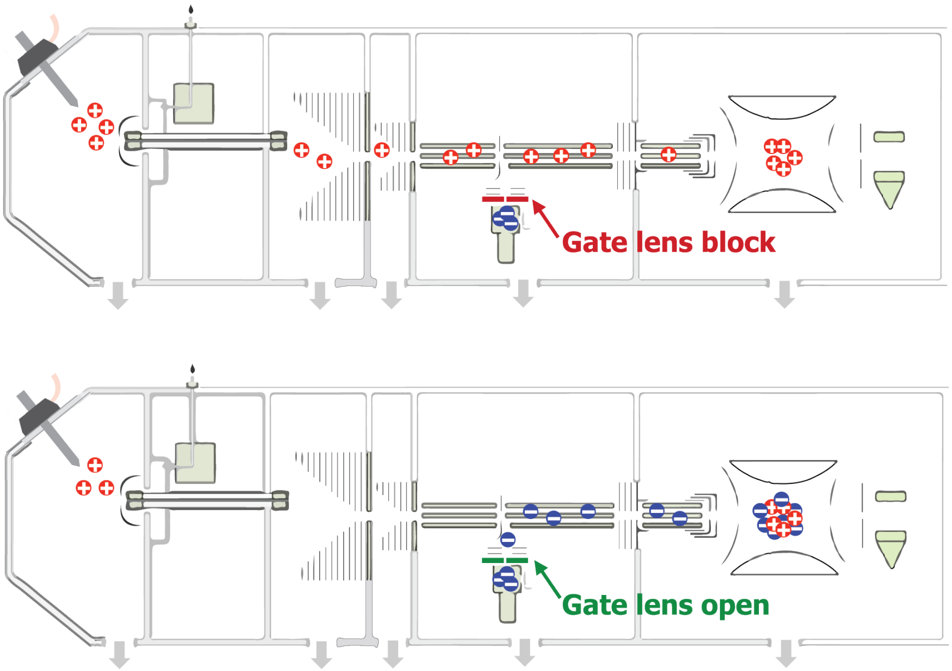

Figure 1.11. Within the QIT MS, ETD involves the transfer of cations followed by reagent radical anions. Voltage on the gate lenses controls the reagent either to pass or block. Figure is modified from Bruker amaZonETD user manual.

Figure 1.12 shows the accumulation of ETR reagent, which is controlled and guided by a stack of three lenses into the octopole ion guide. Lenses in the middle focus the flux and the transfer-lenses transfer the ions directly into the path of octopole ion guide. Each stage is controlled by different voltages. The ion/ion reaction occurs while the cations and anions are being co-trapped for about 200-350 ms, which was found here to be optimum for all experiments. An electron is transferred from the reagent anion to the cation, resulting in an odd-electron cation. The reagent anion becomes neutral and leaves the trap.

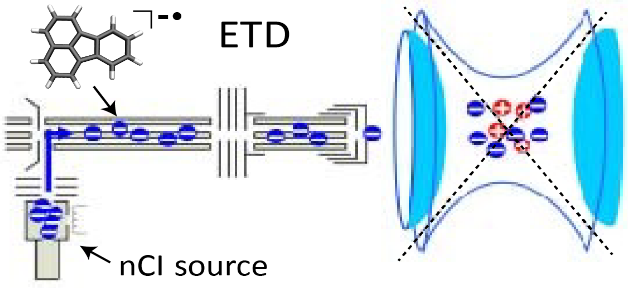

Figure 1.12. ETD reagent accumulation with previously isolated cations results in an ion/ion reaction. Blue and red circles represent the fluoranthene radical anion and the previously isolated cations respectively.

The fluoranthene radical anion is formed from solid fluoranthene in a crucible attached with the nCI source [99]. The crucible is heated up to 60°C which causes the neutral fluoranthene to sublime into the nCI source. Methane gas at 0.1 mbar is used inside the nCI chamber, where electrons from a filament ionize (electron energy 60-80 eV) the methane gas. Methane acts as a mediator. Three-body collisions between methane molecular ions, electrons and the neutral methane gas occur because of the high pressure in the ionization chamber. A chemical ionization plasma is created through an array of reactions. The plasma has thermal electrons that attach to neutral fluoranthene (an electron acceptor) resulting in the formation of radical anions. Several alternatives have been employed instead of fluoranthene, such as anthracene, azobenzene, azulene, biquinoline [99, 100].

Figure 1.13 shows the formation of the fluoranthene radical anion at *m/z* 202, which is exclusively generated with a –6.0V ionization voltage. For lower ionization voltages, the generation of fluoranthene radical anion decreases significantly, and instead another reagent at *m/z* 203, referred to as the proton transfer reagent (PTR), is generated. Both these reagent ions have been characterized using IRIS recently, where comparisons with the linear IR spectra computed with the aid of DFT unambiguously establish their structures [101].

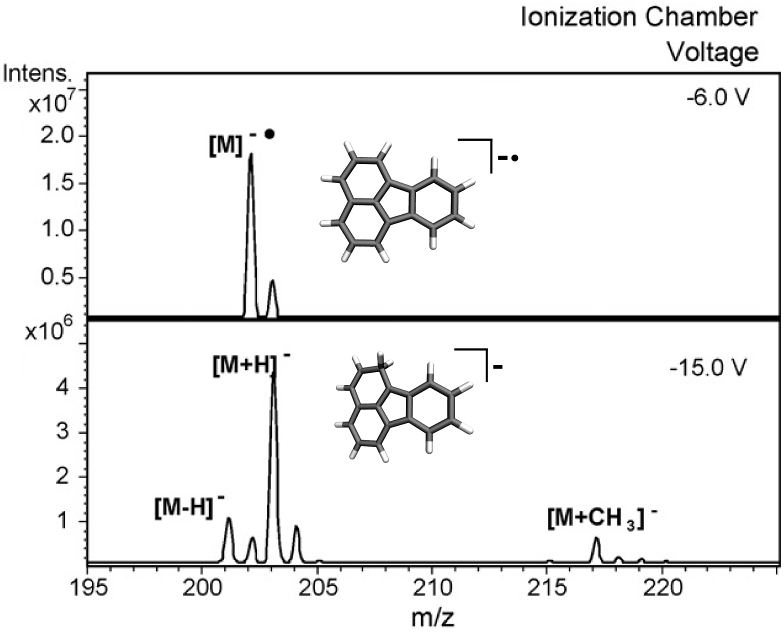

Figure 1.13. Production of the fluoranthene radical anion (*m/z* 202) and the PTR-reagent anion (*m/z* 203) at ionization voltages of (a) –6.0V and (b) –15.0V respectively. DFT predicted structures are shown in the inset. Figure modified from Hartmer et. al. [99].

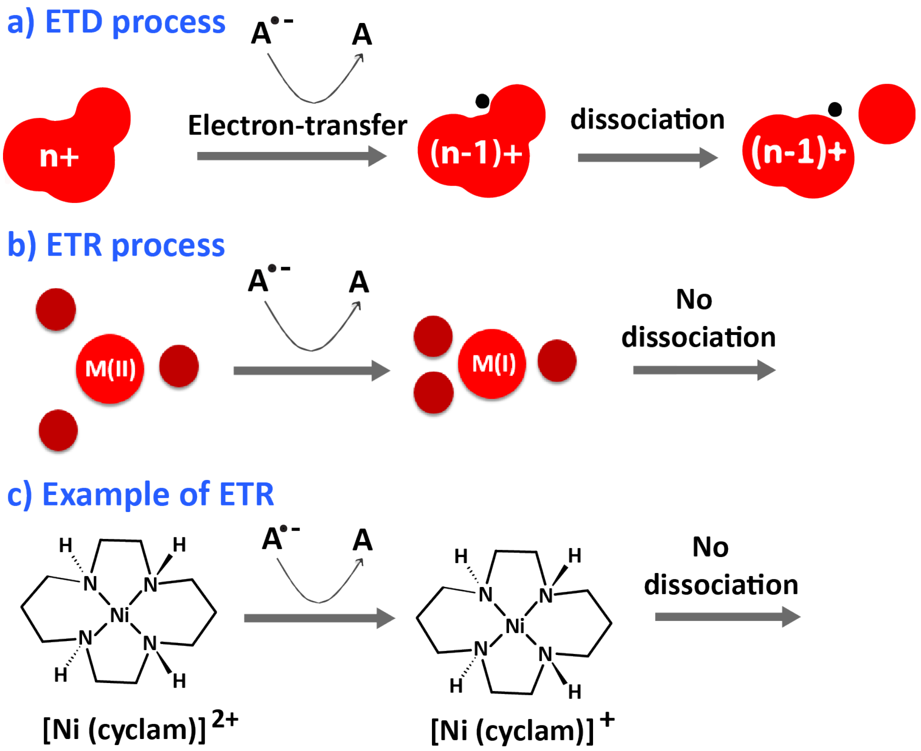

Figure 1.14. Schematic ETD process within the QIT MS, where this option can be used as a method to charge-reduce metal-ligand complexes without dissociation. An example of intact charge reduction of the Ni(cyclam) complex is shown.

Figure 1.14 illustrates the basic principles of ETD. Although ETD was originally designed as an alternative to CID in protein sequencing [102, 103], our main interest is to employ ETD as a means of charge reduction without further dissociation of the precursor ion, yielding an intact charge reduced ion.

Figure 1.15 depicts an example of efficient electron transfer reduction (ETR) of a metal-ligand complex with negligible ETD induced fragments. Once the precursor and the reagent anion are co-trapped in the QIT, the ion/ion reaction can be optimized by the reaction time and the low mass cut-off, which confines the ions ensuring contact between the reactants, hence increasing the efficiency. The figure shows that within 300 ms with the low mass cut-off at 160, about 70% charge reduced ions are generated while only 2% of the total ions undergo fragmentation due to the exothermic recombination reaction. The QIT has the capacity to isolate a single isotopomer of the ruthenium bpy_3 coordination complex at *m/z* 285, which after charge-reduction gives a reduced ion at *m/z* 570. The CID MS of the reduced ion gives *m/z* 414, which is a Ru ion with two bpy units due to the loss of a neutral bpy.

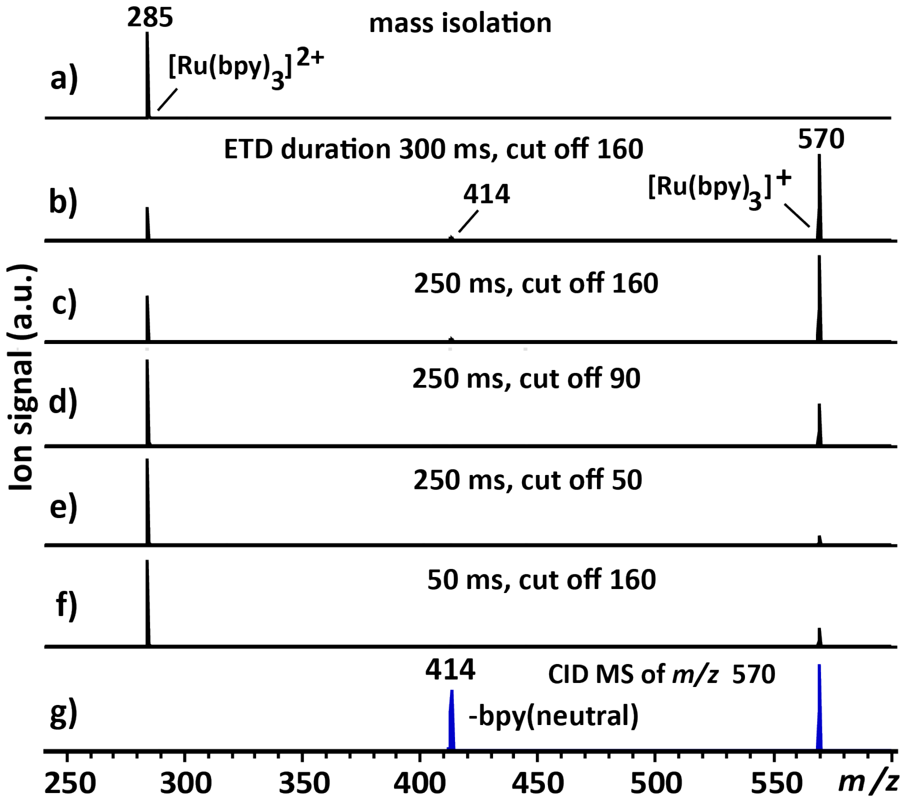

Figure 1.15. (a) Mass isolation of $[Ru(bpy)_3]^{2+}$ from the ESI source. (b) Generation of $[Ru(bpy)_3]^{+}$ from the dication *via* ETD option with (b-f) varying reaction time and mass cut-off. (g) CID MS shows a neutral bpy loss from $[Ru(bpy)_3]^{+}$. Structural characterization of the redox pair using IRIS is presented in chapter 5.

Thus, the ETD option is used successfully to charge reduce metal-ligand complexes as an effective method to selectively synthesize individual members of a metal-ligand redox pair in the gas-phase, which is demonstrated with complete structural characterization using IRIS and quantum-chemical calculations. The main advantage of ETR is that it allows unique access to oxidation states of the coordination complex that are otherwise difficult to access.

One alternative way to generate charge reduced species was presented by Jana Roitová and co-workers [73], who used a collision cell in the ion path from the ESI source to the ion trap. Neutral gaseous tetrakis(dimethylamino)ethylene (TDAE) is used as a reducing agent, which donates an electron to the multiply-charged cations. Nielsen et. al. [104, 105] reported another similar example of charge reduction inside a small (4-cm long) collision cell *via* collisional electron transfer from one of the reducing agents atomic Na, Cs or O_2.

1.7.4 Additional experimental setup (FTICR MS)

Additional experiments described in this thesis have been performed in a home built Fourier Transform Ion Cyclotron Resonance (FTICR) mass spectrometer, which is coupled to several laser sources including FELIX, an IR OPO, an ultraviolet (UV) laser, and a CO_2 laser [47, 48, 106]. An extensive description of this FTICR can be found in [9, 47]. The setup is depicted in Figure 1.16.

This instrument was employed here to record the IR spectra of the radical cation of triphenylamine ($TPA^{\cdot+}$) (chapter 6) and the Cu^{2+}/Ni^{2+}-(cyclam) complex (chapter 3 and 4) in order to circumvent the competitive collisional quenching during IR excitation, which occurs for IRMPD spectra recorded in the QIT MS. These systems are rather difficult to photo-fragment because of their high thresholds to dissociation and some of them have low-intensity bands that are crucial for structural assignment and isomeric identification. Therefore, in this section the FTICR is briefly described, including the most relevant differences as compared with the QIT.

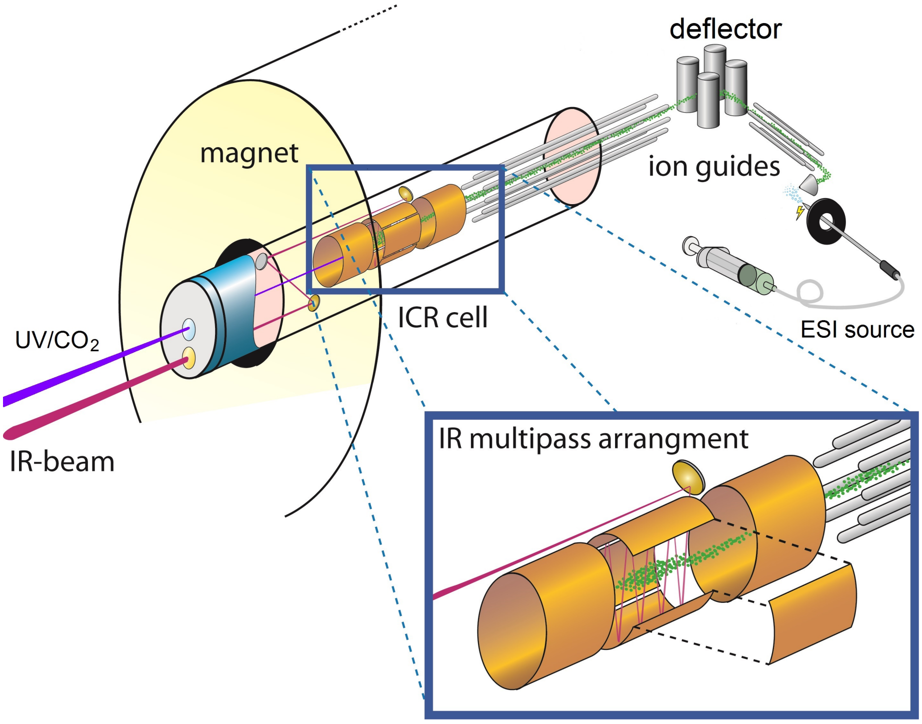

Figure 1.16. FTICR MS with ESI source. Ions are guided from the source using a hexapole followed by an octopole before being injected into the ICR cell. The inside of the copper excite electrodes of ICR are polished such that they act as a multipass reflection surface for the lasers. The laser beam crosses the ion cloud approximately 10 times. Adapted from [7].

In the FTICR MS shown in Figure 1.16, ions are generated from approximately 1 mM solutions using an ESI source (Z-spray, Micromass, UK) and accumulated for several seconds in a linear hexapole trap before being injected into the ICR cell through an electrostatic quadrupole deflector and an rf octopole ion guide. The kinetic energy of the incoming ions is reduced just before entering the ICR cell by switching the DC bias of the octopole guide, ensuring efficient trapping [106]. Therefore no buffer gas is needed to reduce the speed of the ions, and the pressure in the ICR cell is always 10^{-7} - 10^{-8} mbar.

The ions are trapped in the ICR cell, which is a so-called Penning trap with a spatially homogeneous static magnetic field of 4.7 T generated by an actively shielded superconducting magnet. An axial electric field of two ring electrodes at a DC voltage of ≈4.0 V confines the ions axially (see Figure 1.16). Trapped ions are excited at their resonant cyclotron frequencies [26, 107] to a larger cyclotron radius by an rf field orthogonal to magnetic field lines, which is supplied at the two excite-electrodes. After excitation, the ions orbit the magnetic field axis in phase and they induce an image current in the two detect-electrodes. This image current signal (transient) is an interferogram of the signals from all ions. Fourier transformation of the transient gives the frequency components, which straightforwardly converted to a mass spectrum.

As in the QIT, ions of interest can be isolated depending on their *m/z* value. In this FTICR, mass isolation is performed using a stored waveform inverse Fourier transform (SWIFT) excitation pulse at the excite-electrodes [108]. Optical access to the ions is achieved *via* two windows as shown in Figure 1.16. One window (barium fluoride, BaF_2) is located on-axis with the magnetic field and is used to irradiate the stored ions with the UV laser or the CO_2 laser. The other window (KRS-5) is used for the tunable IR light from FELIX or the OPO and is placed off-axis, which allows us to use the excite-plates of the ICR cell as an "optical multi-pass cell". This multi-pass geometry improves the IR induced dissociation yield by a factor of about 3 [60], and more importantly, makes the setup less sensitive to small changes in optical alignment.

Differences between this FTICR setup and the QIT that are particularly relevant for our experiments include: i) the sensitivity of the commercial QIT is much higher presumably due to better ion transfer optics, ii) the mass resolution of the FTICR is higher, iii) the FTICR has better optical access, which allows to use multiple lasers, iv) the ion cloud in the QIT is smaller and the IR laser beam is more focused, v) the pressure in the ion trapping region is orders of magnitude lower in the FTICR than in the QIT. The low pressure of the FTICR's trapping region is the main reason why the FTICR has been used for additional experiments as is explained further in section subsection 1.10.2.

1.8 Infrared lasers

Here we give a brief overview of the Free Electron Laser for Infrared eXperiments (FELIX) and OPO laser systems. Wavelength tunability and high power of these IR laser sources are important parameters to record IRMPD spectra of gas-phase molecular ions.

1.8.1 Free-Electron Laser for Infrared eXperiments (FELIX)

Figure 1.17 depicts the layout of the FELIX free electron laser (FEL). A FEL employs relativistic electrons to generate tuanable laser radiation. The operation consists of the generation of electron bunches which are accelerated by a linear particle accelerator (LINAC) to nearly the speed of light (c) before being guided through an undulator, an array of permanent magnets with alternating polarity. This polarity alternation induces a wiggle motion on the electrons and results in a change in the direction of their velocity vectors, which generates synchrotron radiation. High-reflectivity gold-platted mirrors are placed on both sides of the undulator and function as an optical resonator. Newly injected electron packets interact with the radiation circulating inside the resonator, resulting in gain on each successive pass.

The observed wavelength, λ_{obs} is dictated by the period of the undulator field, λ_u, the relativistic energy of the electrons, γmc^2, and a dimensionless parameter, K, which depends on the amplitude of the undulator magnetic field through the relation

$$\lambda_{obs} = \frac{\lambda_u}{2\gamma^2}(1 + K^2)$$

where

$$\gamma = \frac{1}{\sqrt{1 - \frac{v^2}{c^2}}}$$

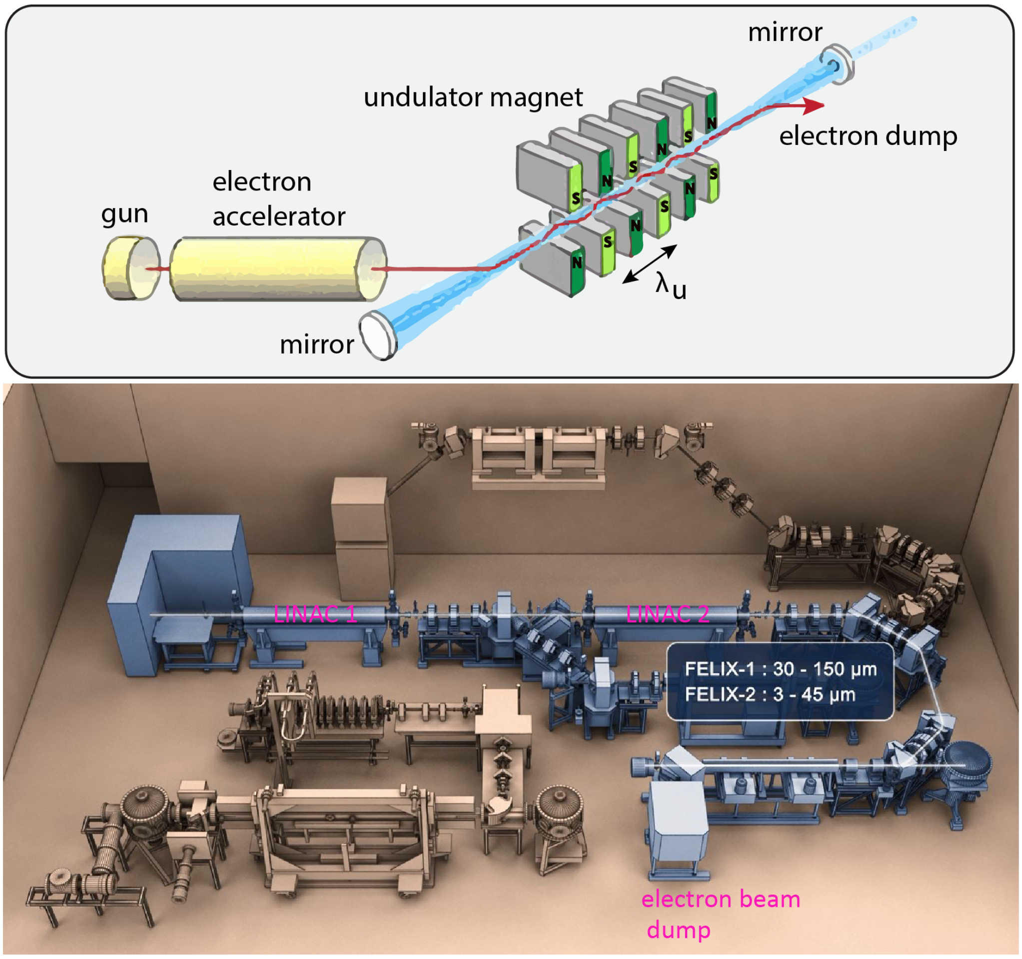

Figure 1.17. (Top panel) Core components of FELIX [11]. Electrons from an electron gun are accelerated to relativistic energies. They are injected into the magnetic field created by the undulator, where they undergo oscillations and emit radiation. The radiation is captured and amplified in an optical cavity formed by two mirrors. (Bottom panel) Schematic of the FELIX laser sources where several FEL sources cover the wavelength range between 3 and 1500 µm. In this thesis FELIX-2 is employed.

From this relation, it is seen that the magnetic field of the undulator or the energy of the relativistic electrons can be changed to tune the wavelength of the IR radiation. During an IR scan, the wavelength is tuned by changing the gap between the two arrays of magnets, which changes the strength of the magnetic field for a given electron beam energy. The wavelength of the FELIX is calibrated using a grating spectrometer.

Figure 1.18 shows the typical power curve and the pulse structure of the FELIX radiation as used in this thesis. FELIX produces 5 µs long macropulses which are composed of a train of short 5 ps-long micropulses at a 1 GHz repetition rate. Hence, each macropulse consists of about 5000 micropulses. Calibration

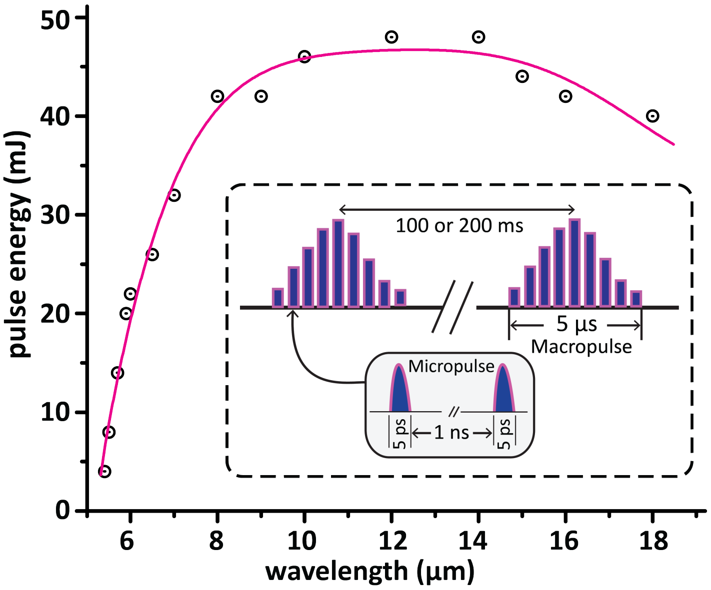

Figure 1.18. Typical FELIX power curve as a function of wavelength. The FELIX pulse structure is shown in the inset. Every µs-long pulse consists of a train of a few thousand ps-long micropulses.

of the power is necessary because the power over the wavelength tuning range is not constant.

Table 1.1 shows the specifications of the FEL source used in this thesis [11]. The pulse structure of FELIX is such that it facilitates efficient IRMPD: the high instantaneous power of the micropulse ensures efficient photon absorption, and the interval between micropulses falls within the IVR lifetime, enabling re-absorption at the fundamental transition. On the other hand, the macropulse time interval (e.g., 100 ms at 10 Hz) is considered to be sufficiently long for radiative cooling [6], so that undissociated molecular ions relax back to the ground state after each macropulse and then absorb photons from the next macropulse.

Table 1.1. Specifications of the free electron laser for IR experiments

Beam energy (MeV)	15-45
Wavelength (µm)	3-150
Macropulse energy (mJ)	≤150
Macropulse repetition rate (Hz)	≤10
Macropulse duration (µs)	≤10
Spectral bandwidth (%)	0.2-5

1.8.2 Optical Parametric Oscillator / Amplifier

The OPO laser at the FELIX laboratory employs an Innolas Spitlight 600 pulsed Nd:YAG laser at 1064 nm as the pump laser source. Its radiation is converted into tunable mid-IR radiation with a bandwidth of about 3 cm^{-1}.

In our LaserVision OPO, the pump laser beam is split in two, where one goes to an OPO stage and the other to an OPA [7]. The frequency of the pump beam is doubled to 532 nm using a nonlinear potassium titanyl phosphate (KTP) crystal (the residual is dumped). The 532 nm beam enters the OPO cavity, where a KTP crystal splits each photon in two photons, generating a signal beam (around 780 nm) and an idler beam (around 1.6 μm). By rotating the KTP crystal, the wavelength of both the *signal* and *idler* are varied as a consequence of the changing phase-matching condition. The *idler* beam generated from the OPO stage mixes with the 1064 nm light in the OPA through difference frequency generation in four potassium titanyl phosphate arsenate (KTA) crystals, thus the 1.6 μm signal beam is amplified and an idler beam at 3 μm is generated. By using a dichroic filter, the remaining 1064 nm light is removed and a polarizer filters out the signal beam, resulting in the idler beam at wavelengths tunable in the 3 μm range, which is used for IRMPD spectroscopy.

By tuning the angles of the nonlinear crystals in OPO and OPA stages, the IR frequency can be scanned between 2200 to 4500 cm^{-1}. The OPO delivers pulse energies up to 20 mJ at 4000 cm^{-1} and 15 mJ at 3000 cm^{-1} per 5 ns long pulse. The wavelength of the OPO is calibrated using a wavemeter (HighFinesse WS5).

1.8.3 Additional CO_2 laser to boost up IRMPD yield

Since some of the systems studied in this thesis were rather difficult to photofragment using FELIX and OPO alone, an additional CO_2 laser is sometimes used for such systems. Such experiments were reported previously [6, 49–51]. The benefit of using an additional CO_2 laser is illustrated in Figure 1.19. After each FELIX or OPO pulse, a short burst of the laser post-excites the ions to increase the on-resonance fragmentation yield.

The continuous-wave CO_2 laser has an output power of 30 W. In the example shown in Figure 1.19, additional CO_2 laser irradiation of 30-40 ms is applied directly after each OPO pulse (140 pulses) to record the IR spectra of bare

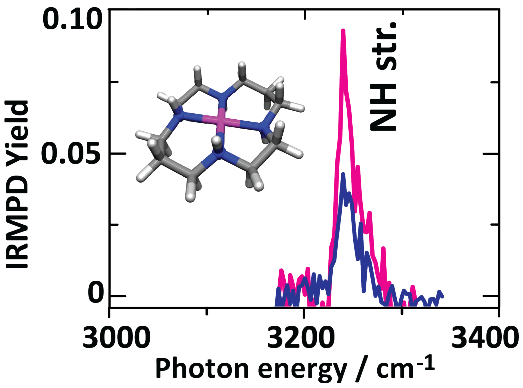

Figure 1.19. Additional 30 ms (blue), 40 ms (magenta) CO_2-laser irradiation after each OPO pulse (140 pulses from OPO) in order to boost the on-resonance IRMPD yield of bare Ni^{2+}(cyclam) in FTICR MS.

Ni^{2+}(cyclam) complex. The duration of CO_2 laser irradiation is chosen in such a way that the CO_2 laser alone does not induce any observable fragmentation of the ions. Clearly, many ions were just below the dissociation threshold while irradiated using 14 s OPO + 30 ms CO_2-laser, since the yield is nearly doubled with an extra 10 ms CO_2-laser (14 s OPO + 40 ms CO_2) irradiation. This technique is very useful to pick up IR bands with relatively low intensity. More examples will be presented in chapter 3, 5, and 6.

1.9 Synchronization of IR laser with QIT MS

Figure 1.20 illustrates the MS scan sequence for an electrosprayed ion during the IRMPD experiment. The experiment is initiated by the master trigger generated by the laser system (black trace), which is synchronized with the IR laser pulse. The green trace is the laser pulse (at 10 Hz) monitored on a sensor after the IR beam exits the trap. The pink trace is the RF signal from the end caps which is visualized on an oscilloscope to follow the MS scan sequence: (**I**) ion accumulation, (**II**) precursor ion isolation, (**III**) an MS/MS window used as the IRMPD stage, (**IV**) scanning the ions out of the trap, and (**V**) delay time before the instrument starts the next sequence. If the experiment involves an ETD or CID stage, an additional window would be added before the IRMPD window, to generate the IR spectra of the CID/ETD induced product ions. The blue trace indicates a trigger from the auxiliary interface of the MS set by the user during the MS/MS (IRMPD) window, which opens a mechanical shutter allowing the laser beam to enter the trap. Since the total time of the MS scan sequence can

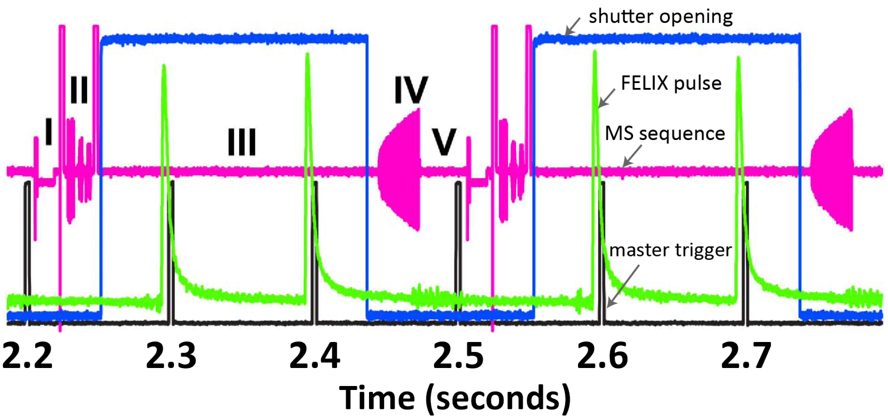

Figure 1.20. Synchronization of the MS-sequence with IR laser pulse. Voltage of the end caps (*pink trace*) allows visualization of each part of the MS-sequence. A trigger pulse (*blue*) is generated by the instrument for a selected element of the MS-sequence—which controls a shutter to allow the lase pulse to enter the trap for a chosen period (irradiation time) as IRMPD stage. The master trigger (*black*) (10 Hz) generated by the laser initiates the MS-sequence. Laser pulse (green) detected by the power meter after exiting the trap. Adapted from [60]

vary (precursor ion accumulation, isolation and possible MS/MS: ETD, CID), a delay generator is used to adjust the time delay between the laser trigger and the laser pulse, ensuring the laser pulses are not clipped by the shutter.

Note that two pulses from the laser are used to irradiate the ions and the whole MS sequence takes 300 ms. Depending on the number of averages, the IR spectral range (typically 600-1850 cm^{-1}), the step size of the laser frequency (*e.g.*, 3 to 5 cm^{-1}), and the frequency stepping time (depends on the laser system), the data acquisition time to record an entire spectrum varies. In this example a three-fold averaged IR data point takes approximately one second and within $\sim$10-20 min, a typical IRMPD spectrum is recorded over the IR fingerprint range. Typically, each data point in the IRMPD spectra is obtained from 3 to 6 averaged mass spectra.

1.10 IRMPD in QIT

This section explains how the photofragmentation yield is affected by experimental conditions, such as the density of ions, the collisional quenching due to the helium buffer gas, irradiation time, power of the laser(s) pulse (see section 1.8), attenuation of the power. High laser power is essential for systems which are difficult to photo-fragment, especially to observe IR bands with relatively low intensities. Several such examples are encountered in this work. In addition, the mechanism of the IRMPD process (in general) in the QIT MS is described.

Since IRMPD involves the absorption of many photons [7, 29], the IRMPD yield is not necessarily directly proportional to the absorption cross-section. The IRMPD yield (intensities) are therefore not always directly comparable with the intensities of a linear IR spectrum, although they can often be considered close to it. Therefore, if the photon flux stays roughly constant over a range of wavelengths [109], the relative intensities observed in an IRMPD spectrum can be directly comparable with relative absorption cross sections. An important consequence is that we can usually safely compare the relative intensities of the IRMPD spectrum with those of linear absorption spectra computed using DFT calculations. Somewhat in contrast to spectral intensities, the positions of the IRMPD bands are usually comparable with linear IR spectra, which has been demonstrated for many systems [3–7].

The irradiation time (or the number of IR laser pulses) is chosen based on the extent of fragmentation induced. The molecular ions are believed to dissociate roughly within the macropulse duration i.e., 5-6 μs. This implies that by increasing the number of pulses, ions will not break if they they do not break within the first macropulse. Generally, 5 to 30% depletion of the precursor ions is sufficient for recording IRMPD spectra. The extent of dissociation and depletion depends on the ion's stability; fragile ions may require only a fraction of a macropulse. For instance, the IR spectrum of $[Ru(bpy)_3]^{2+}$ (Figure 1.24) was recorded using 20 macro pulses of FELIX without any attenuation of the power, but the charge-reduced ion required only 2 pulses with 5 dB attenuation, reducing the power per pulse by $\sim$66% (see chapter 5).

The power of the FELIX IR radiation is reduced using a set of attenuators [110, 111]. If required, the FEL power can be attenuated up to 38 dB combining the set of neutral density attenuators of 3, 5, 10, 10, 10 dB. Usually, several scans are required with different laser power to observe both weak and intense bands in an IRMPD spectrum. A careful power calibration is required to combine data from different scans. The fragmentation rate is directly proportional to the number of pulses. The only limitation is that beyond saturation (fragmentation yield > 0.5) this proportionality deviates, because not enough ions are available for further fragmentation. The plotted IRMPD yield is corrected linearly for the frequency dependent variations in laser power (see in section 1.8) assuming a linear power dependence.

If the photon flux stays nearly constant for a range of wavelengths i.e., 5-10 μm [109] then the relative intensities observed in the IRMPD spectrum are directly comparable with their relative absorption probabilities. The higher relative IR intensities provide higher photo-fragmentation yield. In other word, the molecular ions reach the fragmentation threshold faster from the intense IR bands than from the weak IR bands. That is why we can compare the relative intensities of the IRMPD spectrum with that of the linear absorption spectrum. Since the experimental linear absorption spectra of molecular ions are scarce, we often compare with the theoretically calculated linear absorption spectra.

1.10.1 Infrared multiple-photon dissociation

From a mechanistic view point, multiple photon absorption is believed to be non-coherent [112, 113], where the absorbed energy is redistributed after each photon absorption into the bath of available vibrational degrees of freedom through intra-molecular vibrational redistribution (IVR) [114]. The internal energy of the ion rises (heating) as it absorbs photons sequentially, until the fragmentation threshold is reached (Figure 1.21).

Molecular vibrations are anharmonic, i.e., the spacing between subsequent vibrational levels in a potential well is not equal. Rather, it becomes smaller at higher energies. In absence of IVR, when the first photon is absorbed resonantly, the next photon of the same energy would not be absorbed because of the anharmonicity of the vibrations. In contrast to this hypothetical ladder-climbing (i.e., $v_0 \rightarrow v_1 \rightarrow v_2 \rightarrow ...$), IVR enables the anharmonicity bottleneck to be avoided. This means that depending on the available density of states (large for larger molecules) [1, 112], IVR quickly shifts the population from the excited state into the bath of background vibrational modes because of the anharmonic couplings between vibrational modes, such that the molecule can absorb the next photon with the same frequency. In this way IVR induces a short vibrational lifetime leading to broadening of the IR absorption lines [1, 6]. At higher internal energies, a quasi-continuum is reached where all incident frequencies are absorbed significantly. One example is the application of the CO_2 laser to enhance the IRMPD yield (subsection 1.10.3).

IVR lifetime is crucial in IRMPD spectroscopy. At room temperature, aromatic molecules were reported to have lifetimes of typically <1 ns [115, 116]. The IVR

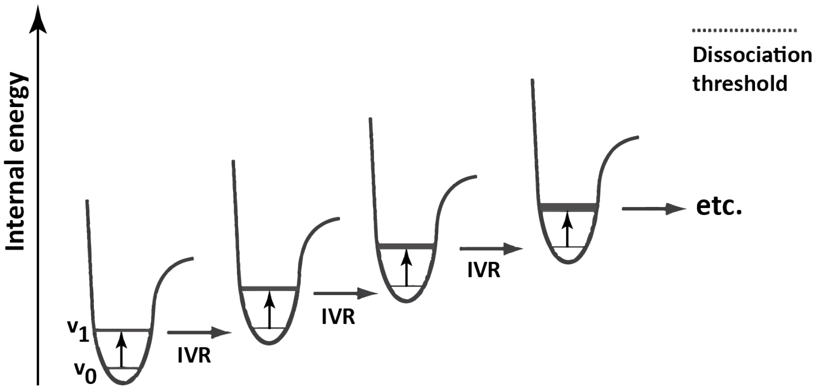

Figure 1.21. Schematic representation of the IRMPD mechanism. The energy due to photon absorption at the fundamental vibrational transition is quickly dissipated into the background coupled vibrational modes through IVR, resulting in the increase of the internal energy. This continues sequentially until the unimolecular dissociation. At higher energies the density of states is indicated by broadening the v_1 linewidth. Adopted from Polfer et. al. [6]

rate does not depend directly on the density of states of the molecule, but rather on the presence of low-level coupled vibrational states [114]. However, the density of states presents the statistical boundary and defines the irreversibility of the energy flow between the vibrational modes [117]. IVR lifetimes (e.g., of polyaromatic molecules) of less than 1 ns perfectly match the micropulse structure of FELIX (see section 1.8): the excited vibrational normal mode is de-excited through IVR within the time between two micropulses, so that the molecule is ready to absorb the next micropulse of FELIX [1].

A quasi-classical approximation of the DoS for polyatomic molecules suggests that the DoS increases exponentially with internal energy and the vibrational degrees of freedom [1]. In this approximation the DoS of coronene (10^4 - 10^5) was so high at room temperature that it can be considered to be already in a quasi-continuum, as opposed to naphthalene (single digit, <10). Yet, the IRMPD spectrum of coronene was recorded showing (partially) resolved vibrational bands [118]. A huge DoS probably ensures efficient photon absorption and the absorbed energy is efficiently dissipated into the vast vibrational repository.

Energy loss pathways also push this limit further, making IRMPD challenging if there is any spontaneous (radiative) emission, stimulated emission, collisions with background buffer gas etc. Collisional quenching in ultra-high vacuum is negligible. The estimated pressure limit to achieve such collisionless environments is $< 10^{-7}$ mbar [119] — (e.g., ICR cell of FTICR-MS has pressure 10^{-8}

mbar). This ensures minimization of collisional relaxation, hence favoring a higher dissociation yield. Spontaneous emission plays a role always but is relatively slow at IR wavelengths; stimulated emission is weaker compared to absorption because of the higher number of degenerate excited states.

In conclusion, the main parameters that affect the overall fragmentation yield between the instruments used here are the ion internal energy, the density of ion cloud, presence of the background buffer gas (in QIT MS) and most importantly the focusing of the IR laser with respect to the geometry of the ion cloud (section subsection 1.7.4). IRMPD is challenging at weak transitions, for instance, for transitions with integrated intensities of <20 km mol^{-1}. IRMPD is also difficult for species with high binding energies and for very small molecules. As the system size decreases, the DoS decreases, hence limiting the IVR rates.

1.10.2 IRMPD in QIT *vs* FTICR

Figure 1.22 shows how the helium buffer gas affects the IRMPD yield in the QIT. The dilemma with the helium buffer gas is that it is crucial for efficient ion trapping, but that it inhibits efficient excitation during IRMPD spectroscopic experiments. Collisional quenching suppresses IR laser induced photo-fragmentation. All IRMPD spectra measured in the QIT MS are influenced, where stable systems are affected more than ones that are easy to photo-fragment. By reducing the helium pressure inside the trap, this problem can be mitigated at the cost of a lower signal-to-noise ratio because of the low number of trapped ions.

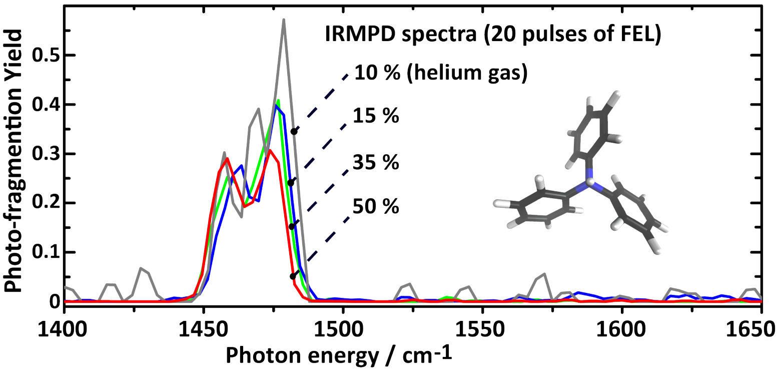

Figure 1.22. IRMPD spectra of protonated triphenylamine (inset) recorded using FELIX with varying helium buffer gas in the QIT MS. Lowering the gas pressure increases the yield while decreasing signal-to-noise ratio, providing noisy spectra.

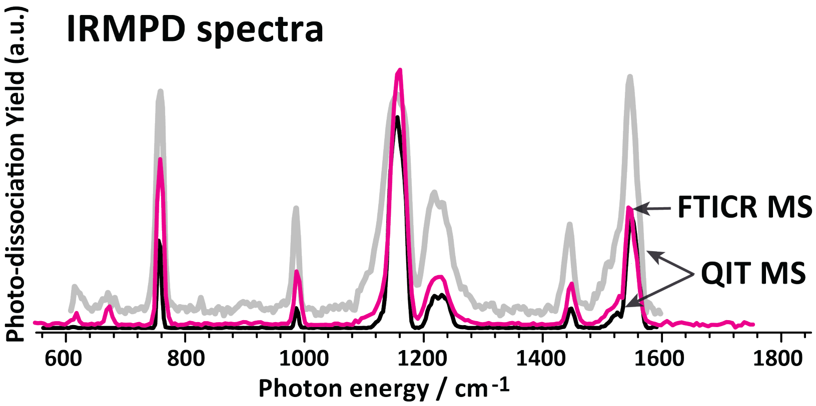

Figure 1.23. IRMPD spectra of the TPA$^{\cdot+}$ recorded in the QIT (where grey and black trace represent without and with buffer gas respectively) are compared with that in FTICR (magenta). Lowering the gas pressure increases the IRMPD yield while decreasing the ion count and hence the signal-to-noise ratio, leading to noisy spectra.

As well, band shapes alter depending on the pressure conditions in the trap. The effect of helium buffer gas on IRMPD spectra [60] in terms of the band shape and position is demonstrated with an example in Figure 1.23, which compares spectra taken in the collisionless ultra-high vacuum of 10^{-8} mbar in the FTICR MS with a spectrum recorded in the QIT. The figure further shows how the yield varies for different experimental conditions, including the irradiation time (number of IR pulses), and the presence and absence of the background buffer gas. In the QIT MS, IRMPD spectra are recorded using 2-4 macropulses. Note, upon removal of buffer gas from the QIT, the bands near 700 cm^{-1} become visible (*grey trace*) whereas they are invisible in the presence of buffer gas (*black trace*) due to the collisional quenching that competes with IR laser heating, preventing fragmentation.

Figure 1.23 shows how the yield varies at different experimental conditions, the irradiation time (number of IR pulses), presence and absence of the background buffer gas. In the FTICR MS (*magenta trace*), 57 macropulses of FELIX were used with additional 5 ms CO_2 laser irradiation after each FELIX pulse to record the same IRMPD spectrum, where 2-4 pulses were used in the QIT MS. Even though the buffer gas is absent in the FTICR MS, it required much longer irradiation to obtain a spectrum. This is mostly related to the focus of the laser relative to the size of the ion cloud (subsection 1.7.4). The smaller focus in the QIT results is a much higher laser fluence than in the FTICR, resulting in a high photo-fragmentation yield with only a few pulses.

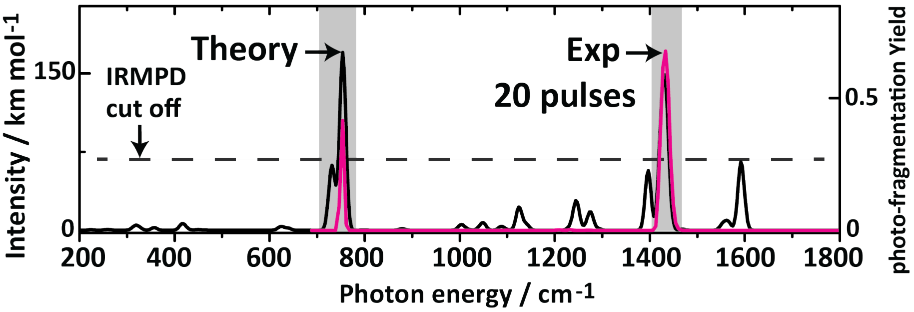

Figure 1.24. The IRMPD spectrum of tris(2,2′-bipyridine)Ru(II) recorded in the QIT with the default helium pressure is compared with calculated harmonic frequencies. The dotted line indicates an apparent cut-off: below ∼65 km mol^{-1}, IR bands are invisible in the experiment, relating to a fragmentation threshold. Lowering the helium gas pressure (not shown) also did not help reaching these bands.

Figure 1.24 shows how a high dissociation threshold influences the yield such that below a certain cut-off intensity (≤65 km mol^{-1}) IRMPD fails. Irradiation at weak IR bands does not allow the system to reach the fragmentation threshold. Here, the loss of one bpy ligand is the lowest energy channel with a calculated threshold of about 4.5 eV. Despite the 85% depletion of the precursor ions at a high intensity band (1436 cm^{-1}), low intensity IR bands calculated theoretically remain unobserved experimentally. This indicates that the low intensity bands are suppressed completely, as a consequence of collisional quenching by the buffer gas. The measured IR band shape is also affected so that the width of the observed IR bands shrinks slightly. This is evident in Figure 1.23 where the spectrum taken in the presence of the buffer gas has a smaller bandwidth than that without a buffer gas. The band at 757 cm^{-1} has a shoulder which is not observed in the experiment due to the IRMPD threshold.

For the 1+ charge state of the tris(2,2′-bipyridine)Ru complex, the calculated binding energy of bpy changes to 2.6 eV and the IRMPD spectrum reflects almost all theoretical IR bands because of the low fragmentation threshold. This ion required only 2 pulses with attenuated power to record the IRMPD spectrum as opposed to 20 pulses (see for details chapter 5).

The shape of the ion cloud is small (∼1 mm diameter) in the RF QIT, which has the advantage to have the maximum overlap between the ion cloud and the focal point of the laser beam. The shape of the ion cloud is maintained with relatively high buffer gas pressures of 10^{-3} mbar, which quenches the ions to the center of the trap. However, this collisional quenching also competes with IR heating. Lowering the buffer gas pressure (10^{-5} mbar) can partially solve this problem, but if the ion of interest involves MS/MS steps (CID, ETD) prior to IRMPD measurement, then using a reduced buffer gas pressure is not possible. In such cases, using a CO_2 laser can be an alternative for CID (for some systems). Of course, without helium buffer gas the ion temperature is higher than room temperature.

In addition, RF heating due to the trapping field is a notable disadvantage of the Paul trap, which may increase the internal energy of the trapped ions, possibly limiting the trapping of fragile ions. In contrast, the ultra-high vacuum conditions (10^{-9} mbar) of the FTICR MS minimizes collisional relaxation and prohibits collisional heating.

The main demerit in terms of IRMPD spectroscopy in the FTICR is the shape of the ion cloud which is known as "cigar"-shaped [6]. The radial dimension is on the order of < 1 mm while the axial dimension is a few cm, depending on the length of the trap. Due to the distribution of the ions within the volume of the ICR cell, there is only fractional overlap with the laser beam so that a larger number of pulses are required to reach sufficient fragment yields as compared to the QIT MS (subsection 1.7.1).

1.10.3 IRMPD *vs* messenger-tagging IR spectra

As mentioned earlier, IRMPD is clearly a highly dynamic process, governed by many competing parameters. It is known to produce slightly red-shifted and somewhat broadened spectra as compared to linear IR spectra. Nevertheless, IRMPD spectra are often found to closely resemble linear IR absorption spectra [1, 7].

Infrared predissociation (IRPD) technique is the closest action spectroscopic technique to investigate the IR spectroscopy of molecular ions. This technique is considered to be a linear absorption spectroscopy technique. A noble gas atom or N_2 or H_2 molecule is attached to the ion of interest as a tag (or messenger); the weakly bound complex is stable at the cryogenic temperatures (down to $\sim$4 k) of the ion trap. The tagged complex is irradiated resonantly so that upon resonance, the tag is evaporated from the complex, which is used as the signal in the IRPD spectrum. Conventional IR laser sources with relatively low powers can be used as a single photon is enough to remove the tag from the complex. It is also known as messenger-tagging IR spectroscopy.

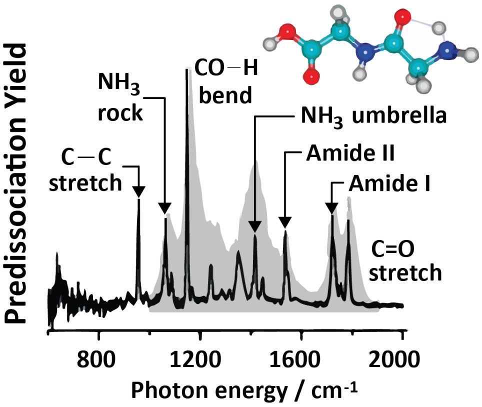

Figure 1.25. The vibrational predissociation spectrum (black trace) of an H_2-tagged model peptide ($GlyGlyH^+$) compared with the IRMPD spectrum (gray) of the same bare peptide. Modified from ref. [120].

Roitová et al. [38] reported an example illustrating the effect of the tag on IRPD spectra, showing the difference between helium and argon atoms as the tags. They found that the argon atom was not a good choice for IRPD spectroscopy, because Ar atom is more strongly bound (37 kJ mol^{-1}) distorting the geometry of the ionic compound, yielding a different IRPD spectrum. On the other hand, helium is sufficiently weakly bound (1 kJ mol^{-1}) so that it does not affect the geometry of the compound, and hence its IR spectrum.

Johnson et al. [120] showed an interesting contrast between the IRMPD spectrum of a bare peptide [121] at 300 K with that of its cryogenic H_2-tagged IRPD spectrum at 10 K (Figure 1.25). Both spectra display similar features, indicating a nearly negligible effect of the H_2-tag. The comparison moreover shows that the IRPD peaks are narrower than the IRMPD peaks.

Figure 1.26 illustrates a similar example taken from chapter 4. In this example IRMPD spectra of the bare cation match closely with the IRPD spectra of the vibrationally cold N_2-tagged cation, which is only a few cm^{-1} red-shifted compared to IRPD. This shift is well within the band-width of the OPO laser ($\leq$6 cm^{-1}) [120]. Note, only 5-10% ions are fragmented to generate this IRMPD spectrum. Despite the large temperature difference between the experiments, the IRMPD and IRPD spectra show minimal differences. Observed IRPD bands are not affected much by the N_2-tag, which is further confirmed by calculations on the tagged ion (see for details chapter 4).

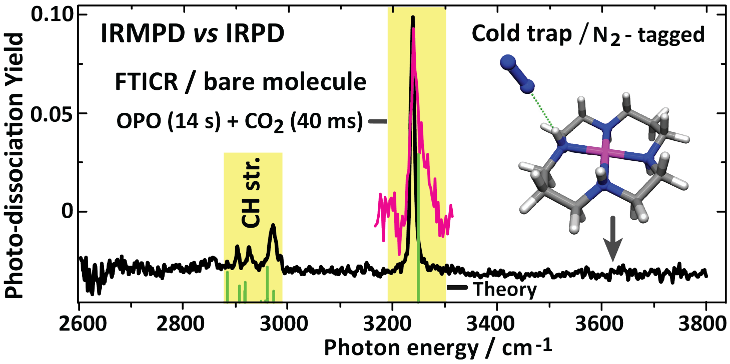

Figure 1.26. IRMPD spectra of bare Ni^{2+}(cyclam) taken in the FTICR MS in the 3 μm range (magenta) near room temperature. The photo-dissociation yield is given for the IRMPD spectrum. The single-photon N_2 predissociation spectrum (black) was taken at 30 K. The IRPD band at 3239 cm^{-1} is predicted to be at 3251 cm^{-1}. Stick spectra display the DFT computed harmonic frequencies for the bare complex. IRPD spectra and theoretical spectra have been given an offset for clarity.

1.10.4 IRMPD as a quantitative tool to probe isomer populations

IRMPD spectroscopy can be used to quantify the ratio of isomers having the same mass (*m/z*), if they possess diagnostic IR bands. This method has been reported previously by [122, 123]. An example of such experiment is illustrated for protonated indigo and isoindigo in chapter 7. By parking the IR laser on a diagnostic band for one of the isomers, this isomer population can be completely photo-fragmented by increasing the number of IR laser pulses gradually. The other isomer is transparent to the laser frequency and remains intact in the trap. One must verify that it is possible to deplete all ions in the trap when there is only one isomer (to verify laser overlap with the ion cloud). By determining the fraction of precursor depletion at a large number of IR pulses, the relative quantity of the isomer can be established. This method requires that interconversion of isomers does not occur during the irradiation [124].

References

[1] Jos Oomens, Boris G Sartakov, Gerard Meijer, and Gert Von Helden. Gas-phase infrared multiple photon dissociation spectroscopy of mass-selected molecular ions. *Int. J. Mass Spectrom.*, 254(1-2):1–19, 2006.

[2] AJ Richard. The 3D quadrupole ion trap mass spectrometer as a complete chemical laboratory for fundamental gas-phase studies of metal mediated chemistry. *Chem. Commun.*, (14):1469–1481, 2006.

[3] Luke MacAleese and Philippe Maitre. Infrared spectroscopy of organometallic ions in the gas phase: from model to real world complexes. *Mass Spectrom. Rev.*, 26(4):583–605, 2007.

[4] Travis D Fridgen. Infrared consequence spectroscopy of gaseous protonated and metal ion cationized complexes. *Mass Spectrom. Rev.*, 28(4):586–607, 2009.

[5] Nick C Polfer and Jos Oomens. Vibrational spectroscopy of bare and solvated ionic complexes of biological relevance. *Mass Spectrom. Rev.*, 28(3):468–494, 2009.

[6] Nick C Polfer. Infrared multiple photon dissociation spectroscopy of trapped ions. *Chem. Soc. Rev.*, 40(5):2211–2221, 2011.

[7] Anouk M Rijs and Jos Oomens. *Gas-phase IR spectroscopy and structure of biological molecules*, volume 364. Springer, 2015.

[8] Jonathan Martens, Josipa Grzetic, Giel Berden, and Jos Oomens. Structural identification of electron transfer dissociation products in mass spectrometry using infrared ion spectroscopy. *Nat. Commun.*, 7:11754, 2016.

[9] Josipa Grzetic. *Chemistry of peptide fragmentation: molecular structures by ion spectroscopy*. PhD thesis, Radboud University, January 2014.

[10] LJM Kempkes. *Reaction Mechanisms of Collision and Electron Induced Peptide Dissociation Revealed by Ion Spectroscopy*. PhD thesis, Radboud University, March 2019.

[11] D Oepts, AFG Van der Meer, and PW Van Amersfoort. The free-electron-laser user facility felix. *Infrared physics & technology*, 36(1):297–308, 1995.

[12] RL Woodin, DS Bomse, and JL Beauchamp. Multiphoton dissociation of molecules with low power continuous wave infrared laser radiation. *J. Am. Chem. Soc.*, 100(10):3248–3250, 1978.

[13] DS Bomse, RL Woodin, and JL Beauchamp. Molecular activation with low-intensity cw infrared laser radiation. multiphoton dissociation of ions derived from diethyl ether. *J. Am. Chem. Soc.*, 101(19):5503–5512, 1979.

[14] DS Bomse, RL Woodin, and JL Beauchamp. Multiphoton dissociation of molecules with low power cw infrared lasers. In *Advances in Laser Chemistry*, pages 362–373. Springer, 1978.

[15] RL Woodin, DS Bomse, and JL Beauchamp. Multiphoton dissociation of molecules with low power cw infrared lasers: collisional enhancement of

dissociation probabilities. *Chem. Phys. Lett.*, 63(3):630–636, 1979.

[16] YM Eva Fung, Thierry Besson, Joël Lemaire, Philippe Maitre, and Roman A Zubarev. Room-temperature infrared spectroscopy combined with mass spectrometry distinguishes gas-phase protein isomers. *Angew. Chem. Int. Ed.*, 48(44):8340–8342, 2009.

[17] John R Eyler. Infrared multiple photon dissociation spectroscopy of ions in penning traps. *Mass Spectrom. Rev.*, 28(3):448–467, 2009.

[18] HanBin Oh, Kathrin Breuker, Siu Kwan Sze, Ying Ge, Barry K Carpenter, and Fred W McLafferty. Secondary and tertiary structures of gaseous protein ions characterized by electron capture dissociation mass spectrometry and photofragment spectroscopy. *Proc. Royal Soc. Lond.*, 99(25):15863–15868, 2002.

[19] Jos Oomens, Nick Polfer, David T Moore, Lex van der Meer, Alan G Marshall, John R Eyler, Gerard Meijer, and Gert von Helden. Charge-state resolved mid-infrared spectroscopy of a gas-phase protein. *Phys. Chem. Chem. Phys.*, 7(7):1345–1348, 2005.

[20] Yijie Yang, Guanhua Liao, and Xianglei Kong. Charge-state resolved infrared multiple photon dissociation (IRMPD) spectroscopy of ubiquitin ions in the gas phase. *Sci. Rep.*, 7(1):16592, 2017.

[21] Jos Oomens, AGGM Tielens, Boris G Sartakov, Gert von Helden, and Gerard Meijer. Laboratory infrared spectroscopy of cationic polycyclic aromatic hydrocarbon molecules. *Astrophys. J.*, 591(2):968, 2003.

[22] RR Corderman and WC Lineberger. Negative ion spectroscopy. *Annu. Rev. Phys. Chem.*, 30(1):347–378, 1979.

[23] James P Reilly. Ultraviolet photofragmentation of biomolecular ions. *Mass Spectrom. Rev.*, 28(3):425–447, 2009.

[24] John B Fenn, Matthias Mann, Chin Kai Meng, Shek Fu Wong, and Craig M Whitehouse. Electrospray ionization for mass spectrometry of large biomolecules. *Science*, 246(4926):64–71, 1989.

[25] Koichi Tanaka. Detection of high mass molecules by laser desorption time-of-flight mass spectrometry. In *Proceedings of the Second Japan-China Joint Symposium on Mass Spectrometry*, 1987.

[26] Alan G Marshall. Fourier transform ion cyclotron resonance mass spectrometry. *Acc. Chem. Res.*, 18(10):316–322, 1985.

[27] Alan G Marshall and Christopher L Hendrickson. Fourier transform ion

cyclotron resonance detection: principles and experimental configurations. *Int. J. Mass Spectrom.*, 215(1-3):59–75, 2002.

[28] AG Marshall, CL Hendrickson, Mark R Emmett, RP Rodgers, GT Blakney, and CL Nilsson. Fourier transform ion cyclotron resonance: state of the art. *Eur. J. Mass Spectrom.*, 13(1):57–59, 2007.

[29] Jos Oomens, André JA van Roij, Gerard Meijer, and Gert von Helden. Gas-phase infrared photodissociation spectroscopy of cationic polyaromatic hydrocarbons. *Astrophys. J.*, 542(1):404, 2000.

[30] Reiner Lindner, Hans-Jörg Dietrich, and Klaus Müller-Dethlefs. Basic principles of zeke spectroscopy. optimized resolution and accurate ionization energy. *Chem. Phys. Lett.*, 228(4-5):417–425, 1994.

[31] Edward R Grant and Michael G White. Zeke threshold photoelectron spectroscopy. *Nature*, 354(6350):249, 1991.

[32] Xiaohang Zhang, Nils B Brauer, Giel Berden, Anouk M Rijs, and Marcel Drabbels. Mid-infrared spectroscopy of molecular ions in helium nanodroplets. *J. Chem. Phys.*, 136(4):044305, 2012.

[33] Martin CR Cockett. Photoelectron spectroscopy without photoelectrons: Twenty years of zeke spectroscopy. *Chem. Soc. Rev.*, 34(11):935–948, 2005.

[34] Shengfu Yang and Andrew M Ellis. Helium droplets: a chemistry perspective. *Chem. Soc. Rev.*, 42(2):472–484, 2013.

[35] Deepak Verma, Rico Mayro P Tanyag, Sean M O O'Connell, and Andrey F Vilesov. Infrared spectroscopy in superfluid helium droplets. *Advances in Physics: X*, 4(1):1553569, 2019.

[36] Anouk M Rijs, Nadja Sändig, Martine N Blom, Jos Oomens, Jeffrey S Hannam, David A Leigh, Francesco Zerbetto, and Wybren J Buma. Controlled hydrogen-bond breaking in a rotaxane by discrete solvation. *Angew. Chem. Int. Ed.*, 49(23):3896–3900, 2010.

[37] James M Lisy. Infrared studies of ionic clusters: The influence of Yuan T. Lee. *J. Chem. Phys.*, 125(13):132302, 2006.

[38] Juraj Jašík, Ján Žabka, Jana Roithová, and Dieter Gerlich. Infrared spectroscopy of trapped molecular dications below 4 k. *Int. J. Mass Spectrom.*, 354:204–210, 2013.

[39] Oskar Asvany, Sandra Brünken, Lars Kluge, and Stephan Schlemmer. Coltrap: a 22-pole ion trapping machine for spectroscopy at 4 k. *Appl. Phys. B*, 114(1-2):203–211, 2014.

[40] Adam P Cismesia, Laura S Bailey, Matthew R Bell, Larry F Tesler, and

Nicolas C Polfer. Making mass spectrometry see the light: the promises and challenges of cryogenic infrared ion spectroscopy as a bioanalytical technique. *J. Am. Soc. Mass. Spectrom.*, 27(5):757–766, 2016.

[41] Knut R Asmis and Daniel M Neumark. Vibrational spectroscopy of microhydrated conjugate base anions. *Acc. Chem. Res.*, 45(1):43–52, 2011.

[42] Daniel J Goebbert, Torsten Wende, Risshu Bergmann, Gerard Meijer, and Knut R Asmis. Messenger-tagging electrosprayed ions: Vibrational spectroscopy of suberate dianions. *J. Phys. Chem. A*, 113(20):5874–5880, 2009.

[43] Nadja Heine, Matias R Fagiani, Mariana Rossi, Torsten Wende, Giel Berden, Volker Blum, and Knut R Asmis. Isomer-selective detection of hydrogen-bond vibrations in the protonated water hexamer. *J. Am. Chem. Soc.*, 135(22):8266–8273, 2013.

[44] M Okumura, LI Yeh, JD Myers, and Yuan T Lee. Infrared spectra of the solvated hydronium ion: Vibrational predissociation spectroscopy of mass-selected $H_3O^+\bullet(H_2O)n\bullet(H_2)m$. *J. Phys. Chem.*, 94(9):3416–3427, 1990.

[45] R Prazeres, F Glotin, C Insa, DA Jaroszynski, and JM Ortega. Two-colour operation of a free-electron laser and applications in the mid-infrared. *Eur. Phys. J. D*, 3(1):87–93, 1998.

[46] R Prazeres, F Glotin, and JM Ortega. New results of the 'CLIO'infrared FEL. In *Free Electron Lasers 2003*, pages 83–87. Elsevier, 2004.

[47] Jose J Valle, John R Eyler, Jos Oomens, David T Moore, AFG Van Der Meer, Gert von Helden, Gerard Meijer, Christopher L Hendrickson, Alan G Marshall, and Gregory T Blakney. Free electron laser-fourier transform ion cyclotron resonance mass spectrometry facility for obtaining infrared multiphoton dissociation spectra of gaseous ions. *Rev. Sci. Instrum.*, 76(2):023103, 2005.

[48] Nick C Polfer and Jos Oomens. Reaction products in mass spectrometry elucidated with infrared spectroscopy. *Phys. Chem. Chem. Phys.*, 9(29):3804–3817, 2007.

[49] RDF Settle and TR Rizzo. CO_2 laser assisted vibrational overtone spectroscopy. *J. Chem. Phys.*, 97(4):2823–2825, 1992.

[50] Rajeev K Sinha, Undine Erlekam, Benjamin J Bythell, Béla Paizs, and Philippe Maître. Diagnosing the protonation site of b2 peptide fragment ions using IRMPD in the X-H (X= O, N, and C) stretching region. *J. Am. Soc. Mass. Spectrom.*, 22(9):1645, 2011.

[51] Mitra Almasian, Josipa Grzetic, Johanne van Maurik, Jeffrey D Steill, Giel Berden, Steen Ingemann, Wybren Jan Buma, and Jos Oomens. Non-equilibrium isomer distribution of the gas-phase photoactive yellow protein chromophore. *J. Phys. Chem. Lett.*, 3(16):2259–2263, 2012.

[52] G Mauclaire, J Lemaire, P Boissel, G Bellec, and M Heninger. MICRA: a compact permanent magnet fourier transform ion cyclotron resonance mass spectrometer. *Eur. J. Mass Spectrom.*, 10(2):155–162, 2004.

[53] Joost M Bakker, Thierry Besson, Joël Lemaire, Debora Scuderi, and Philippe Maître. Gas-phase structure of a π-allyl-palladium complex: efficient infrared spectroscopy in a 7 T fourier transform mass spectrometer. *J. Phys. Chem. A*, 111(51):13415–13424, 2007.

[54] Luke Mac Aleese, Aude Simon, Terrance B McMahon, Jean-Michel Ortega, Debora Scuderi, Joël Lemaire, and Philippe Maître. Mid-IR spectroscopy of protonated leucine methyl ester performed with an FTICR or a paul type ion-trap. *Int. J. Mass Spectrom.*, 249:14–20, 2006.

[55] Kazuhiko Fukui, Yasutoshi Takada, Tetsumi Sumiyoshi, Takayuki Imai, and Katsutoshi Takahashi. Infrared multiphoton dissociation spectroscopic analysis of peptides and oligosaccharides by using fourier transform ion cyclotron resonance mass spectrometry with a midinfrared free-electron laser. *J. Phys. Chem. B*, 110(32):16111–16116, 2006.

[56] Wieland Schöllkopf, Sandy Gewinner, Heinz Junkes, Alexander Paarmann, Gert von Helden, Hans P Bluem, and Alan MM Todd. The new IR and THz FEL facility at the Fritz Haber Institute in Berlin. In *Advances in X-ray Free-Electron Lasers Instrumentation III*, volume 9512, page 95121L. International Society for Optics and Photonics, 2015.

[57] Matthew F Bush, Jeremy T O'Brien, James S Prell, Richard J Saykally, and Evan R Williams. Infrared spectroscopy of cationized arginine in the gas phase: direct evidence for the transition from nonzwitterionic to zwitterionic structure. *J. Am. Chem. Soc.*, 129(6):1612–1622, 2007.

[58] Han-Bin Oh, Cheng Lin, Harold Y Hwang, Huili Zhai, Kathrin Breuker, Vladimir Zabrouskov, Barry K Carpenter, and Fred W McLafferty. Infrared photodissociation spectroscopy of electrosprayed ions in a fourier transform mass spectrometer. *J. Am. Chem. Soc.*, 127(11):4076–4083, 2005.

[59] Warren K Mino Jr, Kerim Gulyuz, Da Wang, Corey N Stedwell, and Nick C Polfer. Gas-phase structure and dissociation chemistry of protonated tryptophan elucidated by infrared multiple-photon dissociation

spectroscopy. *J. Phys. Chem. Lett.*, 2(4):299–304, 2011.

[60] Jonathan Martens, Giel Berden, Christoph R Gebhardt, and Jos Oomens. Infrared ion spectroscopy in a modified quadrupole ion trap mass spectrometer at the FELIX free electron laser laboratory. *Rev. Sci. Instrum.*, 87(10):103108, 2016.

[61] Scott Gronert. Estimation of effective ion temperatures in a quadrupole ion trap. *J. Am. Soc. Mass. Spectrom.*, 9(8):845–848, 1998.

[62] Raymond E March. An introduction to quadrupole ion trap mass spectrometry. *J. Mass Spectrom.*, 32(4):351–369, 1997.

[63] Scott A McLuckey and Douglas E Goeringer. Special feature: tutorial slow heating methods in tandem mass spectrometry. *J. Mass Spectrom.*, 32(5):461–474, 1997.

[64] Nicholas M Riley and Joshua J Coon. The role of electron transfer dissociation in modern proteomics. *Anal. Chem.*, 90(1):40–64, 2017.

[65] Roman A Zubarev, Neil L Kelleher, and Fred W McLafferty. Electron capture dissociation of multiply charged protein cations. a nonergodic process. *J. Am. Chem. Soc.*, 120(13):3265–3266, 1998.

[66] Roman A Zubarev. Electron-capture dissociation tandem mass spectrometry. *Curr. Opin. Biotechnol.*, 15(1):12–16, 2004.

[67] Joshua J Coon. Collisions or electrons? protein sequence analysis in the 21st century. *Anal. Chem.*, 8(19):3208–3215, 2009.

[68] Aron J Cohen, Paula Mori-Sánchez, and Weitao Yang. Insights into current limitations of density functional theory. *Science*, 321(5890):792–794, 2008.

[69] Yan Zhao and Donald G Truhlar. Density functionals with broad applicability in chemistry. *Acc. Chem. Res.*, 41(2):157–167, 2008.

[70] Filipp Furche and John P Perdew. The performance of semilocal and hybrid density functionals in 3 d transition-metal chemistry. *J. Chem. Phys.*, 124(4):044103, 2006.

[71] Dejian Huang, Patrick R Koren, Kirsten Folting, Ernest R Davidson, and Kenneth G Caulton. Facile and reversible cleavage of C-F Bonds. Contrasting Thermodynamic Selectivity for Ru CF_2H vs FOs CFH. *J. Am. Chem. Soc.*, 122(37):8916–8931, 2000.

[72] Vincenzo Balzani, Alberto Juris, Margherita Venturi, Sebastiano Campagna, and Scolastica Serroni. Luminescent and redox-active polynuclear transition metal complexes. *Chem. Rev.*, 96(2):759–834, 1996.

[73] Erik Andris, Rafael Navrátil, Juraj Jasik, Mayank Puri, Miquel Costas, Lawrence Que Jr, and Jana Roithová. Trapping iron(iii)–oxo species at the boundary of the "oxo wall": Insights into the nature of the Fe(iii)–O bond. *J. Am. Chem. Soc.*, 140(43):14391–14400, 2018.

[74] James H Takemoto and Bennett Hutchinson. Effect of magnetic crossover on the low-frequency IR spectrum of [Fe (1, 10-phenanthroline) 2 (NCS) 2]. *Inorg. Nucl. Chem. Lett.*, 8(9):769–772, 1972.

[75] Fabian S Menges, Stephanie M Craig, Niklas Tötsch, Aaron Bloomfield, Subrata Ghosh, Hans-Jörg Krüger, and Mark A Johnson. Capture of CO_2 by a cationic nickel (i) complex in the gas phase and characterization of the bound, activated CO_2 molecule by cryogenic ion vibrational predissociation spectroscopy. *Angewandte Chemie*, 128(4):1304–1307, 2016.

[76] Brian O'regan and Michael Grätzel. A low-cost, high-efficiency solar cell based on dye-sensitized colloidal TiO_2 films. *Nature*, 353(6346):737, 1991.

[77] Gerrit Boschloo and Anders Hagfeldt. Characteristics of the iodide/triiodide redox mediator in dye-sensitized solar cells. *Acc. Chem. Res.*, 42(11):1819–1826, 2009.

[78] M Khaja Nazeeruddin, Amin Kay, Ignacio Rodicio, Robin Humphry-Baker, E Müller, Petr Liska, Nick Vlachopoulos, and M Grätzel. Conversion of light to electricity by cis-x2bis (2, 2'-bipyridyl-4, 4'-dicarboxylate) ruthenium (ii) charge-transfer sensitizers (X= Cl-, Br-, I-, CN-, and SCN-) on nanocrystalline titanium dioxide electrodes. *J. Am. Chem. Soc.*, 115(14):6382–6390, 1993.

[79] Mohammad K Nazeeruddin, Peter Pechy, Thierry Renouard, Shaik M Zakeeruddin, Robin Humphry-Baker, Pascal Comte, Paul Liska, Le Cevey, Emiliana Costa, Valery Shklover, et al. Engineering of efficient panchromatic sensitizers for nanocrystalline TiO_2-based solar cells. *J. Am. Chem. Soc.*, 123(8):1613–1624, 2001.

[80] Helmut Tributsch. Dye sensitization solar cells: a critical assessment of the learning curve. *Coord. Chem. Rev.*, 248(13-14):1511–1530, 2004.

[81] Shuang Xu, James ET Smith, and J Mathias Weber. The electronic spectrum of cryogenic ruthenium-tris-bipyridine dications in vacuo. *J. Chem. Phys.*, 145(2):024304, 2016.

[82] MH Stockett and S Brøndsted Nielsen. Communication: Does a single CH_3CN molecule attached to $Ru(bipy)_3{}^{2+}$ affect its absorption spectrum? *J. Chem. Phys.*, 142(17):171102, 2015.

[83] K Kalyanasundaram and M Grätzel. Applications of functionalized transition metal complexes in photonic and optoelectronic devices. *Coord. Chem. Rev.*, 177(1):347–414, 1998.

[84] Kiyoshi CD Robson, Bryan D Koivisto, Aswani Yella, Barbora Sporinova, Mohammad K Nazeeruddin, Thomas Baumgartner, Michael Grätzel, and Curtis P Berlinguette. Design and development of functionalized cyclometalated ruthenium chromophores for light-harvesting applications. *Inorg. Chem.*, 50(12):5494–5508, 2011.

[85] Chun Sakong, Hae Joong Kim, Se Hun Kim, Jin Woong Namgoong, Jong Ho Park, Jang-Hyun Ryu, Boeun Kim, Min Jae Ko, and Jae Pil Kim. Synthesis and applications of new triphenylamine dyes with donor–donor–(bridge)–acceptor structure for organic dye-sensitized solar cells. *New J. Chem.*, 36(10):2025–2032, 2012.

[86] Zhiming Wang, Xiaohui Song, Lingling Ma, Ying Feng, Cheng Gu, Xiaojuan Zhang, Ping Lu, and Yuguang Ma. A triphenylamine-capped solution-processable wholly aromatic organic molecule with electrochemical stability and its potential application in photovoltaic devices. *New J. Chem.*, 37(8):2440–2447, 2013.

[87] Wei Zhang, Peng Liu, Azar Sadollahkhani, Yuanyuan Li, Biaobiao Zhang, Fuguo Zhang, Majid Safdari, Yan Hao, Yong Hua, and Lars Kloo. Investigation of triphenylamine (TPA)-based metal complexes and their application in perovskite solar cells. *ACS Omega*, 2(12):9231–9240, 2017.

[88] An-Na Cho, Nallan Chakravarthi, Kakaraparthi Kranthiraja, Saripally Sudhaker Reddy, Hui-Seon Kim, Sung-Ho Jin, and Nam-Gyu Park. Acridine-based novel hole transporting material for high efficiency perovskite solar cells. *J. Mater. Chem.A*, 5(16):7603–7611, 2017.

[89] Philippe Blanchard, Claudia Malacrida, Clément Cabanetos, Jean Roncali, and Sabine Ludwigs. Triphenylamine and some of its derivatives as versatile building blocks for organic electronic applications. *Polym. Int.*, 68(4):589–606, 2019.

[90] ed. P. J. Linstrom and W. G. Mallard. NIST Chemistry Webbook, NIST Standard Reference Database Number 69, National Institute of Standards and Technology, Gaithersburg MD, 20899 (accessed: May 2015).

[91] Ben L Feringa. The art of building small: from molecular switches to molecular motors. *J. Org. Chem.*, 72(18):6635–6652, 2007.

[92] George M Wyman. The cis-trans isomerization of conjugated compounds. *Chem. Rev.*, 55(4):625–657, 1955.

[93] Emma C Nicholls-Allison, Graeme Nawn, Brian O Patrick, and Robin G Hicks. Protoisomerization of indigo di-and monoimines. *Chem. Commun.*, 51(62):12482–12485, 2015.

[94] Laurence Hajjar, Robin G Hicks, and Tao Zeng. A computational study of the protoisomerization of indigo and its imine derivatives. *J. Phys. Chem. A*, 120(38):7569–7576, 2016.

[95] B Lucas, G Gregoire, J Lemaire, P Maitre, F Glotin, JP Schermann, and C Desfrancois. Infrared multiphoton dissociation spectroscopy of protonated n-acetyl-alanine and alanyl-histidine. *Int. J. Mass Spectrom.*, 243(2):105–113, 2005.

[96] Giel Berden, Mathijs Derksen, Kas J Houthuijs, Jonathan Martens, and Jos Oomens. An automatic variable laser attenuator for irmpd spectroscopy and analysis of power-dependence in fragmentation spectra. *Int. J. Mass Spectrom.*, 443:1–8, 2019.

[97] International Crystal Laboratories. `http://www.internationalcrystal.net/optics_02.htm`. accessed: June, 2019).

[98] Yu Xia and Scott A McLuckey. Evolution of instrumentation for the study of gas-phase ion/ion chemistry via mass spectrometry. *J. Am. Soc. Mass. Spectrom.*, 19(2):173–189, 2008.

[99] Ralf Hartmer, Desmond A Kaplan, Christoph R Gebhardt, Thorsten Ledertheil, and Andreas Brekenfeld. Multiple ion/ion reactions in the 3D ion trap: Selective reagent anion production for ETD and PTR from a single compound. *Int. J. Mass Spectrom.*, 276(2-3):82–90, 2008.

[100] Philip D Compton, Joseph V Strukl, Dina L Bai, Jeffrey Shabanowitz, and Donald F Hunt. Optimization of electron transfer dissociation via informed selection of reagents and operating parameters. *Anal. Chem.*, 84(3):1781–1785, 2012.

[101] Jonathan Martens, Giel Berden, and Jos Oomens. Structures of fluoranthene reagent anions used in electron transfer dissociation and proton transfer reaction tandem mass spectrometry. *Anal. Chem.*, 88(12):6126–6129, 2016.

[102] Scott A McLuckey and Teng-Yi Huang. Ion/ion reactions: new chemistry for analytical MS. *Anal. Chem.*, 81(21):8669–8676, 2009.

[103] Min-Sik Kim and Akhilesh Pandey. Electron transfer dissociation mass spectrometry in proteomics. *Proteomics*, 12(4-5):530–542, 2012.

[104] Anders Baardseth Nielsen, Preben Hvelplund, and Steen Brøndsted Nielsen. Ruthenium diimine complexes in unusual charge states formed in collisional electron transfer. *Int. J. Mass Spectrom.*, 232(1):79–82, 2004.

[105] Camilla Skinnerup Byskov, J Mathias Weber, and Steen Brøndsted Nielsen. Gas-phase spectroscopy of singly reduced tris(bipyridine) ruthenium ions, $\mathrm{Ru(bipy)_3}^+$. *Phys. Chem. Chem. Phys.*, 17(8):5561–5564, 2015.

[106] Nick C Polfer, Jos Oomens, David T Moore, Gert von Helden, Gerard Meijer, and Robert C Dunbar. Infrared spectroscopy of phenylalanine Ag(I) and Zn(II) complexes in the gas phase. *J. Am. Chem. Soc.*, 128(2):517–525, 2006.

[107] Shenheng Guan and Alan G Marshall. Ion traps for fourier transform ion cyclotron resonance mass spectrometry: principles and design of geometric and electric configurations. *Int. J. Mass Spectrom. Ion Processes*, 146:261–296, 1995.

[108] Shenheng Guan and Alan G Marshall. Stored waveform inverse fourier transform (SWIFT) ion excitation in trapped-ion mass spectometry: Theory and applications. *Int. J. Mass Spectrom. Ion Processes*, 157:5–37, 1996.

[109] Bruno Lucas, Gilles Grégoire, Joël Lemaire, Philippe Maître, Jean-Michel Ortega, Alisa Rupenyan, Bernd Reimann, Jean Pierre Schermann, and Charles Desfrançois. Investigation of the protonation site in the dialanine peptide by infrared multiphoton dissociation spectroscopy. *Phys. Chem. Chem. Phys.*, 6(10):2659–2663, 2004.

[110] Fritz Keilmann. Precision broadband far-infrared attenuator. In *Far-Infrared Science and Technology*, volume 666, pages 213–219. International Society for Optics and Photonics, 1986.

[111] GMH Knippels and AFG Van Der Meer. Fel diagnostics and user control. *Nucl. Instrum. Methods Phys. Res., Sect. B*, 144(1-4):32–39, 1998.

[112] VN Bagratashvili, VS Letokhov, AA Makarov, and EA Ryabov. Multiple-photon infrared laser photophysics and photochemistry. i. *Laser Chem.*, 1(5):211–342, 1983.

[113] Donald W Lupo and Martin Quack. IR-laser photochemistry. *Chem. Rev.*, 87(1):181–216, 1987.

[114] KK Lehmann, G Scoles, and BH Pate. Intramolecular dynamics from

eigenstate-resolved infrared spectra. *Annu. Rev. Phys. Chem.*, 45(1):241–274, 1994.

[115] Peter M Felker and Ahmed H Zewail. Dynamics of intramolecular vibrational-energy redistribution (IVR). ii. excess energy dependence. *J. Chem. Phys.*, 82(7):2975–2993, 1985.

[116] A Callegari, U Merker, P Engels, HK Srivastava, KK Lehmann, and G Scoles. Intramolecular vibrational redistribution in aromatic molecules. I. eigenstate resolved CH stretch first overtone spectra of benzene. *J. Chem. Phys.*, 113(23):10583–10596, 2000.

[117] Mordechai Bixon and Joshua Jortner. Intramolecular radiationless transitions. *J. Chem. Phys.*, 48(2):715–726, 1968.

[118] Jos Oomens, Boris G Sartakov, AGGM Tielens, Gerard Meijer, and Gert von Helden. Gas-phase infrared spectrum of the coronene cation. *Astrophys. J. Lett.*, 560(1):L99, 2001.

[119] RC Dunbar and TB McMahon. Activation of unimolecular reactions by ambient blackbody radiation. *Science*, 279(5348):194–197, 1998.

[120] Michael Z Kamrath, Etienne Garand, Peter A Jordan, Christopher M Leavitt, Arron B Wolk, Michael J Van Stipdonk, Scott J Miller, and Mark A Johnson. Vibrational characterization of simple peptides using cryogenic infrared photodissociation of H_2-tagged, mass-selected ions. *J. Am. Chem. Soc.*, 133(16):6440–6448, 2011.

[121] Ronghu Wu and Terry B McMahon. Protonation sites and conformations of peptides of glycine ($Gly_{1-5}H^+$) by IRMPD spectroscopy. *J. Phys. Chem. B*, 113(25):8767–8775, 2009.

[122] James S Prell, Terrence M Chang, Jeffrey A Biles, Giel Berden, Jos Oomens, and Evan R Williams. Isomer population analysis of gaseous ions from infrared multiple photon dissociation kinetics. *J. Phys. Chem. A*, 115(13):2745–2751, 2011.

[123] Paul D Schnier and Evan R Williams. Analysis of isomeric mixtures using blackbody infrared radiative dissociation: Determining isomeric purity and obtaining individual tandem mass spectra simultaneously. *Anal. Chem.*, 70(14):3033–3041, 1998.

[124] Mathias Schäfer, Katrin Peckelsen, Mathias Paul, Jonathan Martens, Jos Oomens, Giel Berden, Albrecht Berkessel, and Anthony JHM Meijer. Hydrogen tunneling above room temperature evidenced by infrared ion spectroscopy. *J. Am. Chem. Soc.*, 139(16):5779–5786, 2017.

Chapter 2

Theoretical Methods and Computational Modeling

It is also a good rule not to put too much confidence in experimental results until they have been confirmed by Theory. – Sir Arthur Eddington

2.1 Introduction

In this thesis, experimentally recorded infrared spectra in the gas phase are directly compared with the computed vibrational frequencies of the possible structures which then either confirms or disproves the prediction providing the detail structural information *via* matching of IR fingerprint signature. In this way, experimental IR spectra serve as a reference to verify the quality of the used theoretical methods.

This section briefly outlines the theoretical methods applied throughout this thesis although these theoretical concepts are comprehensively described in text books. The particular focus is laid on density functional theory (DFT) which is applicable to large molecular systems where no other methods provide comparable accuracy at the same computational cost. This section is divided into several subsections starting from the introduction of the Schrödinger equation. Next two subsections briefly talk about Born-Oppenheimer approximation and mean-field Hartree-Fock (HF) approximation in quantum chemical calculations. DFT follows next. In addition, the basic concepts of functionals and basis sets are also included. This section ends with a brief explanation to compute the harmonic vibrational frequencies of the predicted geometries.

2.2 Electronic Structure Theory

The goal of electronic structure theory is to solve the many-body Schrödinger equation

$$\hat{H}\Psi(\{R_A\},\{r_i,\sigma_i\}) = E\Psi(\{R_A\},\{r_i,\sigma_i\}) \tag{2.1}$$

For a system having M nuclei and N electrons the wave-function (Ψ) is a function of all spatial coordinates of nuclei ($\{R_A\}$,A = 1, ..., M) and spatial and spin coordinates of electrons ($\{r_i,\sigma_i\}$, i = 1,..., N). The Hamiltonian ($\hat{H}$) includes all possible interactions between electrons and nuclei. In atomic units the Hamiltonian can be written as:

$$\hat{H} = -\frac{1}{2}\sum_{i=1}^{N}\nabla_i^2 - \frac{1}{2}\sum_{A=1}^{M}\frac{1}{M_A}\nabla_A^2 + \sum_{i=1}^{N}\sum_{j>i}^{N}\frac{1}{|r_i-r_j|} + \sum_{A=1}^{M}\sum_{B>A}^{M}\frac{Z_AZ_B}{|R_A-R_B|} - \sum_{i=1}^{N}\sum_{A=1}^{M}\frac{Z_A}{|r_i-R_A|} \tag{2.2}$$

In the above equation, M_A represents the ratio of the mass of nucleus A to the mass of an electron, and Z_A represents the atomic number of nucleus A. The ∇_i^2 and ∇_A^2 are the Laplacian operators. The first and second term of the Equation 2.2 represent the kinetic energies of all the electrons and nuclei, respectively. The next two terms represent the Coulomb repulsion between electrons and between nuclei, respectively. The fifth term corresponds to the Coulomb attraction between electrons and nuclei. Although the Equation 2.2 looks simple, it is enormously difficult to solve. Since formulation many approximations have been proposed in order to reduce the complexity. The very first approximation is based on decoupling the dynamics of the electrons and the nuclei suggested by Born and Oppenheimer [1].

2.3 Born-Oppenheimer Approximation

The Born-Oppenheimer Approximation relies on the fact that the nuclei are much heavier than the electrons. Point to note is that the lightest nucleus, a proton is approximately 2000 times heavier than an electron. Therefore the electrons move much faster than the nuclei allowing the dynamics of the electrons and nuclei to be separable. In this approximation nuclei are treated as classical particles and are held clamped with respect to the electrons. Therefore, for any given nuclear geometry the electronic Schrödinger equation can be solved where the electrons are in the static potential arising from the nuclei in that particular arrangement. By solving the Schrödinger equation for a set of nuclear coordinates we can construct the molecular potential energy surface to identify the equilibrium conformation of the molecular species as the minimum energy point on this hyper surface. This approximation is reliable for predicting ground electronic states whereas less reliable for electronically excited states.

In this approximation, one can consider that the electrons are moving in the field of fixed nuclei. Therefore, the kinetic energy of the nuclei can be neglected and the fourth term, the repulsion between the nuclei can be considered as a constant in Equation 2.2. The rest is called the electronic Hamiltonian,

$$\hat{H}_e = -\frac{1}{2}\sum_{i=1}^{N}\nabla_i^2 - \sum_{i=1}^{N}\sum_{A=1}^{M}\frac{Z_A}{|r_i - R_A|} + \sum_{i=1}^{N}\sum_{j>i}^{N}\frac{1}{|r_i - r_j|} \tag{2.3}$$

The solution to a Schrödinger equation involving the electronic Hamiltonian becomes

$$\hat{H}_e\Psi_e(\{R_A\},\{r_i,\sigma_i\}) = E_e\Psi_e(\{R_A\},\{r_i,\sigma_i\}) \tag{2.4}$$

The electronic wavefunction Ψ_e now parametrically depends on the nuclear coordinates ($\{R_A\}$).

The main complication in solving the Equation 2.4 is due to the interaction between electrons. Since the movement of the electrons are correlated, meaning electrons avoid each other all the time, the instantaneous coordinates of each electron should be known. This demands the treatment of variables in the order 3^N for an N-electron system which is almost intractable. Despite this difficulty, many approximate methods have been developed in order to solve Schrödinger-like equations, where the N-electron Schrödinger equation is divided into a set of effective 1-electron Schrödinger-like equations. One of the popular approximate methods is Density Functional Theory (DFT) where electron density is the key quantity. Throughout this thesis DFT is chosen for almost all systems. In the following, the DFT method is described starting from the Hartree-Fock approximation.

2.4 The Hartree-Fock Approximation

The Hartree-Fock (HF) approximation is considered as the first step of quantum chemistry. The wave function of N electrons $(\{\Psi(\mathrm{x_i})\})$, can essentially be described with a single Slater determinant (Equation 2.5). A Slater determinant is also a linear combination of the product of independent electron wave functions, known as spin orbitals $(\{\chi_\mathrm{i}(\mathrm{x_i})\})$. Most importantly, the beauty of the Slater determinant is that it obeys the antisymmetric property of the electronic wave functions implied by Pauli's exclusion principle because the electrons are fermions. For a system having N electrons the HF wavefunction that is a Slater determinant

$$\Psi(\{\mathrm{x_i}\}) \approx \Psi_{\mathrm{SD}}(\{\mathrm{x_i}\}) = \frac{1}{\sqrt{\mathrm{N!}}} \begin{vmatrix} \chi_\mathrm{i}(\mathrm{x_i}) & \chi_\mathrm{j}(\mathrm{x_i}) & \cdots & \chi_\mathrm{N}(\mathrm{x_i}) \\ \chi_\mathrm{i}(\mathrm{x_j}) & \chi_\mathrm{j}(\mathrm{x_j}) & \cdots & \chi_\mathrm{N}(\mathrm{x_j}) \\ \vdots & \vdots & \ddots & \vdots \\ \chi_\mathrm{i}(\mathrm{x_N}) & \chi_\mathrm{j}(\mathrm{x_N}) & \cdots & \chi_\mathrm{N}(\mathrm{x_N}) \end{vmatrix} \tag{2.5}$$

Each column of this Slater determinant is labeled by spin orbitals while each row is labelled by electrons. Here, interchange of any two electron coordinates will swap two columns, satisfying the antisymmetric property. Moreover, due to this property, two electrons with same spin can not occupy the same spatial orbital meaning this Slater determinant also takes care of the correlation between the electrons with parallel spins but the correlation between the opposite spins is not. This determinant (Equation 2.5) describes a system in its ground state having N one-electron system with an effective potential. According to the variational principle the energy of this wavefunction can be minimized based on the choice of the basis functions.

2.5 Density Functional Theory (DFT)

The electron density $\rho(\mathrm{r})$ is used as the central quantity in density-functional theory (DFT), which reduces the dimensionality as opposed to wave function methods. The density is always 3-dimensional regardless of the number of electrons in a system. This enables DFT to be applied to larger systems having hundreds or even thousands of atoms. Therefore, DFT has become popular particularly among condensed matter physicist and chemist communities for calculating electronic structure.

2.5.1 Kohn-Sham Equations

In 1965 the publication of the paper by Kohn and Sham transformed DFT into a practical electronic structure theory [2]. They realized that the Thomas-Fermi model failed mainly because of the poor description of the kinetic energy. As a solution they re-introduced the idea of totally *non-interacting* electrons moving in an effective field which is similar to the Hartree-Fock approach.

In Equation 2.6 the energy functional, $E[\rho(r)]$ is expressed as a sum of kinetic energy of the non-interacting electrons, the interaction between the nuclei and electrons, the classical electron-electron repulsion and the correlation to the kinetic energy of the electrons, and all quantum correlations of the electron-electron repulsion energy.

$$E[\rho(r)] = T_{ni}[\rho(r)] + V_{ne}[\rho(r)] + V_{ee}[\rho(r)] + \Delta T[\rho(r)] + \Delta V_{ee}[\rho(r)] \tag{2.6}$$

Here the kinetic energy is simply the sum of individual electronic kinetic energies for a non-interacting system of electrons. However, in order to solve this equation, we must know the density. The trick here is to use the density calculated via Slater-determinantal wave function. Therefore, Equation 2.6 may be written as Equation 2.7 by expressing the density in the orbital basis

$$\begin{aligned} E[\rho(r)] = &\sum_{i}^{N} \left(\langle \chi_i | -\frac{1}{2}\nabla_i^2 | \chi_i \rangle - \langle \chi_i | \sum_{k}^{\text{nuclei}} \frac{Z_k}{|r_i - r_k|} | \chi_i \rangle \right) \\ &+ \sum_{i}^{N} \langle \chi_i | \frac{1}{2} \int \frac{\rho(r\prime)}{|r_i - r'|} | \chi_i \rangle + E_{xc}[\rho(r)] \end{aligned} \tag{2.7}$$

where the density is desired from the Slater-determinantal wave function χ (Equation 2.5). The terms ΔT and ΔV_{ee} together is called exchange-correlation (XC) energy, $E_{xc}[\rho(r)]$. Keep in mind that the Slater-determinantal wavefunction is an exact eigenfunction for the non-interacting system and χ is directly related to the density as

$$\rho = \sum_{i=1}^{N} \langle \chi_i | \chi_i \rangle \tag{2.8}$$

Now if we apply the variational principle and find the orbitals χ minimizing the energy in Equation 2.7, we are actually solving the pseudoeigenvalue equations

$$h_i^{KS}\chi_i = \varepsilon_i\chi_i \tag{2.9}$$

where the one-electron Kohn-Sham (KS) operator is defined as

$$h_i^{KS} = -\frac{1}{2}\nabla_i^2 - \sum_k^{\text{nuclei}} \frac{Z_k}{|r_i - r_k|} + \int \frac{\rho(r')}{|r_i - r'|}dr' + V_{xc} \tag{2.10}$$

and

$$V_{xc} = \frac{\delta E_{xc}}{\delta\rho} \tag{2.11}$$

V_{xc} is the XC potential. Since we are minimizing the E of Equation 2.6, the χ must yield the exact density. These are the orbitals forming the Slater-determinantal eigenfunction for non-interacting Hamiltonian in Equation 2.10, i.e.,

$$\sum_{i=1}^{N} h_i^{KS}|\chi_1\chi_2...\chi_N\rangle = \sum_{i=1}^{N}\varepsilon_i|\chi_1\chi_2...\chi_N\rangle \tag{2.12}$$

Now in order to determine the KS orbitals, molecular orbital theory is applied where the χ in Equation 2.12 is expressed in a basis set of functions $\{\varphi\}$ (see Equation 2.14), i.e., linear combination of atomic orbitals (LCAO), and then the individual orbital coefficients are determined from Equation 2.13.

$$K_{\mu\nu} = \langle\varphi_\mu| -\frac{1}{2}\nabla^2 - \sum_k^{\text{nuclei}} \frac{Z_k}{|r - r_k|} + \int \frac{\rho(r')}{|r - r'|} + V_{xc}|\varphi_\nu\rangle \tag{2.13}$$

where $K_{\mu\nu}$ is the orbital energy and

$$\chi_i = \sum_n c_n\varphi_n \tag{2.14}$$

Here the solutions of Equation 2.13 are completely analogous to that employed for HF theory. If we look carefully, we see that the density is necessary to compute the matrix elements (of Equation 2.13), therefore the KS equations must be solved in an iterative self-consistent field (SCF) process. The general way is to start with an initial guess of the electron density, and then obtain the KS orbitals from Equation 2.9. Based on these Kohn-Sham orbitals, a new electron density is obtained from Equation 2.8 and this process is repeated until the convergence is accomplished. Then the total energy is calculated from Equation 2.7 employing the final electron density.

If we know each term in the KS energy functional, we may calculate the exact ground state density and the net energy. Unfortunately, the XC functional (E_{XC}) is not known and contains not only the difference between the classical and quantum mechanical electron-electron repulsion energy, but also the difference in kinetic energy between the real and the fictitious non-interacting system. Therefore, it is imperative to approximate it, which is the focus of the following section.

2.5.2 Exchange-Correlation Functionals

From a practical view point, we must know the form of the XC functional to apply the KS equations. Since there is no direct recipe to determine the exact form of E_{XC}, some approximations have been suggested and used. Since the birth of DFT there exist a numerous approximated functionals with differing levels of complexity. J. P. Perdew and K. Schmidt showed a useful way of classifying the functionals that exists known as ”Jacob’s ladder”(Figure 2.1) [3]. The functionals are segregated with respect to their complexity on the rungs of a ladder starting from the Hartree approximation on ”earth” till the exact XC functional in ”heaven” of chemical accuracy. Functionals are also grouped based on *non-empirical* fitting observed atomic and molecular properties called *empirical*. Below some of the functionals are briefly discussed which are widely used and out of which some of them are employed in this thesis.

XC potentials mentioned earlier (Equation 2.11) often break up into exchange and correlation parts and are written in terms of to the energy per particle, ε_X and ε_C.

$$E_{XC}[\rho] = E_X[\rho] + E_C[\rho] = \int \rho(r)\varepsilon_X[\rho(r)]dr + \int \rho(r)\varepsilon_C[\rho(r)]dr \tag{2.15}$$

In the following some of the XC potentials are described briefly.

Local and semilocal XC energy functionals satisfy the general form

$$\begin{aligned} E_{XC}[\rho_\uparrow, \rho_\downarrow] = \int dr\rho(r)\varepsilon_{XC}(\rho_\uparrow(r), \rho_\downarrow(r), \nabla\rho_\uparrow(r), \nabla\rho_\downarrow(r), \\ \nabla^2\rho_\uparrow(r), \nabla^2\rho_\downarrow(r), \tau_\uparrow(r), \tau_\downarrow(r)) \end{aligned} \tag{2.16}$$

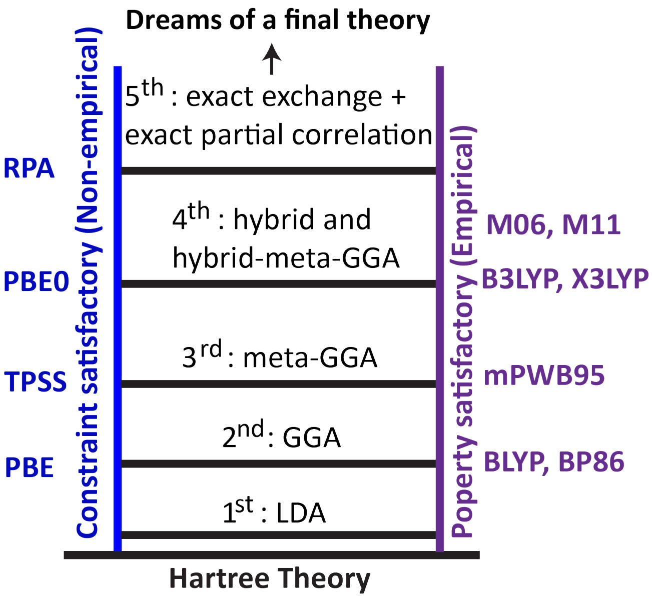

Figure 2.1. Schematic diagram of "Jacob's ladder" of exchange-correlation functionals suggested by J. P. Perdew and K. Schmidt [3].

where $\rho_\uparrow(r)$ and $\rho_\downarrow(r)$ are the spin up and down densities, $\rho(r) = \rho_\uparrow(r) + \rho_\downarrow(r)$ is the charge density, and ε_{XC} is the per particle XC energy. If ε_{XC} depends on the spin densities then this is called local spin density approximation (LSDA) [4–8]. LSDA works well for slowly varying densities. Despite this limitation it performs reasonably well for atomic, molecular and solid phase systems. On the other hand, for rapidly varying densities, LSDA underestimates the exchange energy by about 14% and overestimates the correlation energy by a factor of 2.5; more often these errors cancel each other [9, 10].

The next improvement on the LSDA is the inclusion of the semilocal approximations where strongly inhomogeneous densities are considered for real systems. Within the generalized gradient approximation (GGA), ε_{XC} not only depends on the spin densities but also on their gradients $\nabla\rho_\sigma(r)$ $(\sigma = \uparrow, \downarrow)$ [10–13]. From the GGA type, BLYP and BP86 functionals have been tested for some of the systems studied in this thesis. These functionals are generally much better for quick geometries and vibrational frequencies for transition metal-ligand complexes. BLYP functional was also tested for organic triphenylamine radical cation which yielded better frequencies than B3LYP (chapter 6).

In the so-called meta-GGA [14–16], the second derivatives of the spin densities $\nabla^2\rho_\sigma(r)$, and/or the kinetic energy densities $\tau_\sigma(r)$ are included as additional degrees of freedom within the ε_{xc}.

$$\tau_\sigma(r) = \frac{1}{2}\sum_{i\sigma}^{occ.} f_{i\sigma} \mid \nabla\psi_{i\sigma}(r) \mid^2 \tag{2.17}$$

where $f_{i\sigma}$ and $\psi_{i\sigma}$ are the occupation number and the spin-orbital of the *i*th σ-type single-particle level taken from the KS system which is noninteracting, and the summation runs over the occupied spin-orbitals only.

Next functionals are the hybrid functions; conceptually these functionals are based on the adiabatic connection formalism [17–19]. These XC energy functionals have an explicit contribution of the nonlocal HF exchange energy [20, 21]:

$$E_x^{HF}[\rho_\uparrow,\rho_\downarrow] = -\frac{1}{2}\sum_{\sigma=\uparrow,\downarrow}\sum_{i,j}^{occ.}\iint dr_1 dr_2 \psi_{i\sigma}^*(r_1)\psi_{j\sigma}^*(r_1)\frac{1}{r_{12}}\psi_{i\sigma}(r_2)\psi_{j\sigma}(r_2) \tag{2.18}$$

These functionals explicitly rely on the KS spin-orbitals which are occupied and can be generally expressed ($E_x^{HF}[\rho_\uparrow,\rho_\downarrow] \equiv E_x^{HF}[\{\psi_{i\sigma}\}_{i\sigma\in occ}]$)

$$E_{xc}^{hyb}[\rho_\uparrow,\rho_\downarrow] = a_x E_x^{HF}[\rho_\uparrow,\rho_\downarrow] + (1-a_x)E_x^{sem}[\rho_\uparrow,\rho_\downarrow] + E_c^{sem}[\rho_\uparrow,\rho_\downarrow] \tag{2.19}$$

where a_x is the HF contribution, and E_x^{sem} and E_c^{sem} are semilocal exchange and correlation functionals.

For instance, a 3-parameter functional (B3) developed by Becke (1993) has the general form of Equation 2.20. As well, B3PW91 [20] (Equation 2.21) and the most popular B3LYP (Equation 2.22) functionals [22] share identical parameters differing in the choice of correlation functional.

$$E_{xc}^{B3} = aE_x^{HF} + (1-a)E_x^{LSDA} + b\Delta E_x^{B88} + (1-c)E_c^{LSDA} + c\Delta E_c^{GGA} \tag{2.20}$$

$$E_{xc}^{B3PW91} = aE_x^{HF} + (1-a)E_x^{LSDA} + b\Delta E_x^{B88} + (1-c)E_c^{LSDA} + c\Delta E_c^{PW91} \tag{2.21}$$

$$E_{xc}^{B3LYP} = aE_x^{HF} + (1-a)E_x^{LSDA} + b\Delta E_x^{B88} + (1-c)E_c^{LSDA} + c\Delta E_c^{LYP} \tag{2.22}$$

a,b,c parameters were optimized to 0.20, 0.72 and 0.81 based on the fittings with experimental data and the chosen forms of GGA functions. The B3LYP functional contains 20% HF contribution as a default value. Moreover, if the HF contribution is reduced to 15% this is denoted as B3LYP*. On the basis of comparing against experimental data, hybrid functionals with reduced HF exchange are reported to be the best suited for the description of the properties of transition-metal complexes, especially their spin-state energetics [23–26].

In chapter 5 we have shown a reduced HF contribution in B3LYP functional can reproduce the experimental metal-ligand bond length while simultaneously the computed harmonic frequencies agree with the experimental IR spectra for the $[Ru(bpy)_3]^+$ complex. Furthermore, the relative bond lengths (metal-ligand) as opposed to the analogous dication qualitatively correlate with the loss of a bpy moiety from both complexes if reduced HF (13-15% HF) B3LYP functional is chosen for the $[Ru(bpy)_3]^+$ complex. A comparison of the performance of various functionals is described in order to reproduce the experimental IR spectra of both members of the $[Ru(bpy)_3]^{2+/+}$ redox pair.

B3PW91 was the first functional where molecular data was used in the fitting parameter and a maximum of 10 parameters were used [27]. After that Truhlar group has chosen 20-50 parameters [28–31]. These functionals are called Minnesota (or meta) functionals [4, 31]. Some of these functionals are also tested in this thesis. Various functionals including global hybrid functionals were extensively reviewed recently reporting their performances until the last 50 years for predicting molecular and condensed matter properties [5, 27, 32, 33]. The Minnesota functional family seems to work better with broad accuracy than the previously popular functionals for thermochemistry, kinetics, and noncovalent interactions [4, 31].

Climbing up through the Jacob's ladder does not necessarily ensure better results although climbing higher on the ladder involves inclusion of highly complex functions and more constraints on the functionals. In chapter 5, this will be more apparent where some of the functionals are tested for $[Ru(bpy)_3]^{2+/+}$ redox pair in predicting the IR spectra of the ground state molecular systems and the corresponding structural properties in gas phase.

2.6 Selection of Basis Sets

Basis sets are essential to practically solve the Schrödinger equation. A set of basis functions is used to expand the unknown wave function in all electronic structure methods. Various types of basis functions exist such as exponential, Gaussian, polynomial, plane-wave, Slater type orbitals, and numerical atomic orbitals. In quantum chemistry, the basis set usually refers to the set of (nonorthogonal) one-electron functions used to construct molecular orbitals. In most quantum chemistry programs atomic orbitals represented by atom-centered Gaussian type orbitals (GTOs) are used. Some older programs including Amsterdam Density Functional (ADF) program use Slater type orbitals (STOs). Plane wave basis sets are popular in solid state physics for regular systems such as crystal lattices. However, in this thesis mostly GTOs are used although STOs are also tested. Therefore, the basic differences are described briefly between the two mathematical formalisms of the GTOs and STOs.

2.6.1 Slater *vs* Gaussian type basis sets

STOs were used as basis functions because they have similarity with the exact solutions of hydrogen atom. STOs have the following form in Cartesian coordinates,

$$\varphi_{abc}^{STO}(x, y, z) = Nx^a y^b z^c e^{-\zeta r} \tag{2.23}$$

where N is the normalization constant, and a, b, c control the angular momentum with the relation L=a+b+c. ζ controls the width of the orbital (larger ζ gives tight function, small ζ yields diffuse function). The values of ζ are decided based on the fitting of STOs to the numerically computed atomic wavefunctions. Most importantly, the STOs characterized by the exponential part which has the first power of the variable. Note that STOs do not have any radial nodes, but nodes in the radial part are introduced by the linear combination of STOs. For instance, 1s orbital of hydrogen atom has no radial node whereas 2s orbital has one radial node. In addition, STOs have correct short and long range behavior.

On the other hand, GTOs have the following form in Cartesian coordinates,

$$\varphi_{abc}^{GTO}(x, y, z) = Nx^a y^b z^c e^{-\zeta r^2} \tag{2.24}$$

where N, a,b,c and ζ all have same attribute as for the STOs in Equation 2.23. The solutions of GTOs are no longer H-atom-like, even for 1s. STOs are more accurate but it takes longer to compute integrals using them. The solution to this problem is to use a linear combination of enough GTOs to mimic an STO.

Figure 2.2 represents the difference between the STO and GTO functions. The r^2 dependence of GTO function makes it inferior to the STOs in two respects. GTO has a zero slope at the nucleus whereas STO has a ”cusp” (discontinuity).

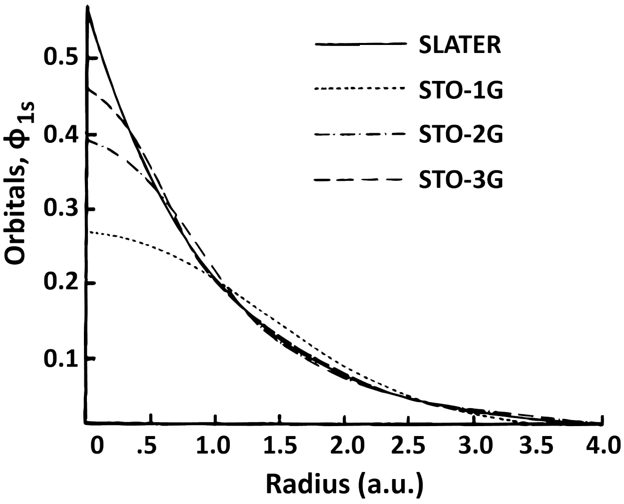

Figure 2.2. Comparison of the quality of the least-squares fit of a Slater function (ζ=1.0) modelled by a linear combination of GTOs (STO-nG; n=1-3).

As a result, GTOs have problems representing the proper behavior close to the nucleus. The second problem is that GTOs fall off sooner than STOs leading to a poor representation far from the nucleus. The most important advantage of the GTOs is that they are much easier to compute because of the Gaussian product theorem (products of Gaussian functions yield Gaussian functions). Therefore GTOs are almost universally used which is reviewed [34] beautifully. However, the above considerations indicate that many GTOs are required for reaching a given level of accuracy in modelling STOs.

When several GTOs are grouped, this is known as contracted Gaussian functions. These contracted functions are linear combination of the original or primitive Gaussian functions centered on the same atomic nucleus. Due to this contraction the computational cost can be reduced through the optimization of several coefficients at once. When it comes to the simplest basis set selection the minimal basis set must be used corresponding to the number of atomic orbitals in the system.

It is common to use more Gaussians for the valence electrons than for the core known as *split-valence* basis set in recognition of the fact that the valence electrons are responsible for making bonds (or reactivity). This also reduces the computational cost. Furthermore, the formation of the bonds in a molecule results in deforming (or polarizing) the atomic orbitals by the adjacent atoms. This deformation can be taken into account by including functions with larger angular momentum. For instance, addition of *p*-function and *d*-function are used to explain the deformation of *s*-orbital and *p*-orbital respectively. Diffuse functions are sometimes included to describe the large distance far from the nuclei. Addition of diffuse function is almost imperative for anions where the electron is loosely bound to the nuclei. The inclusion of polarization function with DZ basis set yields in a double-zeta plus polarization basis (DZP basis). For instance, in a DZP basis for ammonia (NH_3) has a set of additional three $2p$-functions for each hydrogen atom and a set of six $3d$-functions for nitrogen atom.

2.6.2 Pople and Dunning Basis Sets

In this thesis two different types of Gaussian basis sets are mostly used: Pople basis sets and the correlation consistent basis sets designed by Dunning and co-workers [35]. We take several examples in order to explain the Pople-type basis sets. For instance, a *3-21G* basis set is a split valence basis set where the core orbitals are described by one contracted Gaussian function consisting of three primitive Gaussians and the valence orbitals are splitted into two contracted Gaussians, one consists of two primitive Gaussians and the other one of only one primitive Gaussian.

Similarly, *6-311G* basis set has one contracted Gaussian function composed of six primitive Gaussians and the valence orbitals are split into three contracted Gaussians, consisting of three, one and one primitive Gaussians, respectively. Each of the above basis sets can have additional diffuse and/or polarization functions included with them. One of the most used basis set here has this form, *6-311++G(d,p)*. Here, the first + indicates one set of diffuse *s*- and *p*-functions on heavy atoms and the second + indicates a diffuse *s*-function to hydrogen atoms. Furthermore, the polarization functions are indicated after the G with separate notation for heavy atoms and hydrogen. Despite the added diffuse functions in the *6-311++G(d,p)* basis set, one *d*-function on heavy atoms, and one *p*-function on hydrogen are also added as additional polarization functions which is denoted by the (d,p) after G. This basis set with B3LYP functional has proven to work well for both molecular cations and anions especially for predicting ground state geometries and corresponding harmonic frequencies in the gas-phase [36, 37].

Dunning realized that the optimization of the basis set at the Hartree-Fock level might not be appropriate for correlated computations [35]. Therefore, the correlation consistent basis sets were constructed suitable for the post-Hartree-Fock methods in order to recover the correlation energy in a systematic fashion with the increasing size of the basis sets. Correlation consistent basis sets are designed such that the functions which contribute similar amount of correlation energy are grouped. For instance, $2d$- and $1f$-functions contribute almost the same correlation energy individually, therefore they belong to the same group. In this way, Dunning correlation-consistent polarized valence X-zeta basis sets are constructed that are denoted by cc-pVXZ where X=D, T, Q, 5, 6, 7. For instance, cc-pVDZ, cc-pVTZ and cc-pVQZ for C atom are composed of 3s2p1d, 4s3p2d1f and 5s4p3d2f1g contracted Gaussian functions respectively. These basis sets can also be augmented by adding one diffuse function having a small exponent for every angular momentum present in the basis. The augmented version of cc-pVDZ is denoted as aug-cc-pVDZ and it has s,p,d diffuse functions. Augmented basis sets are useful for explaining weakly bound systems. Furthermore, if core electrons are not kept frozen then core correlation can be modeled with cc-pCVXZ or aug-cc-pCVXZ basis sets where "C" denotes core correlation. Another useful feature of these basis sets is that they converge smoothly towards the complete (infinite) basis set limit. Similarly, polarization consistent basis sets are also constructed and reported to converge much faster than the correlation consistent basis sets [38].

2.7 Harmonic frequency calculations

The main goal of the DFT computations in this thesis is to predict the vibrational frequencies of the systems in the ground state. This requires the geometry optimization meaning finding the stationary points on the molecular potential energy surface and then locating the minimum. This type of method requires the calculation of the potential energy surface gradients either using analytical or numerical derivatives.

The vibrational frequency $\tilde{\nu}$ (in cm^{-1}) of a diatomic molecule can be calculated according to the harmonic approximation

$$\tilde{\nu} = \frac{1}{2\pi c}\sqrt{\frac{k}{\mu}} \tag{2.25}$$

where μ is the reduced mass, k is the linear force constant for the vibration and c is the velocity of light. By generalizing this relation the vibrational frequencies can be calculated for a polyatomic molecule. On the right hand side of this relation the force constant k is the only unknown parameter. Harmonic approximation assumes that the restoring force generated as the molecular bond is stretched follows Hooke's law. For a true Hooke's law spring, the second derivative of the molecular potential is equal to the force constant k for all values of the internal coordinates. Due to this approximation the molecular potential has an exact parabolic shape. When the potential energy surface (PES) is approximated by a parabola, the vibrational motion resembles a harmonic oscillator.

To calculate the force constants that belong to the vibrational modes in a polyatomic molecule, the second derivatives of the potential function are evaluated with respect to the internal coordinates. The matrix with the second derivatives or the force constant matrix is called the Hessian. The Hessian is important for geometry optimization, finding the stationary points as minima, transition states, and for computing IR spectra. This Hessian needs to be diagonalized in order to determine the normal mode frequencies of a molecule, i.e., the directions and frequencies of the atomic motions. Mass-weighting (the effect of the masses of the atoms) the force constants provides the vibrational frequencies from this relation (Equation 2.25).

Vibrational frequencies are useful to obtain IR spectra, to check stationary points on the PES, and to calculate zero point energies. Computed IR frequencies are typically higher than the fundamental transitions observed experimentally, that is then brought into reasonable agreement by multiplying them by an empirical scaling factor, commonly about 0.9 [39, 40]. The sources of this disagreement are the neglect of anharmonicity effects, inaccuracy of electron correlation and the use of finite basis sets in the theoretical treatment.

References

[1] Max Born and Robert Oppenheimer. Zur quantentheorie der molekeln. *Annalen der Physik*, 389(20):457–484, 1927.

[2] Walter Kohn and Lu Jeu Sham. Self-consistent equations including exchange and correlation effects. *Phys. Rev.*, 140(4A):A1133, 1965.

[3] John P Perdew and Karla Schmidt. Jacob's ladder of density functional approximations for the exchange-correlation energy. In *AIP Conference Proceedings*, volume 577, pages 1–20. AIP, 2001.

[4] Roberto Peverati and Donald G Truhlar. Quest for a universal density functional: the accuracy of density functionals across a broad spectrum of databases in chemistry and physics. *Philos. Trans. Royal Soc. A*, 372(2011):20120476, 2014.

[5] Aron J Cohen, Paula Mori-Sánchez, and Weitao Yang. Challenges for density functional theory. *Chem. Rev*, 112(1):289–320, 2011.

[6] Seymour H Vosko, Leslie Wilk, and Marwan Nusair. Accurate spin-dependent electron liquid correlation energies for local spin density calculations: a critical analysis. *Can. J. Phys.*, 58(8):1200–1211, 1980.

[7] Yue Wang and John P Perdew. Correlation hole of the spin-polarized electron gas, with exact small-wave-vector and high-density scaling. *Phys. Rev. B*, 44(24):13298, 1991.

[8] John C Slater. A simplification of the hartree-fock method. *Phys. Rev.*, 81(3):385, 1951.

[9] Robert O Jones and Olle Gunnarsson. The density functional formalism, its applications and prospects. *Rev. Mod. Phys.*, 61(3):689, 1989.

[10] Axel D Becke. Density-functional exchange-energy approximation with correct asymptotic behavior. *Phys. Rev. A*, 38(6):3098, 1988.

[11] Aron J Cohen, Paula Mori-Sánchez, and Weitao Yang. Insights into current limitations of density functional theory. *Science*, 321(5890):792–794, 2008.

[12] John P Perdew. Density-functional approximation for the correlation energy of the inhomogeneous electron gas. *Phys. Rev. B*, 33(12):8822, 1986.

[13] Keith A Brueckner et al. Correlation energy of an electron gas with a slowly varying high density. *Phys. Rev.*, 165(1):18, 1968.

[14] John P Perdew, Stefan Kurth, Aleš Zupan, and Peter Blaha. Accurate density functional with correct formal properties: A step beyond the generalized gradient approximation. *Phys. Rev. Lett.*, 82(12):2544, 1999.

[15] John P Perdew, Jianmin Tao, Viktor N Staroverov, and Gustavo E Scuseria. Meta-generalized gradient approximation: Explanation of a realistic nonempirical density functional. *J. Chem. Phys.*, 120(15):6898–6911, 2004.

[16] Maziar Nekovee, WMC Foulkes, and RJ Needs. Quantum monte carlo analysis of exchange and correlation in the strongly inhomogeneous electron gas. *Phys. Rev. Lett.*, 87(3):036401, 2001.

[17] J Harris and RO Jones. The surface energy of a bounded electron gas. *J. Phys. Condens. Matter*, 4(8):1170, 1974.

[18] David C Langreth and John P Perdew. The exchange-correlation energy of a metallic surface. *Solid State Commun.*, 17(11):1425–1429, 1975.

[19] O Gunnarsson and BI Lundqvist. Erratum: exchange and correlation in atoms, molecules, and solids by the spin-density-functional formalism. *Phys. Rev. B*, 15(12):6006, 1977.

[20] Axel D Becke. Density-functional thermochemistry. III. the role of exact exchange. *J. Chem. Phys.*, 98(7):5648–5652, 1993.

[21] Axel D Becke. A new mixing of hartree–fock and local density-functional theories. *J. Chem. Phys.*, 98(2):1372–1377, 1993.

[22] Chengteh Lee, Weitao Yang, and Robert G Parr. Development of the colle-salvetti correlation-energy formula into a functional of the electron density. *Phys. Rev. B*, 37(2):785, 1988.

[23] Markus Reiher, Oliver Salomon, and Bernd Artur Hess. Reparameterization of hybrid functionals based on energy differences of states of different multiplicity. *Theor. Chem. Acc.*, 107(1):48–55, 2001.

[24] Oliver Salomon, Markus Reiher, and Bernd Artur Hess. Assertion and validation of the performance of the b3lyp functional for the first transition metal row and the G2 test set. *J. Chem. Phys.*, 117(10):4729–4737, 2002.

[25] Georg Ganzenmüller, Nabil Berkaïne, Antony Fouqueau, Mark E Casida, and Markus Reiher. Comparison of density functionals for differences between the high-(T 2 g 5) and low-(A 1 g 1) spin states of iron (ii) compounds. iv. Results for the ferrous complexes [Fe (L)('NHS 4')]. *J. Chem. Phys.*, 122(23):234321, 2005.

[26] Kasper P Jensen. Bioinorganic chemistry modeled with the tpssh density functional. *Inorg. Chem.*, 47(22):10357–10365, 2008.

[27] Axel D Becke. Perspective: Fifty years of density-functional theory in chemical physics. *J. Chem. Phys.*, 140(18):18A301, 2014.

[28] Troy Van Voorhis and Gustavo E Scuseria. A novel form for the exchange-correlation energy functional. *J. Chem. Phys.*, 109(2):400–410, 1998.

[29] A Daniel Boese and Nicholas C Handy. New exchange-correlation density functionals: The role of the kinetic-energy density. *J. Chem. Phys.*, 116(22):9559–9569, 2002.

[30] Yan Zhao and Donald G Truhlar. The M06 suite of density functionals for

main group thermochemistry, thermochemical kinetics, noncovalent interactions, excited states, and transition elements: two new functionals and systematic testing of four M06-class functionals and 12 other functionals. *Theor. Chem. Acc.*, 120(1-3):215–241, 2008.

[31] Yan Zhao and Donald G Truhlar. Applications and validations of the minnesota density functionals. *Chem. Phys. Lett.*, 502(1-3):1–13, 2011.

[32] Gabor I Csonka, John P Perdew, and Adrienn Ruzsinszky. Global hybrid functionals: A look at the engine under the hood. *J. Chem. Theory Comput.*, 6(12):3688–3703, 2010.

[33] Robert O Jones. Density functional theory: Its origins, rise to prominence, and future. *Rev. Mod. Phys.*, 87(3):897, 2015.

[34] AF Jalbout, F Nazari, and L Turker. Gaussian-based computations in molecular science. *J. Mol. Struct.*, 671(1-3):1–21, 2004.

[35] Thom H Dunning Jr. Gaussian basis sets for use in correlated molecular calculations. i. the atoms boron through neon and hydrogen. *J. Chem. Phys.*, 90(2):1007–1023, 1989.

[36] Jonathan Martens, Josipa Grzetic, Giel Berden, and Jos Oomens. Structural identification of electron transfer dissociation products in mass spectrometry using infrared ion spectroscopy. *Nat. Commun.*, 7:11754, 2016.

[37] Jonathan K Martens, Josipa Grzetic, Giel Berden, and Jos Oomens. Gas-phase conformations of small polyprolines and their fragment ions by irmpd spectroscopy. *Int. J. Mass Spectrom.*, 377:179–187, 2015.

[38] Frank Jensen. Polarization consistent basis sets: Principles. *Chem. Phys.*, 115(20):9113–9125, 2001.

[39] Anthony P Scott and Leo Radom. Harmonic vibrational frequencies: an evaluation of Hartree-Fock, Møller- Plesset, quadratic configuration interaction, density functional theory, and semiempirical scale factors. *J. Phys. Chem.*, 100(41):16502–16513, 1996.

[40] Marie L Laury, Matthew J Carlson, and Angela K Wilson. Vibrational frequency scale factors for density functional theory and the polarization consistent basis sets. *J. Comput. Chem.*, 33(30):2380–2387, 2012.

Chapter 3

IR ion spectroscopic characterization of the [Cu(II/I)(cyclam)] and [(2,2′-bipyridine)Cu(II/I)] redox pairs

3.1 Abstract

We report fingerprint IR spectra of mass-isolated gaseous coordination complexes of 2,2′-bipyridine (bpy) and 1,4,8,11-tetra-azacyclotetradecane (cyclam) with a copper ion in its I and II oxidation states. Experiments are carried out in a quadrupole ion trap (QIT) mass spectrometer coupled to the FELIX infrared free-electron laser. Dications are prepared using electrospray ionization (ESI), while monocations are generated by charge reduction of the dication using electron transfer-reduction (ETR) in the QIT. Interestingly, $[Cu(bpy)_2]^+$ can also be generated directly using ESI, so that its geometry as produced from ETR and from ESI can be compared. The effects of charge reduction on the IR spectra are investigated by comparing the experimental spectra with IR spectra modelled by density functional theory (DFT). Reduction of Cu(II) to the closed-shell Cu(I) ion retains the square-planar geometry of the Cu-cyclam complex. In contrast, for the bis-bpy complex with Cu, charge reduction induces a conversion from a near square-planar to a tetrahedral geometry. The geometry for $[Cu(bpy)_2]^+$ is identical to that for

---

"Reproduced with permission from Musleh Uddin Munshi, Jonathan Martens, Giel Berden and Jos Oomens, *J. Phys. Chem. A* **2019**, 123, 19, 4149-4157. Copyright 2019 American Chemical Society."

the complex generated directly from ESI as a native structure, which indicates that the ETR product ion thermalizes. For $[Cu(cyclam)]^+$, however, the square-planar geometry of the 2+ complex is retained upon charge reduction, despite a (distorted) tetrahedral geometry being predicted to be lower in energy. These differences are attributed to different barriers to rearrangement.

3.2 Introduction

Wavelength tunable infrared lasers coupled with various ion storage mass spectrometers have become invaluable instruments in ion chemistry [1–8]. Ion spectroscopy has enabled the routine recording of IR spectra of mass-selected ions, from which accurate structural information can be derived. Quadrupole ion trap (QIT) mass spectrometers form versatile platforms for ion spectroscopy offering multistage ion chemistry manipulation and analyses, such as collision induced dissociation (CID). Our group has recently constructed an ion spectroscopy platform [9] that allows for the spectroscopic investigation of product ions from ion/ion reactions [10–13]. These include product ions of electron transfer dissociation (ETD) [14–16], but also of electron transfer reduction (ETR) [17], i.e., charge reduction without further dissociation, sometimes dubbed ETnoD. We recently demonstrated that the geometry of the Ni(cyclam) coordination complex remains the same and intact (*trans-III*, see Figure 3.1) upon gas-phase charge reduction of Ni^{2+}(cyclam) to Ni^{+}(cyclam). Both members of this redox pair were spectroscopically probed in complete isolation employing IR ion spectroscopy and structural characterization was aided by DFT calculations.

Here we further investigate this method to spectroscopically probe the two members of metal-ligand redox pairs. For the present study, we choose the Cu(II/I) ion as metal center. Depending on the nature of the ligand, copper has the interesting property that both members of the redox pair can be generated directly by electrospray ionization (ESI), in contrast to most other 1st row transition metals. This enables us to compare spectra of 1+ coordination complexes generated both by ESI directly and by gas-phase ETR from the 2+ complex. In the choice of ligands, we have opted for a cyclic (cyclam) as well as a non-cyclic (bpy) ligand; both ligands form tetradentate coordination complexes with Cu, bpy as a bis-complex and cyclam as a mono-complex. The complexation of cyclam with transition metal ions has been studied [18], but relatively little

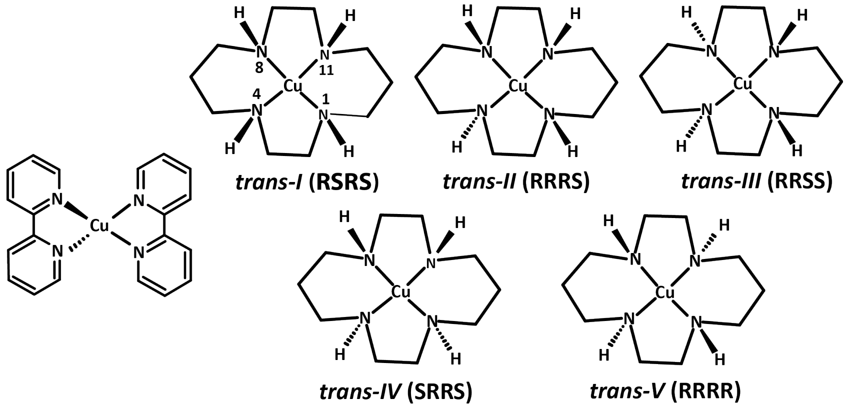

Figure 3.1. The Cu(bpy)$_2$ complex (left) and five diastereomers of the coordination complex of Cu and cyclam. The Cahn-Ingold-Perlog *R/S* chirality of each of the nitrogen centers is indicated in the order 1,4,8,11 (atom numbering indicated for *trans-I*)

information is available about the coordination in the gas phase. Note that although the isolated cyclam molecule is not chiral, coordination of the nitrogen atoms to a metal center induces stereoisomerism. Five distinct diastereomers referred to as *trans-I* through *trans-V* are possible relating to the relative orientation of the four N-H bonds, see Figure 3.1. In the next chapter, we have shown that complexes of Ni(II) and Ni(I) with cyclam form only the *trans-III* diastereomer, which is consistent with the solution stereochemistry for Ni(II)-cyclam, although *trans-I* and *trans-III* were reported to coexist in solution [18].

Macrocyclic saturated tetra-amines generally have high affinity to form stable metal-ligand coordination complexes in solution [19, 20]. In particular, cyclam is known to form square-planar tetradentate complexes with Co(II), Ni(II) and Cu(II). Changes in the length of the alkyl chains connecting the N-atoms affect the structure and the spin state of the complexes in solution [21, 22] and in the solid state [22], which is ascribed to steric hindrance effects as confirmed by UV-Vis absorption spectroscopy in solution [23]. Methyl derivatives of cyclam (e.g., 5,7,7,12,14,14-hexamethyl-1,4,8,11-tetra-azacyclotetradecane) have also been reported to form stable complexes with Cu(II) [19] and coordination of N-tetra-alkylated cyclam ligands with 3d transition metals have been reported to form *trans-I* complexes in solution [24]. From a broader perspective, a significant fraction of enzymes possesses a metal ion as a cofactor at their active site, and their catalytic action often involves shuttling between oxidation states of the metal ion [25, 26]. Copper containing proteins are abundant, including for instance Cytochrome oxidase, Laccase oxidases, superoxidedismutases, di-oxygenases, nitrite reductase, and N_2O reductase. Model metal-peptide complexes have been studied extensively [27, 28] in the gas-phase, including studies employing ion spectroscopy [29–31]. For example, both Ni(II) and Cu(II) have been shown to form low-spin square-planar geometries with tetraglycine having structures that are very similar to each other [30].

In both oxidation states, Cu ions have similar ionic radii: 0.74 Å for Cu(I) versus 0.71 Å for Cu(II) in a four-coordination environment, where they form tetrahedral and square-planar coordination geometries, respectively [19, 32]. Intrinsically, the main distinction between Cu(II) and Cu(I) is the d^9 electronic configuration of the former versus the closed-shell d^{10} configuration of the latter. Jahn-Teller distortion in Cu(II) complexes induces axial elongation of octahedral geometries forming square-pyramidal or square-planar geometries whereas Cu(I) shows structural flexibility taking advantage of the low charge [33, 34].

3.3 Experimental

Experiments have been carried out in a modified QIT MS (Bruker AmaZon Speed ETD, Bremen, Germany) that has been described in detail elsewhere [9, 35]. The modifications mainly involve optical access to the trapped ion cloud enabling us to record IR multiple-photon dissociation (IRMPD) spectra of mass isolated ions.

Coordination complexes of Cu^{2+} with the tetradentate cyclam ligand as well as the bis-complex with bpy ($[Cu(cyclam)]^{2+}$ and $Cu^{2+}(bpy)_2$) were generated via electrospray ionization (ESI), using equimolar solutions (1 µM) of $CuSO_4$ and cyclam or bpy in 1:1 MeOH:H_2O. The singly charged $[Cu(cyclam)]^+$ and $Cu^+(bpy)_2$ were generated by charge reduction using the electron transfer dissociation (ETD) option of the QIT MS. The fluoranthene radical anion acts as a reducing agent in an ion-ion reaction with the mass-isolated dicationic complexes inside the ion trap. The fluoranthene radical anions are produced in a negative chemical ionization source [35, 36] and transferred to the trap, where they undergo the electron transfer reaction. A reaction time of approximately 200-250 ms is found to yield the maximum number of charge-reduced ions for these complexes, while minimizing the number of ETD induced fragment ions. Singly charged $Cu(bpy)_2$ complexes were also produced directly from the ESI source (even when using a Cu(II) salt, which is not uncommon [37]), but this was not possible for cyclam. We qualitatively attribute this difference to hard/soft acid/base (HSAB) effects [38], where the Cu^+ ion, a soft Lewis acid, coordinates more favorably with the soft Lewis basic pyridine N-atoms of bpy than with the hard Lewis-basic alkyl-amine N-atoms of cyclam.

We also investigate IRMPD spectra of $[Cu(cyclam)]^{2+}$ ions recorded in a Fourier Transform Ion Cyclotron Resonance (FTICR) MS, which has been described in detail elsewhere [2, 39]. For this instrument, solutions of approximately 1 mM cyclam with Cu^{2+} in a 1:1 $MeOH:H_2O$ were used. An advantage of the FTICR MS is that no helium buffer gas is used inside the ICR cell, which avoids collisional cooling of the complexes during IR activation by the FEL, leading to more efficient IRMPD (especially important for strongly bound complexes) and thus revealing additional weaker features in the IR spectra that escape observation in the QIT MS [9]. The FTICR MS instrument does not have the possibility to charge-reduce the dications, so that IR spectra of $[Cu(cyclam)]^+$ cannot be recorded on this setup.

In order to record the IRMPD spectra in the range from 500 to 1700 cm^{-1} in the QIT MS, mass-selected (*m/z*) ions are irradiated with 4 to 20 macropulses from the free electron laser FELIX [9]. About 6 μs long macropulses have energies up to 100 mJ and are produced at a 10 Hz repetition rate. When the IR frequency of the laser matches one of the vibrational absorption frequencies of the trapped ions, multiple photons are absorbed, increasing the internal energy of the ions and leading to unimolecular dissociation commonly via the minimum energy channel. A series of mass spectra is saved while varying the IR wavelength, so that an IR spectrum can be reconstructed by plotting the fragmentation yield (yield=$\sum$(fragment ions)/$\sum$(precursor + fragment ions)) at each laser wavelength [1, 40]. Mass spectra are taken at every 3 cm^{-1} step of the laser frequency with 3 to 6 averages. The fragmentation yield is corrected linearly for the frequency dependent laser pulse energy and the frequencies are calibrated using a grating spectrometer.

The IRMPD experiment in the FTICR MS proceeds in an analogous fashion, however, the ions are additionally irradiated for 20 ms by the output of a continuous-wave CO_2-laser (10.6 μm, 30 W) directly after each FEL pulse to enhance the extent of dissociation [41].

3.4 Theoretical modeling

Quantum-chemical calculations are performed using density functional theory (DFT) to assist in structural and vibrational normal mode assignments using the Gaussian 09 revision D01 code [42]. B3LYP [43–45] and UB3LYP levels of theory are employed for closed-shell (Cu^+) and open-shell (Cu^{2+}) systems, respectively. The 6-31++G(d,p) basis set was used on all atoms including the Cu atom. No symmetry constraints are imposed. Cu^{2+} complexes have doublet multiplicity and spin contamination was negligible for these systems. Single-point MP2/6-311+G(d,p) calculations were performed on the optimized B3LYP geometries to refine relative energies.

Harmonic IR frequencies are computed for the optimized geometries and the frequencies are scaled by a factor of 0.975, which was reported to give the best match for various IRMPD spectra [14, 46], including those of Ni-cyclam ions [17], to compensate for anharmonicity and basis set incompleteness. Computed IR frequencies are convoluted with a 15 cm^{-1} full-width at half-maximum (FWHM) Gaussian line shape function for direct comparison with experimental spectra.

3.5 Results and discussion

3.5.1 Mass spectra of the $[Cu(bpy)_2]^{2+/+}$ redox pair

Figure 3.2a shows the ESI mass spectrum of doubly charged $[Cu(bpy)2]^{2+}$ ion. The isotope pattern with the main peak at *m/z* 187.5 in the inset (b) is in agreement with the charge and stoichiometry of this complex. The ion at *m/z* 265.5 is attributed to the $[Cu(bpy)_3]^{2+}$ complex. In addition, the singly charged $[Cu(bpy)_2]^+$ ion is also observed in the MS, confirmed by its characteristic isotope pattern at *m/z* 375 (values are given for the monoisotopic peak, see panel c). In panel d, the $[^{63}Cu(bpy)_2]^{2+}$ ion is mass-isolated and used for (i) IRMPD spectroscopic measurements and (ii) charge reduction by ETR.

The IRMPD spectrum of the isolated $[Cu(bpy)2]^{2+}$ (Figure 3.2a) is recorded monitoring the IR-induced photo-fragments at *m/z* 157, corresponding to protonated bpy. The complementary ion appears at *m/z* 236 as a water adduct, $[Cu(bpy - H)(H_2O)]^+$, due to the relatively high background pressure in the

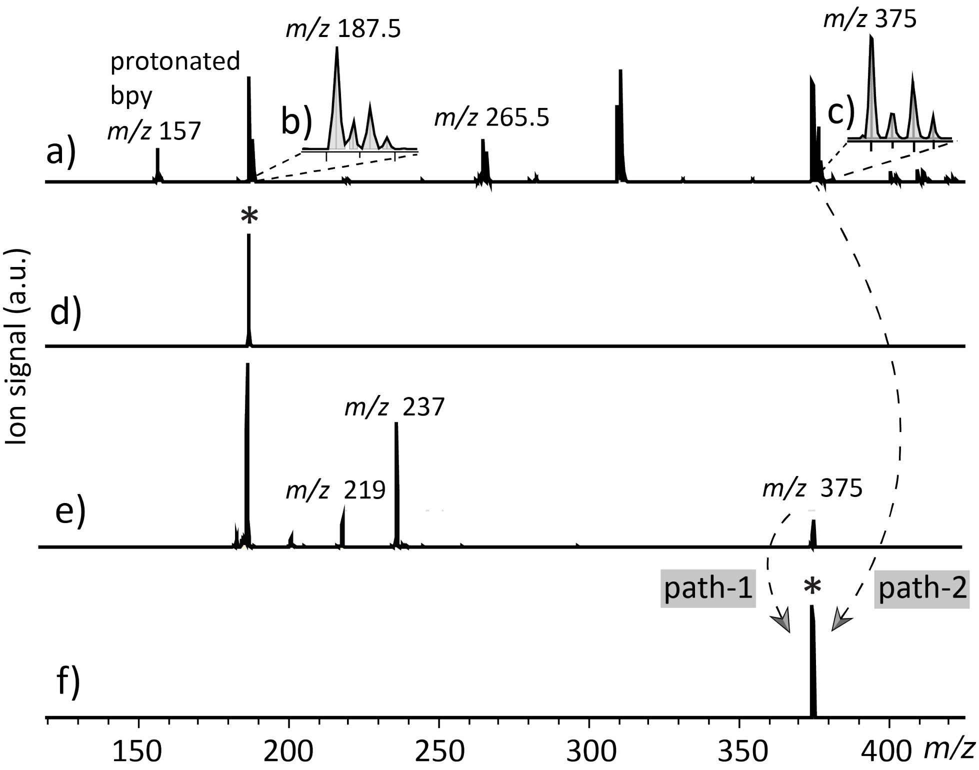

Figure 3.2. (a) The ESI mass spectrum generated from a solution containing bpy and copper(II) sulfate, (b) the isotope distribution of the $[Cu(bpy)_2]^{2+}$ ion with the ^{63}Cu monoisotopic peak at *m/z* 187.5 and (c) $[^{63}Cu(bpy)_2]$+ with its monoisotopic peak at *m/z* 375 . (d) Isotope-selective mass isolation of the $[^{63}Cu(bpy)_2]^{2+}$ ion. (e) ETR reaction of isolated monoisotopic $[Cu(bpy)_2]^{2+}$, which generates a mass peak corresponding to the formation of $[Cu(bpy)_2]^+$ ion at *m/z* 375. ETR induced fragments are also observed: $[Cu(bpy)]^+$ at *m/z* 219 and the water adduct of this ion at *m/z* 237. (f) Isolation of the charge-reduced $[Cu(bpy)_2]^+$ ion (*m/z* 375) from the ETR mass spectrum (path-1) and from direct ESI MS (path-2). Members of the redox pair are indicated with a black star (d, f).

QIT. In addition, the $[Cu(bpy)]^+$ ion is also produced at *m/z* 219 by loss of a neutral bpy unit. These $[Cu(bpy)]^+$ ions also form water adducts (*m/z* 237).

In a separate experiment, charge-reduced $[Cu(bpy)_2]^+$ ions are generated by charge reduction of the mass-isolated dication at *m/z* 187.5 using ETR (Figure 3.2e). In addition to the ETR product ion at m/z 375, ETR-induced fragments are also observed (*m/z* 219 and 237) due to the energy released in the charge recombination (electron transfer dissociation, ETD) [17, 35, 47]. The intact charge-reduced ions are mass isolated (Figure 3.2f, path 1) to record their IRMPD spectrum, shown in Figure 3.2b. The same charge-reduced ions are also isolated directly from the ESI MS (Figure 3.2f, path 2) and their IRMPD spectrum was recorded separately (Figure 3.2c). During the IRMPD scan of the

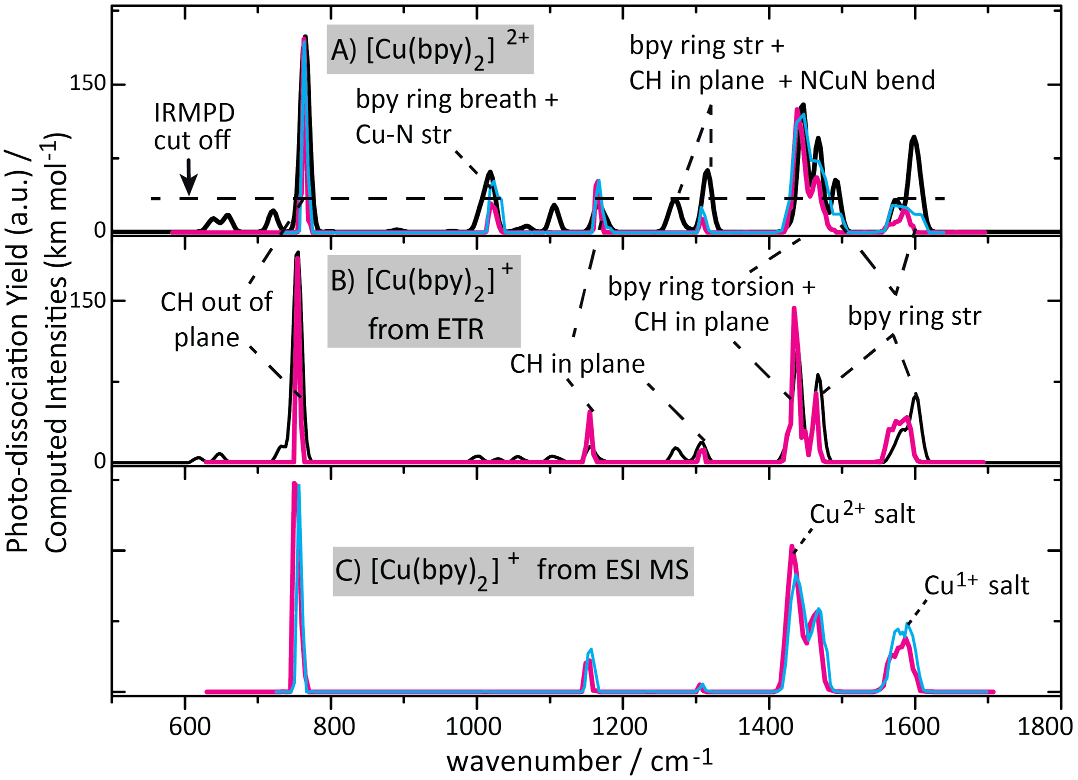

Figure 3.3. IRMPD spectra (magenta trace) of (A) $[Cu(bpy)_2]^{2+}$ and (B) $[Cu(bpy)_2]^+$ generated using ETR and (C) $[Cu(bpy)_2]^+$ generated directly from ESI. The cyan traces represent spectra obtained with a Cu(I) salt in the ESI solution, the magenta traces are obtained with a Cu(II) salt. IRMPD spectra of $[Cu(bpy)_2]^+$ from all three sources appear to be identical (B, C). Both ions were irradiated with 4 macro pulses of the FEL. IRMPD spectra are overlaid with the theoretical IR spectra (black traces) for comparison. Horizontal dotted line indicates an apparent IRMPD cut-off [9, 17, 48, 49].

$[Cu(bpy)_2]^+$ ions formed either via path 1 or 2, IR-induced photo-fragments are formed at *m/z* 219 and 237, consistent with the collision-induced dissociation and ETD product ions (Figure 3.2e).

3.5.2 IR spectra and structural assignments

The experimental IRMPD spectra of $[Cu(bpy)_2]^+$ obtained from ETR and from ESI directly as well as that of $[Cu(bpy)_2]^{2+}$ are shown in Figure 3.3. Experimental spectra are compared with theoretical linear IR spectra (black traces) of the two members of the redox pair. Panel a shows IRMPD spectra of the doubly-charged $[Cu(bpy)_2]^{2+}$ ion using ESI solutions containing either a Cu(II) or a Cu (I) salt ($CuSO_4$ or Cu[acetate]); the two spectra are nearly identical. Panel b shows the IRMPD spectrum of the charge-reduced ion, where the ions are generated from the dication using ETR (path 1 in Figure 3.2). In panel c, the IRMPD spectrum of the same singly-charged ion is shown, but now isolated directly from the ESI MS (path 2 in Figure 3.2); both Cu(II) and Cu(I) salts were used again, but only insignificant differences in the resulting spectra were observed. Moreover, the IRMPD spectra of the charge reduced ions in panels b and c are nearly identical, which indicates that the coordination geometries are the same whether the ion is generated through gas-phase charge reduction from the dication or directly extracted as a 1+ ion from the ion source.

The IR spectra for the singly and doubly charged ions are relatively similar except for an additional IR band at 1020 cm^{-1} for the dication. Also, slight shifts in the IR band positions are observed, which suggests small differences in the structures of the mono- and di-cations. Theoretical spectra reasonably reproduce all observed IRMPD bands for both members of the redox pair in terms of their band position; relative intensities are also in reasonable agreement. The optimized geometries confirm the tetradentate coordination to the metal center and are best characterized as distorted square-planar for the dication and tetrahedral for the monocation (*vide infra*).

The dominant IRMPD band for the dication is observed at 764 cm^{-1}, as correctly predicted by the computation at 766 cm^{-1}, and has primarily C-H out of plane bending character. The band observed at 1020 cm^{-1}, which is diagnostic for the dication, is correctly predicted at 1019 cm^{-1} and is attributed to bpy ring breathing coupled with Cu-N stretching. The band observed and predicted at 1167 cm^{-1} is due to C-H in-plane bending. The low-intensity IRMPD band at 1307 cm^{-1} is slightly blue-shifted in the calculation at 1319 cm^{-1} and has combined bpy ring stretching, C-H in-plane bending, and N-Cu-N bending character. The IR bands observed between 1400 and 1500 cm^{-1} are also well predicted and are due to C-C, C-N stretch of the bpy ring with C-H in-plane bending. The highest-frequency bands observed close to 1600 cm^{-1} are predominantly due to ring CC and NC stretching, typical for nitrogen heterocyclic species.

Generally, the observed intensities are in good overall agreement with the prediction, although theory predicts additional low-intensity bands that are not observed in the experiment for the dication. Even at higher FEL pulse energies, no additional bands were observed in the 1000 – 1400 cm^{-1} range (see Appendix B Figure B.1). The relatively high buffer gas pressure of about 10^{-3} mbar in the QIT MS results in collisional deactivation during the IR multiple-photon excitation process, reducing the IRMPD efficiency for IR transitions with small

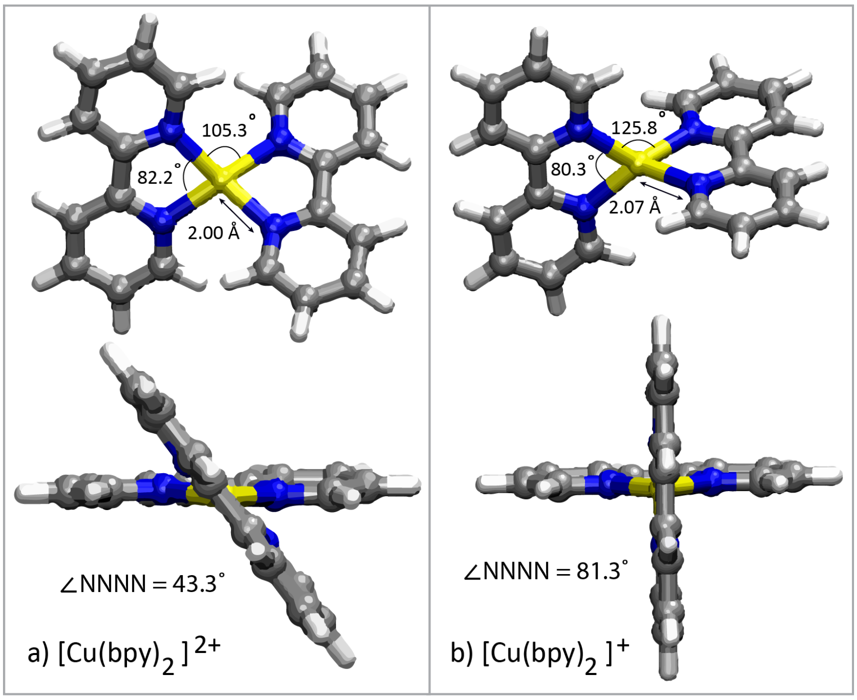

Figure 3.4. Computed structures of (a) $[Cu(bpy)_2]^{2+}$ as distorted square-planar coordination and (b) $[Cu(bpy)_2]^{+}$ as tetrahedral coordination.

absorption cross section [9, 48]. The effect is particularly noticeable for the dication, because of its higher dissociation threshold as compared to the monocation. Experimental bond dissociation energies for the loss of a bpy unit from singly-charged $M(bpy)^{2+}$ were reported by Rodgers and co-workers [50–52] as 2.81 eV for Ni, 2.46 eV for Cu, and 2.33 eV for Zn. Our theoretical value of 2.43 eV for $[Cu(bpy)_2]^{+}$ is in good agreement, which gives confidence in the computed value for the dication of 5.27 eV.

In Figure 3.3b, the observed IRMPD spectrum for the monocation is seen to agree well with the theoretical spectrum, with the only exception being the deviation in the intensity of the band at 1155 cm^{-1}. The band assignments in the range from 1400 to 1700 cm^{-1} are analogous to those for the dication discussed above; bands in this region are mostly due to bpy ring vibrations and CH in-plane bending. Similar also to the dication, the dominant IRMPD band at 754 cm^{-1} is due to C-H out-of-plane bending. A red-shift of about 10 cm^{-1} is observed with respect to the dication. A similar 10 cm^{-1} red-shift is observed for the IRMPD band at 1157 cm^{-1}, predicted also at 1157 cm^{-1}, due to C-H in-plane bending. The band at 1307 cm^{-1} (C-H in-plane-bending) remains unshifted as compared to the dication.

Figure 3.4 shows the optimized geometries of the two members of the Cu-bpy redox pair. The excellent agreement between the observed IR spectra and the computed ones allows a clear assignment of these structures. The geometry of the dication changes from distorted square-planar to tetrahedral upon charge reduction. Distortion from a pure square-planar configuration in the dication is likely due to steric repulsion between the two ligands. The tetrahedral configuration is indeed expected for the closed-shell Cu(I) ion. These observations indicate that thermalization of the monocation occurs after ETR inside the trap. Despite the available energy from the ETR reaction [17, 35, 47], the monocation adopts its minimum energy structure and retains its tetradentate coordination, likely due to helium buffer gas cooling over the 200 - 250 ms duration of the ETR-reaction.

The geometry-change upon charge reduction involves the change of the angle between the bpy ligands, in association with an increase of the average coordination bond-lengths from 2.00 to 2.07 Å and intra-ligand angles (105.3° to 125.8°), while the ligand-bite angle (of the bpy moiety) is slightly decreased from 82° to 80° upon charge reduction (see Figure 3.4).

3.5.3 Mass spectra of the [Cu(II/I)(cyclam)] redox pair

Figure 3.5 shows the mass spectrum obtained by ESI of a solution containing a Cu(II) salt and the macrocycle cyclam (1,4,8,11-tetra-azacyclotetradecane). The $[^{63}\mathrm{Cu(cyclam)}]^{2+}$ isotopomer is observed at *m/z* 131.5 (see panel a and the zoom in panel b). This ion is mass-isolated in panel c for (i) charge reduction and (ii) recording of its IRMPD spectrum as a 2+ species. The charge reduction of this ion by ETR forms the $[^{63}\mathrm{Cu(cyclam)}]^{+}$ ion at *m/z* 263 as indicated by the asterisk in panel d. In addition to charge reduction, ETR of $[\mathrm{Cu(cyclam)}]^{2+}$ ions also leads to ligand deprotonation forming net singly charged ions as well, a process that is known from common application of ETD in protein sequencing [11, 12, 47, 53]. In fact, in the present experiment, the MS/MS product ion resulting from ligand deprotonation (*m/z* 262) is the dominant ion in the MS (d, e). Note that the capability of the QIT MS to isolate a single Cu isotope of the 2+ precursor ion complex enables us to distinguish the one-electron reduction product from the deprotonation product [17] (e). Note also that in this case, we cannot generate the 1+ ion from the ESI directly, as was the case for the bis-bpy complex. Also using a Cu(I) salt did not yield any appreciable amount of the

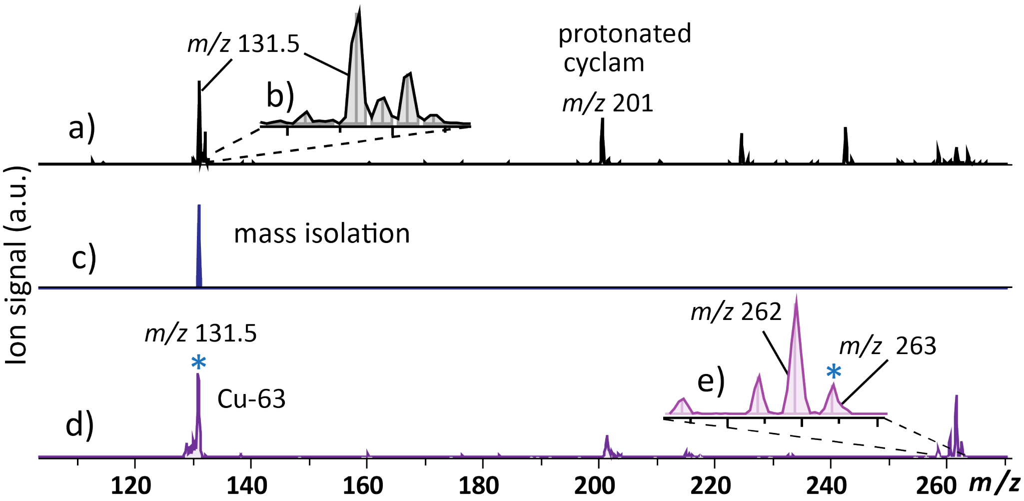

Figure 3.5. QIT ESI MS of a copper/cyclam solution (a) showing the $[^{63}\mathrm{Cu(cyclam)}]^{2+}$ (*m/z* 131.5), with the isotope distribution of $[\mathrm{Cu(cyclam)}]^{2+}$ zoomed-in on in panel b. Isotope-selective mass isolation of the $[^{63}\mathrm{Cu(cyclam)}]^{2+}$ ion is shown in panel c. ETR of isolated monoisotopic $[\mathrm{Cu(cyclam)}]^{2+}$ in panel d shows the formation of the intact charge-reduced $[^{63}\mathrm{Cu(cyclam)}]^{+}$ (*m/z* 263), with ETR induced fragments at *m/z* 262, 261, 258 attributed to the H, 2H, and 4H atom loss products, respectively (zoom in panel e). Members of the redox pair are indicated with blue stars.

1+ coordination complex, so that the gas-phase ETR process is the only way to access the reduced form of the Cu(cyclam) complex.

3.5.4 IR spectra and structural assignments

The complexes of Cu and cyclam can adopt different diastereomeric forms as shown in Figure 3.1. Relative computed energies for these structures are listed in Table 3.1. Single-point MP2/6-311+G(d,p) energies calculated at the B3LYP optimized geometries agree well with the energy ordering predicted by B3LYP/6-31++G(d,p) for the doubly charged complex. For the singly charged complex, the *trans-I* and *trans-III* structures are somewhat higher in energy relative to the *trans-V* minimum at the MP2 level as compared to the B3LYP level, and their relative ordering is reversed, although this is only a marginal difference. In the following discussion, we shall use the B3LYP energies.

In Figure 3.6, infrared spectra for the $[\mathrm{Cu(cyclam)}]^{2+}$ ion and the charge reduced $[\mathrm{Cu(cyclam)}]^{+}$ ion are shown for comparison in the range of 500 to 1750 cm^{-1}. Both spectra share common features, although sensitive shifts of the vibrational bands are observed, indicating that IR spectra are diagnostic for both species. Comparison with calculated spectra allows us to assign the vibrational

Table 3.1. Computed relative energies for the different diastereomeric complexes of $[Cu(cyclam)]^{2+/+}$ in kJ mol^{-1} at the B3LYP/6-31++G(d,p) and single-point MP2/6-311+G(d,p) levels.

	B3LYP/6-31++G(d,p)		sp-MP2/6-311+G(d,p)	
Isomers	Cu^{2+}	Cu^{+}	Cu^{2+}	Cu^{+}
trans-I	10.8	3.1	6.2	14.4
trans-II	39.6	26.3	31.0	29.5
trans-III	0	1.5	0	16.9
trans-IV	68.2	50.6	67.0	55.2
trans-V	33.7	0	30.2	0

normal modes and to derive which out of five possible isomers (see Figure 3.1) are present in the experiments for each member of the redox pair (*vide infra*).

$[Cu(cyclam)]^{2+}$

For the $[Cu(cyclam)]^{2+}$ ion, *trans-III* is the minimum energy isomer (Figure 3.6) and the calculated harmonic IR spectrum indeed reproduces the experimental IR bands accurately. The next higher-energy isomer (+10.8 kJ mol^{-1}) is the *trans-I* isomer, whose theoretical IR spectrum matches well with nearly all experimental bands, although the overall width of the intense unresolved feature near 1000 cm^{-1} is slightly better reproduced by the global minimum energy structure. The remaining diastereomers *trans-II*, *trans-IV* and *trans-V* are at least 30 kJ mol^{-1} higher in energy. Moreover, their computed spectra deviate more significantly from the experimental spectrum, particularly in the ranges 750 – 950 cm^{-1} and 1150 – 1350 cm^{-1}, where several weaker bands (though probably not below the observation threshold) are predicted but not observed experimentally.

We assign the vibrational normal modes for the dication $[Cu(cyclam)]^{2+}$ on the basis of the computed spectrum for the global minimum *trans-III* isomer. The high frequency bands between 1400 and 1500 cm^{-1} are attributed to the CH_2 and NH bending vibrations. The most intense feature centered at 1019 cm^{-1} is relatively broad and accomodates multiple unresolved transitions, in particular, the CN and CC stretching modes as well as NH rocking modes. The low-intensity IRMPD bands at 1300 cm^{-1} and 878 cm^{-1}, which remain unobserved in the QIT MS (see Figure 3.6) presumably due to collisional deactivation [9, 17, 48], correspond to predicted bands at 1320 and 868 cm^{-1}, respectively, which are due to CH_2 twist and CH_2 rocking vibrations.

$[Cu(cyclam)]^{+}$

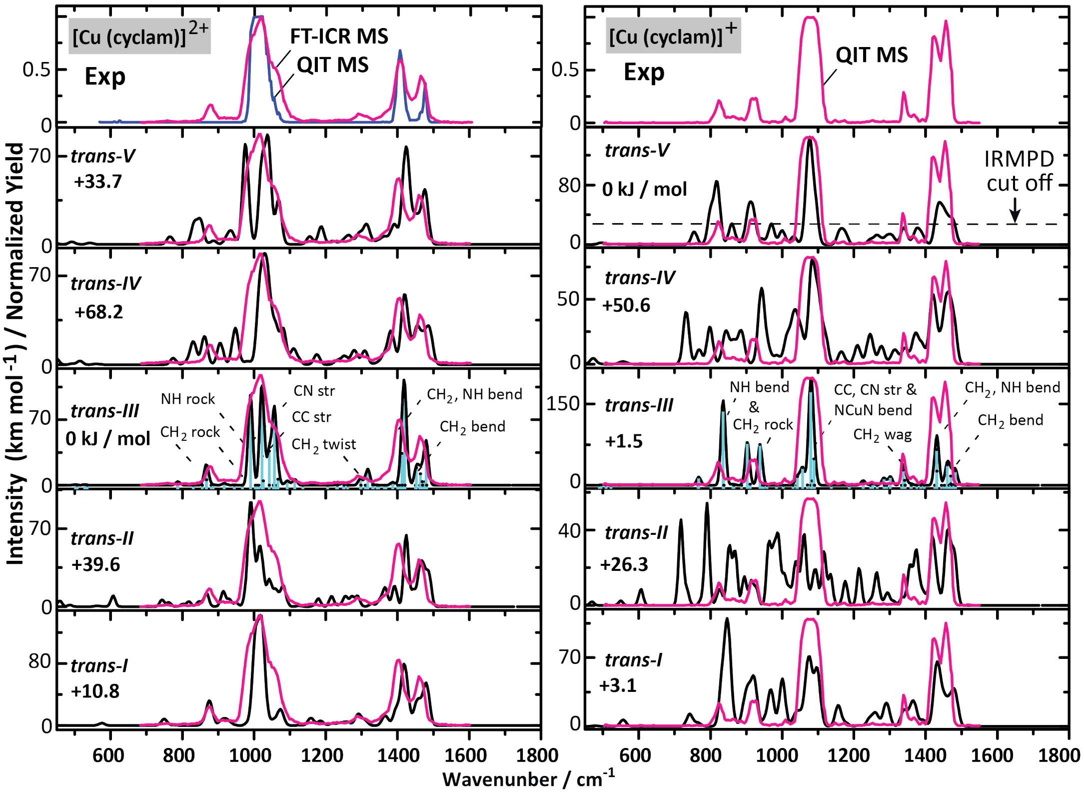

Figure 3.6. IRMPD spectrum of $[Cu(cyclam)]^{2+}$ recorded in QIT (blue trace in the top left panel), and in the FTICR (magenta trace; left panels) and of the charge reduced $[Cu(cyclam)]^{+}$ ion recorded in the QIT (magenta trace in the right panels). IRMPD spectra are overlaid with the theoretical IR spectra computed for the five diastereomers shown in Figure 3.1. Relative Gibbs free energies in kJ mol^{-1} are given inset. *trans-III* is the minumum energy structure for the dication, while *trans-V* is the lowest for the monocation, although *trans-III* is nearly isoenergetic for the 1+ species. All optimized structures are shown in Appendix B Figure B.2.

The IRMPD spectrum of the $[Cu(cyclam)]^{+}$ ion is dominated by three intense bands near 1070, 1422 and 1457 cm^{-1} as well as some lower-intensity bands at 822, 928 and 1340 cm^{-1} (see panels on the right in Figure 3.6). The *trans-V* isomer is the lowest-energy isomer for the complex in this charge state and its theoretical IR spectrum reproduces all features in the experimental spectrum, except for predicted bands at 1167 cm^{-1} and 970 cm^{-1} which are not observed; admittedly, these bands are relatively weak and could be below an IRMPD cut-off. The next higher-energy isomer, *trans-III*, lies at only +1.5 kJ mol^{-1}. Its predicted IR spectrum matches well with the experimental one, even if no or only a very low cut-off is assumed, in agreement with the low dissociation threshold of this species. A small deviation is observed in the splitting of the weak bands just above 900 cm^{-1}, which is slightly larger in the computation than in the experiment. One may therefore argue that the silent range between 1100 and 1400 cm^{-1} is predicted better by *trans-III* than by *trans-V*. Based on the calculated spectrum for *trans-III*, we attribute the bands at 822 and 928 cm^{-1} to CH_2 rocking modes. The highest frequency band at 1422 and 1457 cm^{-1} is due to coupled CH_2 bending and NH bending. The low-intensity band at 1340 cm^{-1} is due to CH_2 wagging.

The next higher-energy isomer is *trans-I* at +3.1 kJ mol^{-1}, which features two IR bands between 1200 and 1300 cm^{-1} in its predicted spectrum that are absent in the experiment. Also the remaining isomers, which are substantially higher in energy (> 25 kJ mol^{-1}), have predicted IR spectra that clearly deviate from the experiment. These diastereomers can safely be excluded to occur in the ion population.

In conclusion, for the dication complex, we assign the *trans-III* isomer. The experiments suggest that charge reduction of this species in the trap retains the stereoisomerism, so that the 1+ complex is also in the *trans-III* form, although a contribution from the *trans-V* form cannot be entirely excluded. Isomerization to *trans-V* would involve the breaking of two Cu–N coordination bonds to allow for inversion of the respective amine groups, followed by restoration of the coordination bonds. We suspect that the energy cost of breaking the coordination bonds is too high, so that this isomerization does not occur. We speculate that although the charge recombination process may release a significant amount of energy virtually instantaneously, subsequent cooling by the buffer gas inside the trap outcompetes possible isomerization.

3.5.5 Structural trend upon charge reduction

Figure 3.7 summarizes the relevant structural parameters of the two members of the Cu[cyclam] redox-pair. Based on the good agreement between theoretical and experimental IR spectra, the isomeric form of the ligands can be confidently determined down to one or two diastereomers. From this assignment, we infer that isomerization is unlikely upon charge reduction of the gaseous $[Cu(cyclam)]^{2+}$ inside the QIT MS.

In the dicationic complexes, copper has a $3d^9$ electron configuration, while after charge reduction the 3d-shell is filled ($3d^{10}$). One expects that the nature of the binding changes from orbital interaction driven to merely electrostatic binding

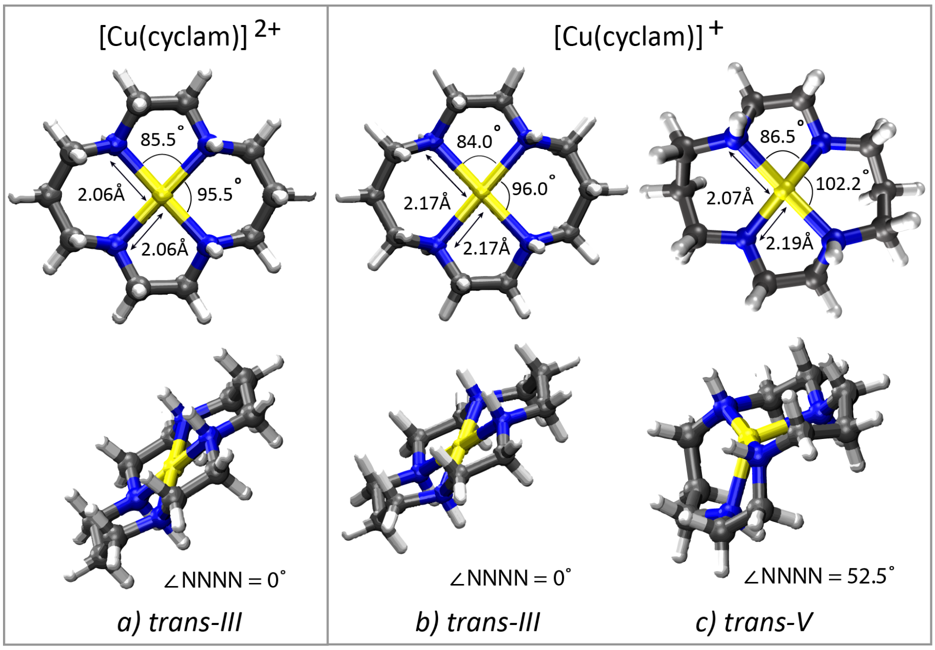

a) trans-III *b) trans-III* *c) trans-V*

Figure 3.7. DFT computed minimum energy structures of (a) the *trans-III* isomer of $[Cu(cyclam)]^{2+}$, (b) the *trans-III* and c) *trans-V* isomers of $[Cu(cyclam)]^{+}$. The four nitrogen atoms of the cyclam ligand scaffold remain square planar of the *trans-III* isomer for both the dication and monocation, whereas a distorted tetrahedral coordination is possible for the *trans-V* isomer.

Table 3.2. Mean bond distances (in Å) from the DFT-optimized minimum-energy conformers of the reduced and oxidized ions of [Ni/Cu(cyclam)]. Parenthesized values are the standard deviations

trans-III		*trans-III*		*trans-V*
Ni^{2+}-N	Ni^{+}-N	Cu^{2+}-N	Cu^{+}-N	Cu^{+}-N
1.98 (0)	2.10 (0)	2.06 (0.01)	2.17 (0)	2.07 (0) and 2.19 (0)

with ligand field effects being minimized [33]. Indeed, for the $Cu(bpy)_2$ complexes, this is reflected in the conversion of the nearly square-planar coordination of the Cu^{2+} center to a tetrahedral coordination around the closed-shell Cu^{1+} metal center. However, for the Cu(cyclam) complex, charge-reduction leads merely to a slight increase of the Cu–N bond lengths, but conversion to a tetrahedral geometry is not observed in the computed structure for the *trans-III* isomer (see Figure 3.7). We attribute this to strain in the macrocycle scaffold imposed by the relative orientations of the NH groups. In the *trans-III* isomer, two pairs of adjacent NH groups have the same orientation with respect to the plane of the complex; in the *trans-V* isomer, two opposite NH groups have the same orientation and this allows for a coordination geometry closer to tetrahedral (see Figure 3.7). Point to note, *trans-V* has a distorted tetrahedral conformer where the space diagonal nitrogen pair has unequal distances (diagonal NN): 3.82 Å versus 4.08 Å and angles (diagonal ∠NCuN): 121.4° versus 162.2° respectively while having the copper ion in the middle (see Figure 3.7) of both diagonal distances. Indeed, the *trans-V* isomer is computed to be lowest in energy. The spectroscopic data presented in Figure 3.6 suggest, however, that conversion to the *trans-V* isomer, and hence to tetrahedral coordination, is not achieved for Cu(cyclam), likely because of the high energetic barriers involved in the breaking of the Cu–N coordination bonds.

An interesting observation is that Ni^+(cyclam) and Cu^{2+}(cyclam) are isoelectronic, both metal ions possessing a $3d^9$ electronic configuration. Since the ionic radius decreases from left to right in the periodic table, we indeed observe that the metal-ligand bond distance (M^{n+}—N) decreases by 0.04 Å for Cu^{2+}(cyclam) relative to Ni^+(cyclam), see Table 3.2 [17]. On the other hand, upon charge reduction, the metal-ligand bond distance increases significantly for both metal ions. UV absorption spectroscopy and electrochemical study in solution suggested that the Cu(II) ion is bigger than Ni(II) [23, 25]. The same is true for the gas-phase where the metal-ligand distance increases for Cu^{2+}(cyclam) relative to Ni^{2+}(cyclam).

3.6 Conclusion

Two copper ligand complexes were spectroscopically investigated in both their 1+ and 2+ charge states to gain further insight in gaseous electron transfer reduction of transition-metal ligand complexes and characterization of both members of the redox pair by IRMPD spectroscopy. The $[Cu(bpy)_2]^+$ ion was generated from its mass-isolated oxidized counterpart, the $[Cu(bpy)_2]^{2+}$ ion. The identical 1+ ion was also generated directly from the ESI source. IRMPD spectra of the singly-charged $[Cu(bpy)_2]^+$ ion were found to be virtually identical irrespective of the source of the ions. This indicates that charge reduction in the gas phase by ETR can be followed by rapid thermalization, removing the energy released by the exothermic ETR reaction and allowing the 1+ complex to adopt its minimum-energy tetrahedral coordination geometry. The conversion from square-planar to tetrahedral coordination is indeed what is expected upon reduction of the metal center from d^9 to d^{10}. Note that the distortion from the ideal square-planar geometry for the $[Cu(bpy)_2]^{2+}$ ion is due to the steric repulsion of CH groups on the two bpy moieties.

The singly-charged $[Cu(bpy)_2]^+$ ion is not formed by ESI, on account of the alkylamine nitrogens being harder Lewis bases than the pyridine nitrogens (and Cu^+ being a soft Lewis acid). The singly-charged $[Cu(cyclam)]^+$ ion can therefore only be accessed by charge reduction of the mass-isolated dication, which uniquely allows us to record the IRMPD spectra of both members of the $[Cu(cyclam)]^{2+/+}$ redox pair. Theoretical investigations indicate that the minimum-energy isomers (diastereomers) for both charge states are different in the gas-phase. However, comparison of theoretical results with the experiment suggests that isomerization is unlikely to occur upon charge reduction of the $[Cu(cyclam)]^{2+}$ ion. In contrast to the $Cu(bpy)_2$ system, the barrier to rearrangement is expected to be much higher as it necessarily involves a temporary detachment of coordination bonds. Hence, we conclude that the ETR process in the QIT MS leaves the cyclam ligand intact and its coordination to the copper center unchanged. This is another indication of rapid thermalization of the energy deposited into the system by the exothermic recombination reaction, attributed to collisional quenching with the helium buffer gas in the trap.

Finally, DFT is capable of identifying the structural changes and accurately explaining the structural trend for such complexes. ETR using the ETD-option of the QIT MS combined with FEL-based IRMPD spectroscopy provides an interesting "gas-phase test tube" for probing redox reactions under isolated conditions.

References

[1] Anouk M Rijs and Jos Oomens. *Gas-phase IR spectroscopy and structure of biological molecules*, volume 364. Springer, 2015.

[2] Nick C Polfer and Jos Oomens. Reaction products in mass spectrometry elucidated with infrared spectroscopy. *Phys. Chem. Chem. Phys.*, 9(29):3804–3817, 2007.

[3] Nick C Polfer and Jos Oomens. Vibrational spectroscopy of bare and solvated ionic complexes of biological relevance. *Mass Spectrom. Rev.*, 28(3):468–494, 2009.

[4] Nick C Polfer. Infrared multiple photon dissociation spectroscopy of trapped ions. *Chem. Soc. Rev.*, 40(5):2211–2221, 2011.

[5] Luke MacAleese and Philippe Maitre. Infrared spectroscopy of organometallic ions in the gas phase: from model to real world complexes. *Mass Spectrom. Rev.*, 26(4):583–605, 2007.

[6] John R Eyler. Infrared multiple photon dissociation spectroscopy of ions in penning traps. *Mass Spectrom. Rev.*, 28(3):448–467, 2009.

[7] Travis D Fridgen. Infrared consequence spectroscopy of gaseous protonated and metal ion cationized complexes. *Mass Spectrom. Rev.*, 28(4):586–607, 2009.

[8] Juraj Jašík, Ján Žabka, Jana Roithová, and Dieter Gerlich. Infrared spectroscopy of trapped molecular dications below 4 K. *Int. J. Mass Spectrom.*, 354:204–210, 2013.

[9] Jonathan Martens, Giel Berden, Christoph R Gebhardt, and Jos Oomens. Infrared ion spectroscopy in a modified quadrupole ion trap mass spectrometer at the FELIX free electron laser laboratory. *Rev. Sci. Instrum.*, 87(10):103108, 2016.

[10] Scott A McLuckey and James L Stephenson. Ion/ion chemistry of high-mass multiply charged ions. *Mass Spectrom. Rev.*, 17(6):369–407, 1998.

[11] John EP Syka, Joshua J Coon, Melanie J Schroeder, Jeffrey Shabanowitz, and Donald F Hunt. Peptide and protein sequence analysis by electron transfer dissociation mass spectrometry. *Proc. Natl. Acad. Sci. U.S.A.*, 101(26):9528–9533, 2004.

[12] Nicholas M Riley and Joshua J Coon. The role of electron transfer dissociation in modern proteomics. *Anal. Chem.*, 90(1):40–64, 2017.

[13] Joshua J Coon. Collisions or electrons? protein sequence analysis in the 21st century. *Anal. Chem.*, 81(9):3208–3215, 2009.

[14] Jonathan Martens, Josipa Grzetic, Giel Berden, and Jos Oomens. Structural identification of electron transfer dissociation products in mass spectrometry using infrared ion spectroscopy. *Nat. Commun.*, 7:11754, 2016.

[15] Lisanne JM Kempkes, Jonathan Martens, Giel Berden, and Jos Oomens. Spectroscopic characterization of an extensive set of c-Type Peptide Fragment Ions Formed by Electron Transfer Dissociation Suggests Exclusive Formation of Amide Isomers. *J. Phys. Chem. Lett.*, 2018.

[16] Lisanne JM Kempkes, Jonathan Martens, Giel Berden, and Jos Oomens. w-Type ions formed by electron transfer dissociation of Cys-containing peptides investigated by infrared ion spectroscopy. *J. Mass Spectrom.*, 53(12):1207–1213, 2018.

[17] Musleh U Munshi, Stephanie M Craig, Giel Berden, Jonathan Martens, Andrew F DeBlase, David J Foreman, Scott A McLuckey, Jos Oomens, and Mark A Johnson. Preparation of labile Ni^+(cyclam) cations in the gas phase using electron-transfer reduction through ion–ion recombination in an ion trap and structural characterization with vibrational spectroscopy. *J. Phys. Chem. Lett.*, 8(20):5047–5052, 2017.

[18] E Joseph Billo, Peter J Connolly, Dennis J Sardella, Jerry P Jasinski, and Ray J Butcher. Conformational characterization of square planar nickel (II) tetraaza macrocyclic complexes by proton NMR. crystal structure of [Ni (13aneN4)] ZnCl4. *Inorg. Chim. Acta*, 230(1-2):19–28, 1995.

[19] Dale K Cabbiness and Dale W Margerum. Macrocyclic effect on the stability of copper (ii) tetramine complexes. *J. Am. Chem. Soc.*, 91(23):6540–6541, 1969.

[20] Daryle H Busch. Distinctive coordination chemistry and biological significance of complexes with macrocyclic ligands. *Acc. Chem. Res.*, 11(10):392–400, 1978.

[21] Ludmila Y Martin, C Robert Sperati, and Daryle H Busch. The spectrochemical properties of tetragonal complexes of high spin nickel (ii) containing macrocyclic ligands. *J. Am. Chem. Soc.*, 99(9):2968–2981, 1977.

[22] Yann Hung, Ludmila Y Martin, Susan C Jackels, A Martin Tait, and Daryle H Busch. Ring size effects among metal complexes with macrocyclic ligands: synthesis, stereochemistry, spectrochemistry, and electrochemistry of cobalt (iii) complexes with unsubstituted, saturated tetraaza macrocycles. *J. Am. Chem. Soc.*, 99(12):4029–4039, 1977.

[23] PK Bhattacharya. Study of Cu(ii) complexes of saturated cyclic tetra amines. *J. Inorg. Nucl. Chem.*, 43(1):41–43, 1981.

[24] E Kent Barefield. Coordination chemistry of N-tetraalkylated cyclam ligands—A status report. *Coord. Chem. Rev.*, 254(15-16):1607–1627, 2010.

[25] Michael K Chan, Swarnalatha Mukund, Arnulf Kletzin, MW Adams, and Douglas C Rees. Structure of a hyperthermophilic tungstopterin enzyme, aldehyde ferredoxin oxidoreductase. *Science*, 267(5203):1463–1469, 1995.

[26] Hermann Schindelin, Caroline Kisker, James Hilton, KV Rajagopalan, and Douglas C Rees. Crystal structure of dmso reductase: redox-linked changes in molybdopterin coordination. *Science*, 272(5268):1615–1621, 1996.

[27] Thomas N Sorrell. Synthetic models for binuclear copper proteins. *Tetrahedron*, 45(1):3–68, 1989.

[28] Bol Johan. *Synthetic Models for Dinuclear Copper Proteins*. PhD dissertation, University of Leiden, 1997.

[29] Robert C Dunbar, Giel Berden, Jonathan K Martens, and Jos Oomens. Divalent metal-ion complexes with dipeptide ligands having Phe and His side-chain anchors: effects of sequence, metal ion, and anchor. *J. Phys. Chem. A*, 119(38):9901–9909, 2015.

[30] Robert C Dunbar, Jonathan Martens, Giel Berden, and Jos Oomens. Complexes of Ni (ii) and Cu (ii) with small peptides: deciding whether to deprotonate. *Phys. Chem. Chem. Phys.*, 18(38):26923–26932, 2016.

[31] Robert C Dunbar, Jonathan Martens, Giel Berden, and Jos Oomens. Transition metal (II) complexes of histidine-containing tripeptides: Structures, and infrared spectroscopy by IRMPD. *Int. J. Mass Spectrom.*, 429:198–205, 2018.

[32] Andrea Anichini, Luigi Fabbrizzi, Piero Paoletti, and Robert M Clay. A microcalorimetric study of the macrocyclic effect. enthalpies of formation of copper (ii) and zinc (ii) complexes with some tetra-aza macrocyclic ligands in aqueous solution. *J. Chem. Soc., Dalton Trans.*, 0(6):577–583, 1978.

[33] Wolfgang Kaim and Jochen Rall. Copper—a “modern” bioelement. *Angew. Chem. Int. Ed. Engl.*, 35(1):43–60, 1996.

[34] BJ Hathaway and DE Billing. The electronic properties and stereochemistry of mono-nuclear complexes of the copper (ii) ion. *Coord. Chem. Rev.*, 5(2):143–207, 1970.

[35] Jonathan Martens, Giel Berden, and Jos Oomens. Structures of fluoranthene reagent anions used in electron transfer dissociation and proton transfer reaction tandem mass spectrometry. *Anal. Chem.*, 88(12):6126–6129, 2016.

[36] Ralf Hartmer, Desmond A Kaplan, Christoph R Gebhardt, Thorsten Ledertheil, and Andreas Brekenfeld. Multiple ion/ion reactions in the 3D ion trap: Selective reagent anion production for ETD and PTR from a single compound. *Int. J. Mass Spectrom.*, 276(2-3):82–90, 2008.

[37] B Chiavarino, Maria Elisa Crestoni, S Fornarini, Simone Taioli, I Mancini, and P Tosi. Infrared spectroscopy of copper-resveratrol complexes: A joint experimental and theoretical study. *The Journal of chemical physics*, 137(2):024307, 2012.

[38] Ralph G Pearson. Hard and soft acids and bases. *J. Am. Chem. Soc.*, 85(22):3533–3539, 1963.

[39] Jose J Valle, John R Eyler, Jos Oomens, David T Moore, AFG Van Der Meer, Gert von Helden, Gerard Meijer, Christopher L Hendrickson, Alan G Marshall, and Gregory T Blakney. Free electron laser-fourier transform ion cyclotron resonance mass spectrometry facility for obtaining infrared multiphoton dissociation spectra of gaseous ions. *Rev. Sci. Instrum.*, 76(2):023103, 2005.

[40] Jos Oomens, Boris G Sartakov, Gerard Meijer, and Gert Von Helden. Gas-phase infrared multiple photon dissociation spectroscopy of mass-selected molecular ions. *Int. J. Mass Spectrom.*, 254(1-2):1–19, 2006.

[41] Mitra Almasian, Josipa Grzetic, Johanne van Maurik, Jeffrey D Steill, Giel Berden, Steen Ingemann, Wybren Jan Buma, and Jos Oomens. Non-equilibrium isomer distribution of the gas-phase photoactive yellow protein chromophore. *J. Phys. Chem. Lett.*, 3(16):2259–2263, 2012.

[42] MJ Frisch, GW Trucks, HB Schlegel, GE Scuseria, MA Robb, JR Cheeseman, G Scalmani, V Barone, B Mennucci, GA Petersson, et al. Gaussian 09, Revision D.01. *Inc., Wallingford CT*, 2013.

[43] Axel D Becke. Density-functional thermochemistry. III. the role of exact exchange. *J. Chem. Phys.*, 98(7):5648–5652, 1993.

[44] Axel D Becke. Three parameter hybrid method using the LYP correlation functional. *J. Chem. Phys.*, 98:5648–5652, 1993.

[45] Chengteh Lee, Weitao Yang, and Robert G Parr. Development of the colle-salvetti correlation-energy formula into a functional of the electron density. *Phys. Rev. B*, 37(2):785, 1988.

[46] Jonathan K Martens, Josipa Grzetic, Giel Berden, and Jos Oomens. Gas-phase conformations of small polyprolines and their fragment ions by IRMPD spectroscopy. *Int. J. Mass Spectrom.*, 377:179–187, 2015.

[47] Frank Sobott, Stephen J Watt, Julia Smith, Mariola J Edelmann, Holger B Kramer, and Benedikt M Kessler. Comparison of CID versus ETD based MS/MS fragmentation for the analysis of protein ubiquitination. *J. Am. Soc. Mass. Spectrom.*, 20(9):1652–1659, 2009.

[48] Musleh Uddin Munshi, Giel Berden, Jonathan Martens, and Jos Oomens. Gas-phase vibrational spectroscopy of triphenylamine: the effect of charge on structure and spectra. *Phys. Chem. Chem. Phys.*, 19(30):19881–19889, 2017.

[49] Robert J Nieckarz, Jos Oomens, Giel Berden, Pavel Sagulenko, and Renato Zenobi. Infrared multiple photon dissociation (IRMPD) spectroscopy of oxazine dyes. *Phys. Chem. Chem. Phys.*, 15(14):5049–5056, 2013.

[50] NS Rannulu and MT Rodgers. Noncovalent Interactions of Cu^+ with N-Donor Ligands (Pyridine, 4,4-Dipyridyl, 2,2-Dipyridyl, and 1,10-Phenanthroline): Collision-Induced Dissociation and Theoretical Studies. *J. Phys. Chem. A*, 111(18):3465–3479, 2007.

[51] NS Rannulu and MT Rodgers. Noncovalent interactions of Ni^+ with N-donor ligands (pyridine, 4, 4-dipyridyl, 2, 2-dipyridyl, and 1, 10-phenanthroline): collision-induced dissociation and theoretical studies. *J. Phys. Chem. A*, 113(16):4534–4548, 2009.

[52] NS Rannulu and MT Rodgers. Noncovalent Interactions of Zn^+ with N-Donor Ligands (Pyridine, 4, 4-Dipyridyl, 2, 2-Dipyridyl, and 1, 10-Phenanthroline): Collision-Induced Dissociation and Theoretical Studies. *J. Phys. Chem. A*, 116(5):1319–1332, 2012.

[53] Didia Coelho Graça, Pierre Lescuyer, Lorella Clerici, Yury O Tsybin, Ralf Hartmer, Markus Meyer, Kaveh Samii, Denis F Hochstrasser, and Alexander Scherl. Electron transfer dissociation mass spectrometry of hemoglobin on clinical samples. *J. Am. Soc. Mass. Spectrom.*, 23(10):1750–1756, 2012.

Chapter 4

Preparation of labile Ni(I)(cyclam) cations in the gas phase using electron-transfer reduction of Ni(II)(cyclam)

4.1 Abstract

Gas-phase ion chemistry methods that capture and characterize the degree of activation of small molecules in the active sites of homogeneous catalysts form a powerful new tool to unravel how ligand environments affect reactivity. A key roadblock in this development, however, is the ability to generate the fragile metal oxidation states that are essential for catalytic activity. Here we demonstrate the preparation of the key Ni(I) center in the widely used cyclam scaffold using ion-ion recombination as a gas-phase alternative to electrochemical reduction. The singly charged Ni^+(cyclam) coordination complex is generated by electron transfer from fluoranthene and azobenzene anions to doubly charged Ni^{2+}(cyclam), using the electron transfer dissociation (ETD) protocol in a commercial quadrupole ion trap instrument and in a custom built octopole RF ion trap. The successful preparation of the Ni^+(cyclam)

"Reproduced with permission from Musleh U. Munshi, Stephanie M. Craig, Giel Berden, Jonathan Martens, Andrew F. DeBlase, David J. Foreman, Scott A. McLuckey, Jos Oomens and Mark A. Johnson, *J. Phys. Chem. Lett.* **2017**, 8, 20, 5047-5052. Copyright 2019 American Chemical Society."

cation is verified through analysis of its vibrational spectrum obtained using the infrared free electron laser FELIX.

4.2 Introduction

Recent advances in mass spectrometry are creating powerful new ways to study the activation of small molecules docked in the active sites of homogeneous catalysts [1–5]. One of these involves a multistep strategy in which transition metal coordination compounds are extracted from solution using ambient ionization methods and fragmented in the gas phase to expose an open coordination site on the metal atom. This allows substrate molecules to be docked directly onto the open site using temperature-controlled condensation in an ion trap. The degree of substrate activation can then be determined through analysis of the substrate vibrational spectrum, obtained by IR photodissociation spectroscopy [4, 6–8]. This approach has been recently demonstrated for N_2, CO, and CO_2 activation by a bis-phenoidal Ni compound [9], which serves to highlight the essential role that the oxidation state of the metal plays in controlling the degree of substrate activation. Indeed, for the case of CO_2, it was observed that CO_2 attachment to the Ni(II) center of the bis-phenoidal ligand, was completely ineffective, while the Ni(I) variation displaced considerable charge onto the CO_2 framework, as evidenced by an approximately 400 cm^{-1} red shift of the antisymmetric CO_2 stretching mode.

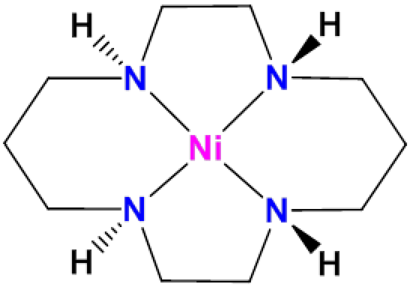

Figure 4.1. Square planar structure of Ni^{2+}(cyclam).

Accessing the key Ni(I) species [4] required a specially designed bimetallic precursor compound that supported stable Ni(I) oxidation states in both metal centers as an overall dication [9, 10]. The singly charged Ni(I)-based macrocycle, with an open coordination site, was then obtained by dissociation of the dicationic precursor upon injection into the mass spectrometer with an electrospray ionization (ESI) interface. While successful in demonstrating gas-phase capture and characterization of substrate activation, this early effort also highlights a key roadblock to the general application of this gas-phase method to contemporary transition-metal based molecular catalysts, such as the Ni(cyclam) system depicted in Figure 4.1 [11–18], which has been shown [19–24] to be an effective catalyst for the reduction of CO_2 due to its high selectivity toward CO (as opposed to H_2) production in aqueous solution. Although the Ni(II) compound in the +2 charge state is readily prepared in routine mass spectrometric analysis using ESI, the more fragile Ni(I) analogue, Ni^+(cyclam), is thought to be the catalytically active species [19, 25]. In the condensed phase, Ni(I) has been accessed through electrochemical reduction at mercury or glassy carbon electrodes [19], and pulse radiolysis has also been shown to reduce Ni^{2+}(cyclam) in the presence of $e_{aq}{}^-$, $CO_2{}^{\cdot -}$, and $H^{\cdot}$ [26]. Generally, these singly-charged metal compounds are extremely reactive, and indeed the Ni^+(cyclam) system has yet to be characterized [19]. Attempts to generate the singly charged Ni^+(cyclam) through manipulation of the chemistry in the ESI source have proven to be very inefficient due to the domination of the proton transfer pathway, resulting in $[Ni(cyclam\text{-}H)]^+$ at *m/z* 257, as illustrated by representative mass spectra in Appendix C Figure C.1.

Here we describe an alternative method to prepare the active species based on redox manipulation in the gas phase of the readily formed Ni(II) complexes from ESI. In particular, because the Ni(II) compound is a dication, ion-ion recombination through electron transfer from an anionic agent presents a promising method

$$Ni^{2+}(\text{ligand}) + A^- \rightarrow Ni^{1+}(\text{ligand}) + A \tag{4.1}$$

to rationally prepare the key Ni(I) species through one-electron reduction. Moreover, this post-ionization reduction method is directly compatible with the gas-phase ion chemistry characterization and spectroscopic investigation with IR-IS. A potential complication in the use of ion-ion collisions for single-electron reduction is that such processes are exoergic. Indeed, electron transfer dissociation (ETD) is a widely used alternative to collision-induced dissociation used frequently in sequencing studies of biopolymers [27, 28]. Commercially available ETD-enabled MS platforms most often use the radical anion fluoranthene [29–33], and in fact ETD was recently coupled to vibrational spectroscopy [33] for structural characterization of the ETD fragments of a tryptic peptide. Here, we demonstrate that the ETD instrumentation can be used as a means to reduce Ni^{2+}(cyclam) to Ni^{+}(cyclam) *without* dissociation (ETnoD) of the ligand framework, effectively creating an electron transfer reduction (ETR) capability for mass spectrometry. Moreover, buffer gas cooling quenches the considerable exothermicity ($\sim$ 8 eV) of the recombination reaction, allowing the product ions to be stabilized and structurally characterized using vibrational spectroscopy in combination with density functional theory calculations.

4.3 Experimental and Computational Details

4.3.1 Mass Spectrometry

The FELIX experiments were carried out using a modified 3D quadrupole ion trap (Bruker, AmaZon Speed ETD, Bremen, Germany) [34]. The Ni^{2+}(cyclam) ions (*m/z* 129 for the ^{58}Ni isotope) were generated directly via electrospray ionization (ESI) from a solution containing 10^{-6} M cyclam and 10^{-5} M $Ni(NO_3)_2$ in 1:1 $MeOH:H_2O$. The $^{58}Ni^{2+}$(cyclam) at *m/z* 129 was then mass isolated, and singly charged $^{58}Ni^{+}$(cyclam) (*m/z* 258) ions were generated by charge reduction using the ETD option of the QIT MS. This involves the transfer of an electron from the reagent anion (fluoranthene radical anion) in an ion-ion reaction directly inside the ion trap [35]. A reaction time of 200-300 ms was found to give optimal conversion to the charge-reduced species. Mass spectra of the reactant ions as well as the products generated by ion-ion recombination are presented in Figure 4.2. In addition to simple charge reduction, substantial fragmentation of the reduced ions by sequential H-atom loss is also observed, a process that is well known from the more common application of ETD in protein sequencing [36]. In fact, the product ion resulting from H atom abstraction from the charged reduced species (*m/z* 257) was the dominant ion in the ETD mass spectrum, though a sufficient number of intact charge-reduced ions Ni^{+}(cyclam) (*m/z* 258) remained for mass isolation and subsequent IRMPD measurements. Note that the removal of Ni isotopes other than ^{58}Ni prior to charge reduction allows us to uniquely mass-isolate the one-electron reduction product and distinguish it from potential H-loss fragments involving higher mass Ni isotopes.

In the FTICR MS, which has been described in detail previously [37, 38], Ni^{2+}-cyclam ions were produced from solutions containing approximately 10^{-3} M

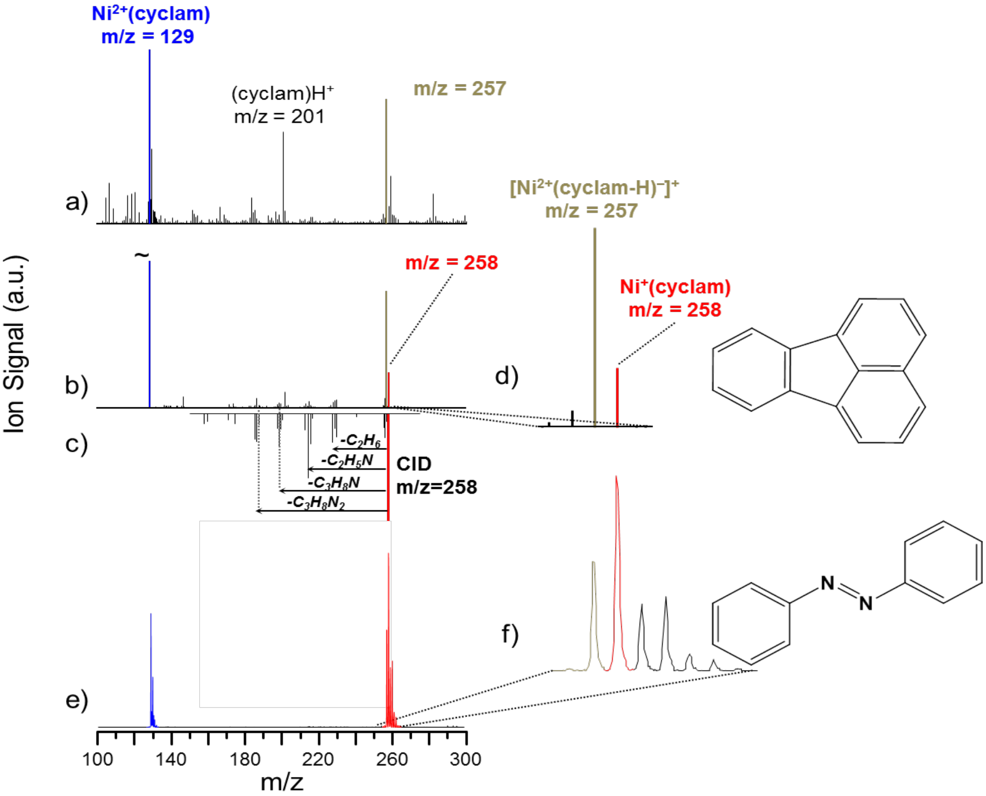

Figure 4.2. QIT mass spectra of a) Ni^{2+}(cyclam) at *m/z* 129 and b) the ETD reaction of isolated mono-isotopic Ni^{2+}(cyclam) with fluoranthene (top structure), which shows a peak corresponding to the formation of Ni^+(cyclam) at *m/z* 258. Trace d) expands the crucial region of trace b). CID on *m/z* 258 results in the mass spectrum in trace c). Traces e) and f) show the analogous reaction of Ni^{2+}(cyclam) with the azobenzene anion (bottom structure).

cyclam and 10^{-3} M Ni(II) in 1:1 MeOH:H_2O by ESI. As this MS has no possibility for charge reduction, only IRMPD spectra for Ni^{2+}(cyclam) ions were measured on this platform.

At Purdue, ETR was performed using a modified QTRAP 4001 (Sciex, Concord, ON, Canada). The instrument was run in mutual ion storage mode, which allowed simultaneous trapping of cations and anions in the q2 linear ion trap (LIT) by applying RF trapping potentials to the exit and entrance lenses as previously reported [39]. The cations were generated by ESI of Ni(cyclam)Cl_2, which was synthesized according to the procedure by Bosnich et al [40]. Azobenzene anions were generated by atmospheric pressure chemical ionization (APCI). As previously described [41], a solid azobenzene sample was attached inside the curtain plate of the Sciex ESI source for the counter-current N_2 so that the flowing gas sampled the headspace to volatilize the organic, which was ionized by a corona discharge on a platinum wire (∼ -2 kV) at atmospheric pressure. Both the azobenzene anion (*m/z* 182) and Ni^{2+}(cyclam) (*m/z* 129) were isolated by a transmission-mode RF/DC mass filter (q1) prior to 10 ms of mutual storage in q2. The products were analyzed by mass selective axial ejection (MSAE) in q3 [42].

4.3.2 IRMPD Spectroscopy

Trapped ions were irradiated for 1.5 (in the QIT) or 6 seconds (in the FTICR) by the tuneable infrared radiation of the FELIX free electron laser (FEL) [33, 43] in the fingerprint region (600-1800 cm^{-1}). Operating at a repetition rate of 10 Hz, FELIX produces 6-10 µs long macropulses with energies up to 100 mJ per pulse. When the frequency of the FEL is resonant with a vibrational mode of the trapped ions, multiple photons are absorbed and the internal energy of the ions increases. Following statistical redistribution throughout the many background states of the ion, unimolecular dissociation occurs along the pathway with the lowest energy barrier. We generate IR spectra by relating the fraction of dissociation (yield=$\sum$(fragment ions)/$\sum$(precursor + fragment ions)) to the IR wavelength as the laser is scanned [43, 44]. The yield is linearly corrected for the wavelength dependence of the laser pulse energy and wavelength is calibrated (online) using a grating spectrometer.

Measurements in the FT-ICR MS proceed analogously as those in the QIT, though for this experiment the ions were additionally irradiated for 20 ms by the output of a continuous-wave CO_2-laser (10.6 µm, 30 W) directly after each FEL pulse or pulses from an optical parametric oscillator/amplifier (OPO/OPA) IR source (Laser Vision, USA) in order to enhance the extent of dissociation [45]. The OPO/OPA allows us to acces the H-stretching region in order to probe the N-H stretching vibrations.

4.3.3 N_2 Tagged Predissociation Spectroscopy

At Yale University, ions were generated from solution in acetonitrile using ESI and introduced into the custom Yale tandem time-of-flight photofragmentation mass spectrometer previously described [46, 47]. After being guided through several regions of differential pumping, the ions were turned 90° by a quadrupole bender into a 3D Paul trap (Jordan), held at a temperature of 30 K by a helium cryostat (Sumitomo). The ions are trapped for 90 ms where they are collisionally cooled by a helium buffer gas doped with 10% N_2 in order to promote N_2 tagging. The tagged ions are then extracted from the trap and enter the time-of-flight region of the mass spectrometer. The ions of interest are then mass selected and interrogated with an OPO/OPA laser (LaserVision) from 800-4000 cm^{-1} in order to induce the loss of the tag, thus forming a photofragment. The formation of this photofragment is measured as a function of photon energy in order to generate a vibrational spectrum.

4.3.4 Computational Details

DFT optimizations and vibrational spectrum calculations were performed at the B3LYP/6-31++G(d,p) level of theory with Gaussian09 [48]. For Ni^{2+}(cyclam), both the singlet and triplet states were calculated, and the triplet state was found to be ∼70 kJ mol^{-1} higher in energy. An overview of these calculations is given in Appendix C, Table C.1. For Ni^{+}(cyclam) a doublet multiplicity was used. An overview of these calculations is given in Appendix C, Table C.1. Natural population analysis (NPA) [49] was performed using the B3LYP/6-31++G(d,p) level of theory using Gaussian09 using the keyword “pop=npa”.

4.4 Results and discussion

To illustrate the generality and versatility of ETR, we carried out the measurements on two different instruments using two different anionic reduction agents: the fluoranthene and azobenzene radical anions with structures indicated in Figure 4.2d and Figure 4.2f, respectively. For fluoranthene, we used the modified 3D quadrupole ion trap (QIT, Bruker, AmaZon Speed ETD) at the FELIX Laboratory, where Ni^{2+}(cyclam) ions were generated by ESI from a solution containing 10^{-6} M cyclam and 10^{-5} M $Ni(NO_3)_2$ as shown in Figure 4.2a. The doubly-charged coordination complex containing the ^{58}Ni isotope at *m/z* 129 was isolated (colored blue in Figure 4.2b), and then charge-reduced using the ETD option of the QIT MS, as further described in the SI. A reaction time of 200-300 ms was found to give optimal conversion to the charge-reduced species, as illustrated in the product mass distribution displayed in Figure 4.2b. The expanded region in the important mass range (Figure 4.2d) reveals efficient generation of ions with *m/z* 258 (red), which is expected for non-dissociative electron transfer to Ni^{2+}(cyclam). In addition to the formation of Ni^{+}(cyclam), the singly charged $[Ni^{2+}(cyclam\text{-}H)^{-}]^{+}$ cation (gold peak in Figure 4.2d) at *m/z* 257 is also generated. This ion likely corresponds to the Ni(II) ion coordinated to the deprotonated ligand, which was exclusively formed in previous attempts to generate singly-charged Ni^{+}(cyclam) using reductive chemistry in the ESI solution (as seen in Appendix C Figure C.1). Note that the isolation of the ^{58}Ni ion prior to charge reduction in the QIT instrument allows us to uniquely identify the one-electron reduction product against background arising from H-loss fragments involving heavier Ni isotopes To establish how the properties of the reagent anion affect the ETR process, we explored a second, commonly used ETD reagent, azobenzene [41], this time using a Sciex QTRAP 4001 hybrid triple quadrupole linear ion trap mass spectrometer at Purdue, which was modified to perform ion-ion reactions in mutual storage mode [39]. Interestingly, carrying out the reduction with azobenzene produced an even larger relative yield of *m/z* 258 corresponding to the stoichiometry of Ni^{+}(cyclam) as compared to the H-loss byproduct at *m/z* 257 (see Figure 4.2e and Figure 4.2f). We note that the reaction time for optimal yield was much shorter (10 ms for azobenzene in the linear quadrupole vs. 200 ms for fluoranthene in the 3D QIT). Concomitantly, the reaction with azobenzene also resulted in a much lower abundance of dissociation products, as shown by the much reduced intensity of the mass peaks at intermediate *m/z* (compare Figure 4.2b and Figure 4.2e). The production of the *m/z* 258 ion is a necessary step in the application of ETR to the preparation of the key $Ni(I)(cyclam)^{+}$ species, but this method of preparation raises the important question of whether the organic scaffold survives the substantial exoergicity, ΔE, inherent to the bimolecular reaction:

$$Ni^{2+}(cyclam) + A^{-} \rightarrow [Ni(cyclam)^{*}]^{+} + A + \Delta E \tag{4.2}$$

$$[Ni(cyclam)^{*}]^{+} \rightarrow \text{fragments} \tag{4.3}$$

A rough estimate of ΔE based on the calculated ionization energy (IE) of Ni^{+}-cyclam of about 8.5 eV and the adiabatic electron affinities (AEA) of the anions (0.2 and 1.6 eV for fluoranthene and azobenene, respectively) [50, 51] sets limiting values of ΔE in the range of 8.3 and 6.9 eV for the two anions (using ΔE=IE-AEA). Interestingly, we note that the more exothermic fluoranthene reaction yields more fragmentation peaks arising from Eq. (3), as expected for the usual ETD processes. These degradation products (interloper peaks in Figure 4.2b) largely arise from sequential neutral losses of 30 and 43 mass units, which are consistent with ejection of C_2H_6 and C_2H_5N groups. To evaluate whether these are characteristic of an excited $[Ni(cyclam)^*]^+$ ion, we measured the decomposition pathways of the *m/z* 258 parent ion using collision-induced dissociation (CID), with the result presented as the inverted trace in Figure 4.2c. The overall similarity in the break-up patterns upon CID and ETD with fluoranthene establishes that a significant fraction of the nascent ETR ions decompose before they can be cooled in the trap. We note that related work involving charge reduction of multiply charged ions in high energy collisions with alkali metal vapors [52–54] has also established partial survival of the nascent ions with considerable internal energy content.

The fact that ETR necessarily occurs with deposition of considerable internal energy into the target ion raises the important question of whether the ligand scaffold can survive intact when the ion is cooled through collisions with a buffer gas. A powerful method to establish the structure of ionic species is through analysis of their vibrational spectrum, which can be obtained through action spectroscopy methods using tunable IR lasers such as the FELIX free electron laser employed here [34, 35, 43].

The 600-1650 cm^{-1} region of the infrared multiple photon dissociation (IRMPD) vibrational spectrum for the mass-isolated *m/z* 258 ion was recorded by irradiating the trapped ions for 1.5 seconds with the FEL operating at a repetition rate of 10 Hz, and producing 6-10 µs long macropulses with energies up to 100 mJ per pulse. When the frequency of the FEL is resonant with a vibrational mode of the trapped ions, multiple photons are absorbed and the internal energy of the ions increases to above the dissociation threshold so that unimolecular dissociation occurs along the pathway with the lowest energy barrier. We generate IR spectra by relating the fraction of dissociation ($\text{yield}=\sum(\text{fragment ions})/\sum(\text{precursor + fragment ions})$) to the IR wavelength as the laser frequency is scanned [43, 55]. The yield is linearly corrected for the wavelength dependence of the laser pulse energy and the wavelength is calibrated (online) using a grating spectrometer. The resulting IRMPD spectrum of $Ni(cyclam)^+$ generated by ETR is shown in Figure 4.3c, and is dominated by three relatively sharp transitions near 850, 1000 and 1450 cm^{-1}, which are attributed to the CH rocking, CN stretching and CH bending fundamentals, respectively.

To quantify the spectral signature of the ligand and to establish the efficacy of

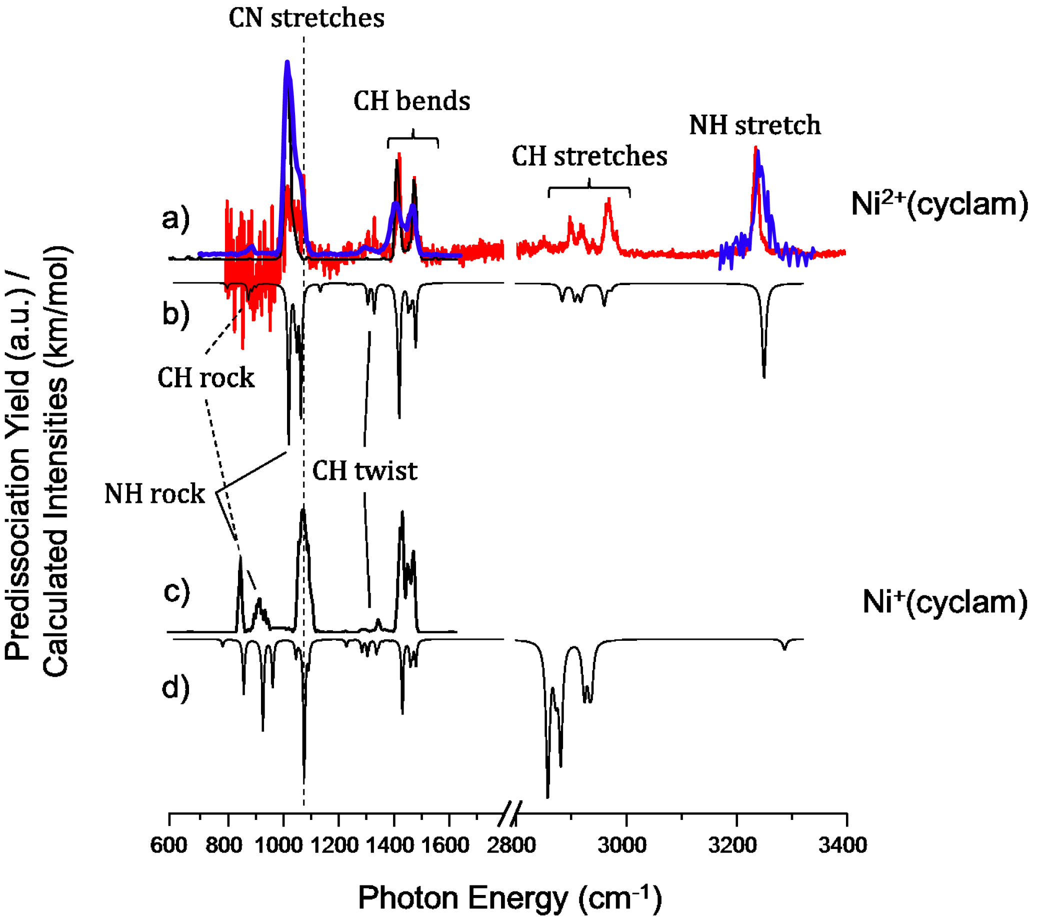

Figure 4.3. IRMPD spectra of a) Ni^{2+}(cyclam) and c) Ni^{+}(cyclam). The single-photon N_2 predissociation spectrum of Ni^{2+}(cyclam), red trace in a), taken at 30 K shows good agreement with the IRMPD data while revealing more detailed fine structure in the spectral signatures. The inverted traces display the computed harmonic spectra for b) Ni^{2+}(cyclam) and d) Ni^{+}(cyclam). Theoretical frequencies are scaled by 0.975 below 2200 cm^{-1} and 0.95 above 2200 cm^{-1}.

theoretical methods used to characterize this system, we also recorded the spectrum of the dicationic Ni^{2+}(cyclam) precursor using both IRMPD spectroscopy at FELIX as well as cryogenic ion spectroscopy at Yale to establish the sensitivity of this spectrum to ion internal energy. The spectrum of the 300 K ion obtained in the QIT MS at FELIX covers the 600-1800 cm^{-1} region. The 30 K ion spectrum obtained via N_2 tagging at Yale using a LaserVision OPO/OPA system covers the 800-3400 cm^{-1} range. The N_2 tag is calculated to attach to the NH groups of the Ni^{2+}(cyclam) ligand and is not believed to be "activated" by the Ni(II) ion [4]. The N_2 tagged spectrum is obtained in a linear action regime and interrogates vibrationally cold ions. Availability of both spectra enables us to confirm that the IRMPD spectra are hardly affected by the higher internal energy of the ions or by the multiple-photon nature of excitation in IRMPD [56], nor is the N_2-tagged spectrum affected by the presence of the tag. Figure 4.3a compares the N_2-tagged Ni^{2+}(cyclam) spectrum (red) with that recorded for the 300 K ion using the IRMPD approach (black trace). Although there are minor differences in the multiplet structure of the strong features, two strong bands at similar frequencies dominate both spectra. Appendix C Figure C.4 displays additional vibrational spectra recorded at 300 K using the FTICR-MS at Nijmegen, where some additional spectral features are recovered as a result of the lower background pressure and the inherently increased efficiency of multiple-photon excitation. Most importantly, analogous features are also found in the *m/z* 258 product ion from ETR, providing strong evidence that the structure of the ligand is retained in spite of the exoergicity involved in the gas-phase one-electron reduction. This isomer, denoted *trans-III*, is the most abundant of the two isomers (the other being *trans-I* with all four NH groups pointing in the same direction) in solution, 85%, as characterized by NMR [57]; isomerization between the *trans-III* and *trans-I* isomers was determined to occur with a rate constant of 121 ± 21 M^{-1} s^{-1} in solution [57]. The trans notation refers to the distortion of the alkyl chains relative to the N-atom plane, as illustrated in the two views of the *trans-III* structure in Figure 4.4.

The fine structure on the bands in the fingerprint region, combined with the CH and NH band patterns in the higher energy range obtained with N_2 tagging, provide the most useful benchmarks for structure determination by comparison with computed spectra for various local minimum geometries. DFT calculations were performed at the B3LYP/6-31++G(d,p) level of theory, and recovered the lowest energy structure of the Ni^{2+}(cyclam) ion displayed in Figure 4.4a, with the corresponding (scaled) harmonic spectrum displayed in Figure 4.3b. In particular, the fine structure associated with the dominant bands at 1000 and 1450 cm^{-1}, as well as the weaker feature at 1320 cm^{-1} (which were not evident in the IRMPD spectrum measured in the QIT, Figure 4.3a, but are evident in the FTICR/FELIX shown in Appendix C Figure C.4), are accurately reproduced by the predicted spectrum. Note that this structure (Figure 4.4a) features two of the proximal NH groups on the three carbon ring oriented in the same direction, roughly orthogonal to the plane containing the Ni atom and the four N atoms.

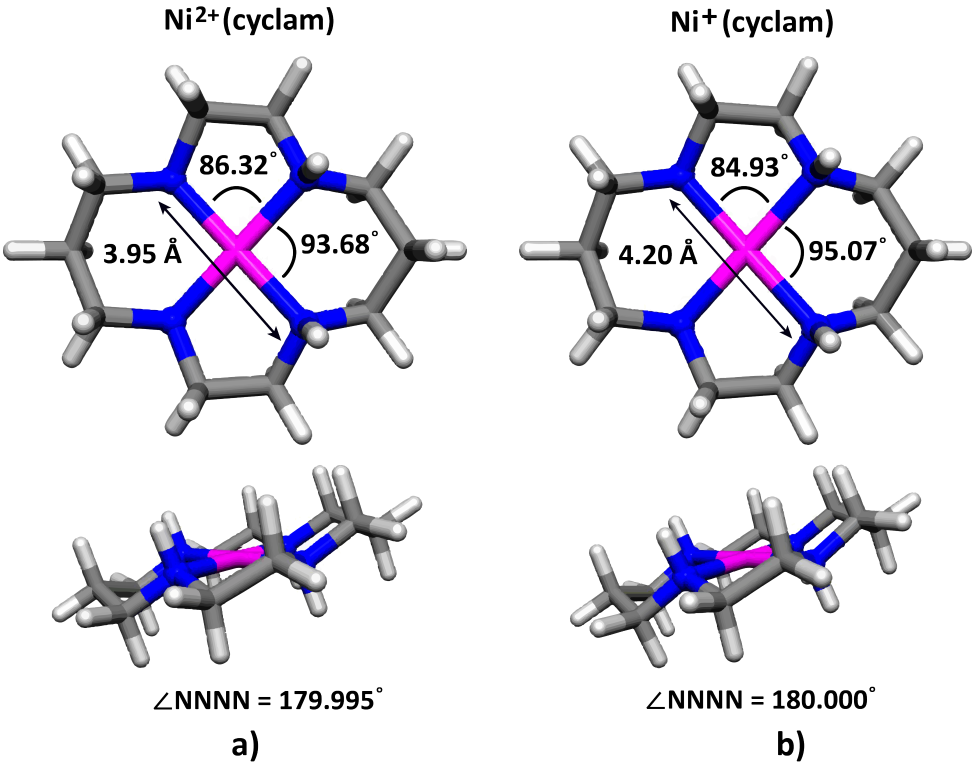

Figure 4.4. Calculated minimum energy structures of the *trans-III* isomers of a) Ni^{2+}(cyclam) and b) Ni^{+}(cyclam) reveal a lengthening of the N-N bond and a change of the N-Ni-N angles upon reduction of the metal center. The four nitrogen atoms of the cyclam macrocycle remain square planar.

The overall spin state of the *trans-III* isomer is a singlet with a d^6 low-spin electron configuration on the Ni center where, by NPA analysis, the largest positive charge per atom lies on the metal center (9% on the Ni, 5% each on the NH protons, with the residual distributed among the CH protons of the ligand (about ∼3% of the fundamental charge on each). The absence of the *trans-I* form in the gas-phase experiments reported here is confirmed by the single sharp NH transition at 3239 cm^{-1}, which is predicted to be split into a doublet spaced by about 45 cm^{-1} in the *trans-I* isomer. Appendix Figure C.2 S2 presents a summary of the five isomers of Ni^{2+}(cyclam), along with the scaled harmonic spectra for the *trans-I* and *trans-III* isomers in Appendix C Figure C.3, and energetics for all five isomers in Table C.1.

Given the fact that the B3LYP/6-31++G(d,p) level accurately recovers both the cold and IRMPD spectra of the Ni^{2+}(cyclam) ion, we next extend this method to consider the structural implications of the IRMPD spectrum of the Ni^{+}(cyclam) prepared by ETR (Figure 4.3c). The computed lowest energy structure is presented in Figure 4.4b, with its computed spectrum in Figure 4.3d, indeed capturing all the strong features in the experimental IRMPD spectrum (Figure 4.3c). Note that there are significant differences between the IRMPD spectra for the two charge states, indicating that there is significant distortion of the ligand as a result of charge reduction of the metal center. In particular, new features appear near 800 and 900 cm^{-1} in the Ni^{+}(cyclam) system, which are accurately recovered in the calculated spectrum and are attributed to NH and CH rocking modes of the ligand scaffold. The structure in Figure 4.4b is also derived from a trans conformation with substantial elongation (0.123 Å) of the Ni-N bonds. The spin state of this structure is a doublet with a d^{9} electron configuration on the Ni center, where the partial positive charge is now quite similar for the metal center and the NH protons. In fact, the NH protons have slightly more positive charge per atom than the Ni atom (6% for each NH proton, 5.7% for Ni, 3% for each of the remaining CH protons).

The spectroscopic measurements establish that ETR indeed provides a straightforward synthetic path for the preparation of the critical Ni(I) oxidation state with retention of the cyclam coordination environment. It is therefore of interest to elucidate the features of the reaction that optimize non-destructive electron attachment to the dication precursor. That is, the anionic reagents used here were optimized for dissociative electron transfer, while suppressing the branching to proton transfer, to provide as a general means to break up biopolymers for sequence analysis [27, 28]. In the case of ETR, we also seek to suppress proton transfer, but strive for less exothermic processes in order to preserve the ligand environment. The observation that azobenzene dramatically reduces the degradation byproducts (compare Figure 4.2c and Figure 4.2d) indicates that lowering the exoergicity by 1.4 eV has a profound effect on the degree of fragmentation. Part of this enhancement likely also results from the strong geometry change in the azobenzene anion framework upon electron detachment, which has been quantified through negative ion photoelectron spectroscopy [50, 51]. This is evident by the degree of vibrational excitation in the neutral upon vertical electron detachment, which in the case of azobenzene deposits considerable (∼1.6 eV) additional energy in the neutral azobenzene moiety, thus reducing the energy partitioned to the nascent Ni^{+}(cyclam) ion. It would therefore be valuable to refine the ETR approach by identifying higher electron affinity electron donors as well as systems which feature large geometry changes upon charge transfer.

4.5 Conclusion

In conclusion, we have demonstrated how the key Ni^+(cyclam) oxidation state can be prepared in vacuum through non-dissociative electron transfer from two molecular anions, fluoranthene and azobenzene, to the stable Ni^{2+}(cyclam) ion in an ion-ion recombination process carried out in RF ion traps. The structure of both the dicationic precursor and the Ni^+(cyclam) product ions were established with vibrational spectroscopy, verifying that the ligand structure is retained despite the large exoergicities of the electron transfer reactions. This chemistry was carried out using the ETD capability of a modified commercial mass spectrometer (Bruker, AmaZon Speed ETD) as well as in a modified triple quadrupole mass spectrometer. The latter instrument is readily adapted to cryogenic ion processing methods which can stabilize small molecules in the active sites of Ni(I) reduction catalysts, and these directions are presently under study.

References

[1] Peter Chen. Electrospray ionization tandem mass spectrometry in high-throughput screening of homogeneous catalysts. *Angew. Chem. Int. Ed.*, 42(25):2832–2847, 2003.

[2] Sandra M Lang, Anja Frank, and Thorsten M Bernhardt. Activation and Catalytic Dehydrogenation of Methane on Small ${Pd_x}^+$ and Pd_xO^+ Clusters. *J. Phys. Chem. C*, 117(19):9791–9800, 2013.

[3] Glenn BS Miller, Tim K Esser, Harald Knorke, Sandy Gewinner, Wieland Schöllkopf, Nadja Heine, Knut R Asmis, and Einar Uggerud. Spectroscopic identification of a bidentate binding motif in the anionic magnesium–CO_2 complex ($[ClMgCO_2]^-$). *Angew. Chem.*, 126(52):14635–14638, 2014.

[4] Fabian S Menges, Stephanie M Craig, Niklas Tötsch, Aaron Bloomfield, Subrata Ghosh, Hans-Jörg Krüger, and Mark A Johnson. Capture of CO_2 by a cationic nickel (I) complex in the gas phase and characterization of

the bound, activated CO_2 molecule by cryogenic ion vibrational predissociation spectroscopy. *Angewandte Chemie*, 128(4):1304–1307, 2016.

[5] Helmut Schwarz. Metal-mediated activation of carbon dioxide in the gas phase: Mechanistic insight derived from a combined experimental/computational approach. *Coord. Chem. Rev.*, 334:112–123, 2017.

[6] Benjamin J Knurr and J Mathias Weber. Solvent-driven reductive activation of carbon dioxide by gold anions. *J. Am. Chem. Soc.*, 134(45):18804–18808, 2012.

[7] Zhi Zhao, Xiangtao Kong, Dong Yang, Qinqin Yuan, Hua Xie, Hongjun Fan, Jijun Zhao, and Ling Jiang. Reactions of copper and silver cations with carbon dioxide: An infrared photodissociation spectroscopic and theoretical study. *J. Phys. Chem. A*, 121(17):3220–3226, 2017.

[8] Andreas Iskra, Alexander S Gentleman, Aras Kartouzian, Michael J Kent, Alastair P Sharp, and Stuart R Mackenzie. Infrared spectroscopy of gas-phase $M^+(CO_2)_n$ (M= Co, Rh, Ir) ion–molecule complexes. *J. Phys. Chem. A*, 121(1):133–140, 2017.

[9] Stephanie M Craig, Fabian S Menges, and Mark A Johnson. Application of gas phase cryogenic vibrational spectroscopy to characterize the CO_2, CO, N_2 and N_2O interactions with the open coordination site on a Ni (I) macrocycle using dual cryogenic ion traps. *J. Mol. Spectrosc.*, 332:117–123, 2017.

[10] Hans-Jörg Krüger. Spin transition in octahedral metal complexes containing tetraazamacrocyclic ligands. *Coord. Chem. Rev.*, 253(19-20):2450–2459, 2009.

[11] Shenglai Yao and Matthias Driess. Lessons from isolable nickel (I) precursor complexes for small molecule activation. *Acc. Chem. Res.*, 45(2):276–287, 2011.

[12] Richard H Perry, Kristen R Brownell, Konstantin Chingin, Thomas J Cahill, Robert M Waymouth, and Richard N Zare. Transient Ru-methyl formate intermediates generated with bifunctional transfer hydrogenation catalysts. *Proc. Natl. Acad. Sci. U.S.A*, 109(7):2246–2250, 2012.

[13] Jacob Schneider, Hongfei Jia, James T Muckerman, and Etsuko Fujita. Thermodynamics and kinetics of CO_2, CO, and H^+ binding to the metal centre of CO_2 reduction catalysts. *Chem. Soc. Rev.*, 41(6):2036–2051, 2012.

[14] Mark B Knickelbein. Reactions of transition metal clusters with small molecules. *Annu. Rev. Phys. Chem.*, 50(1):79–115, 1999.

[15] Chul-Ho Jun. Transition metal-catalyzed carbon–carbon bond activation. *Chem. Soc. Rev.*, 33(9):610–618, 2004.

[16] Alexander E Shilov and Georgiy B Shul'pin. Activation of C-H bonds by metal complexes. *Chem. Rev.*, 97(8):2879–2932, 1997.

[17] Mirza Cokoja, Christian Bruckmeier, Bernhard Rieger, Wolfgang A Herrmann, and Fritz E Kuehn. Transformation of carbon dioxide with homogeneous transition-metal catalysts: a molecular solution to a global challenge? *Angew. Chem. Int. Ed.*, 50(37):8510–8537, 2011.

[18] Etsuko Fujita, Bruce S Brunschwig, Tomoyuki Ogata, and Shozo Yanagida. Toward photochemical carbon dioxide activation by transition metal complexes. *Coord. Chem. Rev.*, 132:195–200, 1994.

[19] Jesse D Froehlich and Clifford P Kubiak. Homogeneous CO_2 reduction by Ni(cyclam) at a glassy carbon electrode. *Inorg. Chem.*, 51(7):3932–3934, 2012.

[20] Jinshuai Song, Eric L Klein, Frank Neese, and Shengfa Ye. The mechanism of homogeneous CO_2 reduction by Ni(cyclam): Product selectivity, concerted proton–electron transfer and C–O bond cleavage. *Inorg. Chem.*, 53(14):7500–7507, 2014.

[21] Eric E Benson, Clifford P Kubiak, Aaron J Sathrum, and Jonathan M Smieja. Electrocatalytic and homogeneous approaches to conversion of CO_2 to liquid fuels. *Chem. Soc. Rev.*, 38(1):89–99, 2009.

[22] Marc Beley, Jean Paul Collin, Romain Ruppert, and Jean Pierre Sauvage. Electrocatalytic reduction of carbon dioxide by nickel cyclam^{2+} in water: study of the factors affecting the efficiency and the selectivity of the process. *J. Am. Chem. Soc.*, 108(24):7461–7467, 1986.

[23] Marc Beley, Jean-Paul Collin, Romain Ruppert, and Jean-Pierre Sauvage. Nickel (II)-cyclam: an extremely selective electrocatalyst for reduction of CO_2 in water. *J. Chem. Soc., Chem. Commun.*, (19):1315–1316, 1984.

[24] Carl A Craig, Larry O Spreer, John W Otvos, and Melvin Calvin. Photochemical reduction of carbon dioxide using nickel tetraazamacrocycles. *J. Phys. Chem.*, 94(20):7957–7960, 1990.

[25] G Bryan Balazs and Fred C Anson. The adsorption of Ni(cyclam)$^+$ at mercury electrodes and its relation to the electrocatalytic reduction of CO_2. *J. Electroanal. Chem.*, 322(1-2):325–345, 1992.

[26] Craig A Kelly, Elliott L Blinn, Nadia Camaioni, Mila D'Angelantonio, and Quinto G Mulazzani. Mechanism of CO_2 and H^+ reduction by ni(cyclam)$^+$

in aqueous solution. a pulse and continuous radiolysis study. *Inorg. Chem.*, 38(7):1579–1584, 1999.

[27] Min-Sik Kim and Akhilesh Pandey. Electron transfer dissociation mass spectrometry in proteomics. *Proteomics*, 12(4-5):530–542, 2012.

[28] Scott A McLuckey and Teng-Yi Huang. Ion/ion reactions: new chemistry for analytical MS. *Anal. Chem.*, 81(21):8669–8676, 2009.

[29] Roman A Zubarev, Neil L Kelleher, and Fred W McLafferty. Electron capture dissociation of multiply charged protein cations. a nonergodic process. *J. Am. Chem. Soc.*, 120(13):3265–3266, 1998.

[30] Mariah L Parker and Scott Gronert. Investigating reduced metal species via sequential ion/ion and ion/molecule reactions: The reactions of transition metal phenanthrolines with allyl iodide. *Int. J. Mass Spectrom.*, 418:73–78, 2017.

[31] John EP Syka, Joshua J Coon, Melanie J Schroeder, Jeffrey Shabanowitz, and Donald F Hunt. Peptide and protein sequence analysis by electron transfer dissociation mass spectrometry. *Proc. Natl. Acad. Sci. U.S.A*, 101(26):9528–9533, 2004.

[32] Harsha P Gunawardena, Lev Gorenstein, David E Erickson, Yu Xia, and Scott A McLuckey. Electron transfer dissociation of multiply protonated and fixed charge disulfide linked polypeptides. *Int. J. Mass Spectrom.*, 265(2-3):130–138, 2007.

[33] Jonathan Martens, Josipa Grzetic, Giel Berden, and Jos Oomens. Structural identification of electron transfer dissociation products in mass spectrometry using infrared ion spectroscopy. *Nat. Commun.*, 7:11754, 2016.

[34] Jonathan Martens, Giel Berden, Christoph R Gebhardt, and Jos Oomens. Infrared ion spectroscopy in a modified quadrupole ion trap mass spectrometer at the FELIX free electron laser laboratory. *Rev. Sci. Instrum.*, 87(10):103108, 2016.

[35] Jonathan Martens, Giel Berden, and Jos Oomens. Structures of fluoranthene reagent anions used in electron transfer dissociation and proton transfer reaction tandem mass spectrometry. *Anal. Chem.*, 88(12):6126–6129, 2016.

[36] Didia Coelho Graça, Pierre Lescuyer, Lorella Clerici, Yury O Tsybin, Ralf Hartmer, Markus Meyer, Kaveh Samii, Denis F Hochstrasser, and Alexander Scherl. Electron transfer dissociation mass spectrometry of

hemoglobin on clinical samples. *J. Am. Soc. Mass. Spectrom.*, 23(10):1750–1756, 2012.

[37] Jose J Valle, John R Eyler, Jos Oomens, David T Moore, AFG Van Der Meer, Gert von Helden, Gerard Meijer, Christopher L Hendrickson, Alan G Marshall, and Gregory T Blakney. Free electron laser-fourier transform ion cyclotron resonance mass spectrometry facility for obtaining infrared multiphoton dissociation spectra of gaseous ions. *Rev. Sci. Instrum.*, 76(2):023103, 2005.

[38] Nick C Polfer and Jos Oomens. Reaction products in mass spectrometry elucidated with infrared spectroscopy. *Phys. Chem. Chem. Phys.*, 9(29):3804–3817, 2007.

[39] Yu Xia, Jin Wu, Scott A McLuckey, Frank A Londry, and James W Hager. Mutual storage mode ion/ion reactions in a hybrid linear ion trap. *J. Am. Soc. Mass. Spectrom.*, 16(1):71–81, 2005.

[40] B Bosnich, ML Tobe, and GA Webb. Complexes of nickel (II) with a cyclic tetradentate secondary amine. *Inorg. Chem.*, 4(8):1109–1112, 1965.

[41] Yu Xia, Hongling Han, and Scott A McLuckey. Activation of intact electron-transfer products of polypeptides and proteins in cation transmission mode ion/ion reactions. *Anal. Chem.*, 80(4):1111–1117, 2008.

[42] FA Londry and James W Hager. Mass selective axial ion ejection from a linear quadrupole ion trap. *J. Am. Soc. Mass. Spectrom.*, 14(10):1130–1147, 2003.

[43] Jos Oomens, Boris G Sartakov, Gerard Meijer, and Gert Von Helden. Gas-phase infrared multiple photon dissociation spectroscopy of mass-selected molecular ions. *Int. J. Mass Spectrom.*, 254(1-2):1–19, 2006.

[44] Anouk M Rijs and Jos Oomens. Ir spectroscopic techniques to study isolated biomolecules. In *Gas-Phase IR Spectroscopy and Structure of Biological Molecules*, pages 1–42. Springer, 2014.

[45] Mitra Almasian, Josipa Grzetic, Johanne van Maurik, Jeffrey D Steill, Giel Berden, Steen Ingemann, Wybren Jan Buma, and Jos Oomens. Non-equilibrium isomer distribution of the gas-phase photoactive yellow protein chromophore. *J. Phys. Chem. Lett.*, 3(16):2259–2263, 2012.

[46] Michael Z Kamrath, Etienne Garand, Peter A Jordan, Christopher M Leavitt, Arron B Wolk, Michael J Van Stipdonk, Scott J Miller, and Mark A Johnson. Vibrational characterization of simple peptides using cryogenic infrared photodissociation of h2-tagged, mass-selected ions. *J. Am. Chem.*

Soc., 133(16):6440–6448, 2011.

[47] Arron B Wolk, Christopher M Leavitt, Etienne Garand, and Mark A Johnson. Cryogenic ion chemistry and spectroscopy. *Acc. Chem. Res.*, 47(1):202–210, 2013.

[48] MJ Frisch, GW Trucks, HB Schlegel, GE Scuseria, MA Robb, JR Cheeseman, G Scalmani, V Barone, B Mennucci, GA Petersson, et al. Gaussian 09, Revision D.01. *Inc., Wallingford CT*, 2013.

[49] Alan E Reed, Robert B Weinstock, and Frank Weinhold. Natural population analysis. *J. Chem. Phys.*, 83(2):735–746, 1985.

[50] WF Frey, RN Compton, WT Naff, and HC Schweinler. Electron impact studies of some cyclic hydrocarbons. *Int. J. Mass Spectrom. Ion Phys.*, 12(1):19–32, 1973.

[51] D Hern Paik, J Spencer Baskin, Nam Joon Kim, and Ahmed H Zewail. Ultrafast vectorial and scalar dynamics of ionic clusters: Azobenzene solvated by oxygen. *J. Chem. Phys.*, 125(13):133408, 2006.

[52] Camilla Skinnerup Byskov and Steen Brøndsted Nielsen. On the formation, stability, and dissociation of peptide radicals after femtosecond electron transfer from alkali metal atoms. *Int. J. Mass Spectrom.*, 390:2–13, 2015.

[53] Camilla Skinnerup Byskov, J Mathias Weber, and Steen Brøndsted Nielsen. Gas-phase spectroscopy of singly reduced tris(bipyridine) ruthenium ions, $\mathrm{Ru(bipy)_3}^+$. *Phys. Chem. Chem. Phys.*, 17(8):5561–5564, 2015.

[54] Frantisek Turecek, AI Holm, Subhasis Panja, Steen Bronsted Nielsen, and Preben Hvelplund. Transition metals as electron traps. ii. structures, energetics and electron transfer dissociations of ternary co, ni and zn-peptide complexes in the gas phase. *J. Mass Spectrom.*, 44(10):1518–1531, 2009.

[55] Anouk M Rijs and Jos Oomens. *Gas-phase IR spectroscopy and structure of biological molecules*, volume 364. Springer, 2015.

[56] Tara I Yacovitch, Nadja Heine, Claudia Brieger, Torsten Wende, Christian Hock, Daniel M Neumark, and Knut R Asmis. Vibrational spectroscopy of bisulfate/sulfuric acid/water clusters: Structure, stability, and infrared multiple-photon dissociation intensities. *J. Phys. Chem. A*, 117(32):7081–7090, 2013.

[57] Peter J Connolly and E Joseph Billo. Hydrogen-1 NMR evidence for the R, S, R, S isomer of the (1, 4, 8, 11-tetraazacyclotetradecane) nickel (II) ion. *Inorg. Chem.*, 26(19):3224–3226, 1987.

Chapter 5

Vibrational spectra of the ruthenium-tris-bipyridine dication and its reduced form in vacuo

5.1 Abstract

Experimental IR spectra in the fingerprint region (500 to 1850 cm^{-1}) are presented for the isolated, gaseous redox ions pair $[Ru(bpy)_3]^{2+}$ and $[Ru(bpy)_3]^{+}$, where bpy = 2,2′-bipyridine. Based on their observed gas-phase fragmentation propensities by IR photo-fragmentation, the $[Ru(bpy)_3]^{+}$ ion is found to be much more weakly bound than the $[Ru(bpy)_3]^{2+}$ ion. Experimental spectra are compared against computed spectra predicted by density functional theory (DFT) and we have explored the applicability of several DFT functionals for this. For the closed-shell $[Ru(bpy)_3]^{2+}$ ion, the match of the IR spectra between experiment and theory is very good, however this is not the case for the $[Ru(bpy)_3]^{+}$ ion, which demands additional theoretical investigation for which the experimental IR spectra presented here can serve as a benchmark. We obvserve that better agreement with experiment is obtained upon reduction of the Hartree-Fock exact exchange from 20% to 13-15% when using the hybrid B3LYP functional. Additionally, calculations using the M06 functional appear to be promising in terms of the prediction of IR spectra, however it is unclear if the correct electronic structure is obtained. The M06

"Manuscript under preparation."

and B3LYP functionals indicate that the added electron in $[Ru(bpy)_3]^+$ is delocalized over all three bpy ligands, while the long range-corrected LC-BLYP and the CAM-B3LYP functionals show it to be more localized on a single bpy ligand — although the later levels of theory fail to produce matching IR spectra.

5.2 Introduction

The tris(2,2′-bipyridine)-ruthenium coordination complex ion $[Ru(bpy)_3]^{2+}$ is a classical metal-organic ingredient used, for instance, in dye-sensitized solar cells (DSSCs) [1–6], sensors [7, 8], in organic synthesis as a photoredox catalyst [9–11] and in artificial photosynthetic schemes [12–14]. This dicationic $[Ru(bpy)_3]^{2+}$ coordination complex is known to possess a high absorption cross section in the visible range of the spectrum. In DSSCs, light absorption occurs predominantly on transitions with metal-to-ligand charge transfer (MLCT) character [15], leading eventually to an oxidation of the dye. The oxidized dye is reduced back typically by the I^-/I_3^- redox shuttle in an ion-ion recombination reaction in solution [16]. $[Ru(bpy)_3]^{2+}$ may also be reduced back to $[Ru(bpy)_3]^+$ by accepting an electron before photo-oxidation and influence the visible solar absorption envelop [17]. These successive reductions give rise to a series of oxidation states of the dye sensitizer [14]. Structure, stability, excited state reactivity and photo-dynamics are dependent on the oxidation state, and studies of these complexes in complete isolation can contribute to a better understanding of their properties. One particularly interesting aspect of gas-phase studies is that they can serve as critical benchmarks for high-level theoretical models used to describe these systems.

In order to unravel the underlying mechanisms at each stage, this dye and many of its derivatives have been the subject of a vast number of experimental and theoretical studies [5, 6, 15, 19–26]. The long-term stability of the dyes used in DSSCs is a crucial issue in their practical applicability. For instance, although Ru(bpy)-based complexes exhibit solar-cell efficiencies of about 11% in outdoor conditions [16, 27, 28], they degrade over time [29, 30] and reductive quenching (reduction of the dye instead of oxidation in DSSC) [16] also influences the efficiency (Figure 5.1). Various structural fabrications have been suggested, in particular, the replacement of the mono-dentate thiocyanate ligands by anionic aromatic tris(bidentate) or bis(tridentate) ligands [31–40]. Apart from these

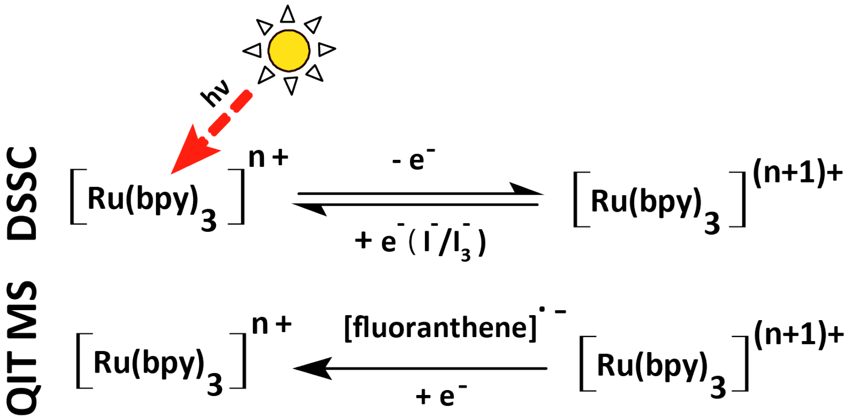

Figure 5.1. Schematic representation of the key redox reactions in the dye-sensitized solar cell (DSSC) and, the generation of the redox pairs through charge reduction via one electron addition in the quadrupole ion trap mass spectrometer (QIT MS). In the DSSC the oxidized dye is reduced back again through an ion-ion recombination reaction with the redox shuttle (I^-/I^{3-}) [16]. The same reduction process is mimicked inside the QIT MS in the gas-phase by using the fluoranthene radical anion as a reducing agent [18].

considerations, the excited state reactivity is another crucial factor in their design. For instance, tris(bidentate) complexes have relatively long excited state lifetimes compared to those of the bis(tridentate) complexes [19, 41]. Longer lifetimes of the excited states may induce dissociation of the dye sensitizers and degrade their performance over time. In contrast, the fast regeneration of the oxidized species may prevent degradation.

IR and resonance Raman spectroscopy was employed to study $[Ru(bpy)_3]^{2+}$ ion [42] and its deuterated analog in solution along with valence force field [43, 44] calculation to assign the observed frequencies [45]. Transient infrared absorption spectroscopy [46, 47] was used to study the ground and the excited triplet MLCT state of $[Ru(bpy)_3]^{2+}$ in solution [48, 49]. It was concluded that the excited electron is highly localized in one of the bpy ligands rather than delocalized throughout the whole molecule [42]. The same conclusion was drawn from broadband femtosecond fluorescence spectroscopy of $[Ru(bpy)_3]^{2+}$ in water [50]. A similar conclusion was also proposed for the reduced $[Ru(bpy)_3]^{+}$ ion on the basis of electron spin resonance (ESR) spectroscopy in solution [51]. In contrast, gas-phase experiments suggest an opposite conclusion for the 1+ ion on the basis of electronic absorption spectroscopy; the added electron is likely to be delocalized over the three bpy ligands [52].

The bpy ligand is, naturally, more strongly bound to the dication than to the monocation analog, which was shown experimentally using visible photo dissociation spectroscopy in the gas-phase [52, 53]. In these experiments, gaseous $[Ru(bpy)_3]^+$ was prepared by charge reduction of $[Ru(bpy)_3]^{2+}$ by electron transfer from cesium vapor. The UV spectrum recorded for the monocation showed much broader bands than the dication analogue, which were also red-shifted with respect to those for the dication. Here, we investigate the same gaseous $Ru(bpy)_3$ complex in the 1+ and 2+ oxidation states using IR spectroscopy in the fingerprint range and address whether the change of the oxidation state from 2+ to 1+ affects the structure as reflected in the IR spectra.

Numerous studies using electronic structure calculations have been reported for the $[Ru(bpy)_3]^{2+}$ ion [54–57]. Density functional theory (DFT) has been extensively used to predict the physico-chemical properties of the species in the gas phase and in solution. However, solution based studies apparently lack the selectivity and the influence of the solvent medium obstruct a clear understanding of intrinsic molecular properties [58]. Mainly as a result of experimental challenges, the availability of gas-phase data that is able to directly validate the various theoretical methods is rather limited. Here, we provide gas-phase IR spectra of isolated $[Ru(bpy)_3]^{2+}$ and its charge-reduced $[Ru(bpy)_3]^+$ counterpart. Our methodology is based on IR multiple photon dissociation (IRMPD) spectroscopy of mass-selected ions in a quadrupole ion trap mass spectrometer (QIT-MS) [59]. $[Ru(bpy)_3]^{2+}$ ions are produced by electrospray ionization (ESI) and its reduced analog is produced in a gas-phase electron transfer reaction with an anionic reagent, thus giving unique spectroscopic access to the two members of the redox-pair in complete isolation [60]. We compare our experimental spectra with DFT computed IR spectra and with relevant data derived from previous gas-phase electronic spectra of bare [52] and tagged [53, 61–63] $[Ru(bpy)_3]^{2+}$ ions obtained *via* UV-photo-fragmentation spectroscopy.

5.3 Methods

5.3.1 Experimental

All experiments have been performed in a modified quadrupole ion trap mass spectrometer (QIT MS, Bruker, AmaZon Speed ETD, Bremen, Germany) which has been described in detail elsewhere [59]. The dication of interest, $[Ru(bpy)_3]^{2+}$ was generated via ESI starting from a solution containing a few μM $[Ru(bpy)_3]Cl_3$ salt and 10 μM bpy in 1:1 $MeOH:H_2O$. The $[Ru(bpy)_3]^{2+}$ ion at *m/z* 285 was mass-isolated, retaining only the 102-isotope of ruthenium. Then, from the isotopically pure dication, the charge-reduced $[^{102}Ru(bpy)_3]^+$ ion at *m/z* 570 is generated by one-electron charge reduction using the electron-transfer dissociation (ETD) option of the QIT-MS. During the charge-reduction reaction, an electron is transferred from the fluoranthene radical anion to the Ru-complex dication. Fluoranthene radical anions are generated in a negative chemical-ionization ion source and are transferred to the quadrupole trap, where they engage in an ion-ion reaction for 250-300 ms with the previously isolated $[Ru(bpy)_3]^{2+}$ dication [18, 60]. The intact charge-reduced monocation can then be mass-isolated for subsequent IRMPD spectroscopic interrogation.

Fingerprint IRMPD spectra of either both of the mass-selected $[Ru(bpy)_3]^{2+/+}$ ions were recorded from 500 to 1850 cm^{-1} using the tunable infrared radiation from the FELIX free electron laser (FEL) [64, 65]. Operating at a repetition rate of 10 Hz, FELIX [66, 67] produces macropulses of 6-10 μs duration with energies up to 100 mJ per pulse. The mass-to-charge isolated ions are irradiated with the FEL radiation, which induces vibrational excitation when the laser frequency is in resonance with one of the normal modes of the ions. Multiple photons are absorbed while statistical redistribution of energy takes place, thus increasing the internal energy of the ions. Once the energy exceeds the lowest energy dissociation threshold in the molecule, the ion undergoes dissociation. $[Ru(bpy)_3]^{2+}$ ions were irradiated with 20 FEL macro pulses at maximum pulse energy. The charge-reduced ions, $[Ru(bpy)_3]^+$, were irradiated with only 2 pulses with the pulse energy reduced by a factor of three to prevent saturation by complete depletion of the precursor ions. This difference in settings is a clear indication of a greatly reduced dissociation threshold of the 1+ complex as compared to the 2+ species. IR spectra were generated by plotting the natural logarithm of the fragmentation yield,

$$-\ln\left[1-\frac{\sum \text{Intensity}_{\text{Fragments}}}{\sum \text{Intensity}_{\text{Fragments}}+\text{Intensity}_{\text{Precursor}}}\right],$$

as a function of the IR laser frequency [68, 69]. At each wavelength point, five mass spectra were averaged. The laser frequency step size was 3 cm^{-1}. The yield is linearly corrected for frequency-dependent variations in the laser pulse energy and the IR frequencies are calibrated using a grating spectrometer.

5.3.2 Computational modeling

Geometries were optimized at several levels of theory to test the applicability of various functionals for these particular systems. The B3LYP [70, 71] and range-separated [72] LC-BLYP levels of theory were used with the def2-TZVP [73, 74] basis set for all atoms. Additionally, B3LYP, and several meta functionals developed by Truhlar group [75] namely M06, M06L, M06-2X levels with an effective core pseudopotential (ECP) on the ruthenium atom in combination with 6-311+G(d,p) basis set for C, N, and H atoms [76] were employed for comparison. The range-separated CAM-B3LYP level of theory was also used only for the charge reduced monocation. In all cases, the ECP used was aug-cc-pVTZ-pp [77]. To refine the relative energies among different functionals, single-point MP2/6-311+G(2d,2P) calculations were also performed. Relativistic effects were not taken into account using these level of theories. Natural population analysis (NPA) [78] was performed using the keyword “pop=npa". All calculations described above were performed using the Gaussian 09 revision D 01 [79] computational program package.

Alternatively, the Amsterdam Density Functional (ADF) program package [80–82] was used. The B3LYP, M06 and O3LYP (developed by Cohen and Handy [83]) functionals were employed with uncontracted Slater type orbitals (STOs) of triple-ζ quality including two sets of polarization basis functions (TZ2P [84]). The hybrid O3LYP [83] functional is similar to B3LYP functional, however O3LYP uses 12% HF exact exchange instead of 20% in B3LYP. Relativistic effects were taken into account using the Zero Order Regular Approximation (ZORA) [85–88] method within the ADF program package.

With the optimized geometries, vibrational frequencies were calculated within the harmonic approximation. All stationary points were confirmed to be true minima with no imaginary frequencies. Doubly charged Ru(II) has a d^6 electron configuration, and a singlet spin configuration was chosen in all calculations. The charge-reduced Ru(I) has a d^7-configuration and a doublet spin state was chosen within an approximately octahedral ligand environment (Figure 5.2). Computed harmonic IR frequencies were convoluted using a 15 cm^{-1} full-width at half-maximum (FWHM) Gaussian line shape function and harmonic frequencies were scaled by a factor of 0.965 for all level of theories to evaluate their performance by comparison with the gas phase experiment.

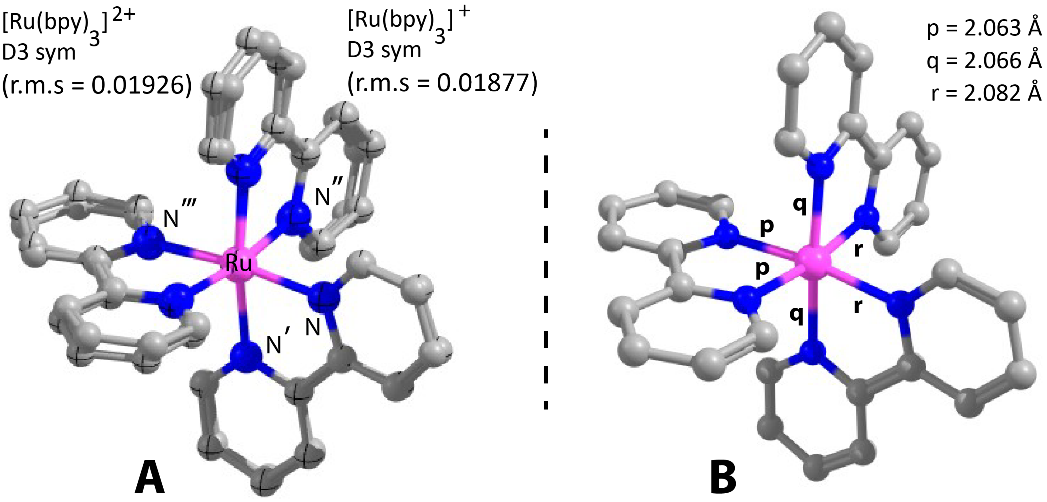

Figure 5.2. (A) DFT computed structure of $[Ru(bpy)_3]^+$ is overlaid with $[Ru(bpy)_3]^{2+}$ where the M06/aug-cc-pVTZ-pp level of theory is chosen from the Gaussian09 program package. The structures are very similar (Table 5.2) possessing D_3 symmetry (see inset r.m.s values) but their finger-print IR spectra (500 to 1850 cm^{-1}) are significantly different (Figure 5.4). Hydrogen atoms are omitted for clarity. Coordinate-labeling is also shown used in Table 5.2. (B) Optimized structure of the $[Ru(bpy)_3]^+$ at the LC-BLYP/def2-TZVP level is shown with Ru-N bond lengths.

As shown below, computations employing the M06/6-311+G(d,p) density functional are the best matching of all levels of theory used for the prediction of IR spectra for the two members of the redox pair, and therefore, results at this level of theory are exclusively discussed throughout the text unless otherwise noted. We note, that although M06 predicts the IR spectra relatively well, it fails to reproduce the expected relative Ru-N bond lengths which would be expected as the system goes from 2+ to 1+ — the much more weakly bound 1+ complex would be expected to have somewhat longer Ru-N bond lengths.

5.4 Results and discussion

5.4.1 Mass spectrometry

The mass spectrum recorded after electrospray ionization of the $[Ru(bpy)_3]Cl_3$ solution is shown in Figure 5.3a. Clearly visible is the $[Ru(bpy)_3]^{2+}$ ion peak with its characteristic isotope pattern, which is enlarged in the inset Figure 5.3b. After isolating the only the ^{102}Ru-containing ions at *m/z* 285, the ions were resonantly irradiated with the FEL at 1436 cm^{-1}. The main fragment is found at *m/z*

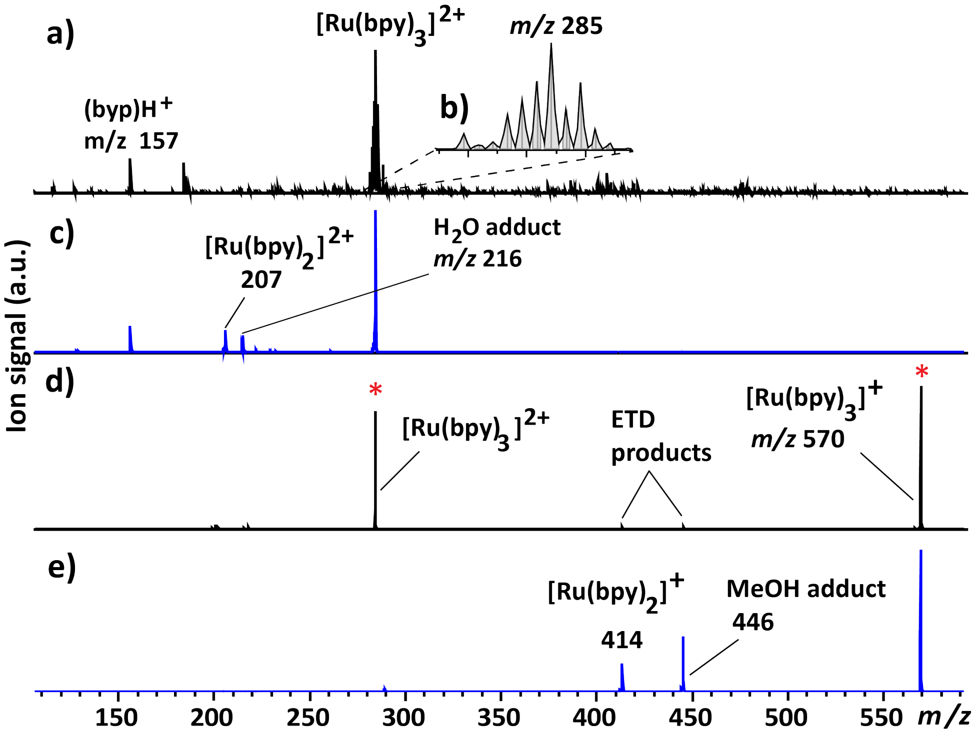

Figure 5.3. Mass spectra of (a) ESI of the Ru-bpy solution generating $[Ru(bpy)_3]^{2+}$ at *m/z* 285 and (b) isotope distribution of $[Ru(bpy)_3]^{2+}$ ion (zoomed in) (c) infrared photo dissociation of isolated $[^{102}Ru(bpy)_3]^{2+}$(d) ETR of isolated $[^{102}Ru(bpy)_3]^{2+}$ which shows a peak corresponding to the formation of charge reduced $[Ru(bpy)_3]^{+}$ ion at *m/z*570 including ETD induced fragments at *m/z* 414 and *m/z* 446, (e) infrared photo dissociation of isolated $[^{102}Ru(bpy)_3]^{+}$.

157 corresponding to a protonated bpy ligand, with the complementary ion appearing at *m/z* 413, corresponding to $[Ru(bpy)(bpy\text{-}H)]^{+}$ (Figure 5.3c). An additional fragment is found at *m/z* 207, which is attributed to the $[^{102}Ru(bpy)_2]^{2+}$ ion; an undercoordinated 2+ ion which easily picks up a background water molecule in the QIT and gives a peak at *m/z* 216.

In a separate experiment, the mass-isolated $[^{102}Ru(bpy)_3]^{2+}$ ion was charge-reduced using ETR, resulting in the singly charged $[^{102}Ru(bpy)_3]^{+}$ ion at *m/z* 570 (Figure 5.3d). The ETR reaction time was optimized to maximize the amount of charge-reduced ions. In this particular ETR reaction approximately 55% of the dication is charge-reduced. After mass isolation, the $[Ru(bpy)_3]^{+}$ ion was resonantly irradiated by the FEL at 1360 cm^{-1}, which primarily produced a fragment at *m/z* 414, which can be attributed to the $[Ru(bpy)_2]^{+}$ ion [52] (Figure 5.3e). Additionally, a peak at *m/z* 446 is observed, which is presumably a methanol adduct of $[Ru(bpy)_2]^{+}$.

5.4.2 Spectroscopy and structural properties of $[Ru(bpy)_3]^{2+/+}$

As presented in Figure 5.4, the spectrum of $[Ru(bpy)_3]^{2+}$ shows only two dominant relatively narrow IR absorption bands. In contrast, substantial changes in the IR spectrum are observed upon charge reduction to $[Ru(bpy)_3]^{+}$, where the $[Ru(bpy)_3]^{+}$ spectrum shows an increased number of strong and broadened IR bands (see also Table 5.1). As described above, in comparison with theory (pink all panels), all levels of theories produce a relatively satisfactory match for the dication, however, this is not the case for the charge-reduced monocation, for which the M06 functional appears to give the closest match with the experimental frequencies.

In order to record the spectra in Figure 5.4, the $[Ru(bpy)_3]^{2+}$ ions were irradiated by 20 IR laser pulses, whereas the charge reduced $[Ru(bpy)_3]^{+}$ ions were irradiated by only 2 pulses, attenuated to a third of the original pulse energy produced by FELIX. This difference in irradiation conditions indicates that $[Ru(bpy)_3]^{+}$ the monocation requires 30 times less energy to photo-dissociate than $[Ru(bpy)_3]^{2+}$. This is in agreement with the work of Nielsen and co-workers who investigated these ions in the gas phase by photo-dissociation spectroscopy using visible radiation (1.94-2.95 eV) [52, 53]. In the literature, experimental gas-phase bond dissociation energies for the loss of a bpy ligand from $M(bpy)_2{}^{+}$, were reported by Rodgers and co-workers [89–91] to be 2.33 eV for Zn, 2.46 eV for Cu, and 2.81 eV for Ni. We calculate a value of 3.59 eV for the loss of a bpy unit from $[Ru(bpy)_2]^{2+}$ and 6.55 eV from $[Ru(bpy)_2]^{2+}$, showing that binding to the dication is significantly more stronger. For the complex with three ligands, Nielsen and co-workers calculated a dissociation energy of 2 eV (B3LYP/def2-TZVP) for $[Ru(bpy)_3]^{+}$ [52], while we calculated values of 2.57 eV for $[Ru(bpy)_3]^{+}$ and 4.53 eV for $[Ru(bpy)_3]^{2+}$ at the M06 level. The larger calculated stability of the dication is qualitatively consistent with the visible and infrared photo-dissociation experiments, in which photodissociation of the dicationic complex was observed to require significantly harsher irradiation conditions.

The experimental IR bands have been assigned with an approximate vibrational mode description from the DFT predicted harmonic vibrational spectra for both $[Ru(bpy)_3]^{2+}$ and $[Ru(bpy)_3]^{+}$, as listed in Table 5.1. In the case of $[Ru(bpy)_3]^{2+}$, the IRMPD experiment yields two bands centered at 1436 cm^{-1}

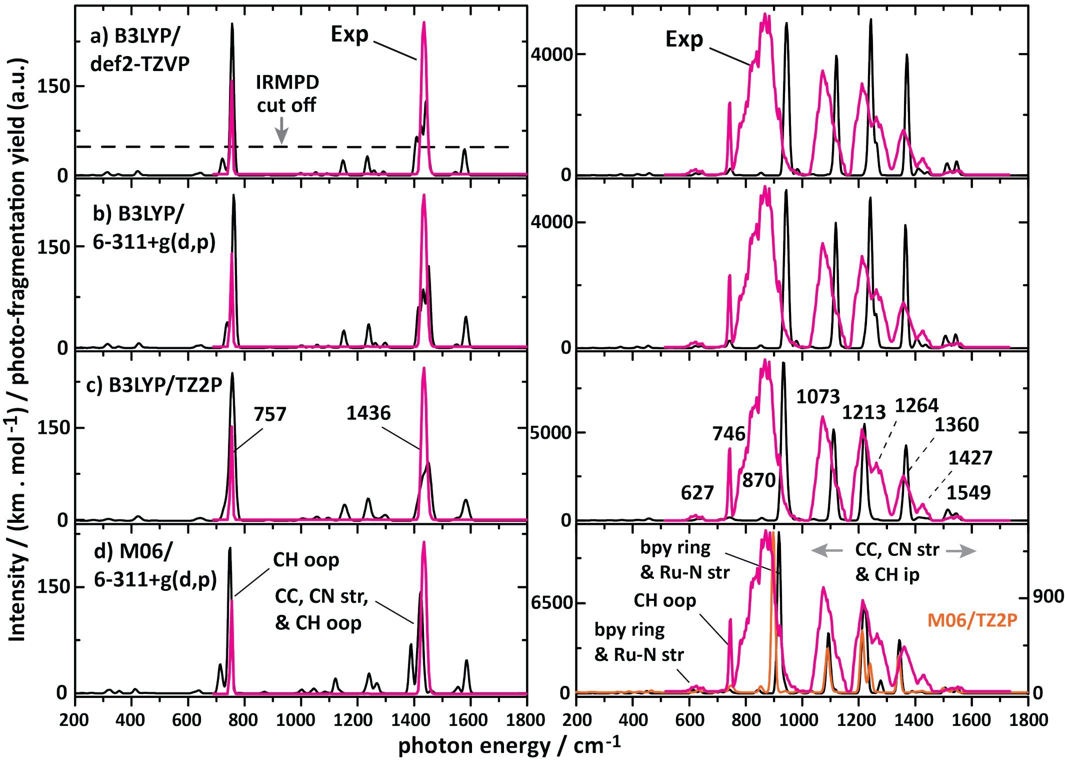

Figure 5.4. Gas phase experimental IRMPD spectra(magenta) of $[Ru(bpy)_3]^{2+}$(left) and analogous charge-reduced $[Ru(bpy)_3]^{+}$(right) complexes recorded in the QIT MS are overlaid with the calculated IR spectra (black) at several levels of DFT theories. Additionally, theoretical spectra at the M06/TZ2P level of theory (intensity on the right) for the monocation is overlaid in panel d. Experimental band maxima are labeled (panel c) and their approximate dominant mode characters are also indicated (panel d). Computed spectra for the dication are in good agreement with experiment at all levels of theory at the selected scaling factor 0.965. Some weak bands are not observed which we attribute to non-linearity of the IRMPD process leading to an apparent cut-off (dashed line) for this strongly bound complex. For the monocation, the IR frequencies show significantly more variation. The M06 method appears to outperform others (panel d).

and 757 cm^{-1} that are closely predicted at 1424 cm^{-1} and 750 cm^{-1}, respectively (left panel of Figure 5.4d). In general, all four levels of theory presented in Figure 5.4 accurately identify these two main IR bands, although their relative intensities are reversed as compared to the experiment. The higher frequency band shows dominant CC and CN stretch character combined with C—H in-plane bending. The lower frequency mode is predominantly due to the C—H out of plane bending motion. Theoretical bands with lower intensity are not observed in the experimental spectrum, which we attribute to collisional deactivation of the ions by the helium buffer gas inside QIT during IR activation; this prevents the ions from reaching the dissociation threshold [59, 60, 92]. Especially for ions with a relatively high dissociation threshold,

Table 5.1. Experimental vibrational frequencies (in cm^{-1}) of the $[Ru(bpy)_3]^+/[Ru(bpy)_3]^{2+}$ redox pair compared with scaled harmonic frequencies computed at the M06 level. Theoretical intensities (in km mol^{-1}) are shown as subscripts. Values in parentheses are observed IR spectral bandwidths (FWHM in cm^{-1}). Mode descriptions for the IR bands indicate the dominant contributions

Exp	Theory (DFT)		Assignments[a]
	M06/6-31++G(d,p)	M06/TZ2P	
$[Ru(bpy)_3]^{2+}$			
	1583_{13}	1602_{25}	CC str (s), CN str (w)
1436(25)	1424_{99}	1451_{105}	CC str (s), CN str (w), CHip bend (s)
	1389_{32}	1437_{40}	CHip bend (s), CC str (s), CN str (w)
757(9)	750_{48}	763_{73}	CHoop bend (s), bpy ring breath (w)
$[Ru(bpy)_3]^{+}$			
1549(∼50)	1550_{216}	1538_{228}	CC str (s), CN str (w), CHip bend (s)
1427(33)	1422_{106}	1425_{127}	CC str (w), CN str (w), CHip bend (s)
1360(47)	1343_{1996}	1342_{1761}	CC str (w), CN str (w), CHip bend (s)
1264[b](50)	1278_{463}	1240_{1380}	NRuN bend (s), CC str (s), CN str (s)
	1226_{2469}	1219_{808}	CHip bend (s), CC str (w)
1213(∼42)	1215_{2577}	1213_{2419}	CHip bend (s), CC str (w)
	1093_{2166}	1093_{1688}	bpy ring breath (w), CHip bend (w)
870(100)	917_{6085}	899_{7802}	Ru-N sym str (s), bpy ring breath (s), CHip bend (w)
	846_{89}	855_{288}	bpy-oop (m), CHoop bend (w)
746 (11)	743_{128}	758_{198}	NRuN bend (s), bpy ring breath (s), CHoop (s)
627(41)	615_{127}	635_{133}	Ru-N asym str (s), bpy ring deformation (s)

[a] str-stretch; ip— in-plane bending mode; oop—out of plane bending; bpy ring breath— bipyridine ring breathing; ring deformation—bipyridine ring deformation mode; sym—symmetric; asym—asymmetric; s—strong band; m—medium; w—weak.
[b] Shoulder.

such as $[Ru(bpy)_3]^{2+}$, this effect leads to an apparent IRMPD cut-off, indicated with a dashed line in Figure 5.4a.

A KBr pellet IR spectrum of $[Ru(bpy)_3]^{2+}$ was reported from 1000-1800 cm^{-1} by Sun et al. [26] and 1000-1700 cm^{-1} by Mukuta et al. [48]. The dominant IR bands in the KBr pellet spectrum are close to our experimental band at 1436 cm^{-1} (FWHM=25 cm^{-1}), reported [48] at 1424, 1447 and 1465 cm^{-1}. Some low intensity IR bands observed [48] in the pellet spectrum were reported at 1314, 1271, 1161 cm^{-1}. These bands were too weak to be observed by IRMPD and the IR range below 1000 cm^{-1} was not reported by either Sun et al [26] or Mukuta et al [48].

We now turn to the charge-reduced $[Ru(bpy)_3]^+$ ion, for which an experimental IR spectrum has, to the best of our knowledge, until now not been reported. As discussed above, this slightly-changed ion has much lower threshold to dissociate, thus nearly all IR bands predicted by theory can be correlated with bands observed in the IRMPD spectrum, although several bands are significantly shifted in frequency and some have deviating intensities (right panel

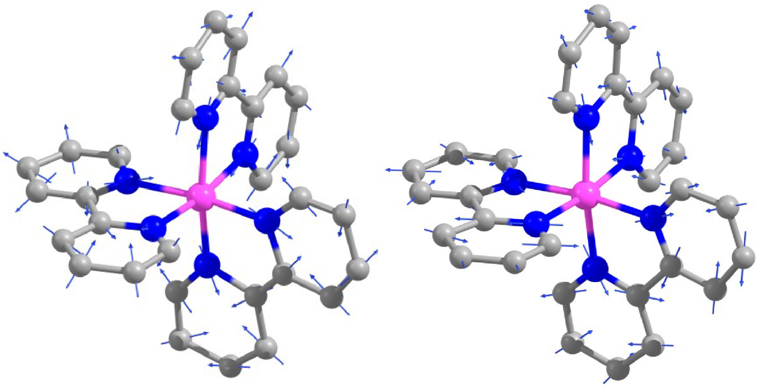

a) 870 cm^{-1} (FWHM = 100 cm^{-1}) **b) 1073 cm^{-1} (FWHM = 60 cm^{-1})**

Figure 5.5. Two of the vibrational normal modes at the M06 level of theory indicated with arrows. These modes are assigned to the observed IRMPD bands at M06/aug-cc-pVTZ-pp level of theory ndicated with arrows. These modes are assigned to the observed IRMPD bands at a) 870 cm^{-1} (FWHM = 100 cm^{-1}) and b) 1073 cm^{-1} (FWHM = 60 cm^{-1}). Theory predicts them to be at 917 and 1093 cm^{-1} respectively (Table 5.1).

of Figure 5.4). It is notable that the spectra computed by the different theoretical methods vary more for the 1+ than observed for the 2+ ion in both the positions and intensities of the bands. The B3LYP calculated spectra are quite similar with small differences seen depending on the basis set used, however the overall deviation from the experimental spectrum is substantial in all cases. A significant improvement is gained using the M06 functional (Figure 5.4d), which is consistent with recent suggestions of the suitability of this functional for transition metal complexes [93, 94]. For instance, the IRMPD band at 1073 cm^{-1} (FWHM = 60 cm^{-1}) can be matched to the band predicted at 1093 cm^{-1} using the M06 functional (while this band is calculated to be at 1119 cm^{-1} at the B3LYP/def2-TZVP level) (Figure 5.4a). The experimental band at 1213 cm^{-1} agrees well with the M06 predicted band at 1215 cm^{-1}. This experimental band has a shoulder at 1264 cm^{-1}, which is also closely predicted at 1278 cm^{-1}. Finally, the most intense band in the computed spectrum (917 cm^{-1}), is also in relatively close agreement with the strong experimental band at 870 cm^{-1}.

Very similar infrared spectra are also obtained at the M06/TZ2P level of theory for the charge-reduced $[Ru(bpy)_3]^+$ ion in comparison to the M06/6-311+G(d,p) calculated spectrum, although a few differences should be noted (Figure 5.4 and Table 5.1). At the M06/TZ2P level, the dominent band predicted at 899 cm^{-1} apparently moves closer towards the experiment by 18 cm^{-1} however, the band at 1240 cm^{-1} appears to be further shifted from the experimental peak. As well, slight difference are also observed for the low

Table 5.2. M06/6-311+G(d,p) optimized average Ru—N distances (Å), Ru centered bond angles (°) of $[Ru(bpy)_3]^{2+}$ and $[Ru(bpy)_3]^{+}$ ions in the gas-phase are compared with crystallographic literature data [95]. Similar values for B3LYP/def2-TZVP level is also shown including the reduced Hartree-Fock (13% HF) level for the $[Ru(bpy)_3]^{+}$ ion. Atom labels are shown in Figure 5.2. Parenthesized values are standard deviations in units of the last quoted digit

	$[Ru(bpy)_3]^{2+}$			$[Ru(bpy)_3]^{+}$		
Parameter	M06	B3LYP	Exp	M06	B3LYP	B3LYP (13% HF)
d(Ru-N)	2.081(0)	2.096(0)	2.065(2)	2.069(0)	2.084(0)	2.109(0)
bond angle (°)						
$\angle$N-Ru-N$'$	78.0(0)	77.9(0)	78.7(1)	78.4(0)	77.9(0)	78.3(0)
$\angle$N-Ru-N$''$	88.2(0)	88.5(1)	89.1(1)	89.8(0)	88.5(1)	89.8(1)
$\angle$N-Ru-N$'''$	173.3(1)	173.0(0)	173.0(1)	172.3(2)	173.0(0)	172.3(1)
$\angle$N$'$-Ru-N$''$	97.1(1)	96.8(4)	96.3(1)	96.2(1)	97.0(0)	96.2(0)

intensity bands (Table 5.1). Structural parameters (Appendix D Table D.1) remain very similar to those calculated at the M06/6-311+G(d,p) level.

A peculiar finding is that the calculated intensities (in km mol^{-1}) suggested by the M06 results are about 50 times (20-35 times at B3LYP level) higher for $[Ru(bpy)_3]^{+}$ as compared to $[Ru(bpy)_3]^{2+}$ (Figure 5.4). A simple unrestricted Hartree Fock (UHF) (see Appendix D Figure D.1) calculation shows that the calculated intensities are ∼7 times higher for $[Ru(bpy)_3]^{+}$ ion as compared to 2+ ion which seems crudely reasonable — although the predicted IR spectra of the $[Ru(bpy)_3]^{+}$ do not match the experiment. Comparison of the relative intensities at the Hartree Fock level versus the B3LYP and M06 indicates that the electron self-interaction error (SIE) [96, 97] might be predominantly responsible for the abnormal IR intensities of the $[Ru(bpy)_3]^{+}$ ion.

A careful inspection of the displacements of the vibrational modes shows that all levels of theory yield very similar normal mode characters (Figure 5.4, Table 5.1). The most intense and strongly broadened experimental band at 870 cm^{-1}, assigned to the band calculated at 917 cm^{-1} (M06), is best characterized as a symmetric bpy ring breathing motion that involves a symmetric Ru—N stretching motion (Figure 5.5). Therefore, the large 47 cm^{-1} (29 cm^{-1} at the M06/TZ2P) blue shift with respect to the experiment suggests that the central Ru-ligand coordination bonds probably are not as strong as theory predicts.

Selected structural parameters resulting from the calculations for both members of the redox pair are summarized in Table 5.2. For $[Ru(bpy)_3]^{2+}$ ion, the average Ru—N bond length is 2.081 Å and the bpy ligand bite angle with Ru is predicted to be 78.0°. For $[Ru(bpy)_3]^{2+}$, Ru—N bond lengths and bond angles are compared with values obtained from X-ray data [95], which indicates that the Ru—N distance is overestimated by only 0.016 Å and the bpy ligand-bite-angle is correct to within 0.7°). The computed gas-phase data are thus in reasonable agreement with a pseudo-octahedral ligand environment. Furthermore, the ion is thought to have D_3 symmetry [56, 98, 99] and the symmetry-unconstrained DFT structure is indeed very close (rms deviation = 0.0193). Upon charge reduction of 2+ ion, overall structural parameters remain similar, maintaining the pseudo-octahedral geometry and optimized structure also retains the D_3 symmetry [52] within an rms deviation of 0.0188. As well, Ru-centered ligand-angles rearrange minimally upon charge-reduction.

Perhaps most striking, and seemingly counterintuitive, is the average Ru—N bond length, which contracts slightly (-0.012 Å) upon charge reduction. As well, it is interesting that despite these minimal structural changes, the IR spectrum changes significantly. We could attribute this inconsistency perhaps to the poor approximation of the metal—ligand coordination potential in the computations for the 1+ system. The hybrid B3LYP functional uses 20% Hartree Fock (HF) exact exchange as introduced by Becke [100, 101], while M06 has 27% HF [75, 102]. Inclusion of higher HF exchange contribution in the DFT functional can lead to overbinding [103]/underbinding [104] of the complexes. We evaluate this trend using M06-L (0% HF) and M06-2X (54% HF), which clearly fail to reproduce the observed IR spectrum of the monocation (Appendix D, Figure D.1) where the average Ru-N distances are found to be 2.077(±0.002)Å and 2.099(±0.016)Å respectively.

Interestingly, the hybrid O3LYP/TZ2P level has been able to reproduce the right trend of the Ru-N distance where the bond length of the dication is reduced relative to that of the monocation (2.003±0.001Å vs. 2.017±0Å) [95] (Appendix D, Table D.1), however while this level of theory correctly reproduces the IR spectra for the dication (data not shown), it fails for the charge reduced ion (Appendix D, Figure D.1).

The computed (slight) contraction of the Ru—N bond length for $[Ru(bpy)_3]^{+}$ relative to $[Ru(bpy)_3]^{2+}$ ion suggests an increased bond energy, which is at odds with chemical intuition, and more importantly with experimental observations. First, IR induced dissociation of $[Ru(bpy)_3]^{+}$ is ∼30 times more facile than dissociation of $[Ru(bpy)_3]^{2+}$ ion, clearly suggesting weaker bonding. Secondly, the dominant experimental IR band involving significant Ru—N stretching character (870 cm^{-1}) is red-shifted relative to the predicted band frequency, whereas other IR bands appear to match relatively well. Moreover, several bands appear broadened in the IR spectrum, which may be an indication of a relatively shallow potential along the Ru—N coordinate. Despite the better performance of the M06 functional in predicting the IR frequencies, it also predicts a contracted Ru—N distance relative to the dication. Similar holds also for the B3LYP level. Therefore, we reduced the HF contribution manually in the B3LYP functional to investigate the effect especially on the IR spectra and the Ru—N distances.

Figure 5.6 illustrates the effect of the gradual reduction of the HF contribution from its original value of 20% at the B3LYP/def2-TZVP level and clearly shows the main IR features shifting to lower frequencies, in the direction of the experimentally observed positions. Relative intensities also appear to converge towards experimentally observed values. At the same time, the average Ru—N bond length (shown inset of Figure 5.6) increases as expected for a weaker metal-ligand bonding and the hexa-dentate coordination is maintained. At an HF contribution of about 13-15%, we qualitatively find an optimum match between experimental and computed IR spectra and further reduction appears to be worse. At the value of 13%, the average computed Ru—N distance is 2.11 Å, which is approximately 0.03 Å longer than in the dication and qualitatively in agreement with the expectation of an increase in bond length upon charge reduction.

The most significant improvements in experimental versus computed frequencies occur for the dominant IR bands. For the 13% HF calculation, the (broadened) bands centered at 870, 1073 and 1213 cm^{-1} are predicted at 880, 1076 and 1210 cm^{-1} with the approximate mode descriptions unchanged from those in Table 5.1. In addition, the weak and broad experimental feature centered around 625 cm^{-1} is more closely predicted to be due to two absorptions at 618 and 640 cm^{-1}. Conversely, the position of the sharp band observed at 746 cm^{-1} appears to be better predicted by the computations including a higher percentage of exact exchange.

We conclude that B3LYP/def2TZVP with the reduced HF exact exchange contribution gives the optimum results in terms of predictions of IR spectra and metal-ligand bond lengths which would be fitting with the experiment. Reiher

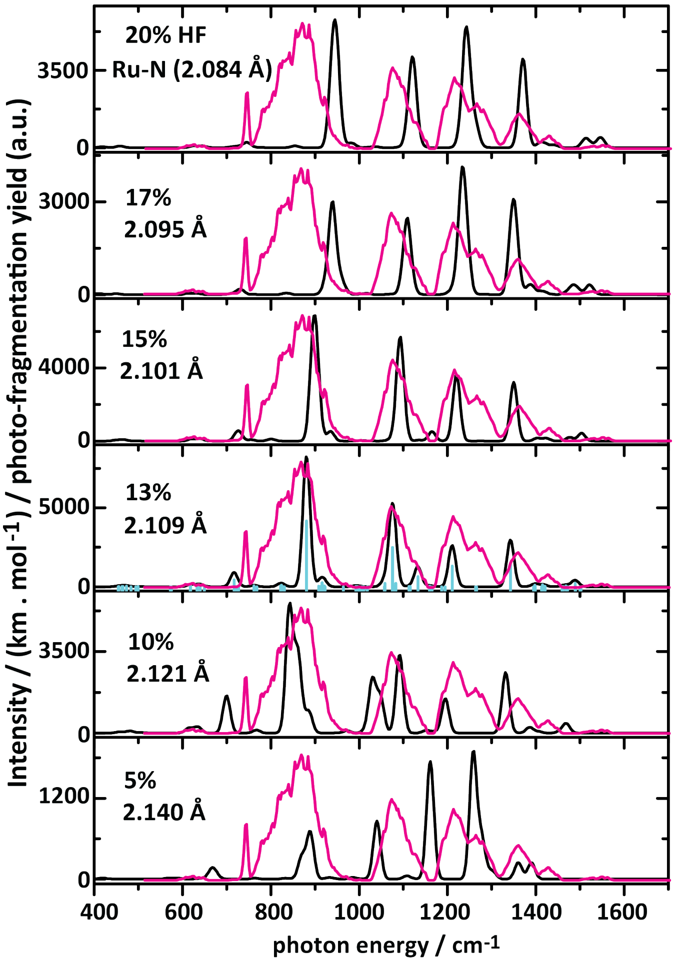

Figure 5.6. Theoretical IR spectra at the B3LYP/def2-TZVP level of theory with varying levels of Hartree Fock contribution, starting from the default 20% (top panel) down to 5% (bottom panel) compared with the experimental IRMPD spectrum (magenta trace) for $[Ru(bpy)_3]^+$. The average Ru-N bond length is given for each calculation and is seen to increase with reducing HF contribution.

et al. [104] also suggested to reduce HF exchange to 15% to better reproduce experimental data, especially in terms of the spin multiplicity for Fe-ligand complexes. Similarly, Moritz et. al. [105] reported an improved modelling of the binding of N_2 to Sellmann-type Fe(II) compounds upon reducing the default 20% HF to 15%.

Now, we would like to expore the "location" of the added electron upon charge reduction of the dication. Gilson et. al [97] modelled the process of charge reduction upon attachment of an electron to a multiply charged peptide cation making it a radical cation. They reported that the additional electron remained as a delocalized unpaired electron (which is unphysical) if a conventional DFT

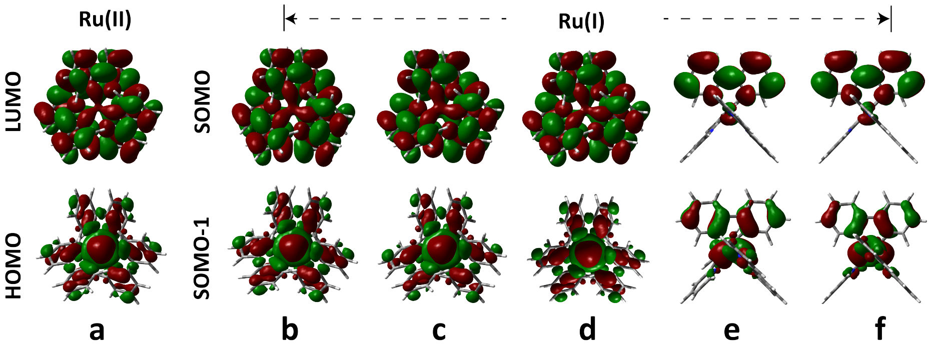

Figure 5.7. B3LYP/6-311+g(d,p) computed HOMO and LUMO of $[Ru(bpy)_3]^{2+}$ (a) and SOMO, SOMO-1 for the $[Ru(bpy)_3]^+$ ion (b). For the charge-reduced ion, the same MOs calculated at the M06 (c), B3LYP (HF=13%)/def2-TZVP (d), LC-BLYP/def2-TZVP (e) and at the CAM-B3LYP/6-311+G(d,p) (f) levels of theory are also shown. Isosurface value 0.015 is chosen for all orbitals.

functional (e.g., hybrid B3LYP) was chosen. On the other hand, several post-HF methods (MP2, CCSD) and long-range corrected functionals (e.g., LC-BLYP, CAM-B3LYP [106]) predict the attached electron to be localized on the group with the highest electron affinity of the precursor cation.

In order to avoid electron SIE [96, 97], we computed the $[Ru(bpy)_3]^+$ complex at the LC-BLYP/def2-TZVP and CAM-B3LYP/6-311+G(d,p) level and found that the relative IR intensities are in the same order as the dication but the corresponding IR spectra do not match the experiment (Appendix D, Figure D.1).

The optimized structure at the LC-BLYP/def2-TZVP (Figure 5.2) shows that the two Ru—N bonds with a single bpy ligand (out of three ligands) are slightly (equally) shorter (Ru-N: 2.063Å) than for the other two ligands (2.082Å).

Here, the singly occupied molecular orbital (SOMO) plot confirms that the electron is significantly localized on that bpy moiety which has shorter Ru-N distances (Figure 5.7). Note similar results are also obtained at the simple UHF level in terms of the Ru-N distance, infrared intensities (Appendix D, Figure D.1) and a slightly localized electron densities (data not shown). Based on these observations, binding of the bpy moieties to the metal center in the $[Ru(bpy)_3]^+$ complex may be thought as having $[Ru(II)(bpy)_2(bpy)^{\cdot-}]^+$ character.

Figure 5.7 shows the frontier molecular orbitals (MO's) for $[Ru(bpy)_3]^{2+}$ and $[Ru(bpy)_3]^+$. While the highest occupied molecular orbital (HOMO) is primarily centered on the Ru atom for $[Ru(bpy)_3]^{2+}$, the lowest unoccupied molecular

Table 5.3. NPA results are summarized for the 2+ and 1+ complexes at the B3LYP/6-311+G(d,p), M06/6-311+G(d,p), CAM-B3LYP/6-311+G(d,p) and LC-BLYP/def2-TZVP level of theories where the calculated values are shown for the central Ru atom and for all the six attached N atoms

		B3LYP		M06	LC-BLYP	CAM-B3LYP
	atom	2+	1+	1+	1+	1+
ligand	Ru	0.160	0.161	0.144	0.069	0.139
bpy (1st)	N	-0.379	-0.389	-0.400	-0.401	-0.453
	N	-0.379	-0.389	-0.399	-0.401	-0.453
bpy (2nd)	N	-0.379	-0.388	-0.400	-0.310	-0.371
	N	-0.379	-0.389	-0.399	-0.303	-0.361
bpy (3rd)	N	-0.379	-0.388	-0.400	-0.310	-0.371
	N	-0.379	-0.388	-0.399	-0.303	-0.361

orbital (LUMO) is mostly delocalized on the bpy ligands. The singly occupied MO (SOMO) for $[Ru(bpy)_3]^+$ indeed nearly corresponds to the LUMO of $[Ru(bpy)_3]^{2+}$ (Figure 5.7b-d) and remains mostly delocalized on the bpy ligands and on the metal center. On the contrary, a dominant amplitude localization is observed on a single bpy moiety with a slight contribution on the metal center at the LC-BLYP and CAM-B3LYP levels (Figure 5.7e-f). These observations are supported by the NPA results. In addition, the SOMO-1 of $[Ru(bpy)_3]^+$ is very similar to the HOMO for the $[Ru(bpy)_3]^{2+}$ shown in this figure except at LC-BLYP and CAM-B3LYP level of theories. These later levels shows slight differences where most of the amplitude in SOMO-1 is at the metal center having a significant overlap with one of the bpy moieties.

Table 5.3 summarizes the relevant NPA results. The NPA analysis indicates that the largest positive charge per atom 0.187 lies on the six C atoms (which connect two aromatic rings of the individual bpy ligand) and a similar charge of 0.160 is also concentrated on the central Ru atom for $[Ru(bpy)_3]^{2+}$ of the optimized geometry at the B3LYP/6-311+G(d,p) level. On the other hand, the largest negative charge per atom (0.379) lies on the six N atoms. Upon charge reduction from, the positive charge drops to 0.161 on C but it remains almost unchanged (0.161) on the Ru atom. This indicates that the added electron is delocalized especially on the bpy ligands. Similar charge delocalization is observed at the M06/6-311+G(d,p) level. On the contrary, a slightly more negative charge localization is calculated on the N atoms at the LC-BLYP/def2-TZVP and CAM-B3LYP/6-311+G(d,p) levels.

Single point MP2 calculations (see Table 5.4) on the optimized geometries

Table 5.4. Computed relative energies at the single-point MP2/6-311+G(2d,2p) level for the charge reduced $[Ru(bpy)_3]^+$ complex in kJ mol^{-1}

Optimized geometries at different level of theories	MP2/6-311+G(2d,2p)
B3LYP/def2TZVP	66.2
B3LYP/6-311+G(d,p)	82.2
M06/6-311+G(d,p)	37.7
CAM-B3LYP/6-311+G(d,p)	26.4
LC-BLYP/def2TZVP	0

calculated using different functionals for the $[Ru(bpy)_3]^+$ ion reveal that the range separated LC-BLYP functional has the minimum energy structure while M06 holds the third lowest position. Despite the small energy difference (38 kJ mol^{-1}) between them, they have dramatically different IR spectra—where one (M06) reproduces the experimental IR spectrum and others (LC-BLYP and CAM-B3LYP) do not. Therefore, based on the close relative energies and the comparison of the predicted IR spectra to the experimental one, we find it unlikely that the structures predicted by the LC-BLYP and CAM-B3LYP are correct.

Daku et. al [107] recently reported a comparative study of 30 density functionals of the GGA, meta-GGA, global hybrid, range-separated hybrid (RSH) and double-hybrid types with truncated coupled-cluster CCSD(T) and mult-configurational perturbation methods namely CASPT2 on the transition metal complexes, $[M(NCH)_6]^{2+}$ (M=Fe, Co) for their spin-state energetics. This study suggested that it was impossible to find a common density functional for the complexes which would reproduce the electronic properties as derived from the experiment or ab initio theories. However, the range separated functionals (e.g., CAM-B3LYP, LC-BLYP, CAM-PBE0) performed relatively well in comparison to the CASPT2 and CCSD(T) results. For the ruthenium-bpy redox pair, such high level calculations are beyond the scope of this study.

5.5 Conclusion

We have measured the IRMPD spectra of isolated $[Ru(bpy)_3]^{2+}$ and its charge-reduced analog $[Ru(bpy)_3]^+$ in the gas-phase. The stability of the $[Ru(bpy)_3]^+$ ion is clearly much lower than that of its oxidized counterpart $[Ru(bpy)_3]^{2+}$.

Their IR spectra are also very distinct and while DFT computations have no difficulties reproducing the IR spectrum of the closed-shell dication, the IR spectrum of the monocation contains a large number of bands that appear to be broadened and difficult to reproduce at all DFT levels employed in this study. Reducing the HF exact exchange contribution in the B3LYP/def2-TZVP level of theory results in a lengthening of the metal-ligand bond, consistent with the experimentally observed lowering of the dissociation energy upon charge reduction. Moreover, it also gives a much improved prediction of the experimental IRMPD spectrum. In general, we find that all ligands remain intact and in the same octahedral configuration after the charge reduction at all levels of theory used here. As noted, the change of the oxidation state significantly changes the stability, which could help to understand the degradation of the dye in the DSSCs. Computations using the M06 and B3LYP functionals suggest that the added electron in $[Ru(bpy)_3]^+$ is delocalized throughout all three bpy ligands, while the LC-BLYP and CAM-B3LYP results suggest it to be more localized on a single bpy ligand than the others (in the gas-phase). These later methods, however, fail to reproduce the experimental IR spectra and further computational work is needed to have a clearer interpretation of why this is the case. Perhaps most importantly, the fingerprint IR spectra of the bare metal-ligand redox pair that we provide here can be used to benchmark theoretical methods for $[Ru(bpy)_3]^+$, and other such ions that have oxidation states that are not readily accessible experimentally.

References

[1] Michael Grätzel. Photoelectrochemical cells. *Nature*, 414(6861):338, 2001.

[2] Michael Grätzel. Dye-sensitized solar cells. *J. Photochem. Photobiol., C*, 4(2):145–153, 2003.

[3] Michael Grätzel. Solar energy conversion by dye-sensitized photovoltaic cells. *Inorg. Chem.*, 44(20):6841–6851, 2005.

[4] Anders Hagfeldt, Gerrit Boschloo, Licheng Sun, Lars Kloo, and Henrik Pettersson. Dye-sensitized solar cells. *Chem. Rev.*, 110(11):6595–6663, 2010.

[5] Kuppuswamy Kalyanasundaram. Photophysics, photochemistry and solar energy conversion with tris (bipyridyl) ruthenium (II) and its analogues. *Coord. Chem. Rev.*, 46:159–244, 1982.

[6] K Kalyanasundaram and M Grätzel. Applications of functionalized transition metal complexes in photonic and optoelectronic devices. *Coord. Chem. Rev.*, 177(1):347–414, 1998.

[7] Paul D Beer and James Cadman. Electrochemical and optical sensing of anions by transition metal based receptors. *Coord. Chem. Rev.*, 205(1):131–155, 2000.

[8] Johannes G Vos and John M Kelly. Ruthenium polypyridyl chemistry; from basic research to applications and back again. *Dalton Trans.*, (41):4869–4883, 2006.

[9] Christopher K Prier, Danica A Rankic, and David WC MacMillan. Visible light photoredox catalysis with transition metal complexes: applications in organic synthesis. *Chem. Rev.*, 113(7):5322–5363, 2013.

[10] Danielle M Schultz and Tehshik P Yoon. Solar synthesis: prospects in visible light photocatalysis. *Science*, 343(6174):1239176, 2014.

[11] Jack Twilton, Patricia Zhang, Megan H Shaw, Ryan W Evans, David WC MacMillan, et al. The merger of transition metal and photocatalysis. *Nat. Rev. Chem.*, 1(7):0052, 2017.

[12] Javier J Concepcion, Jonah W Jurss, M Kyle Brennaman, Paul G Hoertz, Antonio Otávio T Patrocinio, Neyde Yukie Murakami Iha, Joseph L Templeton, and Thomas J Meyer. Making oxygen with ruthenium complexes. *Acc. Chem. Res.*, 42(12):1954–1965, 2009.

[13] Derek J Wasylenko, Chelladurai Ganesamoorthy, Bryan D Koivisto, Matthew A Henderson, and Curtis P Berlinguette. Insight into water oxidation by mononuclear polypyridyl ru catalysts. *Inorg. Chem.*, 49(5):2202–2209, 2010.

[14] James H Alstrum-Acevedo, M Kyle Brennaman, and Thomas J Meyer. Chemical approaches to artificial photosynthesis. 2. *Inorg. Chem.*, 44(20):6802–6827, 2005.

[15] Vincenzo Balzani, Alberto Juris, Margherita Venturi, Sebastiano Campagna, and Scolastica Serroni. Luminescent and redox-active polynuclear transition metal complexes. *Chem. Rev.*, 96(2):759–834, 1996.

[16] Gerrit Boschloo and Anders Hagfeldt. Characteristics of the iodide/triiodide redox mediator in dye-sensitized solar cells. *Acc. Chem. Res.*, 42(11):1819–1826, 2009.

[17] Paola Ceroni, Giacomo Bergamini, and Vincenzo Balzani. Old molecules, new concepts:$[Ru(bipy)_3]^{2+}$ as a molecular encoder–decoder. *Angew.*

Chem. Int. Ed., 48(45):8516–8518, 2009.

[18] Jonathan Martens, Giel Berden, and Jos Oomens. Structures of fluoranthene reagent anions used in electron transfer dissociation and proton transfer reaction tandem mass spectrometry. *Anal. Chem.*, 88(12):6126–6129, 2016.

[19] A Juris, V Balzani, F Barigelletti, S Campagna, P Belser, and A Von Zelewsky. Ru(II) polypyridine complexes: photophysics, photochemistry, eletrochemistry, and chemiluminescence. *Coord. Chem. Rev.*, 84:85–277, 1988.

[20] Sarah E Angell, Yan Zhang, Cerrie W Rogers, Michael O Wolf, and Wayne E Jones. Photophysical properties of Ru(II) bipyridyl complexes containing hemilabile phosphine- ether ligands. *Inorg. Chem.*, 44(21):7377–7384, 2005.

[21] Elaine A Medlycott and Garry S Hanan. Designing tridentate ligands for ruthenium(II) complexes with prolonged room temperature luminescence lifetimes. *Chem. Soc. Rev.*, 34(2):133–142, 2005.

[22] Darius Kuciauskas, Jeremy E Monat, Randy Villahermosa, Harry B Gray, Nathan S Lewis, and James K McCusker. Transient absorption spectroscopy of ruthenium and osmium polypyridyl complexes adsorbed onto nanocrystalline TiO_2 photoelectrodes. *J. Phys. Chem. B*, 106(36):9347–9358, 2002.

[23] Del Guerzo, Stéphanie Leroy, Frédéric Fages, and Russell H Schmehl. Photophysics of Re(I) and Ru(II) diimine complexes covalently linked to pyrene: contributions from intra-ligand charge transfer states. *Inorg. Chem.*, 41(2):359–366, 2002.

[24] Xian-Yong Wang, Andre Del Guerzo, Hari Tunuguntla, and Russell H Schmehl. Photophysical behavior of Ru (II) and Os (II) terpyridyl phenylene vinylene complexes: perturbation of MLCT state by intra-ligand charge-transfer state. *Res. Chem. Intermed.*, 33(1-2):63–77, 2007.

[25] Alvin T Yeh, Charles V Shank, and James K McCusker. Ultrafast electron localization dynamics following photo-induced charge transfer. *Science*, 289(5481):935–938, 2000.

[26] Qinchao Sun, Bogdan Dereka, Eric Vauthey, Latévi M Lawson Daku, and Andreas Hauser. Ultrafast transient IR spectroscopy and DFT calculations of ruthenium (II) polypyridyl complexes. *Chem. Sci.*, 8(1):223–230, 2017.

[27] M Khaja Nazeeruddin, Amin Kay, Ignacio Rodicio, Robin Humphry-Baker, E Müller, Petr Liska, Nick Vlachopoulos, and M Grätzel. Conversion of light to electricity by cis-X_2bis (2, 2′-bipyridyl-4, 4′-dicarboxylate) ruthenium (II) charge-transfer sensitizers (X= Cl^-, Br^-, I^-, CN^-, and SCN^-) on nanocrystalline titanium dioxide electrodes. *J. Am. Chem. Soc.*, 115(14):6382–6390, 1993.

[28] Helmut Tributsch. Dye sensitization solar cells: a critical assessment of the learning curve. *Coord. Chem. Rev.*, 248(13-14):1511–1530, 2004.

[29] R Grünwald and H Tributsch. Mechanisms of instability in Ru-based dye sensitization solar cells. *J. Phys. Chem. B*, 101(14):2564–2575, 1997.

[30] Ravi Harikisun and Hans Desilvestro. Long-term stability of dye solar cells. *Sol. Energy*, 85(6):1179–1188, 2011.

[31] Paolo G Bomben, Kiyoshi CD Robson, Pavel A Sedach, and Curtis P Berlinguette. On the viability of cyclometalated Ru (II) complexes for light-harvesting applications. *Inorg. Chem.*, 48(20):9631–9643, 2009.

[32] Bryan D Koivisto, Kiyoshi CD Robson, and Curtis P Berlinguette. Systematic manipulation of the light-harvesting properties for tridentate cyclometalated ruthenium(II) complexes. *Inorg. Chem.*, 48(20):9644–9652, 2009.

[33] Takeru Bessho, Eiji Yoneda, Jun-Ho Yum, Matteo Guglielmi, Ivano Tavernelli, Hachiro Imai, Ursula Rothlisberger, Mohammad K Nazeeruddin, and Michael Grätzel. New paradigm in molecular engineering of sensitizers for solar cell applications. *J. Am. Chem. Soc.*, 131(16):5930–5934, 2009.

[34] Paolo G Bomben, Bryan D Koivisto, and Curtis P Berlinguette. Cyclometalated Ru complexes of type $[Ru^{II} (N^{\wedge}N)_2(C^{\wedge}N)]^z$: physicochemical response to substituents installed on the anionic ligand. *Inorg. Chem.*, 49(11):4960–4971, 2010.

[35] Paolo G Bomben, Kim D Thériault, and Curtis P Berlinguette. Strategies for Optimizing the Performance of Cyclometalated Ruthenium Sensitizers for Dye-Sensitized Solar Cells. *Eur. J. Inorg. Chem.*, 2011(11):1806–1814, 2011.

[36] Kiyoshi CD Robson, Barbora Sporinova, Bryan D Koivisto, Eduardo Schott, Douglas G Brown, and Curtis P Berlinguette. Systematic modulation of a bichromic cyclometalated ruthenium (II) scaffold bearing a redox-active triphenylamine constituent. *Inorg. Chem.*, 50(13):6019–6028,

2011.

[37] Kiyoshi CD Robson, Bryan D Koivisto, Aswani Yella, Barbora Sporinova, Mohammad K Nazeeruddin, Thomas Baumgartner, Michael Grätzel, and Curtis P Berlinguette. Design and development of functionalized cyclometalated ruthenium chromophores for light-harvesting applications. *Inorg. Chem.*, 50(12):5494–5508, 2011.

[38] Sipke H Wadman, Jan M Kroon, Klaas Bakker, Martin Lutz, Anthony L Spek, Gerard PM van Klink, and Gerard van Koten. Cyclometalated ruthenium complexes for sensitizing nanocrystalline TiO_2 solar cells. *Chem. Commun.*, (19):1907–1909, 2007.

[39] Paolo G Bomben, Terry J Gordon, Eduardo Schott, and Curtis P Berlinguette. A Trisheteroleptic Cyclometalated Ru(II) Sensitizer that Enables High Power Output in a Dye-Sensitized Solar Cell. *Angew. Chem. Int. Ed.*, 50(45):10682–10685, 2011.

[40] Sipke H Wadman, Martin Lutz, Duncan M Tooke, Anthony L Spek, František Hartl, Remco WA Havenith, Gerard PM van Klink, and Gerard van Koten. Consequences of N, C, N-and C, N, N-coordination modes on electronic and photophysical properties of cyclometalated aryl ruthenium (II) complexes. *Inorg. Chem.*, 48(5):1887–1900, 2009.

[41] Jean Pierre Sauvage, Jean Paul Collin, Jean Claude Chambron, Stephane Guillerez, Christophe Coudret, Vincenzo Balzani, Francesco Barigelletti, Luisa De Cola, and Lucia Flamigni. Ruthenium (II) and osmium (II) bis (terpyridine) complexes in covalently-linked multicomponent systems: synthesis, electrochemical behavior, absorption spectra, and photochemical and photophysical properties. *Chem. Rev.*, 94(4):993–1019, 1994.

[42] Martin Forster and Ronald E Hester. Resonance raman investigation of electronically excited ru (bipyridine)$^{2+}{}_3$ using a cw laser. *Chem. Phys. Lett.*, 81(1):42–47, 1981.

[43] MJP Musgrave and John Anthony Pople. A general valence force field for diamond. *Proc. Royal Soc. Lond.*, 268(1335):474–484, 1962.

[44] Frank Grosse and Jörg Neugebauer. Limits and accuracy of valence force field models for In_x $Ga_{1-x}N$ alloys. *Phys. Rev. B*, 63(8):085207, 2001.

[45] Prabal K Mallick, Gerald D Danzer, Dennis P Strommen, and James R Kincaid. Vibrational spectra and normal-coordinate analysis of tris (bipyridine) ruthenium (II). *J. Phys. Chem.*, 92(20):5628–5634, 1988.

[46] Jennifer M Butler, Michael W George, Jon R Schoonover, Dana M Dattelbaum, and Thomas J Meyer. Application of transient infrared and near infrared spectroscopy to transition metal complex excited states and intermediates. *Coord. Chem. Rev.*, 251(3-4):492–514, 2007.

[47] Jon R Schoonover, Carlo A Bignozzi, and Thomas J Meyer. Application of transient vibrational spectroscopies to the excited states of metal polypyridyl complexes. *Coord. Chem. Rev.*, 165:239–266, 1997.

[48] Tatsuhiko Mukuta, Naoto Fukazawa, Kei Murata, Akiko Inagaki, Munetaka Akita, Sei'ichi Tanaka, Shin-ya Koshihara, and Ken Onda. Infrared vibrational spectroscopy of $[Ru(bpy)_2(bpm)]^{2+}$ and $[Ru(bipy)_3]^{2+}$ in the excited triplet state. *Inorg. Chem.*, 53(5):2481–2490, 2014.

[49] Kristin M Omberg, Jon R Schoonover, Joseph A Treadway, Robert M Leasure, R Brian Dyer, and Thomas J Meyer. Mid-infrared spectrum of $[Ru(bipy)_3]^{2+}$. *J. Am. Chem. Soc.*, 119(30):7013–7018, 1997.

[50] Andrea Cannizzo, Frank van Mourik, Wojciech Gawelda, Goran Zgrablic, Christian Bressler, and Majed Chergui. Broadband femtosecond fluorescence spectroscopy of $[Ru(bipy)_3]^{2+}$. *Angew. Chem. Int. Ed.*, 45(19):3174–3176, 2006.

[51] Ann G Motten, Kenneth Hanck, and M Keith DeArmound. ESR of the reduction products of $[Fe(bipy)_3]^{2+}$ and $[Ru(bipy)_3]^{2+}$. *Chem. Phys. Lett.*, 79(3):541–546, 1981.

[52] Camilla Skinnerup Byskov, J Mathias Weber, and Steen Brøndsted Nielsen. Gas-phase spectroscopy of singly reduced tris (bipyridine) ruthenium ions, $Ru(bipy)_3{}^{+}$. *Phys. Chem. Chem. Phys.*, 17(8):5561–5564, 2015.

[53] MH Stockett and S Brøndsted Nielsen. Communication: Does a single CH_3CN molecule attached to $Ru(bipy)_3{}^{2+}$ affect its absorption spectrum? *J. Chem. Phys.*, 142(17):171102, 2015.

[54] Bryan Mayoh and Peter Day. The excited states of bipyridyl and phenanthroline complexes of Fe(III), Ru(II) and Ru(III): A molecular orbital study. *Theor. Chim. Acta*, 49(3):259–275, 1978.

[55] Francesco Barigelletti, Alberto Juris, Vincenzo Balzani, Peter Belser, and Alex Von Zelewsky. Excited-state properties of complexes of the tris (diimine) ruthenium (2+) ion family. *Inorg. Chem.*, 22(22):3335–3339, 1983.

[56] James Ferguson and Fritz Herren. A model for the interpretation of the electronic spectra of the complex ions $M(bpy)_3{}^{2+}$(M= Fe, Ru, Os) in D3

and C2 sites. *Chem. Phys.*, 76(1):45–59, 1983.

[57] D Paul Rillema, G Allen, TJ Meyer, and D Conrad. Redox properties of ruthenium (II) tris chelate complexes containing the ligands 2, 2′-bipyrazine, 2, 2′-bipyridine, and 2, 2′-bipyrimidine. *Inorg. Chem.*, 22(11):1617–1622, 1983.

[58] Etienne Garand. Spectroscopy of Reactive Complexes and Solvated Clusters: A Bottom-Up Approach Using Cryogenic Ion Traps. *J. Phys. Chem. A*, 122(32):6479–6490, 2018.

[59] Jonathan Martens, Giel Berden, Christoph R Gebhardt, and Jos Oomens. Infrared ion spectroscopy in a modified quadrupole ion trap mass spectrometer at the FELIX free electron laser laboratory. *Rev. Sci. Instrum.*, 87(10):103108, 2016.

[60] Musleh U Munshi, Stephanie M Craig, Giel Berden, Jonathan Martens, Andrew F DeBlase, David J Foreman, Scott A McLuckey, Jos Oomens, and Mark A Johnson. Preparation of labile Ni^+(cyclam) cations in the gas phase using electron-transfer reduction through ion–ion recombination in an ion trap and structural characterization with vibrational spectroscopy. *J. Phys. Chem. Lett.*, 8(20):5047–5052, 2017.

[61] Maj-Britt Suhr Kirketerp and Steen Brøndsted Nielsen. Absorption spectrum of isolated tris (2, 2-bipyridine) ruthenium (II) dications in vacuo. *Int. J. Mass Spectrom.*, 297(1-3):63–66, 2010.

[62] Shuang Xu, James ET Smith, and J Mathias Weber. UV Spectra of Tris (2, 2-bipyridine)–M (II) Complex Ions in Vacuo (M= Mn, Fe, Co, Ni, Cu, Zn). *Inorg. Chem.*, 55(22):11937–11943, 2016.

[63] Shuang Xu and J Mathias Weber. Absorption spectrum of a Ru(II)-aquo complex in vacuo: resolving individual charge-transfer transitions. *J. Phys. Chem. A*, 119(47):11509–11513, 2015.

[64] Jos Oomens, Boris G Sartakov, Gerard Meijer, and Gert Von Helden. Gas-phase infrared multiple photon dissociation spectroscopy of mass-selected molecular ions. *Int. J. Mass Spectrom.*, 254(1-2):1–19, 2006.

[65] Jonathan Martens, Josipa Grzetic, Giel Berden, and Jos Oomens. Structural identification of electron transfer dissociation products in mass spectrometry using infrared ion spectroscopy. *Nat. Commun.*, 7:11754, 2016.

[66] D Oepts, AFG Van der Meer, and PW Van Amersfoort. The free-electron-laser user facility FELIX. *Infrared Phys. Technol.*, 36(1):297–308, 1995.

[67] GMH Knippels and AFG Van Der Meer. FEL diagnostics and user control. *Nucl. Instrum. Methods Phys. Res., Sect. B*, 144(1-4):32–39, 1998.

[68] B Lucas, G Gregoire, J Lemaire, P Maitre, F Glotin, JP Schermann, and C Desfrancois. Infrared multiphoton dissociation spectroscopy of protonated N-acetyl-alanine and alanyl-histidine. *Int. J. Mass Spectrom.*, 243(2):105–113, 2005.

[69] Giel Berden, Mathijs Derksen, Kas J Houthuijs, Jonathan Martens, and Jos Oomens. An automatic variable laser attenuator for IRMPD spectroscopy and analysis of power-dependence in fragmentation spectra. *Int. J. Mass Spectrom.*, 2019.

[70] Chengteh Lee, Weitao Yang, and Robert G Parr. Development of the Colle-Salvetti correlation-energy formula into a functional of the electron density. *Phys. Rev. B*, 37(2):785, 1988.

[71] Axel D Becke. Becke's three parameter hybrid method using the LYP correlation functional. *J. Chem. Phys.*, 98(7):5648–5652, 1993.

[72] Aron J Cohen, Paula Mori-Sánchez, and Weitao Yang. Challenges for density functional theory. *Chem. Rev.*, 112(1):289–320, 2011.

[73] Florian Weigend and Reinhart Ahlrichs. Balanced basis sets of split valence, triple zeta valence and quadruple zeta valence quality for H to Rn: Design and assessment of accuracy. *Phys. Chem. Chem. Phys.*, 7(18):3297–3305, 2005.

[74] Hisayoshi Iikura, Takao Tsuneda, Takeshi Yanai, and Kimihiko Hirao. A long-range correction scheme for generalized-gradient-approximation exchange functionals. *J. Chem. Phys.*, 115(8):3540–3544, 2001.

[75] Roberto Peverati and Donald G Truhlar. Quest for a universal density functional: the accuracy of density functionals across a broad spectrum of databases in chemistry and physics. *Philos. Trans. Royal Soc. A*, 372(2011):20120476, 2014.

[76] Vitaly A Rassolov, Mark A Ratner, John A Pople, Paul C Redfern, and Larry A Curtiss. 6-31g* basis set for third-row atoms. *J. Comput. Chem.*, 22(9):976–984, 2001.

[77] Kirk A Peterson. Systematically convergent basis sets with relativistic pseudopotentials. I. correlation consistent basis sets for the post-d group 13–15 elements. *J. Chem. Phys.*, 119(21):11099–11112, 2003.

[78] Alan E Reed, Robert B Weinstock, and Frank Weinhold. Natural population analysis. *J. Chem. Phys.*, 83(2):735–746, 1985.

[79] MJ Frisch, GW Trucks, HB Schlegel, GE Scuseria, MA Robb, JR Cheeseman, G Scalmani, V Barone, B Mennucci, GA Petersson, et al. Gaussian 09, Revision D.01. *Inc., Wallingford CT*, 2013.

[80] G Te Velde and EJ Baerends. Numerical integration for polyatomic systems. *J. Comput. Phys.*, 99(1):84–98, 1992.

[81] Maurizio Cossi, Nadia Rega, Giovanni Scalmani, and Vincenzo Barone. Energies, structures, and electronic properties of molecules in solution with the C-PCM solvation model. *J. Comput. Chem.*, 24(6):669–681, 2003.

[82] EJ Baerends, DE Ellis, and P Ros. Self-consistent molecular Hartree—Fock—Slater calculations I. The computational procedure. *Chem. Phys.*, 2(1):41–51, 1973.

[83] Aron J Cohen and Nicholas C Handy. Dynamic correlation. *Mol. Phys.*, 99(7):607–615, 2001.

[84] Erik Van Lenthe and Evert Jan Baerends. Optimized Slater-type basis sets for the elements 1–118. *J. Comput. Chem.*, 24(9):1142–1156, 2003.

[85] E van Lenthe, Evert-Jan Baerends, and Jaap G Snijders. Relativistic regular two-component hamiltonians. *J. Chem. Phys.*, 99(6):4597–4610, 1993.

[86] Erik van Lenthe, Andreas Ehlers, and Evert-Jan Baerends. Geometry optimizations in the zero order regular approximation for relativistic effects. *J. Chem. Phys.*, 110(18):8943–8953, 1999.

[87] E v Van Lenthe, JG Snijders, and EJ Baerends. The zero-order regular approximation for relativistic effects: The effect of spin–orbit coupling in closed shell molecules. *J. Chem. Phys.*, 105(15):6505–6516, 1996.

[88] Erik van Lenthe, Evert-Jan Baerends, and Jaap G Snijders. Relativistic total energy using regular approximations. *J. Chem. Phys.*, 101(11):9783–9792, 1994.

[89] NS Rannulu and MT Rodgers. Noncovalent Interactions of Cu^+ with N-Donor Ligands (Pyridine, 4,4-Dipyridyl, 2,2-Dipyridyl, and 1,10-Phenanthroline): Collision-Induced Dissociation and Theoretical Studies. *J. Phys. Chem. A*, 111(18):3465–3479, 2007.

[90] NS Rannulu and MT Rodgers. Noncovalent interactions of Ni^+ with N-donor ligands (pyridine, 4, 4-dipyridyl, 2, 2-dipyridyl, and 1, 10-phenanthroline): collision-induced dissociation and theoretical studies. *J. Phys. Chem. A*, 113(16):4534–4548, 2009.

[91] NS Rannulu and MT Rodgers. Noncovalent Interactions of Zn^+ with

N-Donor Ligands (Pyridine, 4, 4-Dipyridyl, 2, 2-Dipyridyl, and 1, 10-Phenanthroline): Collision-Induced Dissociation and Theoretical Studies. *J. Phys. Chem. A*, 116(5):1319–1332, 2012.

[92] Musleh Uddin Munshi, Giel Berden, Jonathan Martens, and Jos Oomens. Gas-phase vibrational spectroscopy of triphenylamine: the effect of charge on structure and spectra. *Phys. Chem. Chem. Phys.*, 19(30):19881–19889, 2017.

[93] Christopher J Cramer and Donald G Truhlar. Density functional theory for transition metals and transition metal chemistry. *Phys. Chem. Chem. Phys.*, 11(46):10757–10816, 2009.

[94] Yan Zhao and Donald G Truhlar. Density functionals with broad applicability in chemistry. *Acc. Chem. Res.*, 41(2):157–167, 2008.

[95] D Paul Rillema, Daniel S Jones, Clifton Woods, and Henri A Levy. Comparison of the crystal structures of tris heterocyclic ligand complexes of ruthenium (II). *Inorg. Chem.*, 31(13):2935–2938, 1992.

[96] John P Perdew and Alex Zunger. Self-interaction correction to density-functional approximations for many-electron systems. *Phys. Rev. B*, 23(10):5048, 1981.

[97] Amy I Gilson, Guillaume Van Der Rest, Julia Chamot-Rooke, Westin Kurlancheek, Martin Head-Gordon, Denis Jacquemin, and Gilles Frison. Ground electronic state of peptide cation radicals: a delocalized unpaired electron? *J. Phys. Chem. Lett.*, 2(12):1426–1431, 2011.

[98] Claude Daul, Evert J Baerends, and Pieter Vernooijs. A density functional study of the MLCT states of $[ru(bpy)_3]^{2+}$ in d3 symmetry. *Inorg. Chem.*, 33(16):3538–3543, 1994.

[99] Shuang Xu, James ET Smith, Samer Gozem, Anna I Krylov, and J Mathias Weber. Electronic Spectra of Tris (2, 2-bipyridine)-M (II) Complex Ions in Vacuo (M= Fe and Os). *Inorg. Chem.*, 56(12):7029–7037, 2017.

[100] Axel D Becke. Density-functional thermochemistry. III. The role of exact exchange. *J. Chem. Phys.*, 98(7):5648–5652, 1993.

[101] Axel D Becke. A new mixing of Hartree–Fock and local density-functional theories. *J. Chem. Phys.*, 98(2):1372–1377, 1993.

[102] Yihan Shao, Zhengting Gan, Evgeny Epifanovsky, Andrew TB Gilbert, Michael Wormit, Joerg Kussmann, Adrian W Lange, Andrew Behn, Jia Deng, Xintian Feng, et al. Advances in molecular quantum chemistry contained in the Q-Chem 4 program package. *Mol. Phys.*, 113(2):184–215,

2015.

[103] Gabor I Csonka, John P Perdew, and Adrienn Ruzsinszky. Global hybrid functionals: A look at the engine under the hood. *J. Chem. Theory Comput.*, 6(12):3688–3703, 2010.

[104] Markus Reiher, Oliver Salomon, and Bernd Artur Hess. Reparameterization of hybrid functionals based on energy differences of states of different multiplicity. *Theor. Chem. Acc.*, 107(1):48–55, 2001.

[105] Gerrit Moritz, Markus Reiher, and Bernd Artur Hess. Analysis of spin states, spin barriers, and trans-effects involved in the coordination and stabilization of dinitrogen by biomimetic iron complexes. *Theor. Chem. Acc.*, 114(1-3):76–83, 2005.

[106] Takeshi Yanai, David P Tew, and Nicholas C Handy. A new hybrid exchange–correlation functional using the coulomb-attenuating method (CAM-B3LYP). *Chem. Phys. Lett.*, 393(1-3):51–57, 2004.

[107] Latévi Max Lawson Daku, Francesco Aquilante, Timothy W Robinson, and Andreas Hauser. Accurate spin-state energetics of transition metal complexes. 1. CCSD (T), CASPT2, and DFT study of $[\mathrm{M}\ (\mathrm{NCH})_6]^{2+}$(M= Fe, Co). *J. Chem. Theory Comput.*, 8(11):4216–4231, 2012.

Chapter 6

Gas-phase vibrational spectroscopy of triphenylamine: the effect of charge on structure and spectra

6.1 Abstract

The effect of ionization by oxidation and protonation on the structure and IR spectrum of isolated, gas-phase triphenylamine (TPA) has been investigated by infrared multiple photon dissociation (IRMPD) spectroscopy in the fingerprint range from 600 cm^{-1} to 1800 cm^{-1} using an infrared free electron laser. IR spectra calculated using density functional theory (DFT) convincingly reproduce the experimental data. Spectral and structural differences are identified among neutral TPA, $TPA^{\cdot+}$ and protonated TPA and qualitatively related to effects of resonance delocalization. As a consequence of electron delocalization, computed structural parameters for TPA remain virtually unchanged upon removal of an electron. Nonetheless, CC and CN stretching vibrations in the IR spectra of $TPA^{\cdot+}$ undergo a red shift of up to 52 cm^{-1} as compared to those in TPA. Since ionization also strongly influences the relative band intensities, a vibrational projection analysis was used to correlate vibrational modes of TPA with those of $TPA^{\cdot+}$. The experimental IR spectrum of gas-phase protonated

---

Reproduced from Musleh Uddin Munshi, Giel Berden, Jonathan Martens and Jos Oomens, *Phys. Chem. Chem. Phys.* **2017**, 19, 19881-19889 with permission from the PCCP Owner Societies.

TPA indicates that protonation occurs on the nitrogen atom, despite delocalization of the lone electron pair. Upon protonation, the structure changes from the nearly planar geometry to a near-tetrahedral configuration.

6.2 Introduction

Triphenylamine (TPA) is an organic nitrogen-containing compound that can be considered as a derivative of ammonia in which all three hydrogen atoms are substituted by phenyl groups to form a tertiary amine. TPA-based compounds are used in organic light emitting diodes (OLEDs) [1–5], organic field-effect transistors (OFETs) [6], photovoltaics [7], as semiconductors [8], as photoconductors [9–11], as laser dyes [12], and in mechanoluminescent materials [13], because of their high hole-transport properties [14, 15]. In recent years, TPA derivatives have been used in dye-sensitized solar cells (DSSCs) for the photovoltaic conversion of sunlight into electricity [16–24]. TPA moieties (one or multiple units) are used as electron donors and as an additional chromophore when attached to a dye molecule, increasing the electron donating ability and enhancing charge separation, in order to increase the photo-energy conversion [21–26].

The structure and properties of neutral TPA have been thoroughly studied. Contrary to aliphatic amines, TPA has a very low basicity [27] because of resonance delocalization of its lone pair of electrons throughout the entire structure [28]. Unlike ammonia, the three N–C bonds lie in the same plane due to resonance delocalization as depicted in Figure 6.1(b). Such a structure is not necessarily obvious because of the resulting steric hindrance between the phenyl groups. This causes the molecule to adopt a propeller-like structure with the phenyl groups being tilted by more than 40° reducing the overlap between the nitrogen lone-pair p-orbital and the phenyl p-orbitals. The propeller-like geometry avoids molecular aggregation and allows solvent molecules to penetrate effectively. The spectroscopic properties of neutral TPA have been extensively investigated by both theory and experiment in the gas phase using a variety of techniques including (rotationally resolved) laser induced fluorescence (LIF) [29] and gas-phase electron diffraction [30, 31], as well as in condensed phases using crystallography [32] and FTIR absorption spectroscopy in an argon matrix [33]. Experimental UV-VIS absorption spectra of TPA in EtOH were also reported along with theoretical calculations [34]. An experimental

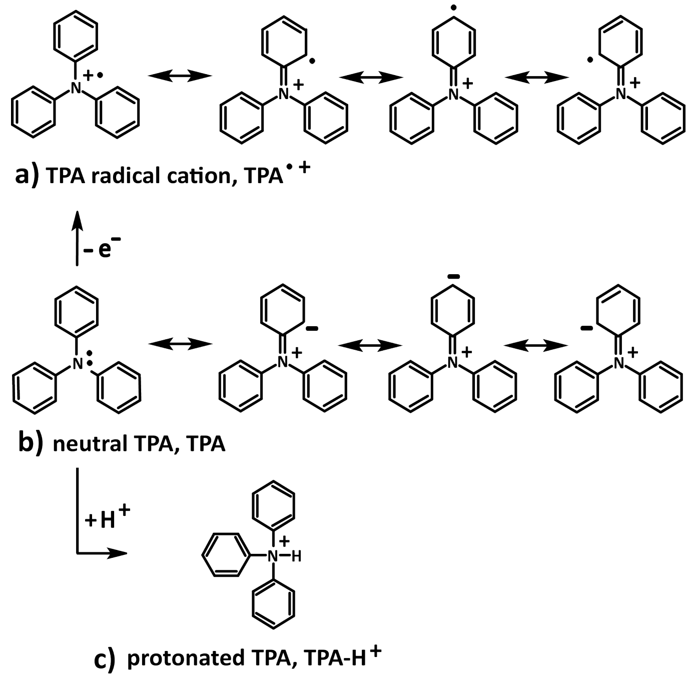

Figure 6.1. Resonance structures for (a) TPA$^{\cdot +}$, (b) neutral TPA. No analogous resonance structures are possible for protonated TPA (c). The resonance hybrid of TPA/TPA$^{\cdot +}$ is a combination of the all possible resonance structures.

gas-phase IR absorption spectrum of neutral TPA is available from the NIST WebBook [35].

The TPA radical cation has received far less attention. In 1979, Duke et al. reported on ultraviolet photoelectron spectroscopy (UPS) of the radical cation both in condensed phases and in the gas phase [36]. They concluded that while the condensedphase structure of the radical is very similar to that of the neutral species, the gas-phase structure of the radical is almost planar. More recently, theoretical investigations of its vibronic coupling constants have been reported in order to explain the favorable hole-transport properties of triphenyl-based molecules [37].

Here, we report gas-phase infrared spectra for the TPA radical cation (TPA$^{\cdot +}$) and protonated TPA (TPA-H^{+}). These spectra are compared to the IR spectrum of the neutral species and to density functional theory (DFT) calculated spectra, which provides detailed information on the structural changes upon oxidation in the gas phase.

6.3 Methods

6.3.1 Experimental

The ions are generated and analyzed in both a home-built Fourier transform ion cyclotron resonance mass spectrometer (FTICR MS) [38, 39] and in a modified commercial quadrupole ion trap (QIT) mass spectrometer [40, 41]. Fingerprint infrared multi-photon dissociation (IRMPD) spectra were recorded for the mass-selected ions by monitoring the wavelength-dependent photofragmentation yield induced by the infrared irradiation from the Free Electron Laser for Infrared eXperiments (FELIX) [42, 43].

In the FTICR MS, $TPA^{\cdot+}$ ions were generated from an approximately 1 mM solution of TPA in methanol using an electrospray ionization source (Z-Spray, Micromass, UK). Ions were accumulated for 7–8 seconds in a linear hexapole before being injected into the ICR cell through an electrostatic quadrupole deflector and an rf octopole ion guide. The TPA ion of interest was isolated using a stored waveform inverse Fourier transform (SWIFT) excitation pulse [44] and subsequently irradiated for 5–6 seconds by the infrared FEL radiation from FELIX operating at a repetition rate of 10 Hz, producing 6 ms long macropulses with energies of 30 to 60 mJ having a bandwidth of approximately 0.4% of the centre frequency. When the frequency of the laser is resonant with a vibrational band of the ion, absorption of multiple photons occurs and results in an increase in internal energy, finally leading to unimolecular dissociation [39, 45].

$TPA^{\cdot+}$ ions studied here are comparatively difficult to dissociate with the infrared FEL radiation alone. To enhance the IR-induced dissociation, the ions were post-excited using 5 ms of irradiation from a continuous wave CO_2-laser (10.6 mm, 30 W) directly after each FEL pulse [46]. After the interaction of the ions with the IR light, a mass spectrum of the ion population in the ICR cell is obtained from an excite-detect procedure described in detail elsewhere [44]. The infrared frequency dependent fragmentation yield, defined as $\sum(\text{fragments})/\sum(\text{precursor} + \text{fragments})$, obtained from 2 summed mass spectra, is plotted as a function of laser frequency in order to provide the infrared spectrum of the ion. The yield was corrected linearly for frequency dependent variations in laser pulse energy. Spectra were recorded from 600 to 1800 cm^{-1} (fingerprint region) with a 5 cm^{-1} step size. The wavelength of the FEL was calibrated using a grating spectrometer.

In the QIT (Bruker, AmaZon Speed ETD, Bremen, Germany), $TPA^{\cdot+}$ and (TPA-H^+) ions were generated via electrospray ionization of ∼1 μM solutions of TPA in acetonitrile/water (1 : 1 ratio). If required, 0.1% of formic acid was added to enhance protonation. At every IR frequency step, the ions were irradiated with the FEL for 0.2–1 s and 3/5-fold averaged mass spectra were stored. No CO_2 laser was used to enhance the dissociation induced by the IR FEL, however the helium pressure in the QIT was reduced in order to reduce collisional de-excitation and hence enhance IR-induced dissociation [40].

6.3.2 Computational modeling

Quantum-chemical calculations at the DFT level were performed to aid in structural and vibrational assignments, using the Gaussian 09 revision D 01 [47] software package. Although TPA is known to posses C3 symmetry [29], no symmetry constraints were imposed in the calculations. Hybrid [48] B3LYP/6-31++G(d,p) and gradient corrected [49, 50] BLYP/cc-pVTZ levels of theories were employed (for consistency purposes only). Harmonic frequencies were computed for the optimized geometry of the molecules. Computed harmonic frequencies were scaled by a factor of 0.975 for the B3LYP/6-31++G(d,p) level (which was found to give the best match for many experimental IRMPD spectra [41, 51], and 0.997 [52] for the BLYP/cc-pVTZ level to account for anharmonicity and basis set incompleteness. All calculated linear IR spectra were convoluted using a 20 cm^{-1} FWHM Gaussian line shape function for comparison with experimental IR spectra. Additionally, single point energy calculations were performed at the MP2(full)/6-311+G(2d,2p) level of theory for all tautomers of protonated TPA (including ortho, meta and para-protonated) to assess their relative stability. Their relative Gibbs free energies and gas-phase proton affinities (PA) at 298.15 K are computed at the MP2(full)/6-311+G(2d,2p) level of theory where zero-point energies are taken from frequency calculation at B3LYP/6-31++G(d,p) level of theory. Charge and bonding properties in the molecule were computationally investigated by natural population analysis (NPA) and natural bond orbital (NBO) analysis as implemented in Gaussian09. Finally, B3LYP/6-31++G(d,p) harmonic frequencies of $TPA^{\cdot+}$ and TPA were employed in a vibrational projection analysis (ViPA) [53, 54] in order to quantitatively identify the similarities of the normal mode characters between $TPA^{\cdot+}$ and TPA.

6.4 Results and discussion

The gas-phase IR spectrum of neutral TPA is taken from the NIST WebBook and is shown in Figure 6.2. The experimental IRMPD spectrum of TPA$^{\cdot+}$ (*m/z* 245) was measured in both the FTICR MS and the QIT MS (see Figure 6.4 a-c). Upon IRMPD, the main fragmentation product was found at *m/z* 244, corresponding to the loss of atomic hydrogen. Additionally, a minor fragment with *m/z* 166 was observed and is attributed to the subsequent loss of a benzene ring from the *m/z* 244 ion. The IRMPD spectra of TPA$^{\cdot+}$ taken in the FTICR and QIT agree well, where the spectrum taken without helium gas in QIT more closely mimics the IR spectrum measured in the FTICR (Figure 6.4). At higher (standard) helium gas pressures in the QIT, collisional deactivation competes with dissociation, reducing the observed fragmentation yield [40].

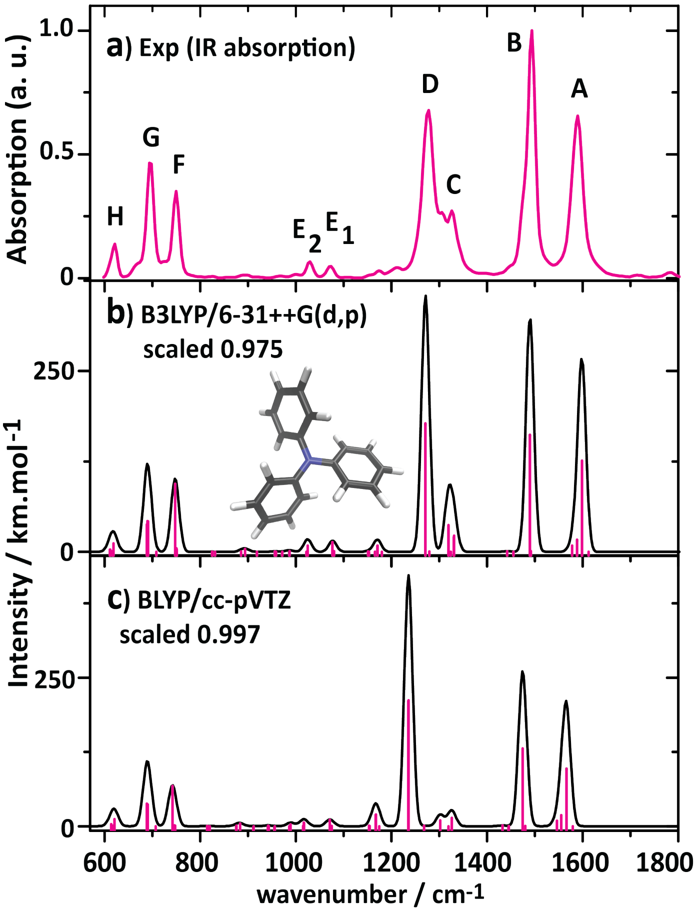

Figure 6.2. Experimental IR absorption spectra of neutral TPA [35] (a), along with the calculated IR spectra at the B3LYP/6-31++G(d,p) (b) and BLYP/ cc-pVTZ (c) levels of theory. The optimised structure is shown in panel (b). Experimental IR bands are labelled from A to H for assignments given in Table 6.1.

In the FTICR, no IR photodissociation of TPA-H$^+$ could be observed. The infrared spectrum of TPA-H$^+$ shown in Figure 6.5(a) was measured in the QIT. Photodissociation yields under 'regular' experimental conditions were very low due to the high stability of protonated TPA for IR photodissociation. In order to be able to record the IRMPD spectrum shown in Figure 6.5, TPA-H$^+$ ions had to be irradiated with 10 macro pulses of the FEL without helium gas in the ion trap. IRMPD fragments of TPA-H$^+$ (*m/z* 246) were found at *m/z* 169 and 92, representing the loss of one and two phenyl groups respectively.

The well-known propeller-like structure of TPA is reproduced by our calculations (see rotational constants in Table E.1); bond lengths and bond angles are given in Table 6.2, and agree well with experiment [29, 31]. Note that the B3LYP CC and CN bond lengths match the experimental values better than BLYP values, which typically provides larger values for these bonds compared to B3LYP [55]. The torsional angle denoted as φ of TPA is well estimated by both levels of theory (within $\sim 3^\circ$).

Inspection of the highest occupied molecular orbital (HOMO) (Figure 6.3) suggests that the lone pair electrons on the nitrogen atom are highly delocalized throughout the structure due to conjugation as also suggested by the resonant Lewis structures in Figure 6.1(b) [56]. In addition to the N-atom, the HOMO has high amplitudes at the phenyl carbon atoms in ortho and para positions, while much less on the meta positions, indeed as suggested by the Lewis structures in Figure 6.1(b). On the other hand, the partial double bond character of the N–C bonds is not obvious since the phenyl rings are twisted by more than 40° reducing the overlap between the nitrogen lone-pair orbital and the phenyl π-orbitals. Indeed, an NBO calculation does not recognize any π-bonds between the nitrogen and the adjacent C-atoms.

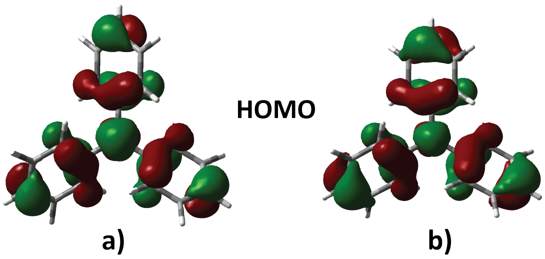

Figure 6.3. HOMO of TPA (a) and its radical cation (b) shown at an isosurface value of 0.03.

6.4.1 Spectroscopy and structure of TPA radical cation

TPA$^{\cdot+}$ has a structure very similar to its neutral counterpart. Table 6.2 compares structural parameters calculated in the present study with values that have been reported in the literature. We note that values reported in ref. [57] (from 1979) used an empirical pseudopotential model (CNDO/S3 model) [57] to mimic gas-phase UPS data. Their reported value for the torsional angle is 29° lower than our B3LYP/6-31++G(d,p) and BLYP/cc-pVTZ values (φ = 39°). Average bond lengths for the CN and CC bonds appear not to change upon ionization by amounts that could be considered significant. The torsional angles of the phenyl rings appear to undergo the largest change, although the 2°-3° change in the direction of a flattening of the ion is very marginal indeed. These computed structures thus suggest that the effects of the removal of an electron are smeared out over the entire molecule to an extent that they become unnoticeable.

The IRMPD spectrum of TPA$^{\cdot+}$ shown in Figure 6.4 is closely reproduced by theory showing maximum deviations between theoretical and experimental vibrational frequencies of only 10 cm^{-1}. For instance, considering the phenyl ring and CN stretching modes experimentally found at 1548 cm^{-1} (band I) are computed exactly at 1548 cm^{-1} by the BLYP/cc-pVTZ method (Table 6.1). This suggests that the effects of resonance delocalization on the vibrational frequencies – and hence on the force constants – are well reproduced by theory. Some of the predicted bands with low intensities remain unobserved, even with the maximum laser power settings, likely because at these frequencies the ions cannot be energized to exceed the dissociation threshold.

The experimental IR bands have been labelled and assigned with an approximate mode description inferred from the computed normal modes (Table 6.1). In the case of TPA$^{\cdot+}$, bands I through K show dominant phenyl ring and C–N stretching character, similar to neutral TPA. To determine the similarities of the normal modes between TPA$^{\cdot+}$ and TPA, we employed a vibrational projection analysis (ViPA) [53, 54], designed for quantitative comparisons between similar systems. ViPA treats the set of normal modes of the considered individual systems as simple vectors; taking the dot product of each of the modes of TPA$^{\cdot+}$ (object molecule) with each of the vectors of the basis molecule TPA then relates their normal modes. We use this relation to compare normal mode frequencies between the neutral and radical cationic system.

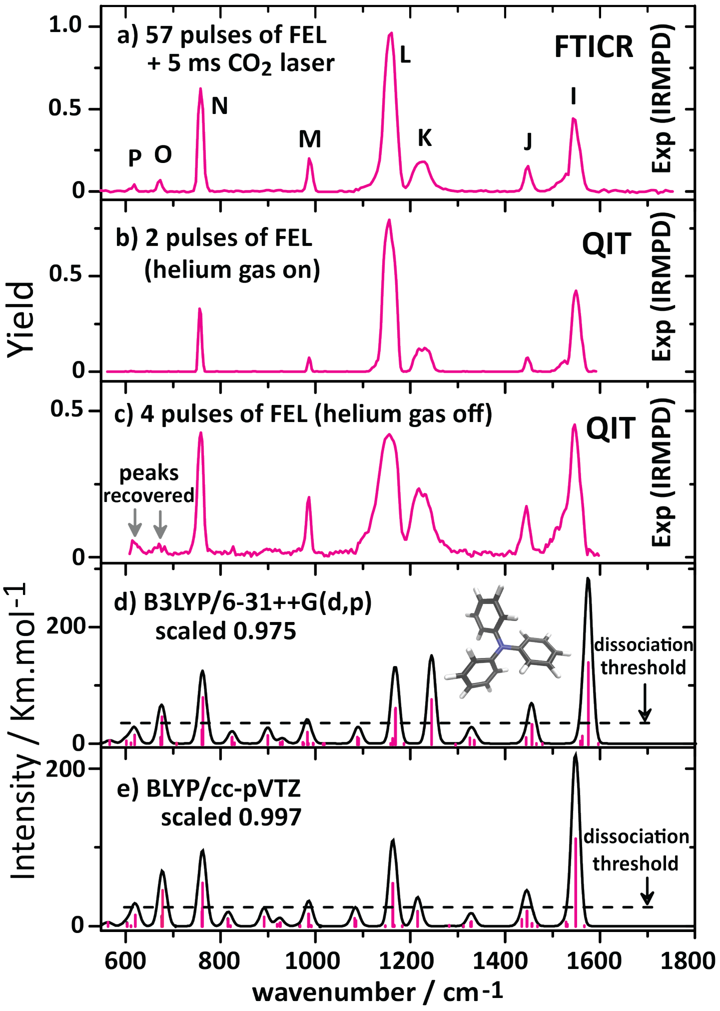

Figure 6.4. IRMPD spectrum of TPA$^{\cdot+}$ taken in the FTICR (a), in the QIT with (b) and without (c) buffer gas. Calculated spectra at the B3LYP/6-31++G(d,p) and BLYP/cc-pVTZ levels are shown in panels (d and e). Experimental IR bands are labelled from I to P for assignments in Table 6.1 and the optimised structure is shown in panel (d). The horizontal dotted line indicates an apparent IRMPD cut-off [40].

Substantial changes in band intensities are observed upon ionization, which makes the ViPA analysis essential to correlate bands in TPA and TPA$^{\cdot+}$. For instance, the band of TPA$^{\cdot+}$ computed at 1456 cm^{-1} (band J in Figure 6.4) possesses only 7% mode character of the dominant band of TPA at 1490 cm^{-1} (band B in Figure 6.2). On the contrary, it has 63% similarity to the band at 1456 cm^{-1} which shows almost no intensity in TPA (see Appendix E Figure E.2).

The results of the ViPA analysis are presented in Appendix E Figure E.2. According to this ViPA analysis, the experimental IR band of TPA$^{\cdot+}$ at 1548 cm^{-1} (band I in Figure 6.4) shows 59% similarity with the experimental IR band at

Table 6.1. Experimental vibrational frequencies (in cm^{-1}) of TPA and TPA$^{\cdot+}$ are compared with harmonic frequencies calculated at the B3LYP/ 6-31++G(d,p) and BLYP/cc-pVTZ levels of theory. Labels refer to Figure 6.2 and Figure 6.4. Experimental and theoretical band shifts (Δν in cm^{-1}) of corresponding vibrational modes between TPA and TPA$^{\cdot+}$ are indicated for similar modes. Experimental band widths (FWHM in cm^{-1}) are shown in parentheses. Assignments of the bands are based on the highest intensity (km mol^{-1}) contribution

Exp			B3LYP			BLYP			
TPA	TPA$^{\cdot+}$	Δν	TPA	TPA$^{\cdot+}$	Δν	TPA	TPA$^{\cdot+}$	Δν	assignments[a]
1590(28)A	1548(23)I	42	1599	1575	24	1566	1548	18	R str(s), CN str(w)
1494(22)B			1490			1474			R str, CN str (s), CH bend
	1446(18)J			1456			1445		CNC, CH bend, R str
1327(∼30)C			1319			1326			CNC, CH bend, R twist
1278(25)D	1226(40)K	52	1271	1245	27	1236	1215	21	CN str (s), CH bend
	1160(28)L			1169			1163		CN str(w), CH bend (s)
1074(16)E_1			1077			1072			CH bend
1030(17)E_2			1024			1018			R str
	988(13)M			983			986		R deformation
750(16)F	758(15)N	-8	748	762	-14	742	761	-19	CH oop
696(19)G	672(12)O	24	691	677	14	688	677	11	CH oop
622(18)H	618(10)P	4	619	619	0	621	620	1	CCC bend

[a] R str–phenyl ring stretch; str–stretch; CH bend–in plane CH bending modes; CH oop–CH out of plane bending movement; R deformation–phenyl ring deformation modes; s–strong; w–weak.

1590 cm^{-1} (band A in Figure 6.2) in TPA. We thus infer a shift of 42 cm^{-1} as a consequence of oxidation of TPA. B3LYP/6-31++G(d,p) level of theory predicts a shift of 24 cm^{-1} or this band. Similarly, the band observed at 1278 cm^{-1} in TPA having predominant CN stretching character can be correlated according to the ViPA analysis to the 1226 cm^{-1} band in TPA$^{\cdot+}$ inferring an experimental red-shift of 52 cm^{-1} upon oxidation. These red shifts are generally reproduced in the calculated IR spectra at both the BLYP/cc-pVTZ and B3LYP/6-31++G(d,p) (Table 6.1) levels of theory.

For both neutral TPA and TPA$^{\cdot+}$, the bands in the lower frequency range (800 to 600 cm^{-1}) are mainly related to C–H out of plane bending with the exception of the peak close to 620 cm^{-1} which results from a weak CCC bend. Ionization appears to have little effect on these low frequency bands.

We interpret these down-field shifts of CC and CN stretching bands upon ionization as evidence for the resonance delocalisation in this molecule: removal of an electron from the HOMO reduces the electron density not only on the nitrogen centre but also in the CN and phenyl CC bonds causing a slight reduction in the corresponding force constants. As a consequence, these stretching bands in TPA$^{\cdot+}$ generally appear at lower frequencies relative to those of neutral TPA. The computed decrease of the torsional angles in TPA$^{\cdot+}$ though small, is also a

Table 6.2. Computed bond lengths (Å) and bond angles (°) are compared to experimental (electron diffraction [30, 31]) values for TPA and reported [36] values for $TPA^{\cdot+}$ in the gas phase. Parenthesized vales are standard deviations

	B3LYP/6-31++G(d,p)		BLYP/cc-pVTZ		Experimental	Reported
Parameter	TPA	$TPA^{\cdot+}$	TPA	$TPA^{\cdot+}$	TPA	$TPA^{\cdot+}$
$C\text{-}N_{mean}$	1.422 (0)	1.415 (0)	1.430(0)	1.423 (0)	1.418 (4)/1.42 (0.04)	
$C\text{-}C_{mean}$	1.399(4)	1.401 (9)	1.402(5)	1.404 (10)	1.399(4)/1.392(0.006)	
$C\text{-}H_{mean}$	1.086(1)	1.085 (1)	1.088 (1)	1.087 (1)	1.123 (2)	
			bond and torsion angle (°)			
$\angle CNC_{mean}$	120 (0.02)	120 (0.05)	120 (0.04)	120 (0.02)	119.9 (1)/116 (2)	120 (2)
ϕ_{mean}	42.08 (0.07)	39.25 (0.18)	42 (0.27)	39.67 (0.05)	45.2 (2.0)/47 (5)	10 (3)

consequence of the reduced force constants in the CN bonds (Table 6.2).

For both neutral TPA and $TPA^{\cdot+}$ the bands in the lower frequency range (800 to 600 cm^{-1}) are mainly related to C–H out of plane bending with the exception of the peak close to 620 cm^{-1}) which results from a weak CCC bend. Ionization appears to have little effect on these low frequency bands.

The NBO analysis suggests that the occupancy of the nitrogen lone pair orbital in TPA is only 1.72, where the missing electron density is largely donated into π^* bonds on the phenyl rings, as reflected in the resonance picture in Figure 6.1(b). Upon ionization, the nitrogen lone pair occupancy drops only slightly to 1.46 (α and β spin orbitals added) and about 0.15e is removed from the π-bonds in each of the phenyl rings. Perhaps somewhat counter-intuitive, the NPA analysis places a -0.480e partial charge on the N-atom in TPA, which changes only slightly to -0.27e in the cation. NPA charges on the carbon atoms (with H-atoms summed) in *para*, *meta* and *ortho* positions also change only slightly, from -0.016, +0.013 and -0.003 in the neutral to +0.094, +0.049 and +0.051 in the cation. We conclude that these trends testify of strong charge delocalization resulting in the negligible structural changes upon ionization (Table 6.2). Nonetheless, the vibrational modes involving CC and CN stretching show small but significant red-shifts revealing the general bond weakening upon loss of an electron.

6.4.2 Spectroscopy and protonation site of TPA

It is of interest to consider also the protonated form of TPA. Protonation on the nitrogen atom engages the lone-pair electrons into a σ-bond binding the proton, so that conjugation with the phenyl-ring π-electrons is disrupted. We investigate the effects on the IR spectrum, however, we shall first verify whether protonation indeed occurs on the nitrogen. Since the lone pair electrons are highly delocalised throughout the TPA structure, protonation on the phenyl ring carbon atoms either in the para- or ortho-positions may become competitive with protonation on the N-atom. A previous study suggests that for gas-phase aniline, ring protonation at the ortho or para position is energetically feasible along with N-protonation as confirmed by infrared photodissociation (IRPD) spectroscopy [58]. Our computations predict that despite the low proton affinity (PA) of TPA, the nitrogen atom remains the preferred protonation site, with protonation on the para- and ortho phenyl carbon atoms being disfavoured by 23 and 40 kJ mol^{-1}, respectively (Figure 6.5). Our theoretical energy (enthalpy) of protonation on the N-atom (913.5 kJ mol^{-1}) (see Appendix E Table E.2) is close to the experimental PA (903.7 ± 8.4 kJ mol^{-1}), determined in the gas phase by mass-spectrometric methods [59]. Almost the same PA (908.8 kJ mol^{-1}) is reported by Hunter and Lias [60].

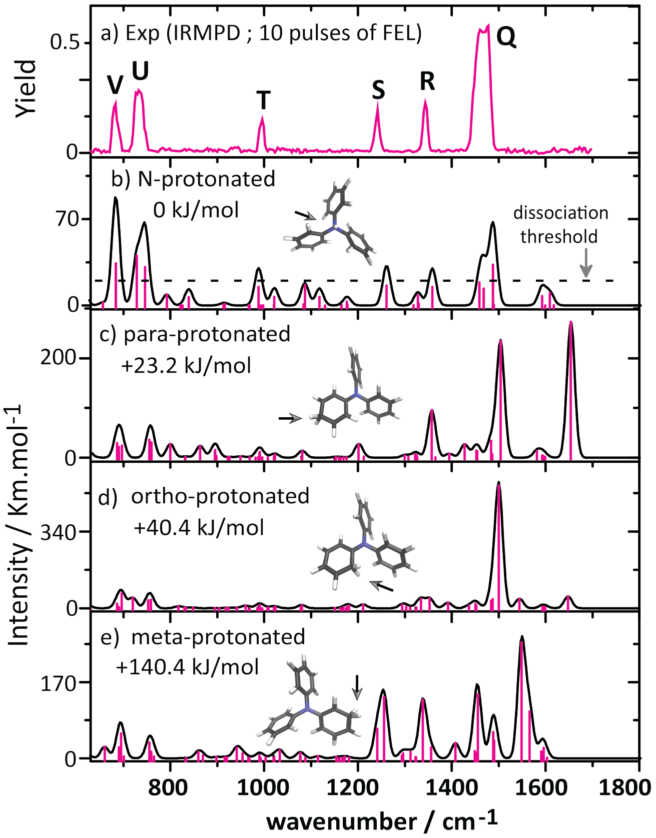

Figure 6.5. IRMPD spectrum recorded in the QIT MS for TPA-H$^+$ without helium buffer gas (a). IR bands are labelled from Q to V for assignments (see Table 6.3). Calculated spectra for the possible protomers are shown in (b–e) with their relative Gibbs free energies. Protonation site is indicated with an arrow. IRMPD spectrum (a) closely matches with the N-protonated isomer (b) which is also the minimum energy structure.

Table 6.3. Experimental vibrational frequencies (in cm^{-1}) of TPA-H^+ compared to theoretical frequencies (scaled) calculated at the B3LYP/6-31++G(d,p) and BLYP/cc-pVTZ levels of theories for the N-protonated isomer only. Values in parentheses are observed spectral bandwidths (FWHM in cm^{-1})

Label	Exp	Theory(DFT)		Assignments[a]
		B3LYP/6-31++G(d,p)	BLYP/cc-pVTZ	
Q[b]	1475(38)	1488	1477	CC str (s), CN str (m), NH bend (s)
	1460	1468	1457	CHip (m), NH bend (s)
		1459	1450	CHip (s)
R	1345(12)	1358	1353	NH bend (s), CNC bend (m)
S	1242(12)	1252	1247	NH bend (s), CNC bend (s), CN bend
T	996(13)	988	991	Ring deformation (s)
U[b]	738(21)	746	741	CH oop (s), CNC bend (m)
	727	728	724	CH oop (s), CNC bend (m)
V	683(14)	683	687	CH oop bend (m)

[a] CC str – CC stretch of the phenyl rings; str – stretch; ip – in-plane bending mode; ring deformation – phenyl ring deformation; oop – out of plane; s – strong band; m – medium band. [b] Bands consist of two unresolved absorptions with almost equal intensity, which is confirmed by the computed spectra.

Figure 6.5(a) presents the fingerprint IRMPD spectrum of TPA-H^+. The calculated IR spectrum for N-protonated TPA agrees well with all bands observed in the experimental IRMPD spectrum. Again, the lower-intensity IR bands remain unobserved in the experiment presumably because at these frequencies the ion cannot be energized to exceed the dissociation threshold. The IR bands are labelled, assigned and compared in Table 6.3.

The IR feature at the high-frequency end of the scan range, labelled as Q in Figure 6.5, has two maxima centred at 1475 and 1460 cm^{-1} and the corresponding calculated values are within $\sim$10 cm^{-1}. The normal modes involve mainly the CC stretch (ring stretch) and NH bending, the latter being particularly characteristic for N-protonated TPA-H^+.

Computed IR spectra of ring protonated TPA isomers do not match the experimental IRMPD spectrum (see Figure 6.5). The predicted spectrum for the ortho protonated isomer exhibits basically only one strong band (near 1500 cm^{-1}), which happens to coincide with a strong band in the experimental spectrum, so that we cannot definitively exclude a partial contribution of this isomer to the ion population. However, based on the close match between the experimental and theoretical spectra of the N-protonated isomer and the computed thermodynamics, the presence of the ortho-protonated species is unlikely.

Table 6.4 lists computed structural parameters for N-protonated TPA. The CNC bond angle is found to be approximately 114°, confirming, as expected, the

Table 6.4. Bond lengths (Å) and bond angles (°) of N-protonated TPA have been calculated at the B3LYP/6-31++G(d,p) and BLYP/cc-pVTZ level of theories. Parenthesized vales are standard deviations

	Theory(DFT)	
Parameter	B3LYP/6-31++G(d,p)	BLYP/cc-pVTZ
C-C	1.396 (2)	1.398 (3)
C-N	1.506 (0)	1.506 (0)
C-H	1.085 (1)	1.087 (3)
N-H	1.025 (0)	1.028 (0)
Bond angles(°)		
∠HNC	104.3 (0)	104.1 (0)
∠CNC	114.1 (0)	114.2 (0.1)

more tetrahedral arrangement of ligands around the nitrogen atom as compared to the neutral and radical cation forms of TPA. Moreover, the C–N bond lengths are significantly longer in TPA-H^+, testifying of the disrupted conjugation between the N-atom and the phenyl ligands and their inherent purely single-bond character.

6.5 Conclusions

Structural characterization and in particular the effects of resonance delocalization in TPA and its ionized forms (radical cation and protonated) have been investigated by IR spectroscopy in the gas phase and quantum-chemical (DFT) calculations.Due to the complete delocalization of the HOMO in the conjugated TPA system, one might expect all CC and CN bond lengths to increase upon ionization of the molecule. However, computed bond lengths are only marginally increased, within what can probably be considered the computational accuracy. Apparently, the strong delocalization causes the effect on each individual bond length to be minimal. On the other hand, vibrational frequencies of the normal modes having predominantly CN and CC stretching character are predicted to undergo a slight red shift upon ionization. The experimental IR spectrum of the gaseous TPA radical cation recorded here confirms these predictions.The experimental IRMPD spectrum and the calculated linear absorption spectrum are generally in excellent agreement.

The strong resonance delocalization also causes the proton affinity of TPA to be strongly reduced in comparison with non-conjugated tertiary amines. It is nonetheless possible to generate protonated TPA in our MS and its IR spectrum was also recorded. The spectrum confirms that despite the relatively low PA, protonation occurs on the nitrogen atom resulting in a near-tetrahedral geometry at the N-centre.

References

[1] Wang-Lin Yu, Jian Pei, Wei Huang, and Alan J Heeger. A novel triarylamine-based conjugated polymer and its unusual light-emitting properties. *Chem. Commun.*, (8):681–682, 2000.

[2] Jian Ping Chen, Hiroshi Tanabe, Xiao-Chang Li, Travis Thoms, Yoshimasa Okamura, and Kazunori Ueno. Novel organic hole transport material with very high tg for light-emitting diodes. *Synth. Met.*, 132(2):173–176, 2003.

[3] D Troadec, G Veriot, and A Moliton. Blue light emitting diodes with bathocuproine layer. *Synth. Met.*, 127(1-3):165–168, 2002.

[4] Tetsuya Noda and Yasuhiko Shirota. A blue-emitting organic electroluminescent device using a novel emitting amorphous molecular material. *J. Lumin.*, 87:1168–1170, 2000.

[5] Chang-Sik Ha, Jung-Ho Shin, Hyuntaek Lim, and Won-Jei Cho. Characterization of organic electroluminescent devices introducing fluorine-containing polyimide to hole-transporting layer. *Mater. Sci. Eng., B*, 85(2-3):195–198, 2001.

[6] Amanda R Murphy and Jean MJ Frechet. Organic semiconducting oligomers for use in thin film transistors. *Chem. Rev.*, 107(4):1066–1096, 2007.

[7] Tzu-Chau Lin, Yong-Fu Chen, Chia-Ling Hu, and Cheng-Sheng Hsu. Two-photon absorption and optical power limiting properties in femtosecond regime of novel multi-branched chromophores based on tri-substituted olefinic scaffolds. *J. Mater. Chem.*, 19(38):7075–7080, 2009.

[8] J Steiger, R Schmechel, and H Von Seggern. Energetic trap distributions in organic semiconductors. *Synth. Met.*, 129(1):1–7, 2002.

[9] RA Holroyd, JM Preses, EH Boettcher, and WF Schmidt. Photoconductivity induced by single-photon excitation of aromatic molecules in liquid hydrocarbons. *J. Phys. Chem.*, 88(4):744–749, 1984.

[10] Jolita Ostrauskaite, Haridas R Karickal, André Leopold, Dietrich Haarer, and Mukundan Thelakkat. Poly [bis (triphenylamine) ether] s with low glass transition temperatures as photoconductors in fast photorefractive systems. *J. Mater. Chem.*, 12(1):58–64, 2002.

[11] Yoshiaki Yasuda, Takuya Kamiyama, and Yasuhiko Shirota. Ionic conductivities of low molecular-weight organic gels and their application as electrochromic materials. *Electrochim. Acta*, 45(8-9):1537–1541, 2000.

[12] W Holzer, Alfons Penzkofer, H-H Hörhold, D Raabe, and M Helbig. Photo-physical and lasing characterization of an aromatic diamine-xylylene copolymer. *Opt. Mater.*, 15(3):225–235, 2000.

[13] BP Chandra. Piezo-Induced Mechanoluminescence and Photoluminescence of Triphenylamine Crystals. *Indian journal of pure and applied physics. New Delhi*, 18(10), 1980.

[14] Jens Cremer and Christoph A Briehn. Novel highly fluorescent triphenylamine-based oligothiophenes. *Chem. Mater.*, 19(17):4155–4165, 2007.

[15] DC Hoesterey and GM Letson. Hole Photoconductivity in Ferrocene, Triphenylamine, and Trans-Stilbene. *J. Chem. Phys.*, 41(3):675–679, 1964.

[16] Anders Hagfeldt, Gerrit Boschloo, Licheng Sun, Lars Kloo, and Henrik Pettersson. Dye-sensitized solar cells. *Chem. Rev.*, 110(11):6595–6663, 2010.

[17] Congbin Fan, Changqing Ye, Xiaomei Wang, Zhigang Chen, Yuyang Zhou, Zuoqin Liang, and Xutang Tao. Synthesis and electrochromic properties of new terpyridine–triphenylamine hybrid polymers. *Macromolecules*, 48(18):6465–6473, 2015.

[18] Yuancheng Qin and Qiang Peng. Ruthenium sensitizers and their applications in dye-sensitized solar cells. *Int. J. Photoenergy*, 2012, 2012.

[19] Jun-Ho Yum, Etienne Baranoff, Sophie Wenger, Md K Nazeeruddin, and Michael Grätzel. Panchromatic engineering for dye-sensitized solar cells. *Energy Environ. Sci.*, 4(3):842–857, 2011.

[20] Kiyoshi CD Robson, Bryan D Koivisto, Aswani Yella, Barbora Sporinova, Mohammad K Nazeeruddin, Thomas Baumgartner, Michael Grätzel, and Curtis P Berlinguette. Design and development of functionalized cyclometalated ruthenium chromophores for light-harvesting applications. *Inorg. Chem.*, 50(12):5494–5508, 2011.

[21] Kohjiro Hara, Tadatake Sato, Ryuzi Katoh, Akihiro Furube, Toshitada Yoshihara, Miki Murai, Mitsuhiko Kurashige, Shunichiro Ito, Akira Shinpo, Sadaharu Suga, et al. Novel conjugated organic dyes for efficient dye-sensitized solar cells. *Adv. Funct. Mater.*, 15(2):246–252, 2005.

[22] Zhong-Sheng Wang, Nagatoshi Koumura, Yan Cui, Masabumi Takahashi, Hiroki Sekiguchi, Atsunori Mori, Toshitaka Kubo, Akihiro Furube, and

Kohjiro Hara. Hexylthiophene-functionalized carbazole dyes for efficient molecular photovoltaics: tuning of solar-cell performance by structural modification. *Chem. Mater.*, 20(12):3993–4003, 2008.

[23] Takuya Dentani, Yasuhiro Kubota, Kazumasa Funabiki, Jiye Jin, Tsukasa Yoshida, Hideki Minoura, Hidetoshi Miura, and Masaki Matsui. Novel thiophene-conjugated indoline dyes for zinc oxide solar cells. *New J. Chem.*, 33(1):93–101, 2009.

[24] Lu Zhang, Yongkang Liu, Zhongyuan Wang, Mao Liang, Zhe Sun, and Song Xue. Synthesis of sensitizers containing donor cascade of triarylamine and dimethylarylamine moieties for dye-sensitized solar cells. *Tetrahedron*, 66(18):3318–3325, 2010.

[25] Haining Tian, Xichuan Yang, Jingxi Pan, Ruikui Chen, Ming Liu, Qingyu Zhang, Anders Hagfeldt, and Licheng Sun. A triphenylamine dye model for the study of intramolecular energy transfer and charge transfer in dye-sensitized solar cells. *Adv. Funct. Mater.*, 18(21):3461–3468, 2008.

[26] K Kalyanasundaram and M Grätzel. Applications of functionalized transition metal complexes in photonic and optoelectronic devices. *Coord. Chem. Rev.*, 177(1):347–414, 1998.

[27] Touraj Manifar and Sohrab Rohani. Synthesis and analysis of triphenylamine: a review. *Can. J. Chem. Eng.*, 82(2):323–334, 2004.

[28] Ivari Kaljurand, Roman Lilleorg, Algis Murumaa, Masaaki Mishima, Peeter Burk, Ivar Koppel, Ilmar A Koppel, and Ivo Leito. The basicity of substituted N, N-dimethylanilines in solution and in the gas phase. *J. Phys. Org. Chem.*, 26(2):171–181, 2013.

[29] Gerard Meijer, Giel Berden, W Leo Meerts, Heinrich E Hunziker, Mattanjah S de Vries, and H Russell Wendt. Spectroscopy on triphenylamine and its van der waals complexes. *Chem. Phys.*, 163(2):209–222, 1992.

[30] Yasushi Sasaki, Katsumi Kimura, and Masaji Kubo. Electron diffraction investigation of triphenylamine. *J. Chem. Phys.*, 31(2):477–481, 1959.

[31] VA Naumov, S Samdal, AV Naumov, S Gundersen, and HV Volden. Molecular structure of triphenylamine in the gas phase. *Russ. J. Gen. Chem.*, 75(12):1956–1961, 2005.

[32] AN Sobolev, VK Belsky, IP Romm, N Yu Chernikova, and EN Guryanova. Structural investigation of the triaryl derivatives of the group V elements. IX. structure of triphenylamine, $C_{18}H_{15}N$. *Acta Crystallogr. C*, 41(6):967–971, 1985.

[33] Igor Reva, Leszek Lapinski, Nitin Chattopadhyay, and Rui Fausto. Vibrational spectrum and molecular structure of triphenylamine monomer: A combined matrix-isolation FTIR and theoretical study. *Phys. Chem. Chem. Phys.*, 5(18):3844–3850, 2003.

[34] Michinori Sumimoto, Daisuke Yokogawa, Masahiro Komeda, Hidetoshi Yamamoto, Kenji Hori, and Hitoshi Fujimoto. Theoretical investigation of the molecular structures and excitation spectra of triphenylamine and its derivatives. *Spectrochim. Acta, Part A*, 81(1):653 – 660, 2011.

[35] ed. P. J. Linstrom and W. G. Mallard. NIST chemistry webbook, NIST standard reference database number 69, national institute of standards and technology, gaithersburg MD, 20899 (accessed May 3, 2015).

[36] C.B. Duke, J.W.-P. Lin, A. Paton, W.R. Salaneck, and K.L. Yip. The geometry of cation radicals: The structure of triphenylamine in the condensed versus the vapor phase. *Chem. Phys. Lett.*, 61(2):402 – 406, 1979.

[37] Katsuyuki Shizu, Tohru Sato, Kazuyoshi Tanaka, and Hironori Kaji. Electron–vibration interactions in triphenylamine cation: Why are triphenylamine-based molecules good hole-transport materials? *Chem. Phys. Lett.*, 486(4-6):130–136, 2010.

[38] Jose J Valle, John R Eyler, Jos Oomens, David T Moore, AFG Van Der Meer, Gert von Helden, Gerard Meijer, Christopher L Hendrickson, Alan G Marshall, and Gregory T Blakney. Free electron laser-fourier transform ion cyclotron resonance mass spectrometry facility for obtaining infrared multiphoton dissociation spectra of gaseous ions. *Rev. Sci. Instrum.*, 76(2):023103, 2005.

[39] Nick C Polfer and Jos Oomens. Reaction products in mass spectrometry elucidated with infrared spectroscopy. *Phys. Chem. Chem. Phys.*, 9(29):3804–3817, 2007.

[40] Jonathan Martens, Giel Berden, Christoph R Gebhardt, and Jos Oomens. Infrared ion spectroscopy in a modified quadrupole ion trap mass spectrometer at the FELIX free electron laser laboratory. *Rev. Sci. Instrum.*, 87(10):103108, 2016.

[41] Jonathan Martens, Josipa Grzetic, Giel Berden, and Jos Oomens. Structural identification of electron transfer dissociation products in mass spectrometry using infrared ion spectroscopy. *Nat. Commun.*, 7:11754, 2016.

[42] Jos Oomens, Boris G Sartakov, Gerard Meijer, and Gert Von Helden. Gas-phase infrared multiple photon dissociation spectroscopy of mass-selected

molecular ions. *Int. J. Mass Spectrom.*, 254(1-2):1–19, 2006.

[43] Anouk M Rijs and Jos Oomens. *Gas-phase IR spectroscopy and structure of biological molecules*, volume 364. Springer, 2015.

[44] Shenheng Guan and Alan G Marshall. Stored waveform inverse fourier transform (SWIFT) ion excitation in trapped-ion mass spectometry: Theory and applications. *Int. J. Mass Spectrom. Ion Processes*, 157:5–37, 1996.

[45] Nick C Polfer and Jos Oomens. Vibrational spectroscopy of bare and solvated ionic complexes of biological relevance. *Mass Spectrom. Rev.*, 28(3):468–494, 2009.

[46] Mitra Almasian, Josipa Grzetic, Johanne van Maurik, Jeffrey D Steill, Giel Berden, Steen Ingemann, Wybren Jan Buma, and Jos Oomens. Non-equilibrium isomer distribution of the gas-phase photoactive yellow protein chromophore. *J. Phys. Chem. Lett.*, 3(16):2259–2263, 2012.

[47] MJ Frisch, GW Trucks, HB Schlegel, GE Scuseria, MA Robb, JR Cheeseman, G Scalmani, V Barone, B Mennucci, GA Petersson, et al. Gaussian 09, Revision D.01. *Inc., Wallingford CT*, 2013.

[48] Axel D Becke. Density-functional thermochemistry. III. the role of exact exchange. *J. Chem. Phys.*, 98(7):5648–5652, 1993.

[49] Axel D Becke. Density-functional exchange-energy approximation with correct asymptotic behavior. *Phys. Rev. A*, 38(6):3098, 1988.

[50] Chengteh Lee, Weitao Yang, and Robert G Parr. Development of the colle-salvetti correlation-energy formula into a functional of the electron density. *Phys. Rev. B*, 37(2):785, 1988.

[51] Jonathan K Martens, Josipa Grzetic, Giel Berden, and Jos Oomens. Gas-phase conformations of small polyprolines and their fragment ions by IRMPD spectroscopy. *Int. J. Mass Spectrom.*, 377:179–187, 2015.

[52] ed. R. D. Johnson III. NIST computational chemistry comparison and benchmark database, NIST Standard Reference Database Number 101, Release 18, 2016.

[53] Anthony K Grafton and Ralph A Wheeler. Vibrational projection analysis: New tool for quantitatively comparing vibrational normal modes of similar molecules. *J. Comput. Chem.*, 19(14):1663–1674, 1998.

[54] Anthony K Grafton and Ralph A Wheeler. ViPA: A computer program for vector projection analysis of normal vibrational modes of molecules. *Comput. Phys. Commun.*, 113(1):78–84, 1998.

[55] Ying Zhang, Anan Wu, Xin Xu, and Yijing Yan. OPBE: A promising density

functional for the calculation of nuclear shielding constants. *Chem. Phys. Lett.*, 421(4-6):383–388, 2006.

[56] G Distefano, S Pignataro, L Szepes, and J Borossay. Photoelectron spectroscopy study of the triphenyl derivatives of the group V elements. *J. Organomet. Chem.*, 102(3):313–316, 1975.

[57] CB Duke. Electronic structure of large molecules: CNDO/S3 model. *Int. J. Quantum Chem.*, 16(S13):267–281, 1979.

[58] Felix M Pasker, Nicola Solcà, and Otto Dopfer. Spectroscopic identification of carbenium and ammonium isomers of protonated aniline (AnH^+): IR spectra of weakly bound AnH^+- L n clusters (L= Ar, N_2). *J. Phys. Chem. A*, 110(47):12793–12804, 2006.

[59] Vinh Thi Tran and Burnaby Munson. Proton affinities by reactant ion monitoring: triphenyl group va compounds. *Org. Mass Spectrom.*, 21(1):41–46, 1986.

[60] Edward PL Hunter and Sharon G Lias. Evaluated gas phase basicities and proton affinities of molecules: an update. *J. Phys. Chem. Ref. Data*, 27(3):413–656, 1998.

Chapter 7

Proto-isomerization of indigo and isoindigo dyes confirmed by gas phase infrared ion spectroscopy

7.1 Abstract

Gas-phase infrared multiple-photon dissociation (IRMPD) spectra are recorded for the protonated dye molecules indigo and isoindigo using a quadrupole ion trap (QIT) mass spectrometer coupled to the free electron laser for infrared experiments (FELIX). From their fingerprint IR spectra (600—1800 cm^{-1}) and comparison with quantum-chemical calculations at the density functional level of theory (B3LYP/6-31++G(d,p)), we derive their structures. We focus particularly on the question of whether *trans-to-cis* isomerization occurs upon protonation and transfer to the gas phase. The trans-configuration is energetically favored in the neutral forms of the dyes in solution and in the gas phase. Instead, the cis-isomer is lower in energy for the protonated forms of both species, but indigo is also notorious for not undergoing double-bond trans-to-cis isomerization in contrast to many other conjugated systems. The IR spectra suggest that proto-isomerization from trans to cis indeed occurs for both dyes. In order to estimate the extent of isomerization, on-resonance kinetics are measured on diagnostic and common vibrational frequencies to determine the ratio of cis to trans isomers. We find

---

"Reprinted with permission from Musleh Uddin Munshi, Jonathan Martens, Giel Berden and Jos Oomens, *J. Phys. Chem. A* **2019**. Copyright 2019 American Chemical Society."

ratios of 65-70% cis and 30-35% trans for indigo, versus 75-80% cis and 20-25% trans for isoindigo. Transition-state calculations for the isomerization reactions have been carried out, which indeed suggest a lower barrier for protonated isoindigo, qualitatively explaining the more efficient isomerization.

7.2 Introduction

Indigo ($C_{16}H_{10}N_2O_2$) is a common pigment with a distinctive blue color. Double-bond isomerization [1] of indigo is of the essence because of its potential use as a molecular switch [2, 3] in the ongoing challenge to harness and exploit the well-defined mechanical properties of molecular compounds and the design of small, molecular-sized devices. *Cis-trans* isomerization around double bonds in conjugated compounds can be triggered by heat, light, or catalysts such as the addition of protons, transition metal ions, Lewis acids, etc. Especially light-induced trans-cis photo-isomerization of indigo and a variety of its derivatives has been widely studied [1, 4–10]. As general conclusion from these studies, it was found that although many of the derivatives undergo double-bond isomerization in the excited state, indigo itself does not. The distinctive ingredients inhibiting photo-isomerization in indigo have been suggested to be the $NH\cdots O{=}C$ hydrogen bonds in the trans isomer, efficient excited-state proton transfer and efficient non-radiative internal conversion quenching the photo-isomerization channel [6, 7, 9, 11]. Indigo's resistance to photo-isomerization is key to its photostability as a pigment [12].

As an alternative to photo-isomerization, proto-isomerization of indigo, i.e., trans-to-cis isomerization induced by protonation, has also been addressed. Indigo and various of its derivatives were characterized experimentally in the condensed phase [13, 14]. Studies of imine derivatives of indigo in strong acids provide evidence for efficient trans-to-cis isomerization, but this could not be established for indigo itself [13]. Theoretical studies of proto-isomerization of indigo and some of its imine derivatives considering both the gas-phase and solution conditions indeed predict lower activation energies for the imine derivatives [15].

Here we address the question of whether and to what extent isomerization to the cis-configuration occurs for protonated indigo, as well as of isoindigo (Figure 7.1), when fully isolated in the gas phase of a mass spectrometer. As neutral

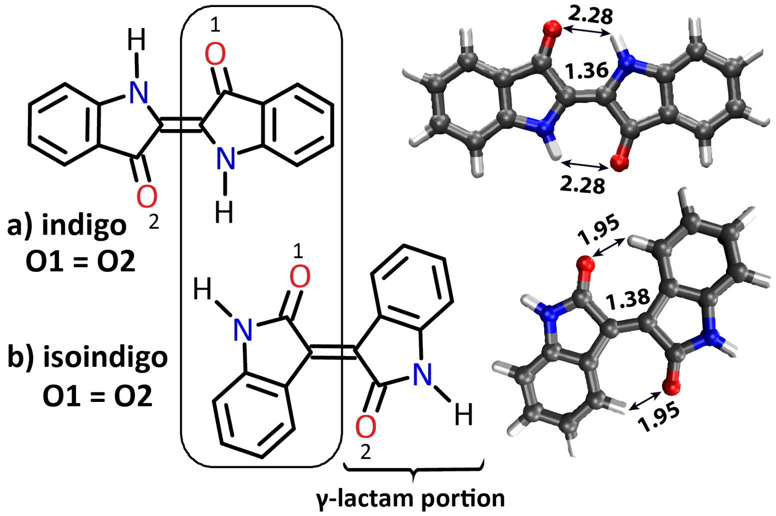

Figure 7.1. Schematic showing neutral a) trans indigo (top) and b) isoindigo. Isoindigo is a structural isomer of indigo and has a 5-membered cyclic amide (γ-lactam) arrangement. Oxygen atoms are identical (O1=O2) in both isomers. DFT optimized structures are also shown with important bond distances (in Å) indicated.

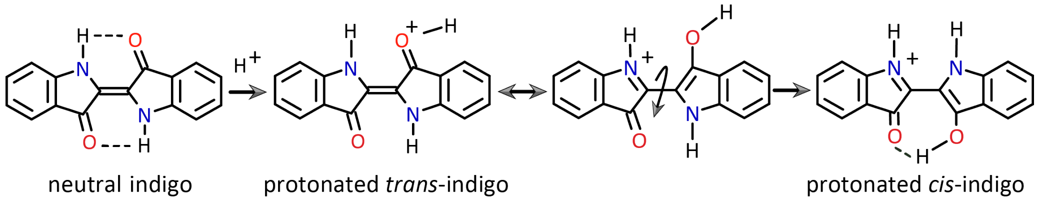

Figure 7.2. Protonation on one of the two identical oxygen atoms in indigo allows for mesomeric structures having a single bond connecting the two subunits, suggesting more facile trans-to-cis isomerization of the protonated species. Similar resonance structures can be drawn for isoindigo.

species, indigo as well as isoindigo are characterized by a trans-configuration ground state, where the carbonyl groups on the two subunits are antiparallel to each other. Two NH$\cdots$O=C hydrogen bonds stabilize the trans-configuration of the indigo molecule with respect to the cis isomer. The absence of H-bonds in isoindigo brings cis- and trans-configurations closer in energy, although the trans configuration is still lower in energy (vide infra).

Of the possible protonation sites (NH nitrogen and C=O oxygen atoms), the oxygen atom is preferred and it is noted that in indigo as well as in isoindigo, both carbonyl oxygens are symmetrically identical. Upon protonation on one of the oxygen atoms, the charge is delocalized over the conjugated system as suggested by the resonance structures shown in Figure 7.2. The reduced double-bond character of the central C=C bond suggested by the resonance structures indicates that trans-to-cis isomerization may become more facile. In the cis-configuration, O-protonated indigo can form a proton bridge between the two carbonyl O-atoms, providing additional stability to the cis-isomer. On the other hand, the trans-configuration is destabilized upon protonation due to the partial positive charge on the protonated carbonyl O-atom, reducing the NH$\cdots$O=C hydrogen bond strength. Computational investigations have indicated that in its protonated form, cis-indigo is indeed lower in energy than trans-indigo, although the barrier to isomerization remains substantial (125 kJ mol^{-1}) [15].

We investigate the molecular structures of the gaseous protonated dyes using infrared multiple-photon dissociation (IRMPD) spectroscopy [16–18] in an ion-trap mass-spectrometer coupled to the beam line of our infrared free electron laser FELIX. Gas-phase IR spectra are employed for structural identification by comparison with harmonic frequency calculations at the density functional theory (DFT) level. In addition, we employ wavelength selective IRMPD kinetics to estimate the relative cis- and trans-isomer abundances.

7.3 Methods

7.3.1 IRMPD spectroscopy

Protonated (iso)indigo ions are generated by electrospray ionization (ESI) and stored in a modified 3D quadrupole ion trap (QIT) mass spectrometer (Bruker, AmaZon Speed ETD, Bremen, Germany) [19]. Solutions containing 1:1 methanol: water and about 1.0 µM of one of the dye molecules and about 0.1% of formic acid (to enhance protonation) are used for ESI. Ions are mass-isolated in the trap and irradiated with two pulses of tunable infrared radiation generated by the FELIX free electron laser (FEL) source [16]. In these experiments, the FEL typically produces radiation in the form of 6 µs long macropulses at a 10 Hz repetition rate, which have approximately 100 mJ of energy and a bandwidth of about 0.4% of the central frequency. Every macropulse consists of a series of micro-pulses of a few ps, separated by a 1-ns time interval. Upon resonance of the FEL frequency with a vibrational transition of the stored ion, absorption of multiple photons occurs, aided by intramolecular vibrational redistribution (IVR) [20], which raises the internal energy of the ions and eventually results in unimolecular dissociation. IR frequency-dependent fragment and precursor ion intensities are monitored in the QIT-MS. The mass spectral data are then converted into an IR spectrum of the precursor ion by plotting the dissociation yield [21–24] as function of the FEL frequency:

$$\text{Yield} = -\ln\left[1 - \frac{\sum \text{Intensity}_{\text{Fragments}}}{\sum \text{Intensity}_{\text{Fragments}} + \text{Intensity}_{\text{Precursor}}}\right]$$

Each data point in the IRMPD spectrum is obtained from 6 averaged mass spectra. The yield is linearly corrected for frequency-dependent variations in FEL pulse energy. The FEL frequency is tuned with a 3 cm^{-1} step size reconstructing the fingerprint IR spectra from 700—1800 cm^{-1}. The FEL wavelength is calibrated using a grating spectrometer.

In addition, isomer selective on-resonance IRMPD kinetics [25, 26] are measured in order to estimate the relative abundance of isomers in the ion population, which eventually yields the extent of proto-isomerization. This method is described in detail in reference [25]. The intensity of the precursor ion (protonated indigo or isoindigo) is measured as a function of the number of FEL pulses at selected IR frequencies. At an IR frequency where both trans and cis isomers absorb, all precursor ions should be dissociated if irradiated sufficiently long. As a result of a non-perfect overlap of the laser focus with the ion cloud, a small fraction of precursor ions survives even after 60 laser pulses (2% in the current experiments, see below). In contrast, irradiation at isomer-specific frequencies selectively depletes only the cis or the trans isomeric ions. The decay of the ion intensity as a function of the number of laser pulses provides information on the relative abundance of isomers in the ion population.

7.3.2 Theoretical modeling

For all calculations, the B3LYP/6-31++G(d,p) level of theory [27–29] is chosen to optimize the geometry and to compute the harmonic frequencies employing Gaussian 09 revision D 01 [30]. In order to compare the computed (linear) IR spectra with IRMPD spectra, the calculated harmonic frequencies are scaled by a factor of 0.975, which is considered to be appropriate at this level of theory, to compensate for anharmonicity and basis set incompleteness [31, 32]. Computed IR spectra are convoluted with a 15 cm^{-1} full-width at half-maximum (FWHM) Gaussian line shape function. The relative Gibbs free energies of the isomers are also considered for comparison. Transition State (TS) geometries for the trans-to-cis isomerization are computed by using the opt=TS keyword and a single negative frequency is confirmed, corresponding to the torsional motion around the central CC-bond of the molecule (*vide infra*).

7.4 Results and discussion

7.4.1 Resonance structures of indigo and isoindigo

Before analyzing the IRMPD spectrum, we first consider the consequences of protonation for the resonance structures in indigo and isoindigo, which can be considered as α,β-unsaturated carbonyl compounds. In particular, the carbonyl moieties are conjugated with the C=C bond connecting the two subunits of the dye. Figure 7.2 shows that protonation at one of the (identical) carbonyl groups allows one to draw mesomeric structures having a single bond connecting the two subunits, which suggests not only that the charge is well delocalized over the entire molecule, but also that the partial single bond character may enhance trans-to-cis isomerization of the system. The calculations confirm the partial single-bond character of the central CC linkage by a lengthening of this bond of 0.01 – 0.02 Å as compared to the neutral molecule. Neutral trans-indigo is stabilized by 68 kJ mol^{-1} due to two N-H$\cdots$O=C hydrogen bonds with respect to the cis isomer. In the protonated form, cis-indigo is stabilized by a shared-proton hydrogen bonding structure (O—H$^{+}\cdots$O). The absence of strong H-bonds in neutral isoindigo brings cis- and trans-configurations closer in energy, with trans being stabilized by 31 kJ mol^{-1}.

Both for indigo and isoindigo, protonation at one of the carbonyl oxygen atoms is expected to significantly affect the carbonyl stretching frequencies. For our IR spectroscopic investigation, the position of the C=O stretch frequency is therefore of special interest as it is expected to be a sensitive probe of the cis/trans structure of the system. If both trans and cis protonated dyes are present, we expect to observe two distinct C=O stretch frequencies.

Finally, we note that the N-protonated forms of indigo and isoindigo are computed to be +54 and +118 kJ mol^{-1} higher in energy than the O-protonated forms, respectively, and that their predicted IR spectra do not match with experiment (see Appendix F Figure F.1); we shall therefore not further consider these alternative protomers.

7.4.2 Protonated indigo

Figure 7.3 shows the IRMPD spectrum of protonated indigo (*m/z* 263) from 600 to 1850 cm^{-1}. It has been recorded by monitoring IR-induced fragments at *m/z* 262, 245, 235, 219, 217, 206 and 190 (Appendix F Figure F.2), which is consistent with observed dissociation channels in collisional induced dissociation (CID) mass spectra of protonated indigo [33, 34]. The dominant experimental IR bands are labelled with their IR frequency for assignment (Figure 7.3a). Computed linear IR absorption spectra for cis (Figure 7.3b) and trans (Figure 7.3c) isomers of protonated indigo are also shown. A quick comparison of the computed and measured spectra shows that (i) in the 600-1550 cm^{-1} range the cis and trans spectra match roughly equally well to the experimental spectrum and (ii) the most striking differences are in the 1550-1800 cm^{-1} range. In the experimental spectrum, a low-intensity band is observed centered at 1725 cm^{-1}, which is attributed to stretching of the unprotonated C=O group that is hydrogen bonded with the neighboring N-H group in the trans isomer. Theory predicts this band with relatively low intensity at 1733 cm^{-1} in the spectrum of protonated trans-indigo. The observation of this band, though weak, suggests the presence of protonated indigo in its *trans* isomeric form.

DFT predicts a similar C=O stretch band at 1675 cm^{-1} for the cis isomer, but experimentally this band is not well resolved. The dominant experimental band is centered at 1604 cm^{-1}, which clearly matches mostly with the cis isomer due to a set of delocalized vibrations of CC stretching and $OH^{+}\cdots O$ in-plane bending character. In addition, the theoretical bands of the cis isomer at 1517 and 1527 cm^{-1} are attributed to C=O stretching of the protonated carbonyl vibration and a ring vibration involving the 5 and 6-membered rings, which is coupled to the OH in-plane bending vibration; the computations match with the experimental band at 1519 cm^{-1}. The experimental band at 1468 cm^{-1} is due to 6-membered-ring vibrations along with OH in-plane bending modes of the cis isomer, which is predicted at 1459 cm^{-1} while the trans-isomer has a band at 1462 cm^{-1} due to a 6-membered-ring vibration alone. The strong experimental band at 1315 cm^{-1} also matches with a predicted band for the cis isomer having mainly ring vibration character combined with CH and NH in-plane bending. Similar vibrations are present in the trans isomer, but their intensities are not as high. The shoulder at 1370 cm^{-1} appears to have dominant contributions from the trans isomer predicted at 1378 and 1385 cm^{-1} and attributed to ring

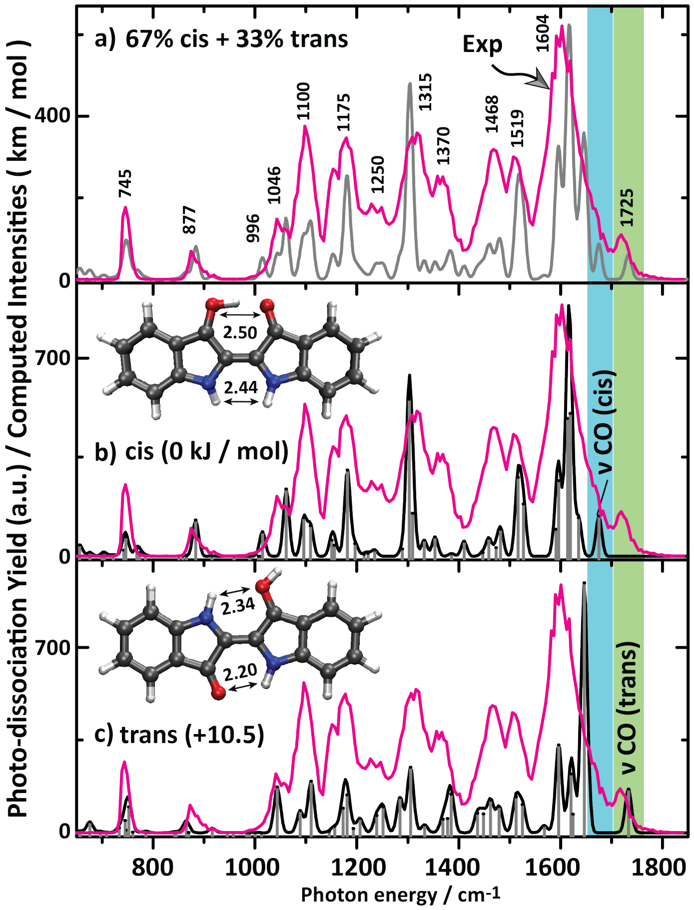

Figure 7.3. (a) Gas-phase IRMPD spectrum of protonated indigo (magenta trace) with band centers for the main experimental bands indicated. The experimental spectrum is compared with computed spectra for (b) the cis and (c) the trans isomer. The gray trace in panel (a) represents the aggregate spectrum of cis and trans isomers assuming fractional populations as suggested by the kinetic measurements described in the text. Computed intensities in km mol^{-1} refer to the stick spectra. Optimized structures along with their relative Gibbs free energies are shown, as well atomic distances (in Å).

vibrations coupled with NH and CH in-plane bending. The band at 1250 cm^{-1} also has more contribution from the trans isomer showing predicted bands at 1239 and 1251 cm^{-1}. Moreover, the predicted band for cis at 1181 cm^{-1} due to a 6-membered ring vibration matches with the experiment at 1175 cm^{-1}. The trans isomer contributes with bands at 1181 and 1173 cm^{-1}. The last dominant experimental band at 1100 cm^{-1} appears to represent contributions from both cis (1109 cm^{-1}) and trans (1110 cm^{-1}) isomers, involving 6-membered ring vibrations combined with CH in-plane bending. The predicted band at 1060 cm^{-1} for cis due to a 5-membered ring vibration coupled to NH in-plane bending matches the experimental band at 1060 cm^{-1}, while the trans isomer has a similar band at 1043 cm^{-1} that also matches the experiment at 1046 cm^{-1}.

Apart from these dominant bands, there are relatively low intensity experimental bands towards the low-frequency region of the IR spectrum. For instance, the OH in-plane bending mode at 1015 cm^{-1} for cis is experimentally confirmed by the shoulder at 1000 cm^{-1} . There is no obvious contribution from the trans isomer to this band. Cis and trans isomers contribute roughly equally to the experimental band at 877 cm^{-1} due to computed intensities at 884 cm^{-1} and 865 cm^{-1}, respectively, with both bands being attributed to in-plane ring vibrations. The low frequency experimental band at 745 cm^{-1} is the typical CH out-of-plane bending mode predicted at 752 cm^{-1} for the cis isomer and at 746 cm^{-1} for trans.

From this analysis of the spectrum, we conclude that both cis and trans species are present in the ion population and therefore that proto-isomerization occurs in part for the ion population. From the kinetic analysis below (involving the 1725 cm^{-1} band diagnostic for trans and the 1604 cm^{-1} band attributed to both isomers) presented below, we estimate a 65-70% cis plus 30-35% trans mixture. Combining the two predicted spectra in this ratio gives the grey trace in Figure 7.3a.

The calculations show a H-bond distance in the cis isomer of 1.48Å which indicates a strong H-bond. The C=C distance (1.38Å) is increased slightly by 0.03Å as opposed to the neutral (trans) indigo. The same increment of the C=C distance is observed for the trans isomer upon protonation.

7.4.3 Protonated isoindigo

Figure 7.4 shows the IRMPD spectrum of protonated isoindigo (*m/z* 263), which has been recorded by monitoring the fragments at *m/z* 245, 235, 219, 217 and 190 (see Appendix F Figure F.2). Theoretical IR spectra of the cis and trans isomers are again overlaid with experiment in panels b and c for comparison. The two highest frequency IR bands in the observed spectrum at 1745 cm^{-1} and at 1686 cm^{-1} are assigned as the carbonyl C=O stretch bands of the trans and cis isomers, respectively. Hence, we conclude immediately that the IRMPD spectrum suggests again the co-existence of the two isomers. The experimental C=O stretch band for the cis isomer appears broadened, possibly due to the strong hydrogen bond of the added proton with the unprotonated carbonyl group, forming a shared proton motif ($O—H^{+} \cdots O$) [35–38]. DFT calculations

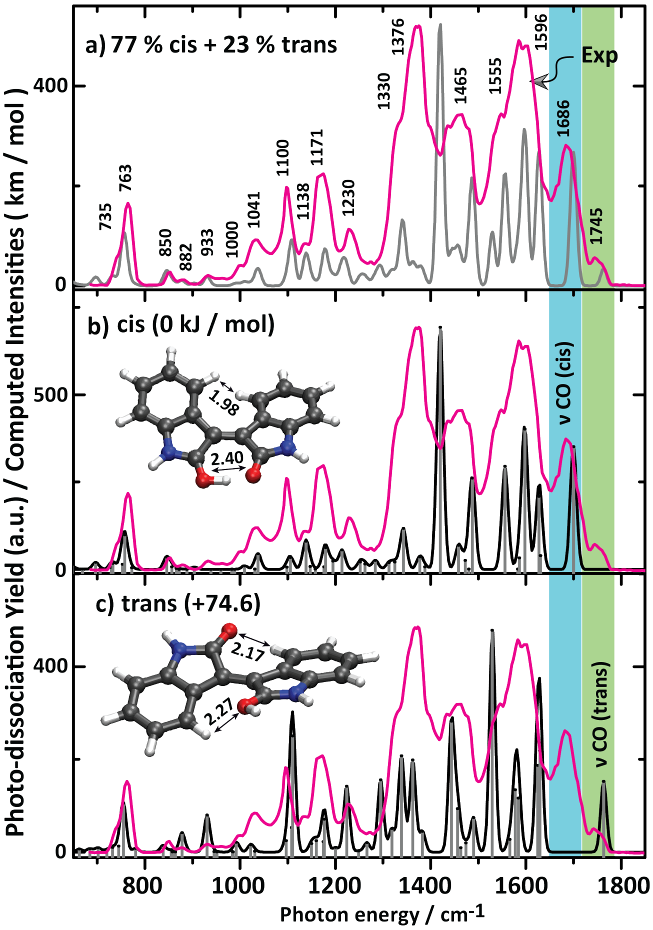

Figure 7.4. (a) Experimental IRMPD spectrum of protonated isoindigo (magenta trace). (b) Overlay of the experimental spectrum with the calculated IR spectrum for the cis isomer and (c) with that of the trans isomer. The gray trace in panel (a) represents an 77/23-ratio mix of the cis/trans computed spectra, as suggested by the kinetic measurements described in the text. Optimized structures along with the relative Gibbs energies are shown, as well as some relevant atomic distances (in Å).

predict the carbonyl stretch bands in both isomers to be separated by 65 cm^{-1}, close to the observed splitting. Absolute band positions are calculated at 1765 cm^{-1} and 1700 cm^{-1} for trans and cis, respectively, showing a slight systematic shift. In contrast to protonated indigo, the band for the cis isomer is well resolved. The trans isomer of protonated isoindigo is computed to lie 75 kJ mol^{-1} higher in energy than the cis isomer so that the presence of any trans isomers must be due to kinetic trapping and a reasonable barrier between the two isomers. IRMPD kinetics experiments (vide infra) suggest that the trans isomer contributes 20-25% to the ion population, where the other 75-80% is cis. Thus isomerization from trans-to-cis indeed occurs upon protonation for the majority of the isoindigo molecules as evidenced by IRMPD spectroscopy.

Analyzing the experimental spectrum in detail, the band centered at 1596 cm^{-1} with a red shoulder at 1555 cm^{-1} is due to three dominant bands of both cis and trans isomers as predicted by theory. The band centered at 1596 cm^{-1} is mostly due to the cis isomer, in particular, attributed to the hydrogen-bonded OH in-plane-bending mode. The dominant band predicted for trans at 1529 cm^{-1} is the C=C stretch of the central CC bond; it is predicted at 1556 cm^{-1} for cis.

The experimental band at 1465 cm^{-1} is broadened and perhaps due to an overlap of bands at 1487 and 1419 cm^{-1} predicted for the cis isomer and a band predicted at 1444 cm^{-1} for the trans isomer. These bands have mainly ring stretching and in-plane CH bending character. The experimental bands at 1376 and 1330 cm^{-1} form the dominant feature in the experimental spectrum, but they are not well reproduced by the computed spectrum for the cis-isomer, which we believe to be dominant in the ion population. In part, this band may be due to the trans isomer which has predicted bands at 1362, 1339 and 1295 cm^{-1} having ring vibration character along with CH in-plane bending. However, the main contribution may be due to the 1419 cm^{-1} predicted band in the cis isomer; this band is due to the O-H stretch vibration of the shared-proton ($OH^{+} \cdots O$), which we suspect to behave particularly anharmonically due to the small OO distance of 2.40Å in protonated cis-isoindigo. The larger OO distance in protonated cis-indigo of 2.50Å reduces the anharmonic behavior of this band, placing it closer to 1600 cm^{-1} and giving a better match with the harmonic calculations. Weaker bands predicted near 1377 and 1342 cm^{-1} may give further contributions to this strong feature.

Experimental features at 1230, 1171 and 1100 cm^{-1} are not accurately reproduced, but are assumed to be due to the overlap of a large number of weaker bands predicted in this range for both cis and trans isomers. They have largely in-plane ring deformation and in-plane CH, NH and OH bending character. The experimental band 1041 cm^{-1} is a well-resolved band which appears to be mainly due to the cis isomer, which features a predicted band at 1038 cm^{-1} with ring vibration character. The observed spectrum below 1000 cm^{-1} matches particularly well with that predicted for the cis-isomer, further confirming its dominant contribution to the ion population. The band observed at 850 cm^{-1} is attributed to a ring-breathing vibration of the cis isomer and the intense band at 763 cm^{-1} is in good agreement with the typical CH out-of-plane bending mode predicted at 758 cm^{-1} for cis (755 for trans). The minor population of trans-isoindigo is evidenced by a weak feature at 933 cm^{-1} which according to the calculations is exclusively due the trans isomer. Overall, the spectrum in this range is well reproduced by the composite spectrum of 77/23 cis/trans protonated isoindigo.

The H-bond distance in the cis isomer is about 1.32Å (C=O$\cdots$H$^+$—O=C) while both O atoms are 2.40Å apart, much shorter than in DNA base pairs [39], indicative of a strong H-bond [35–38]. The central C=C bond length is 1.39Å in cis, which is identical to the bond length in the trans isomer but 0.01Å larger than the neutral.

7.4.4 Determination of relative ion populations by wavelength-selective IR induced dissociation kinetics

IRMPD kinetics are used to probe the relative populations of the cis and trans isomers. First, a kinetic measurement on an IR frequency where both cis and trans absorb has been performed in order to determine the extent of overlap between the laser beam and the ion cloud in the ion trap. The CH out-of-plane bending modes near 750 cm^{-1} were selected for this experiment (see overlap at this frequency for cis and trans isomers in Figure 7.3 and 7.4). Figure 7.5 shows that for both indigo and isoindigo the precursor ion intensities level off after 20 pulses leaving about 2% of the ions undissociated in the trap. A similar result is obtained for indigo exciting the ions at the most intense band at 1604 cm^{-1}.

Next, kinetic measurements are performed at IR frequencies which exclusively probe the cis or the trans isomer of each of the molecules, using the C=O stretch bands. For isoindigo, kinetic measurements at 1745 cm^{-1}, probing trans, and 1686 cm^{-1}, probing cis, are displayed in Figure 7.3. After irradiation with 40 pulses a steady state appears to be reached, suggesting that about 15% of the ions are trans and 85% cis (taking into account that 2% of the ions cannot be dissociated at all). However, the curve for cis shows a plateau around 10 pulses, indicative of a double-exponential decay likely due to another species dissociating at a slower rate upon irradiation at 1686 cm^{-1}.

In Figure 7.5, the normalized precursor ion intensity on the y-axis is defined as the precursor intensity divided by the sum of fragment and precursor intensities. All fragment ions identified as belonging to isoindigo (see Appendix F Figure F.2) are included. Plotting the precursor intensity without normalization

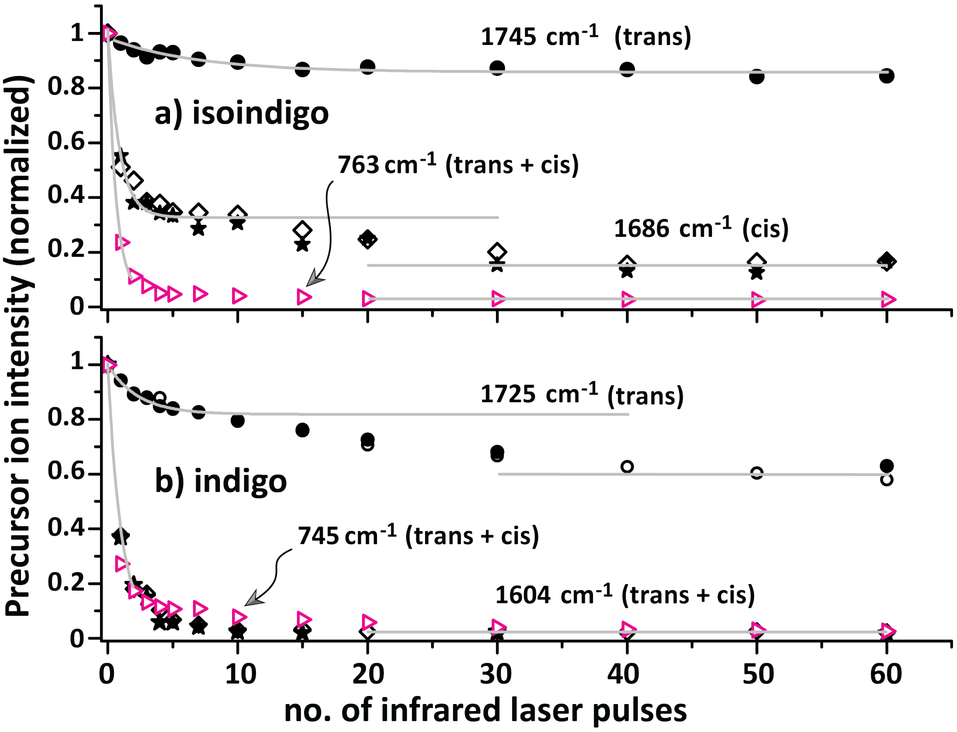

Figure 7.5. (a) Photo–fragmentation decay of the mass-isolated protonated isoindigo (a) and indigo (b) as a function of IR FEL pulses at fixed frequencies diagnostic for the trans at 1745 cm^{-1} (•) and diagnostic for cis species at 1686 cm^{-1} (⋆, ◇ : replicate data). Data points indicated with ▷ were taken with the laser set at 763 cm^{-1}, where both isomers absorb leading to complete depletion of the precursor ion population. (b) Results of similar experiments for protonated indigo, carried out at frequencies resonant with trans (1725 cm^{-1}, •, ○: replicate), and with both cis+trans (1604 cm^{-1}, ⋆, ◇ replicate, and 745 cm^{-1}, ▷). Each data point is obtained from 10 average mass spectra. Solid curves are single exponential decay fits to a limited range of the experimental data points, except for trans-isoindigo where all data points are included.

gives the same curves, albeit more noisy, with the plateau clearly visible. This suggest that the unknown species shares some or all of the same fragment ions. The unknown species appears not to be present in the isoindigo sample as was verified with HPLC measurements.

In a control experiment, ESI of pure 1:1 MeOH:H_2O solvent (without isoindigo) and about 0.1% of formic acid shows that a background ion at *m/z* 263, the mass of isoindigo, is present in our mass spectrometers. The ion intensity is 50 to 100 times lower than that of isoindigo. We have recorded the IRMPD spectrum of this background ion (shown in Appendix F Figure F.3). The dominant fragment ion is *m/z* 235, the same as for isoindigo. The spectrum consists of a broad structured band between 650 and 1300 cm^{-1}, and some weak bands between 1300 and 1720 cm^{-1}. Note that our measurements have been repeated over a period of 10 months on two mass spectrometers; the origin of this contamination is currently unknown.

The presence of this background ion can explain the dynamics of the observed curves for isoindigo (Figure 7.5a). At 763 cm^{-1}, all ions, cis and trans indigo and the background ions, absorb the IR radiation and within 5 to 10 laser pulses all ions are dissociated. The background ion does not absorb at 1745 cm^{-1}, the frequency diagnostic for trans-isoindigo, indicating that about 15% of the total ion population is trans-isoindigo. Note that after about 2 pulses 50% of the trans-isomers has dissociated. At the diagnostic cis-isoindigo frequency (1686 cm^{-1}), the background ion has a weak overlapping absorption band. The observed dissociation yield shows that From a separate measurement on the background ion, it can be seen that about 20 pulses are needed to dissociate 50% of the background ions. This indicates that less than 3% of the background ions dissociate per IR laser pulse at this frequency. The steep decay of the kinetics curve recorded at 1686 cm^{-1} (Figure 7.3a) can then be attributed almost exclusively to cis-isoindigo. This suggest the presence of about 65-70% cis-isoindigo in the ion population, of which 50% has dissociated after 1 to 2 pulses (as for the trans isomer). About 20% of the ion population can be attributed to the background ions, which dissociate at a much slower rate, explaining the plateau in the kinetics plot.

These results indicate that about 20-25% of the protonated isoindigo population is in the trans configuration and 75-80% is cis. In the top panel of Figure 7.2, the experimental IR spectrum is compared to a composite calculated spectrum assuming a trans/cis ratio of 77/23. Note that although 20% of the total ion population is due to the contaminant ions, they have a negligible contribution to the experimental IRMPD spectrum, which was recorded with two pulses of irradiation, thus nearly avoiding any dissociation of the contaminant ions.

For protonated indigo, the experimental situation is different since only the trans isomer has a well-resolved carbonyl band at 1725 cm^{-1} (see Figure 7.3). The kinetics plot recorded at this frequency suggests that about 40% of the ion population is present as trans-indigo. However, the contaminant ions show a low, but non-negligible, IRMPD intensity (see Appendix F Figure F.3), and they are responsible for the barely visible plateau around 10 laser pulses in the kinetics plot. The plateau suggests that about 20% of the ions are protonated trans-indigo and 20% of the ions are contaminant ions. The kinetics plots recorded at 745 and 1604 cm^{-1} have contributions from both trans- and cis-indigo and the contaminant ions, and cannot be used to estimate the fractional cis-indigo population. Therefore, we tentatively attribute the remaining 60% of the ion population to cis-indigo. These results indicate that for protonated indigo, about 30-35% is in the trans configuration and 65-70% is cis. Again, the contaminant ion does not contribute significantly to the IRMPD spectrum of Figure 7.3, since only a minute fraction undergoes dissociation upon irradiation with 2 laser pulses.

7.4.5 Transition state (TS) calculation

Figure 7.6 shows the results of transition state (TS) calculations for trans-to-cis isomerization for protonated indigo and isoindigo. A singlet electronic state is considered at the TS and the C=C bond rotation barrier represents the rate-limiting step; rotation of OH group is disregarded here. Extensive TS calculations on indigo and some of its derivatives have been reported previously [15] and our theoretical method reproduces these TS geometries. The barrier to rotation about the central C=C bond is estimated to be 141 kJ mol^{-1} for protonated trans-indigo in the gas-phase, while 125 kJ mol^{-1} is reported in solution [15].

From a thermochemical viewpoint, trans-to-cis proto-isomerization can be well-understood from the fact that the energetic ordering of trans and cis isomers inverts upon protonation (for both indigo and isoindigo). In their neutral forms, trans-indigo is higher in energy (+22 kJ mol^{-1}) than trans-isoindigo (Figure 7.1).

The relative H-bond stabilization of cis and trans isomers is altered after protonation, destabilizing the trans isomer of both systems. Protonated trans-isoindigo destabilizes more and the geometry also distorts to become non-planar, whereas indigo retains its planar geometry. In protonated trans-indigo, the H-bond between the non-protonated C=O and N-H shortens by 0.08Å but the other H-bond increases by 0.06Å. On the other hand, in protonated trans-isoindigo, both H-bonds are increased significantly (by 0.32Å for the protonated C=O and C-H and 0.22Å for the non-protonated C=O and C-H) as a consequence of the non-planar structure (Figure 7.2). The relatively weak H-bonds and non-planar geometry result in a significant destabilization, but simultaneously in a relatively low trans-to-cis TS barrier of +92 kJ mol^{-1}. On the other

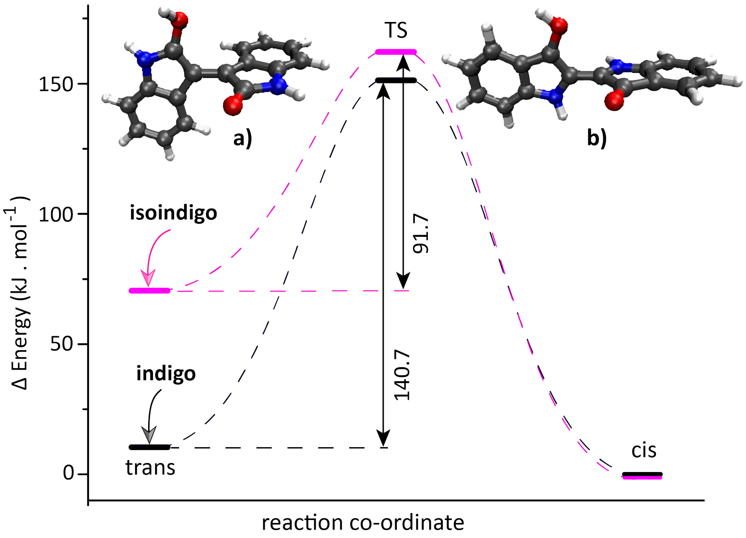

Figure 7.6. Computed TS barriers for trans-to-cis isomerization and optimized TS geometries of protonated isoindigo (a) and indigo (b). Values given for the TS barriers are in kJ mol^{-1} relative to the trans form of the protonated molecules. For the protonated systems, unlike for the neutral molecules, cis is the minimum energy isomer. Although both cis isomers are positioned at the same energy in the plot, protonated cis-isoindigo is 46.3 kJ mol^{-1} more stable than protonated cis-indigo, as a consequence of the stronger shared-proton interaction induced by the smaller OO distance (see Figure 7.3 and 7.4).

hand, destabilization of protonated indigo is limited and the barrier for trans-to-cis isomerization is significantly higher (+141 kJ mol^{-1}).

In addition, the lone-pair electrons on both nitrogen atoms in indigo may participate in conjugation (delocalization) reinforcing the central C=C bond and hence the planar structure. In isoindigo, this effect is smaller because the nitrogen atoms are further away from the central C=C bond. In this respect, it is also interesting to note that in the γ-lactam arrangement of isoindigo (Figure 7.1), the nitrogen lone-pair electrons can participate in resonance with the C=O group, shifting the C=O stretch frequency to higher frequencies than in indigo (1745 cm^{-1} in protonated isoindigo versus 1725 cm^{-1} in protonated indigo).

The computed TS geometry of isoindigo has a nearly perpendicular arrangement with a C-C=C-C dihedral angle of 88°); in protonated indigo, the dihedral angle at the TS is about 82°). Despite the high TS barrier, indigo is clearly observed to undergo proto-isomerization in our experiments. The conversion from trans to cis involves the breaking of existing H-bonds upon rotation around the central C=C bond, as well as rotation of the -O—H group in the required direction to make a new H-bond with the other carbonyl [15].

The rate-limiting step is the rotation about the central CC bond, which relies on its reduced double-bond character upon protonation (Figure 7.2). Experimentally, we clearly observe protonation-induced double bond isomerization in both indigo and isoindigo. Moreover, our isomer population analysis indicates that conversion to the cis isomer is more efficient for isoindigo than for indigo, which is qualitatively corroborated by the difference in computed TS energies for the two systems.

7.5 Conclusion

IRMPD spectra of protonated indigo and isoindigo have been measured using a quadrupole ion trap mass spectrometer coupled to the tunable infrared free electron laser source FELIX. Comparisons of the experimental spectra with DFT computations lead to the identification of two co-existing isomers: cis being the minimum-energy isomer and trans being the ground state in the neutral molecule, for both dyes. As we start with a sample of the neutral molecule in the trans form, protoisomerization from trans to cis is confirmed for both species.

In order to quantify the ratio between the cis and trans isomers present in the mixture, on-resonance IRMPD kinetics are performed on diagnostic IR bands. This provides an estimate of the mixture with 65-70% cis and 30-35% trans for protonated indigo and 75-80% cis and 20-25% trans for isoindigo. Thus, isoindigo appears to be more prone to proto-isomerization than indigo, which is qualitatively explained by significant differences in the DFT computed isomerization barriers. The remaining fraction of trans isomers observed in the spectra are likely kinetically trapped.

References

[1] George M Wyman. The cis-trans isomerization of conjugated compounds. *Chem. Rev.*, 55(4):625–657, 1955.

[2] Ben L Feringa. The art of building small: from molecular switches to molecular motors. *J. Org. Chem.*, 72(18):6635–6652, 2007.

[3] Eric Daniel Głowacki, Gundula Voss, and Niyazi Serdar Sariciftci. 25th anniversary article: Progress in chemistry and applications of functional indigos for organic electronics. *Adv. Mater.*, 25(47):6783–6800, 2013.

[4] George M Wyman and Wallace R Brode. The Relation between the Absorption Spectra and the Chemical Constitution of Dyes XXII. cis-trans Isomerism in Thioindigo Dyes^1. *J. Am. Chem. Soc.*, 73(4):1487–1493, 1951.

[5] Wallace R Brode, John H Gould, and George M Wyman. The relation between the Absorption Spectra and the Chemical Constitution of Dyes. XXV. Phototropism and cis-trans Isomerism in Aromatic Azo Compounds^1. *J. Am. Chem. Soc.*, 74(18):4641–4646, 1952.

[6] Wallace R Brode, Ervin G Pearson, and George M Wyman. The relation between the absorption spectra and the chemical constitution of dyes. XXVII. cis-trans isomerism and hydrogen bonding in indigo Dyes^1. *J. Am. Chem. Soc.*, 76(4):1034–1036, 1954.

[7] Michael R Haggmark, Gregory Gate, Samuel Boldissar, Jacob Berenbeim, Andrzej L Sobolewski, and Mattanjah S de Vries. Evidence for competing proton-transfer and hydrogen-transfer reactions in the s1 state of indigo. *Chem. Phys.*, 515:535–542, 2018.

[8] Denis Jacquemin, Julien Preat, Valérie Wathelet, and Eric A Perpète. Substitution and chemical environment effects on the absorption spectrum of indigo. *J. Chem. Phys.*, 124(7):074104, 2006.

[9] T Kobayashi and PM Rentzepis. On the picosecond kinetics and photostability of indigo and 6, 6-dimethoxyindigo. *J. Chem. Phys.*, 70(2):886–892, 1979.

[10] C Giuliano, L Hess, and J Margerum. Cis-trans isomerization and pulsed laser studies of substituted indigo dyes. *J. Am. Chem. Soc.*, 90(3):587–594, 1968.

[11] Miquel Moreno, Juan Manuel Ortiz-Sánchez, Ricard Gelabert, and José M Lluch. A theoretical study of the photochemistry of indigo in its neutral and dianionic (leucoindigo) forms. *Phys. Chem. Chem. Phys.*, 15(46):20236–20246, 2013.

[12] Costanza Miliani, A Romani, and G Favaro. A spectrophotometric and fluorimetric study of some anthraquinoid and indigoid colorants used in artistic paintings. *Spectrochim. Acta, Part A*, 54(4):581–588, 1998.

[13] Emma C Nicholls-Allison, Graeme Nawn, Brian O Patrick, and Robin G Hicks. Protoisomerization of indigo di-and monoimines. *Chem. Commun.*, 51(62):12482–12485, 2015.

[14] Wallace R Brode and George M Wyman. The relation between the absorption spectra and the chemical constitution of dyes. xxiv. absorption spectra

of some thioindigo dyes in sulfuric acid. *J. Am. Chem. Soc.*, 73(9):4267–4270, 1951.

[15] Laurence Hajjar, Robin G Hicks, and Tao Zeng. A computational Study of the Protoisomerization of Indigo and Its Imine Derivatives. *J. Phys. Chem. A*, 120(38):7569–7576, 2016.

[16] Jos Oomens, Boris G Sartakov, Gerard Meijer, and Gert Von Helden. Gas-phase infrared multiple photon dissociation spectroscopy of mass-selected molecular ions. *Int. J. Mass Spectrom.*, 254(1-2):1–19, 2006.

[17] Nick C Polfer. Infrared multiple photon dissociation spectroscopy of trapped ions. *Chem. Soc. Rev.*, 40(5):2211–2221, 2011.

[18] Anouk M Rijs and Jos Oomens. *Gas-phase IR spectroscopy and structure of biological molecules*, volume 364. Springer, 2015.

[19] Jonathan Martens, Giel Berden, Christoph R Gebhardt, and Jos Oomens. Infrared ion spectroscopy in a modified quadrupole ion trap mass spectrometer at the FELIX free electron laser laboratory. *Rev. Sci. Instrum.*, 87(10):103108, 2016.

[20] KK Lehmann, G Scoles, and BH Pate. Intramolecular dynamics from eigenstate-resolved infrared spectra. *Annu. Rev. Phys. Chem.*, 45(1):241–274, 1994.

[21] B Lucas, G Gregoire, J Lemaire, P Maitre, F Glotin, JP Schermann, and C Desfrancois. Infrared multiphoton dissociation spectroscopy of protonated N-acetyl-alanine and alanyl-histidine. *Int. J. Mass Spectrom.*, 243(2):105–113, 2005.

[22] Juehan Gao, Giel Berden, MT Rodgers, and Jos Oomens. Interaction of Cu^+ with cytosine and formation of i-motif-like C–M^+–C complexes: alkali versus coinage metals. *Phys. Chem. Chem. Phys.*, 18(10):7269–7277, 2016.

[23] James S Prell, Jeremy T O'Brien, and Evan R Williams. IRPD spectroscopy and ensemble measurements: effects of different data acquisition and analysis methods. *J. Am. Soc. Mass. Spectrom.*, 21(5):800–809, 2010.

[24] Giel Berden, Mathijs Derksen, Kas J. Houthuijs, Jonathan Martens, and Jos Oomens. An automatic variable laser attenuator for irmpd spectroscopy and analysis of power-dependence in fragmentation spectra. *Int. J. Mass Spectrom.*, 443:1 – 8, 2019.

[25] James S Prell, Terrence M Chang, Jeffrey A Biles, Giel Berden, Jos Oomens, and Evan R Williams. Isomer population analysis of gaseous ions from infrared multiple photon dissociation kinetics. *J. Phys. Chem. A*,

115(13):2745–2751, 2011.

[26] Amanda L Patrick, Adam P Cismesia, Larry F Tesler, and Nicolas C Polfer. Effects of ESI conditions on kinetic trapping of the solution-phase protonation isomer of p-aminobenzoic acid in the gas phase. *Int. J. Mass Spectrom.*, 418:148–155, 2017.

[27] Axel D Becke. Density-functional thermochemistry. III. The role of exact exchange. *J. Chem. Phys.*, 98(7):5648–5652, 1993.

[28] Axel D Becke. Becke's three parameter hybrid method using the LYP correlation functional. *J. Chem. Phys*, 98:5648–5652, 1993.

[29] Chengteh Lee, Weitao Yang, and Robert G Parr. Development of the Colle-Salvetti correlation-energy formula into a functional of the electron density. *Phys. Rev. B*, 37(2):785, 1988.

[30] MJ Frisch, GW Trucks, HB Schlegel, GE Scuseria, MA Robb, JR Cheeseman, G Scalmani, V Barone, B Mennucci, GA Petersson, et al. Gaussian 09, Revision D.01. *Inc., Wallingford CT*, 2013.

[31] Marie L Laury, Matthew J Carlson, and Angela K Wilson. Vibrational frequency scale factors for density functional theory and the polarization consistent basis sets. *J. Comput. Chem.*, 33(30):2380–2387, 2012.

[32] Anthony P Scott and Leo Radom. Harmonic vibrational frequencies: an evaluation of Hartree- Fock, Møller- Plesset, quadratic configuration interaction, density functional theory, and semiempirical scale factors. *J. Phys. Chem.*, 100(41):16502–16513, 1996.

[33] Peng Zou and Hwee Ling Koh. Determination of indican, isatin, indirubin and indigotin in isatis indigotica by liquid chromatography/electrospray ionization tandem mass spectrometry. *Rapid Commun. Mass Spectrom.*, 21(7):1239–1246, 2007.

[34] Maria Puchalska, Kasia Połeć-Pawlak, Irmina Zadrożna, Helena Hryszko, and Maciej Jarosz. Identification of indigoid dyes in natural organic pigments used in historical art objects by high-performance liquid chromatography coupled to electrospray ionization mass spectrometry. *J. Mass Spectrom.*, 39(12):1441–1449, 2004.

[35] Steven L Baughcum, Richard W Duerst, Walter F Rowe, Zuzana Smith, and E Bright Wilson. Microwave spectroscopic study of malonaldehyde (3-hydroxy-2-propenal). 2. structure, dipole moment, and tunneling. *J. Am. Chem. Soc.*, 103(21):6296–6303, 1981.

[36] C Ceccarelli, GA Jeffrey, and R Taylor. A survey of OH...O hydrogen bond

geometries determined by neutron diffraction. *J. Mol. Struct.*, 70:255–271, 1981.

[37] AR Ubbelohde and KJ Gallagher. Acid-base effects in hydrogen bonds in crystals. *Acta Crystallogr.*, 8(2):71–83, 1955.

[38] Alfred Rene Jean Paul Ubbelohde and Ida Woodward. Structure and thermal properties of crystals, VI. the role of hydrogen bonds in Rochelle salt. *Proc. Royal Soc. Lond.*, 185(1003):448–465, 1946.

[39] Célia Fonseca Guerra, F Matthias Bickelhaupt, Jaap G Snijders, and Evert Jan Baerends. The nature of the hydrogen bond in DNA base pairs: the role of charge transfer and resonance assistance. *Chem.–Eur. J.*, 5(12):3581–3594, 1999.

Appendix A

Experimental methods in IR-IS

A.1 Depletion of radical cation of TPA inside QIT

Frequency dependent laser induced precursor depletion (*m/z* isolated) signal of TPA$^{\cdot+}$ is plotted with the generation of fragment signals (Figure A.1). From these data IRMPD spectra are generated using either -ln(1-yield) (where yield is defined by Equation 1.1) or precursor depletion (see Figure A.2a).

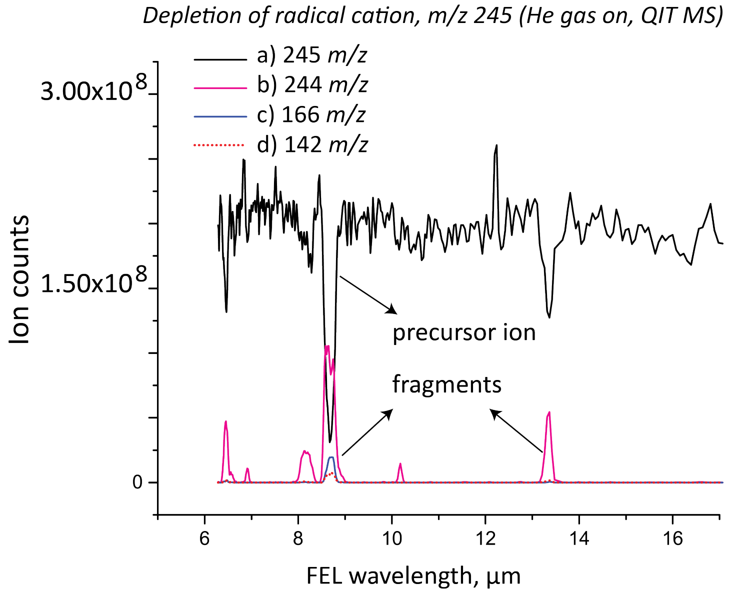

Figure A.1. Depletion of TPA$^{\cdot+}$ ion is indicated as a function of FEL wavelengths (a). Dips are generated at the resonance frequencies and simultaneously the photo-induced fragment peaks are appeared for the (b) 244 *m/z*, (c) 166 and (d) 142.

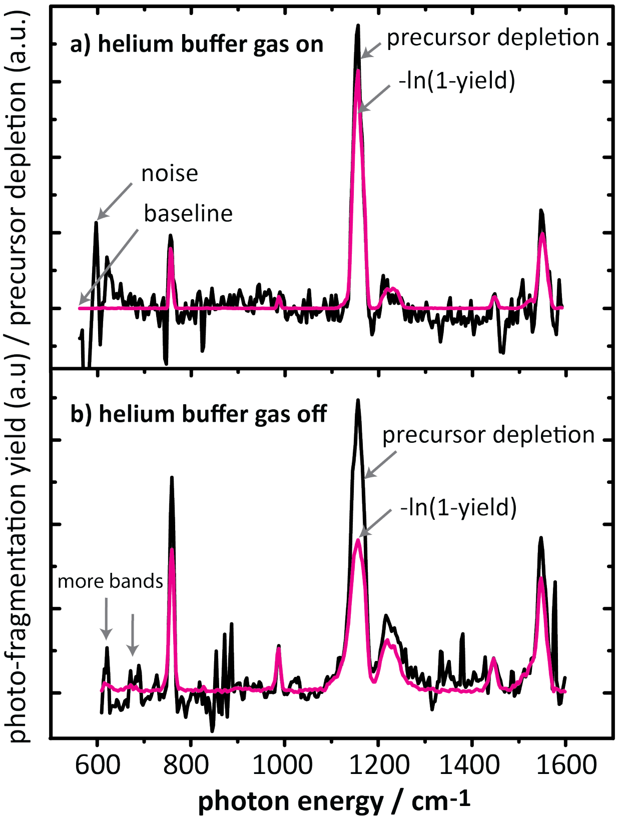

Figure A.2. IRMPD spectra based on the depletion of the precursor versus the calculated -ln(1-yield) of TPA$^{\cdot+}$ ion: with helium buffer gas on (a) and off (b). Additional IRMPD bands are apparent between 600-700 cm^{-1} due to not having collisional cooling effect without the presence of buffer gas.

Figure A.2a shows that the relative intensities of the IRMPD bands (magenta vs black) are consistent with the precursor depletion and the calculated -ln(1-yield). The advantage is that the yield spectrum is noise free.

The same experiment was repeated without the helium buffer gas present (Figure A.2b) and in this case the relative IRMPD intensities are not consistent (magenta vs black). The main reason is well understood—some of the created fragments remain undetected due to the low mass cut-off of the QIT MS. This observation is generally true for all the dominant bands except for the low intensity bands. Nonetheless, removal of buffer gas often helps to detect low intensity bands.

Appendix B

Cu(II/I)-ligand redox pair

B.1 Spectra of $[Cu(II)(bpy)_2]$ complex with high pulse energy

The goal of this experiment was to look for additional bands (possibly with low intensity) in between the observed strong bands.

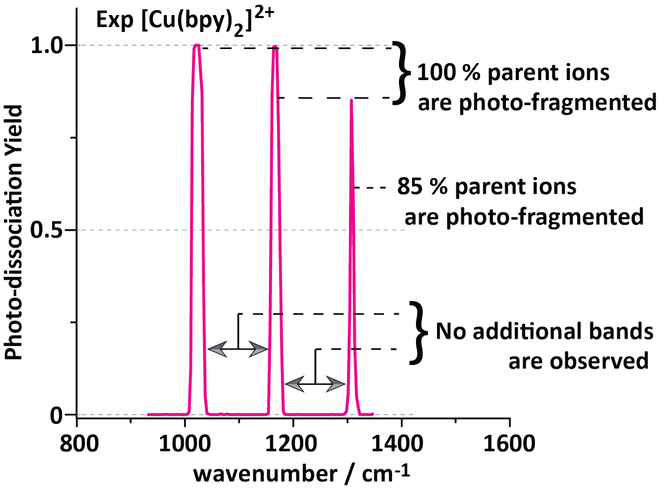

Figure B.1. IRMPD spectrum for the $[Cu(bpy)_2]^{2+}$ ion recorded in the QIT MS with higher IR pulse energies in order to probe the possibility of additional IR bands in between the three strong bands in the 1000-1400 cm^{-1} range. Although the precursor ions are nearly completely photo-fragmented at these main absorption bands, no additional bands are observed.

B.2 Optimized geometries of the [Cu(cyclam)]$^{2+/+}$ redox pair

[Cu(cyclam)] complex can have 5 stereomers due to the relative orientation of the N-H protons with respect to the central Cu atom. This Figure shows all the optimized geometries predicted by DFT where *trans-III* is the minimum for [Cu(cyclam))]$^{2+}$ whereas *trans-V* is for the charge reduced [Cu(cyclam))]$^{+}$ complex. Based on the experimental evidence *trans-III* remained unchanged upon selective charge reduction of [Cu(cyclam))]$^{2+}$ complex inside QIT MS. Note, similar results are also obtained for the analogous [Ni(cyclam))]$^{2+}$ complex (chapter 4).

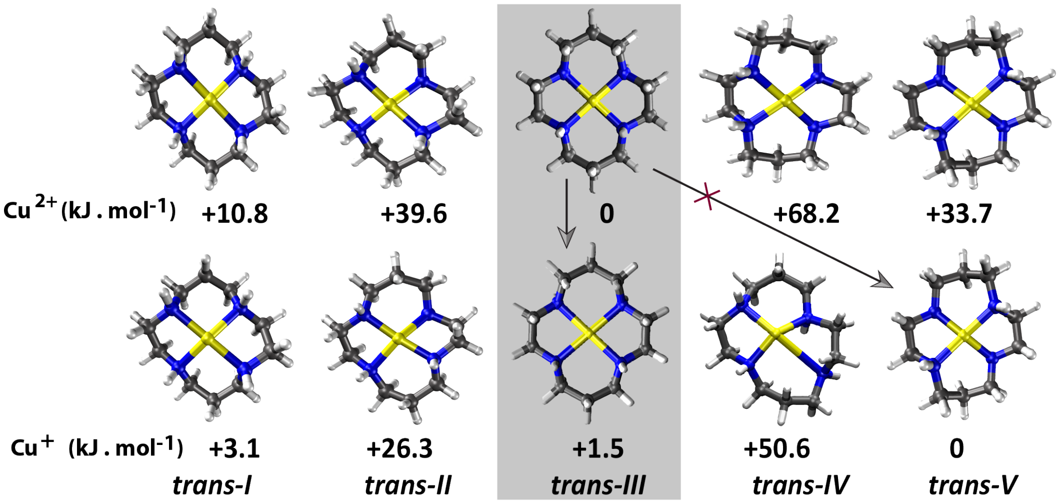

Figure B.2. DFT optimized geometries of Cu(cyclam) complexes for both members of the redox pair. Computed free energies are given in kJ mol^{-1} and the corresponding IR spectra are shown in Figure 3.6 of the main text (see chapter 3).

Appendix C

Ni(II/I)-cyclam redox pair

C.1 Mass spectrum of Ni(II)-cyclam and $[Ni^{2+}(cyclam\text{-}H^{-})]^{+}$

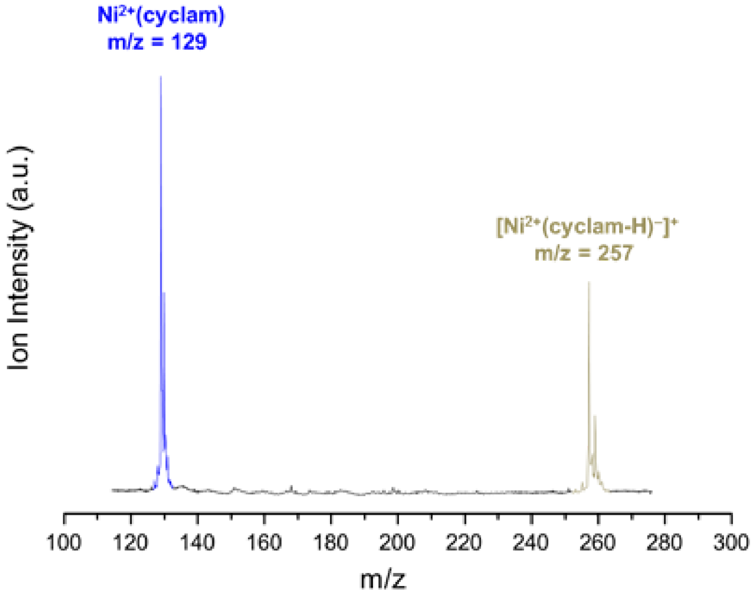

Figure C.1. Mass spectrum of Ni^{2+}(cyclam) (blue) and $[Ni^{2+}(cyclam\text{-}H^{-})]^{+}$ (gold) obtained on the Yale tandem time of flight photofragmentation mass spectrometer.

C.2 Isomers of Ni-cyclam complex

In the [Ni(cyclam)] complex, 5 stereomers are possible due to the relative orientation of the N-H protons with respect to the central Ni atom.

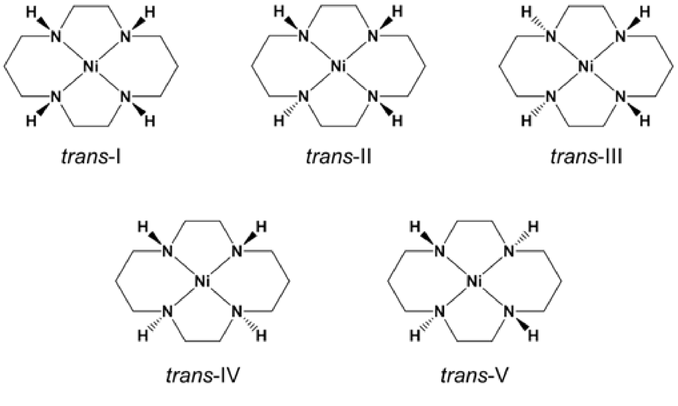

Figure C.2. Structures of the five isomers of Ni^{2+}(cyclam).

C.3 IRMPD spectrun *vs* calculated spectra of Ni(II)-cyclam

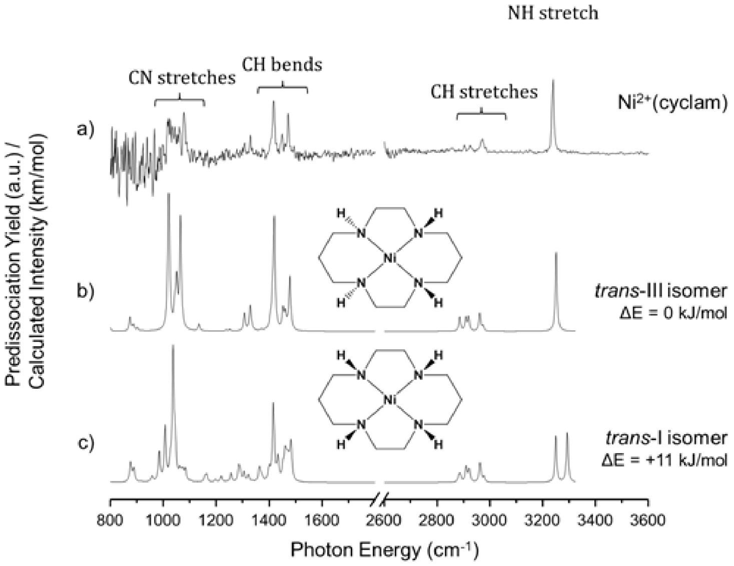

Figure C.3. The vibrational predissociation spectrum of a) Ni^{2+}(cyclam) shows good agreement with the calculated vibrational spectrum of the lowest energy isomer, b) the *trans-III* isomer. The next lowest energy isomer, the *trans-I* isomer, is 11 kJ mol^{-1} higher in energy and c) its calculated vibrational spectrum shows less agreement, especially in the NH stretching region. All calculations were performed at the B3LYP/6-31++G(d,p) level of theory and scaled by 0.975 below 2200 cm^{-1} and by 0.95 above 2200 cm^{-1}.

C.4 Spectral diff. between Ni(II/I)-cyclam and [Ni^{2+}(cyclam-H^{-})]$^{+}$

This Figure below exclusively shows that the IR spectrum of [Ni^{2+}(cyclam-H^{-})]$^{+}$ is different than that of Ni(II/I)-cyclam complexes—despite the fact that

[Ni^{2+}(cyclam-H$^-$)]$^+$ species has one H atom less than Ni(I)-cyclam complex.

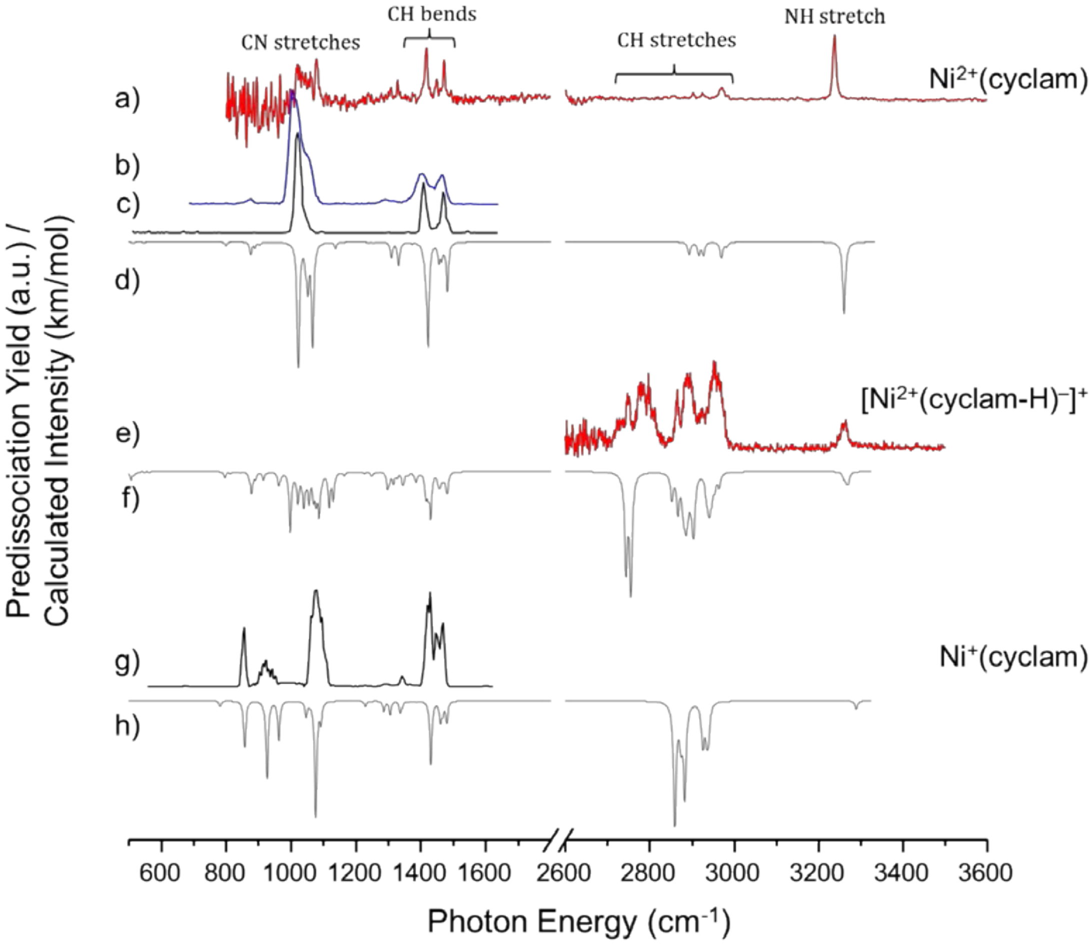

Figure C.4. Vibrational spectra of a-c) Ni^{2+}(cyclam), e) [Ni^{2+}(cyclam-H)$^-$]$^+$, and g) Ni$^+$(cyclam). The red traces indicate N_2 predissociation spectra taken at 30 K, while the black traces indicate IRMPD spectra taken at 300 K. The blue trace (b) shows the IRMPD spectrum of Ni^{2+}(cyclam) recorded in the FTICR-MS at FELIX which recovers more spectral features than the IRMPD spectrum recorded in the QIT. Calculated vibrational spectra are included as the grey inverted traces for b) Ni^{2+}(cyclam), d) [Ni^{2+}(cyclam-H)$^-$]$^+$, and f) Ni$^+$(cyclam). All calculations were performed at the B3LYP/6-31++G(d,p) level of theory and scaled by 0.975 below 2200 cm^{-1} and by 0.95 above 2200 cm^{-1}.

C.5 DFT computed energies of Ni-cyclam complex

Table C.1 shows that out of 5 isomers (as in Figure C.2), *trans-III* is the minimum energy structure for both Ni(II)-cyclam and Ni(I)-cyclam complexes according to DFT calculations. *trans-III* geometry is confirmed by IRMPD spectroscopic measurements for Ni(II/I)-cyclam redox pair. This implies that upon charge reduction of Ni(II)-cyclam complex, the coordination of the metal ion with cyclam remains the same.

Table C.1. DFT derived energies (in kJ mol^{-1}) for the lowest energy structures for the five isomers of Ni^{2+}(cyclam) in the singlet spin state and Ni^{+}(cyclam) in the obvious doublet.

Isomers	Ni^{2+}(cyclam)	Ni^{+}(cyclam)
trans-I	10.96	9.00
trans-II	38.96	40.34
trans-III	0	0
trans-IV	56.58	55.19
trans-V	30.66	31.49

Appendix D

[Ru(II/I)(bpy)$_3$] redox pair

D.1 Structural paramenters of [Ru(bpy)$_3$]$^{2+/+}$ redox pair

Important structural information of [Ru(bpy)$_3$]$^{2+/+}$ redox pair is summarized in the table below. Three different DFT functionals B3LYP, O3LYP and M06 are chosen where Relativistic effect is also taken into account using the Zero Order Regular Approximation (ZORA) method within the ADF program package. The computed Ru-N bond length for the charge reduced [Ru(bpy)$_3$]$^+$ ion is decreased as opposed to the analogous [Ru(bpy)$_3$]$^{2+}$ at all level of theories except O3LYP/TZ2P level, although it fails to reproduce the experimental IRMPD spectra of [Ru(bpy)$_3$]$^+$ (see Figure D.1).

Table D.1. Theoretically calculated average Ru—N distances (Å), Ru centered bond angles (°) of [Ru(bpy)$_3$]$^{2+}$ and [Ru(bpy)$_3$]$^+$ ions in the gas-phase compared with crystallographic literature data of [Ru(bpy)$_3$]$^{2+}$. TZ2P basis set is used with all three functionals. Atom labels are shown in Figure 5.2 main text chapter 5. Parenthesized values are standard deviations in units of the last quoted digit.

	[Ru(bpy)$_3$]$^{2+}$				[Ru(bpy)$_3$]$^+$		
Parameter	B3LYP	O3LYP	M06	Exp	B3LYP	O3LYP	M06
d(Ru-N)	2.095(0)	2.002(0)	2.097(0)	2.065(2)	2.092(0)	2.017(0)	2.069(0)
bond angle (°)							
∠N-Ru-N′	78.2(0)	79(0)	77.8(0)	78.7(1)	78.3(0)	78.8(0)	78.4(0)
∠N-Ru-N″	87.2(0)	88.5(5)	89.2(1)	89.1(1)	88.1(0)	89.7(2)	90(2)
∠N-Ru-N‴	174.0(0)	173.6(4)	172.4(0)	173.0(1)	173.5(1)	172.6(3)	172.1(2)
∠N′-Ru-N″	96.7(0)	96.4(3)	96.7(0)	96.3(1)	97.0(0)	96.0(2)	96.0(1)

D.2 IRMPD spectra *vs* calculated IR spectra of [Ru(bpy)$_3$]$^+$

All level of theories mentioned in this Figure below clearly fail to reproduce the IRMPD specta of [Ru(bpy)$_3$]$^+$. Interestingly the computed IR spectra using the LC-BLYP and CAM-B3LYP functionals turned out to be similar because their optimized structures are similar.

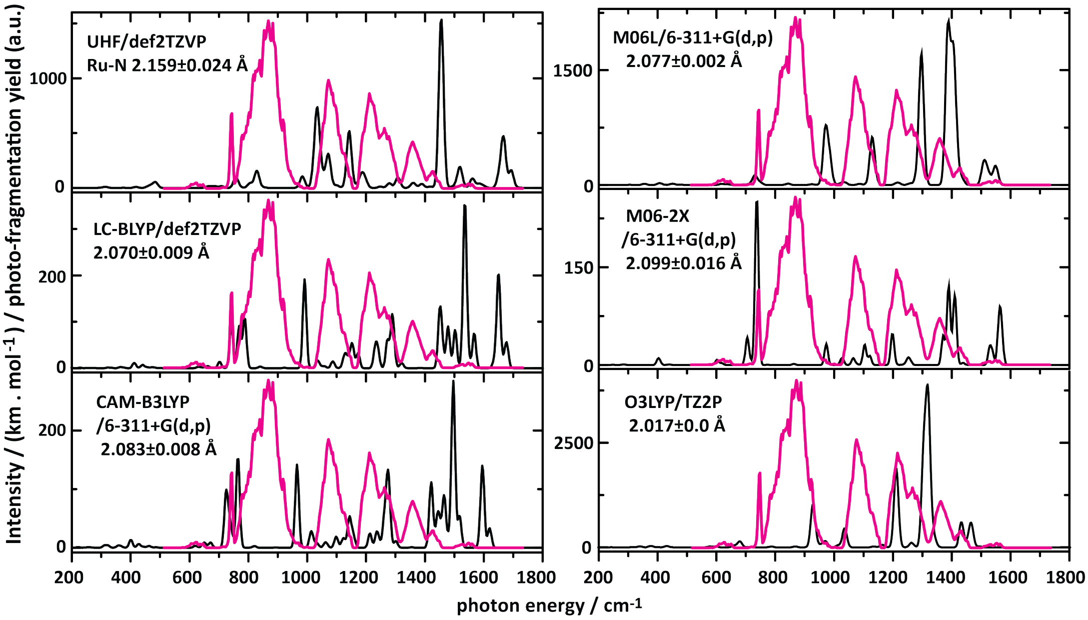

Figure D.1. Theoretical IR spectra at different levels of theory are compared with the experimental infrared spectrum (magenta trace) for [Ru(bpy)$_3$]$^+$ which clearly show that they all fail to reproduce the IR spectra, although the corresponding geometries remain hexa-coordinated (optimized geometries not shown). The average Ru-N distance is provided for each calculation.

Appendix E

Triphenylamine (TPA)

E.1 Scheme: geometry of TPA

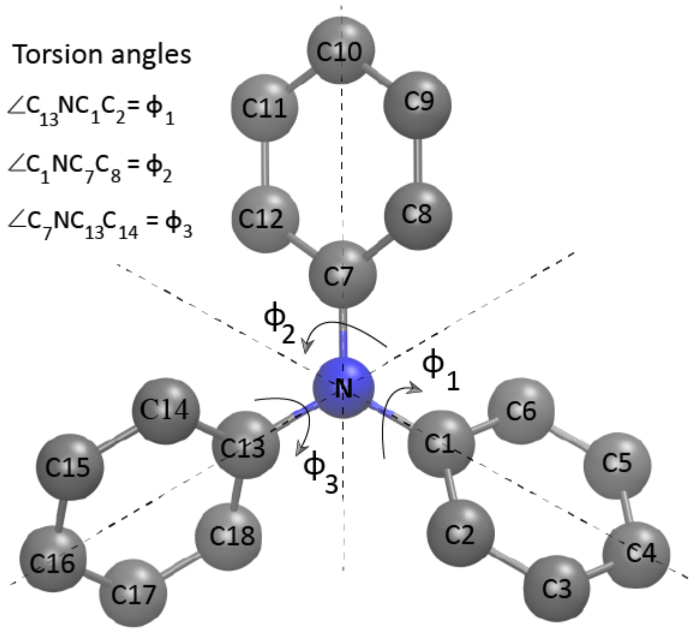

Figure E.1. Schematic representation of TPA (or TPA$^{\cdot+}$) geometry, all atoms are numbered except the nitrogen atom at the centre; H atoms are omitted for clarity. The N atom is considered in the plane of the paper with C atoms C1, C4, C7, C10, C13 and C16. The plane of each of the phenyl moieties makes an angle around the C-N bonds with the plane of the paper; these angles are referred to as torsion angle and are labelled as ϕ_1, ϕ_2 and ϕ_3, where 0° corresponds to all the atoms being in the plane of the paper. All the torsion angles rotate in the same direction around each of the dotted lines.

Table E.1. Computed rotational constants (in GHz) are shown for neutral TPA and radical cation (TPA$^{\cdot+}$) along with the experimentally determined values for neutral TPA in the gas phase. Parenthesized value is the standard deviation

	Rotational constants, (GHz)	
Methods	Neutral TPA	Radical cation, (TPA$^{\cdot+}$)
Exp(LIF)	A=B=0.4047(5),	(Not available)
(for C3 symmetry, A=B)	C=not known	
B3LYP/6-31++G(d,p)	A=0.3999, B=0.3987, C=0.2202	A=0.3993, B=0.3992, C=0.2202
BLYP/cc-pVTZ	A=0.3961, B=0.3955, C=0.2185	A=0.3993, B=0.3992, C=0.2202

Table E.2. Absolute Proton Affinity (in kJ mol^{-1}) for TPA is obtained from DFT

	Absolute proton affinities of the protomers of TPA			
DFT level of theory	N-protonated	para	ortho	meta-protonated
MP2(full)/6-311+G(2d,2p)	913.5	891.1	872.2	769.4

E.2 Vibrational mode projection of TPA$^{\cdot+}$ onto the TPA

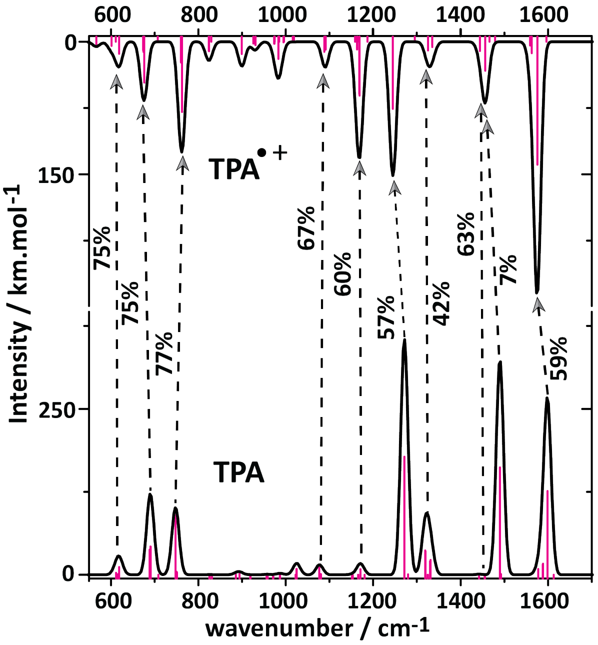

Figure E.2. This figure schematically shows the dominant vibrational projections (%) of the TPA$^{\cdot+}$ (top) onto the TPA (bottom) normal modes employed ViPA. Similar bands are connected with dotted lines and the percentages of the projections are also shown.

Appendix F

Proto-isomerization of (iso)indigo

F.1 IRMPD spectra *vs* computed spectra of N-protonated indigo and isoindigo

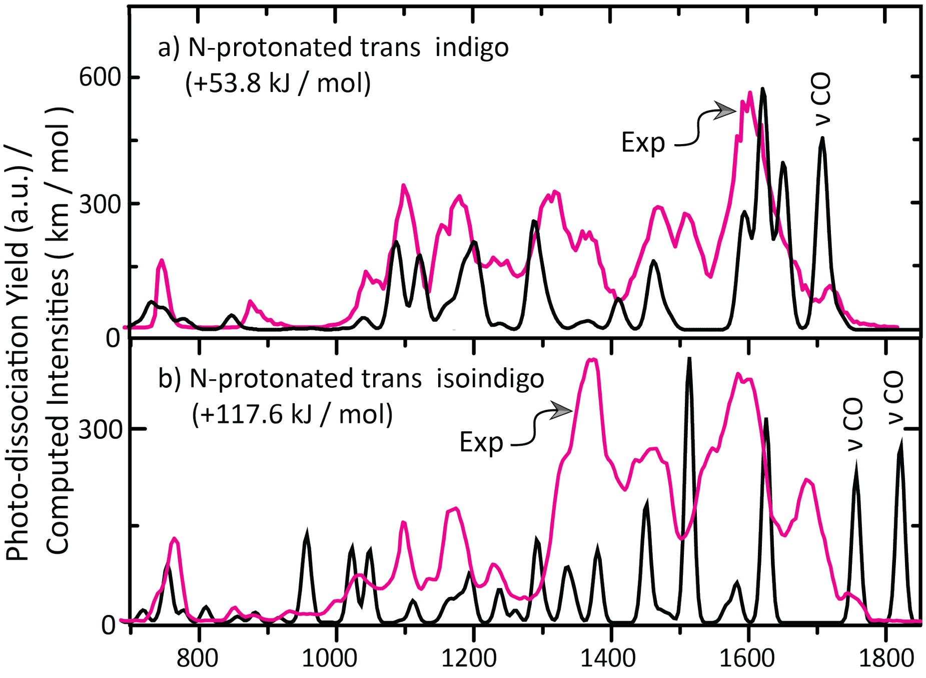

Figure F.1. Gas-phase IRMPD spectra of protonated indigo (a) and protonated isoindigo (b) are compared with computed spectra for N-protonated species in their trans conformations.

F.2 CID MS and FEL induced photo-fragments of dyes

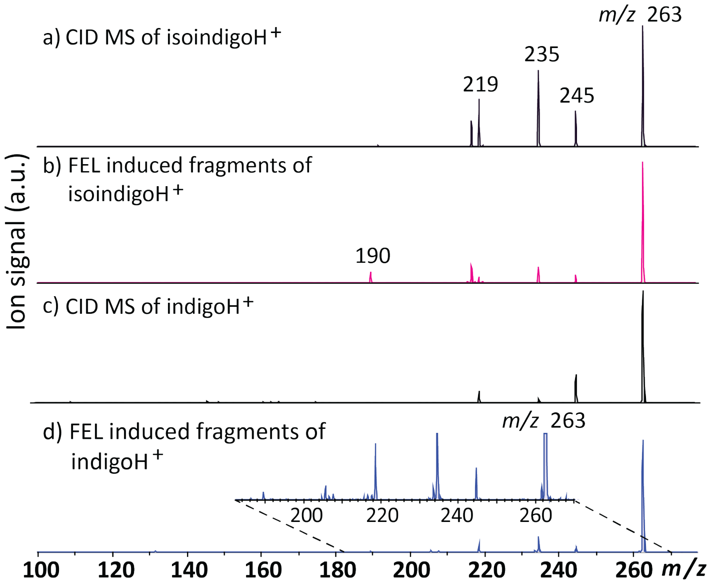

Figure F.2. Mass spectra: CID MS (a) and on-resonance FEL induced photo-fragments at fixed IR laser frequency (b) of the protonated isoindigo (*m/z* 263). Similarly, CID MS (c) and FEL induced photo-fragments at fixed IR laser frequency (d) of the protonated indigo (*m/z* 263) which are very similar to the CID mass-fragments reported in the past.

F.3 IRMPD spectra of mass-isolated background ion

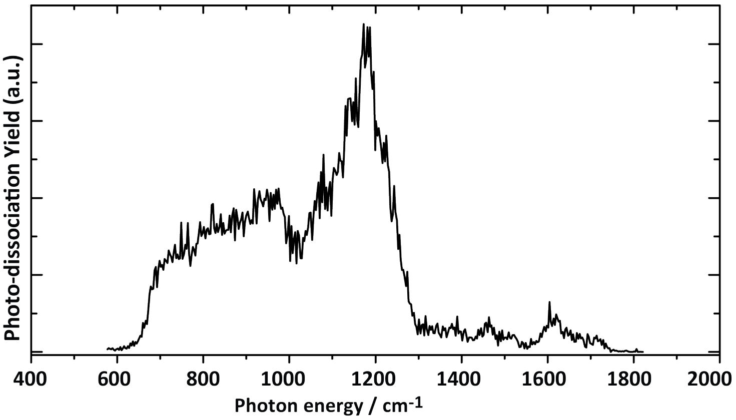

Figure F.3. IRMPD spectrum of the mass isolated (*m/z* 263) background ion. See main text for detailed discussion (chapter 7).

Summary

The aim of this thesis is to gain a broader understanding of the structural characterization of a group of functional molecules in the gas phase, involving oxidation-reduction (redox) reactions, resulting in the change of the charge state by one. In general, how the change of these charge states of molecular systems triggers and causes structural changes are addressed. We focus on the change of charge states, for instance, neutral to mono-cation (i.e., removal an e^-, addition of a H^+), dication (2+) to mono-cation (1+) (i.e., charge-reduction of dication by transferring an e^-). Charge induced structural changes would also open an additional window to employ the molecular mechanical properties. Several important applied functional molecular systems including some model systems have been chosen in order to investigate the intrinsic physico-chemical properties where charge state plays a crucial role in their functions.

Infrared ion spectroscopy (IR-IS) has been tremendously successful in elucidating ionic molecular structures and conformations in the gas phase where infrared lasers coupled to mass spectrometry technique allows to record IR action spectra of molecular ions. Recent coupling of a commercial Bruker quadrupole ion trap (QIT) mass spectrometer (MS) with tunable infrared free electron laser FELIX allows us to utilize various inbuilt utilities — for instance, multi-stage collision induced dissociation (CID) and electron transfer dissociation (ETD) options. ETD is especially designed for protein sequencing in metabolomics where multiple positively charged proteins are allowed to undergo an ion-ion reaction with a radical anion (ETD reagent) which donates an electron to the mass-isolated proteins inside ion trap MS. An exothermic charge recombination reaction occurs which activates the isolated proteins causing dissociation

— based on the ETD products, sequence information is obtained. In this thesis, this ETD feature is chosen and characterized in intact charge reduction without dissociation as a means to manipulate charge state of metal-ligand complexes in the gas phase. Careful optimization of ETD reaction allows us to generate redox pair — for instance, 1+ charge state from 2+ complex without dissociating the precursor complex — thus a systematic intact one electron charge reduction opens a noble method to investigate *open-shell* and *closed-shell* metal-ligand ion complexes in the gas phase. Moreover, this ETD option allows access to metal oxidation states that cannot be produced with ESI. Metal-ligand ion complex with transition metals are often difficult to model, therefore this method would provide experimental infrared spectroscopic evidence directly related to their electronic structures which is necessary in order to check, scrutinize and eventually validate the existing theoretical methods — improved modeling will contribute in search of systems with desired functions. This probably would be the ultimate goal of theoretical methods.

chapter 1 provides a detail description of the modified commercial (Bruker amaZon speed ETD, Bremen, Germany) QIT apparatus where modifications allow optical access for FEL and OPO inside the trap in order to record IR spectra of the mass-isolated molecular ions. This also briefly includes how the charge reduction of the metal-ligand complexes can be accomplished by using the ETD option of the QIT MS. Since some of the experiments were carried out in the home-built FTICR MS as an alternative to circumvent the issues of QIT in recording IRMPD spectra and explore the effects of ion trapping conditions on IRMPD spectra, overall a brief comparison of this apparatus with QIT is also included. IRMPD technique has the reputation of generating slightly red-shifted spectra than a single-photon absorption spectroscopy and IRPD spectroscopy at cryogenic temperature. The differences between IRMPD and linear absorption spectroscopy techniques are also described. In this regard, an example is chosen from this thesis where comparison between a bare complex and an analogous N_2-tagged complex is described.

chapter 2 includes the theoretical methods and computational modeling especially using density functional theory (DFT). Since DFT is the most cost effective method available in terms of accuracy and applicability depending on the system size, mostly DFT is chosen in this thesis. Note, since the birth of DFT, over the last 60 years, it has been tremendously successful in elucidating molecular structures, despite some fundamental issues (e.g., electrons self-interaction errors) still remain. Solutions are suggested, but it would be interesting to see how modern DFT performs to reproduce the experimental results and most importantly help us understand the underlying chemistry of the selected functional molecules. Studied molecules cover both metal-ligand complexes containing transition metals and also some organic molecular ions. This will provide us an overview of the theoretical methods in terms of predicting the geometrical and infrared spectroscopic properties of the ground state *open-shell* functional molecular systems in the gas phase.

chapter 3 explains the generation of (transition) metal-ligand ion complexes in the gas-phase, manipulation of the charge state by one-electron charge-reduction which uniquely allow us to access charge states of the same molecular system as redox pair. Furthermore, charge-reduced ions formed in the solution is also brought into the gas-phase by ESI which allows us to cross-check their structures generated from ETD source. ETD being an exothermic process may potentially allow the excited molecules to find minima other than the global minima. The question is addressed whether the final ETD products are thermalized back or not. $[Cu(bpy)_2]^{2+}$ and $[Cu(bpy)_2]^{+}$ complexes were taken as examples in order to test and validate the experimental approach. In addition, a cyclic ligand, cyclam was chosen instead of two-bpy ligands to have the same tetra-coordinated complex with Cu(II/I) which would allow us to explore the ligand-effect on the complexes in a tetra-coordinated environment. By replacing the Cu ion with Ni, how the metal ion affects the coordination of the complexes was also investigated as we moved from Cu(II/I) to Ni(II/I)-cyclam.

chapter 4 explains the generation of the intact charge-reduced bare Ni^{+}-cyclam species with complete structural characterization. In addition, the IR spectra of the N_2-tagged dication were recorded in cryogenic temperature which allowed us to probe the temperature effect on the IR spectra. This example of redox-pair was taken into consideration where the charge reduced species was not naturally occurring, therefore, limiting the characterization of the system during a chemical process, for instance, Ni^{+}(cyclam) complex in CO_2 catalysis. In this case, the ETD option of the QIT allows access to charge-reduced species selectively from their dication-analogue and subsequently their structures are probed by recording their IR spectra, eventually allowed us to determine the intrinsic structural changes they undergo upon charge-reduction. In the next chapter a hexa-coordinated metal-ligand redox pair is considered.

chapter 5 shows an example of efficient charge-reduction of $[\mathrm{Ru(bpy)_3}]^{2+}$ complex. It has been a model system in the scientific community for decades for various reasons up until now. This got the most attention because of being a potential candidate as the main component in the DSSCs. Structural characterization of the $[\mathrm{Ru(bpy)_3}]^{2+/+}$ redox-pair was explored for the first time using IR ion spectroscopy in the gas-phase. Furthermore, the scope of the DFT method was brought forward in predicting the IR spectra of this important molecular system as a representative of the strongly correlated systems — which are much difficult to model theoretically. Various types of DFT functionals covering from conventional B3LYP to modern M06 including classical pure BLYP were put to the test in order to predict the experimental IRMPD spectra for each member of the $[\mathrm{Ru(bpy)_3}]^{2+/+}$ redox-pair. Not a single functional was found satisfying the experiment — especially for the 1+ *open-shell* complex whereas almost all of them responded much closer or nearly exact for the analogous 2+ *closed-shell* complex than the *open-shell* complex. Of these two complexes the moncation is much less stable than the dication (one could crudely argue about the Coulomb interaction between the metal ion and the neutral ligands) according to our IR photodissociation which is also supported by the previous UV photodissociation experiments on the isolated species in gas phase. Note, photofragmentation channel is the neutral ligand loss for both complexes highlighting explicitly the interaction between metal and ligand. Thus suggesting to have bond lengths shorter for the dication than the analogous monocation. All levels of theories chosen here suggest the opposite that is counter intuitive except O3LYP — which also fails to reproduce the IRMPD spectra for the monocation.

Moreover, range separated functionals (e.g., CAM-B3LYP, LC-BLYP) are also tested especially for the $[\mathrm{Ru(bpy)_3}]^{+}$ ion in order to reproduce the IRMPD spectra and consensus to find where the added electron goes upon reduction of the $[\mathrm{Ru(bpy)_3}]^{2+}$ ion — which is actually a long standing question for this type of molecules particularly in the condensed phase. In the literature electron localization method is generally accepted and suggested for solving this type of questions. Observation according to the range separated functionals was found rather consistent with the more higher level quantum chemical methods e.g., CCSD(T) and CASPT2 for a model peptide ion — where range separated functionals had the tendency to localize the added electron (density) rather than delocalized. Conventional functionals (e.g., B3LYP) are known to generate delocalized electron density which eventually contributes to the electron self interaction error and because of that this gives rise to physically impossible and also chemically meaningless results. Our computation using the range separated functionals for $[Ru(bpy)_3]^+$ ion resulted the added electron being more localized on a single bpy ligand rather than delocalized throughout the whole structure but the key problem still remains that these functionals fail to reproduce the experimental spectra, nonetheless, due to the electron localization slight geometrical changes are noted especially the relevant Ru-N bond distances which seemed chemically intuitive. Now we are in a dilemma in terms of assigning the correct geometry and the underlying chemistry which is meaningful since the theory fails to satisfy the experiment. Certainly, these observations have been able to open a question which DFT level of theory to trust, for instance, to speculate the ground state geometry of this type of *open-shell* molecular ions.

Next two chapters describe totally organic functional molecules. In chapter 6, the experimental IR spectra of the mass selected $TPA^{\cdot +}$ and the protonated TPA in the gas-phase were presented as model systems. Note, this TPA was used in ruthenium-polypyridyl based DSSCs as an additional moiety or the derivative of TPA alone in organic photovoltaics (OPV). Here, our experimental data interpreted by DFT was compared with the available experimental data of the neutral TPA — which unambiguously allowed us to determine the extent of resonance or delocalization of the lone-pair electron of nitrogen in these systems. All these experiments on TPA demonstrated the sensitivity of IRMPD spectroscopy in terms of noticing subtle structural changes.

In chapter 7, how the simple addition of a proton perturbed the resonance of the conjugated double bonds in indigo and isoindigo, eventually triggering isomerization — that was addressed in the gas-phase, qualitatively, quantitatively as well. A systematic investigation of the protoisomerization was explained where indigo or indigo-like molecules had a potential to be used as a molecular motor or switch. Another word, how the mechanical property of a small molecular system could be driven by simple oxidation (addition of H^+), was explored. Although in the past indigo was believed to be less likely to be protoisomerized because of the existing strong H-bonds in its neutral form, it was found to be protoisomerized according to our IR-IS results supported by the DFT interpretation.

To recapitulate, we have been able to successfully characterize the ETD option of the commercial QIT MS in order to manipulate the charge state of the metal-ligand ion complexes by one electron charge reduction without dissociating the precursor ion, as a noble method — where fluoranthene radical anion (ETD reagent) acts as an electron donor during the ion-ion reaction between the ETD reagent and the multiple positively charged cations inside QIT. Thus we have access to redox pairs of metal-ligand complexes in the gas-phase. Since this QIT is coupled to infrared free electron laser source, we have been able to record fingerprint IR spectra of the systems which are then subjected to theoretical interpretations at the DFT level for structural characterization. Comparisons between theory and experiment are generally quite impressive in terms of the harmonic approximation of the vibrational frequency assignments and the corresponding ground state structures, although exceptions are noted — especially for some of the *open-shell* metal-ligand complexes where further theoretical investigations are needed for improved results, probably at higher levels of theory. Certainly, combined infrared ion spectroscopy with modern DFT computational modeling are capable of providing information about functional molecular electronic structures intrinsically relating to their functions in the gas phase.

Samenvatting

Het onderzoek beschreven in dit proefschrift heeft zich gericht op de structurele karakterisatie van een serie functionele molecule in de gasfase. Oxidatie-reductie (redox) reacties die de lading van de moleculen met 1 verhogen of verlagen spelen een centrale rol in de hier onderzochte systemen. We onderzochten hoe de verandering van ladingstoestand de moleculaire geometrie beinvloedt. Zo bestudeerden we het verschil tussen neutraal en cation door verwijdering van een electron (oxidatie) of door toevoeging van een proton, maar ook het verschil tussen 2+ en 1+ ladingstoestanden door reductie van een tweevoudig positief geladen ion. Geometrie veranderingen geïnduceerd door ladingsverandering vormen een mogelijkheid de mechanische eigenschappen van moleculen te benutten. Verschillende functionele moleculaire modelsystemen werden geselecteerd om hun intrinsieke fysisch-chemisch eigenschappen te bestuderen als functie van de ladingstoestand.

Infrarood ion spectroscopie (IRIS) is in de laatste jaren zeer succesvol toegepast om de structuur van geïoniseerde moleculaire systemen in de gasfase te karakteriseren. De koppeling van golflengte-afstembare IR lasers met tandem massa spectrometrie maakt het mogelijk IR spectra van gasvormige, geïsoleerde moleculaire ionen op te nemen. Onze groep heeft recent een commerciële quadrupole ion trap (QIT) massa spectrometer gekoppeld met een breed afstembare IR vrije-electronenlaser (FELIX). Hierdoor kunnen we IR spectroscopie toepassen in combinatie met de verschillende mogelijkheden die dit MS platform biedt: meervoudige botsingsgeïnduceerde dissociatie (CID MS^n) en electron transfer dissociatie (ETD). ETD is een techniek die oorspronkelijk ontwikkeld is voor het sequencen van biopolymeren (met name proteïnen); meervoudig positief geladen proteïnen ondergaan in de ionenval ion-ion reacties met een radicaal anion, de ETD reagent, die een electron doneert aan de proteïne. De exotherme recombinatie reactie activeert de proteïne en leidt tot dissociatie ervan. De massa's van de ETD-geïnduceerde fragmenten geven informatie over de volgorde van aminozuurresiduën in het oorspronkelijke proteïne. In de studies in dit proefschrift gebruiken we de ETD-optie met een ander doel: we kunnen de ladingstoestand van een tweevoudig geladen ion in de gasfase reduceren tot 1+ en zijn geïnteresseerd in het gereduceerde, ongedissocieerde ion. Zo kunnen we de ladingstoestand van metaal-ligand complexen manipuleren, en beide ladingstoestanden van het systeem spectroscopisch onderzoeken. Deze methode laat ons ook oxidatietoestanden van het systeem onderzoeken die niet in de electrospray ionisatie (ESI) bron geproduceerd worden, en die anders moeilijk toegankelijk zijn. Spectroscopische en daarmee structurele informatie over deze exotische oxidatietoestanden van metaal-ligand complexen zijn ook interessant om de performance van theoretische methodes te valideren.

Hoofdstuk 1 beschrijft de hier toegepaste commerciële QIT massa spectrometer (Bruker AmaZon Speed ETD) en de aanpassingen die optische toegang voor FEL en OPO laserstraling tot de opgeslagen ionen mogelijk maken. Hier laten we ook zien hoe de ETD bron gebruikt kan worden om gasvormige metaal-ligand complexen te reduceren zodat hun ladingstoestand met 1 verlaagd wordt. Dit hoofdstuk geeft ook een beknopte beschrijving van een alternatieve massa spectrometer (Fourier Transform Ion Cyclotron Resonance, FTICR-MS) die in sommige experimenten gebruikt is om de nadelen van de relatief hoge achtergronddruk in de ionenval van de QIT te omzeilen. Een vergelijking van beide platforms geven we hier ook. Het is bekend dat infrarood multiple-foton dissociatie (IRMPD) spectroscopie, in vergelijking tot 1-foton spectroscopische technieken, kan leiden tot kleine roodverschuivingen van absortiebanden in het spectrum. We presenteren hier dan ook een beknopte vergelijking tussen IRMPD en verschillende lineaire spectroscopische technieken, waaronder met name methodes gebaseerd op fotodissociatie van niet-covalent N_2-gelabelde systemen in cryogene ionenvallen.

Hoofdstuk 2 introduceert de theoretische methodes en computationele modelering die in dit proefschrift is gebruikt en met name de methodes gebaseerd op dichtheidsfunctionaal theorie (DFT). DFT is voornamlijk gekozen vanwege de combinatie van haar hoge nauwkeurigheid, brede toepasbaarheid en efficiëntie in vergelijking met andere theoretische modellen van vergelijkbare nauwkeurigheid. Sinds haar onstaan zo'n 60 jaar geleden, is DFT zeer succesvol toegepast in het ophelderen van moleculaire structuren, hoewel enkele fundamentele tekortkomingen (zoals de electron zelf-interactie) ook bekend zijn. Hier bekijken we de performance van moderne DFT methodes in het reproduceren van onze experimentele data en gebruiken we de resultaten van de DFT berekeningen voor het begrijpen van de onderliggende chemie van de geselecteerde functionele moleculaire systemen. Hieronder bevinden zich voornamelijk overgangsmetaal-ligand systemen en verschillende open- en gesloten-schil moleculaire ionen. In hoofdstuk 2 gaan we voornamelijk in op het gebruik van de theoretische methodes voor het voorspellen van geometrische en IR-spectroscopische eigenschappen van de ionische systemen.

In hoofdstuk 3 wordt ingegaan op de vorming van ionische (overgangs)metaal-ligand complexen in de gasfase en op de 1-electron reductie van hun ladingstoestand die ons in staat stelt twee verschillende ladingstoestanden van hetzelfde complex spectroscopisch te onderzoeken. We vergelijken deze resultaten onder andere met spectra van gereduceerde complexen gevormd in oplossing en bepalen zo of deze hetzelfde zijn als de gereduceerde complexen gevormd in de gasfase. Omdat ETD een exothermisch proces is, is het mogelijk dat de gevormde complexen zich bevinden in lokale minima die in structuur verschillend zijn van het globale minimum, en de vraag is of de ETD geproduceerde gereduceerde complexen relaxeren naar het thermodynamische minimum. $\mathrm{Cu(II/I)\text{-}(bpy)_2}$ complexen werden geselecteerd om onze methodes te testen en te valideren. In plaats van twee bipyridine (bpy) liganden, werd ook de cyclische ligand cyclam gebruikt; deze vormt ook een 4-voudig gecoördineerd complex met Cu(I/II) maar legt striktere sterische beperkingen op. Voorts werd Cu(I/II) vervangen door Ni(I/II) in de complexen met cyclam; het feit dat Ni(I) alleen via de gasfase ETD reductie reactie toegankelijk is maakt dit systeem vooral interessant

In hoofdstuk 4 wordt dieper ingegaan op het Ni-cyclam complex in de 2+ en de ongebruikelijke 1+ ladingstoestanden en hier wordt een volledige structurele karakterisatie gepresenteerd. In het laboratorium van Prof. Johnson van Yale University werden IR spectra opgenomen van dit complex (in de 2+ ladingstoestand) met behulp van N_2-labeling spectroscopie bij lage temperatuur.

Hierdoor kunnen we ook de effecten van verschillende temperaturen op de spectra onderzoeken. Onze methode van gasfase reductie door gebruikmaking van de ETD optie van de QIT-MS geeft unieke toegang tot het complex in de 1+ toestand, die verantwoordelijk wordt gehouden voor de katalytische reductie van CO_2, een reactie die een belangrijke rol speelt in de ontwikkeling van hernieuwbare, CO_2-neutrale brandstoffen.

Hoofdstuk 5 richt zich op het $[Ru(bpy)_3]^{2+}$ metaal-ligand complex dat vooral erg bekend is vanwege zijn rol als dye sensitizer in bepaalde zonnecellen (dye-sensitized solar cells, DSSCs). Ladingsreductie naar de 1+ toestand speelt ook een rol in dit proces en met behulp van onze ETD gasfase reductie methode bestuderen we dit complex voor het eerst met IR spectroscopie in de twee ladingstoestanden. DFT berekeningen zijn toegepast om de gemeten IR spectra te analyseren, waarbij bleek dat de theorie vooral moeite heeft het open-schil 1+ systeem correct te karakteriseren, mogelijk door effecten van electron zelf-interactie. Een groot aantal verschillende DFT functionalen – van de conventionele B3LYP en klassieke BLYP methodes tot de modernere M06 methode – werd daarom getest op hun performance om de experimentele IR spectra van de twee leden van het $[Ru(bpy)_3]^{2+/+}$ redox-paar te reproduceren. Behalve het IR spectrum werden ook de berekende structuren nader geanalyseerd. Hierbij viel op dat vrijwel alle DFT methodes (met uitzondering van O3LYP) voorspellen dat de gemiddelde Ru – N bondlengtes kleiner zijn in het 1+ systeem dan in het 2+ systeem. Dit lijkt niet te kloppen met het intuïtieve idee dat de electrostatische binding tussen metaal ion en liganden sterker is in het 2-voudig geladen systeem en ook niet met de experimentele waarneming dat de dissociatie threshold voor verlies van een neutrale ligand veel lager is in het enkelvoudig geladen systeem, iets dat ook al uit UV fotodissociatie experimenten was gebleken. Hoewel O3LYP wel de juiste relatieve coordinatie-bondlengtes oplevert, is het voorspelde IR spectrum voor $[Ru(bpy)_3]^{1+}$ slecht in overeenstemming met het experimentele spectrum.

Een andere interessante vraag betreffende het $[Ru(bpy)_3]^{+}$ systeem is waar het extra electron naartoe gaat: naar het Ru^{2+} center of naar de liganden? En in dat laatste geval of het electron dan gedelocaliseerd is over alle drie of juist gelocaliseerd op een van de liganden? Voor enkele model peptides is aangetoond dat zogenaamde range-separated DFT functionalen goed overeenkomen met resultaten van hoog-niveau multi-reference berekeningen zoals CCSD(T) en

CASPT2. Deze range-separated functionalen hebben hier de neiging het extra electron sterker te localiseren dan conventionele functionalen (zoals B3LYP), die juist meer electron delocalisatie laten zien. Deze delocalisatie wordt geacht ten grondslag te liggen aan de onfysische electron zelf-interactie. We hebben daarom ook range-separated functionalen zoals CAM-B3LYP en LC-BLYP toege-past op het $[Ru(bpy)_3]^+$ systeem, die het extra electron inderdaad localiseren op een van de drie bpy-liganden. De $Ru - N$ bondlengtes zijn nu weliswaar intuïtief beter verklaarbaar, maar de voorspelde IR spectra komen veel slechter overeen met het experiment. Dit zou erop kunnen duiden dat het electron niet gelocaliseerd, maar juist over de liganden gedelocaliseerd is. Deze studie laat in ieder geval zien dat het voor dit soort open-schil systemen nog geen uitgemaakte zaak is welke DFT methode de meest betrouwbare resultaten oplevert.

In de volgende twee hoofdstukken bestuderen we puur organische functionele systemen. In hoofdstuk 6 vergelijken we triphenylamine (TPA) als radicaal cation ($TPA^{\cdot +}$) en als geprotoneerd systeem ($TPA{+}H^+$) met neutraal TPA. TPA wordt onder andere toegepast in de hierboven genoemde Ru(II)-polypyridyl DSSCs. Daarnaast worden afgeleiden van TPA vaak toegepast in organische photo-voltaïsche cellen (OPV). Onze spectroscopische studie van deze drie systemen in de gasfase geeft inzicht in de mate van mesomerie en electron delocalisatie in de in de gasfase geïsoleerde systemen. Bovenal laten deze experimenten zien hoe minimale geometrische veranderingen aanleiding kunnen geven tot substantiële veranderingen in het IR spectrum.

Hoofdstuk 7 laat zien hoe de simpele toevoeging van een proton de resonantie van geconjugeerde dubbele bindingen beïnvloedt in de moleculen indigo en iso-indigo. We laten spectroscopisch zien dat dit kan leiden tot cis-trans isomerisatie en kwantificeren deze ook. In tegenstelling tot een eerder gerapporteerde studie geven onze IRIS metingen aan dat isomerisatie van trans naar cis door protonering erg efficiënt is. Door de protoneringstoestand te manipuleren door middel van pH veranderingen, zouden indigo en verwante systemen dus makkelijk mechanisch geactiveerd kunnen worden. Proto-isomerisatie van deze systemen kan mogelijk toepassing vinden als moleculaire motor of moleculaire schakelaar.

Als conclusie kunnen we stellen dat we erin geslaagd zijn de ETD optie van de commerciële QIT MS te benutten om de ladingstoestand van ionische metaal-ligand complexen te manipuleren door middel van 1-electron reductie en om zo beide leden van verschillende redox-paren spectroscopisch te onderzoeken. Ondanks de exothermiciteit van deze 1-electron reductie processen konden we telkens het gereduceerde maar niet gedissocieerde reactieproduct isoleren in de QIT MS. Het radicaal anion van fluoranthene fungeerde in elk van deze experimenten als de electron donor. Deze methode biedt unieke toegang tot bepaalde open-schil ionen die niet direct met ESI geproduceerd kunnen worden. De vrije-electronen laser FELIX die in de QIT ingekoppeld kan worden, stelde ons in staat individuele IR spectra op te nemen van zowel de geoxideerde als de gereduceerde vorm van het metaal-ligand complex. Voor interpretatie van deze spectra en om hieruit geometrische structuren af te leiden werden DFT berekeningen gebruikt. Experimentele IR spectra en berekende harmonische vibrationele spectra voor de ionen in de grondtoestand komen in het algemeen nauw overeen, hoewel vooral voor de open-schil systemen ook significante afwijkingen werden gevonden. Verder theoretisch onderzoek mogelijk op hogere niveaus is hier waarschijnlijk noodzakelijk. Zo kunnen theoretische methodes experimentele data ondersteunen en tevens kunnen experimentele resultaten gebruikt worden om theoretische methodes verder te ontwikkelen.

Acknowledgments

First and foremost, I would like to cordially thank my supervisor prof. dr. Jos Oomens for selecting me as a PhD candidate in your group. Today, I am in a position to say (humbly) that your faith and belief in me have not gone in vain. Indeed, this achievement would have not been possible without your years of guidance and mentorship as well as exposing me towards a ton of opportunities to learn and grow as a PhD candidate and in the long run, I appreciate it. Most importantly, I thank you for sharing your expertise and in-depth knowledge of ion spectroscopy with me. I will not forget your constant encouragement for trying new techniques, your indulgence to make mistakes and active support during difficult times along the way that helped me to reach the ultimate goal. I am thankful for allowing me to participate in relevant summer courses here and also famous spectroscopic conferences overseas in the USA and Finland. I thank you for helping me to finalize this manuscript. I also thank your family for the lovely summer BBQs at your beautiful place in Nijmegen.

Next, I would like to thank my co-promotor dr. Giel Berden with whom I spent a significant amount of time almost daily. As a result, I have the opportunity and privilege to learn about modern laser technology in ion spectroscopy from your experience. I also thank you for being available nearly always to help me fix problems during experiments. You never stopped showing me subtle things about the experimental setups by drawing diagrams on a sheet of paper or my notebook and answering my additional questions about it. Special thanks go to you for giving me company visiting my office, having, of course, a cup of coffee in your hand when there were no other colleagues.

Then I would like to thank dr. Jonathan Martens for introducing and explaining the FELIX experiments in the quadrupole ion trap mass spectrometer. I still remember the first FELIX shift with you when we were scanning protonated indigo, a famous dye molecule to investigate the proto-isomerization of the double bond at the center of the molecule. Although this project kept us puzzled for years, we have been able to crack it, finally! A special thank goes to you for being friendly and available—sometimes even over the phone helping me out fixing problems during the early experiments in the evening. I am also very thankful to all of you for helping me in preparing posters and practicing my talks.

Now, I would like to express my humble gratitude to our local faculty committee members including the members overseas in reading, evaluating and accepting my thesis, Prof. dr. Wybren Jan Buma, Prof. dr. Jana Roithová and Prof. dr. Nicolas C. Polfer. I would also like to thank all the members of the examination committee for accepting our request to be present in the final PhD defense.

Next, I would like to thank and express my appreciation to all the past and present members of the FELIX laboratory for your support and contribution to my PhD work over the past four years. Special thanks go to both of you, dr. Lex van der Meer and dr. Britta Redlich for your dedication to science by keeping FELIX functioning and extending the capabilities of infrared light sources. Alongside, I thank FELIX board members including Jos Oomens and Andrei Kirilyuk for your effort and making a formidable team dedicated to science. I thank the whole FELIX team, which consists of a topnotch crew led by dr. Lex and dr. Britta: Rene van Buuren, Michel Riet, Guus Tielemans, Theo Neuij, Wouter Stumpel, Arjan van Vliet, Victor Claessen and Bryan Willemsen. Someone likes to call himself 'a smooth operator', you know who I mean. I used to have many evening FELIX shifts and I am truly grateful for the wonderful dinners with you.

I would also like to thank our staff members for their help regarding administrative and other miscellaneous matters, especially Henny van Tussenbroek, Bianca Leenders, Inge Derks, and our past and present FELIX secretaries Miriam Heijmerink, Erna Gouwens, as well as Martin van Breukelen, Angela den Hollander and Marloes Gielen. Special thanks to FELIX office management team for allotting me the most beautiful office room alone after the renovation of the FELIX building, probably because of my thesis writing, although I did not ask for it, I appreciate it.

Now, I would like to thank our scientific collaborators overseas. I thank prof. dr. Mark Johnson, Scott McLuckey, Stephanie Craig, Andrew DeBlase and David Foreman from the USA side involved in the project which led to a successful key publication in ion spectroscopy and this has been one of the main goals of this thesis. A special thanks goes to prof. Mark Johnson for making me famous (!) by introducing me in the middle of his talk while explaining spectroscopy of nickel-cyclam complex at the CHAINS conference (2018) and in front of the audience, I (proudly) acknowledged by raising my hand—this precious little joy, I did not forget. Moreover, I also thank prof. dr. Mary T. Rodgers and her team especially Zhu, Hamlow, Strobehn, Roy and Cunningham for the successful collaborations.

Next, I would like to thank fellow Ph.D. candidates, past and present, including B.Sc. & M.Sc. students whom I met, Josipa, Denis, Daniël, Juehan, Lisanne, Aravindh, Bin, Frank, Julianna, Kas, Olga, Pavel, Rianne, Sander, Sjors, Sandra, Arjen, Kasper, Rosina, Ruben, Mathijs, Marion, Stijn, Stefan, Douwe, Marcel, Maan, Thijs, Stach, Michał, Martijn, Johan, Qin, Jan and Thom for making my work enjoyable and keeping our FELIX laboratory alive always. For the same reasons, I thank all the postdoc scientists: Jordy, Arghya, Kamyar, Fred, Nikolas, Nils, Carl, Ilya, and Viktoria. Very big warm thanks go to colleague-scientists working at the FELIX: Anouk Rijs, Sandra Brünken, Joost Bakker and Annemieke Petrignani for their active encouragement, tips and company.

I am grateful to Prof. dr. Ria Broer and dr. Remco W. A. Havenith for your mentorship and being friendly during my stay for the M.Sc. thesis with the theoretical chemistry group at the University of Groningen in the Netherlands. For the same reasons, I would also like to thank dr. Filippo De Angelis from the 'Computational Laboratory for Hybrid and Organic Photovoltaics' in Italy and prof. dr. Paola Belanzoni at the University of Perugia, Italy. Special thanks also to prof. dr. Antonio Laganà and prof. Sergio Clementi for your guidance and help during my stay in Perugia.

I would also like to thank Prof. dr. Jean-François Boily for your mentorship for the M.Sc. thesis at the Umeå University in Sweden. Warm thanks go to dr. Bertil Eliason for your friendly time, guidance and politely listening to my complaints as a study counsellor, I appreciate and I also thank dr. Solomon Tesfalidet for helping me before I left Sweden after finishing my M.Sc.

Next, I would like to express my gratitude to prof. dr. M. Nuruddin Ahmed and Sudhanshu Kumar Roy [Bangladesh Council of Scientific and Industrial Research (BCSIR), Dhaka], who were my graduate school supervisors, for your mentorship. I also thank dr. Saleheen, whom I met in BCSIR as a PhD candidate, for your encouragement. I would also like to thank prof. dr. Gazi M. Ahsanul Kabir for your influence and guidance during my B.Sc.

Now I would like to thank all my school teachers, some of them are not alive today, who knew me the most and admired me from my childhood, especially Abul Bashar and Wahid Ullah.

Hereby I would like especially to thank my friends, Murad and Sharif for your continuous support, care and help. I also thank Gazi, Monir, A. B. Siddique, Mehdi, Kalam, Saka and Bishwajit for all the encouragements. I also thank you brother Mehdi, Lutfor, Farhad, Toky, Niaz and Arman for your encouragement and company before I left for Sweden. Special thanks go to my buddies: Kamal, Nazrul, Masud, Manik, Robiul, Kabir, Saiful Tofazzal and Ala Uddin also for arranging get-together in short notice. Similar thanks go to my cousins: Murad, Farhad, Polash, Zahir, Rahim, Ala Uddin, Zobayer, Rezvi, Bablu, Mojnu and Shamsu for their help, sharing and caring always. Warm thanks go to Rana, Rakib families for your friendly time here in Nijmegen.

Finally, my dearest parents, thank you for giving me the opportunity and blessing with this beautiful life that is filled with tons of excitements, surprises, and uncertainties, and supporting me continuously all the way. Being the youngest in the family, I have not been alone, I thank you for my brother and only beautiful sister including her extended family—my niece and nephews: Sumi, Sohorab and Al-Amin. Special thanks to my wife, Masuma Moly to come to my life, to support me, and to make my life wonderful and filled with happiness in the Netherlands. I thank all of you for your unconditional care and love.

Musleh Uddin
Nijmegen, 2019

Education

Name: Musleh Uddin Munshi
Date of birth: 31 December, 1983
Place of birth: Comilla, Bangladesh

2015-2019	Ph.D. Free Electron Laser for Infrared eXperiment (FELIX) Laboratory, Institute for Molecules and Materials (IMM), Radboud University Nijmegen, The Netherlands
2010-2014	M.Sc. in Chemistry, Umeå University, Sweden Project: Isolation and purification of Enolase from *Saccharomyces cerevisiae* (Yeast). Project: Molecular simulation of Hematite (α-Fe_2O_3)-Water/Vapor interactions.
2011-2013	Erasmus Mundus European Joint Master Degree in Theoretical Chemistry and Computational Modeling (TCCM), University of Perugia, Italy & University of Groningen, the Netherlands Project: Simulation of structural, electronic and optical properties of cyclometalated Ru(II) complexes for solar cells applications.
2002-2009	B.Sc. & M.Sc. (1^{st} class) in Chemistry, Faculty of Science, Jagannath University, Dhaka, Bangladesh